

# Turbulence at the boundary of toroidal plasmas with open and closed magnetic flux surfaces

THÈSE N° 6734 (2015)

PRÉSENTÉE LE 7 SEPTEMBRE 2015  
À LA FACULTÉ DES SCIENCES DE BASE  
CRPP - PHYSIQUE DU TOKAMAK TCV  
PROGRAMME DOCTORAL EN PHYSIQUE

ÉCOLE POLYTECHNIQUE FÉDÉRALE DE LAUSANNE

POUR L'OBTENTION DU GRADE DE DOCTEUR ÈS SCIENCES

PAR

**Fabio AVINO**

acceptée sur proposition du jury:

Prof. V. Savona, président du jury  
Prof. A. Fasoli, Dr I. Furno, directeurs de thèse  
Prof. F. Doveil, rapporteur  
Prof. M. Koepke, rapporteur  
Dr N. Vianello, rapporteur



ÉCOLE POLYTECHNIQUE  
FÉDÉRALE DE LAUSANNE

Suisse  
2015



Science is organized knowledge. Wisdom is organized life.  
— Immanuel Kant

To my family and to Rosa, the smile of my life.



# Abstract

The control and confinement of fusion plasmas are currently limited by a lack of understanding of the physical mechanisms behind the turbulent transport experienced by particles and energy. In-situ investigations of plasma turbulence in fusion experiments are strongly hampered by the high temperatures and densities. Basic plasma physics devices represent an alternative solution to perform turbulence studies with the possibility of rigorously validating numerical codes. One of these experiments is TORPEX, in which a comprehensive characterization of plasma turbulence has been conducted in the presence of open helical magnetic field lines in toroidal geometry. These reproduce the main features of the scrape-off layer (SOL), which is the open flux surface region at the edge of magnetically confined fusion plasmas. The SOL has a key role in the balance of the dynamics that determine the overall plasma confinement.

The first achievement of this thesis work is a technical upgrade of TORPEX that consists in the installation of a toroidal copper conductor inside its vacuum vessel. A poloidal magnetic field is produced by a current flowing inside the conductor, introducing a rotational transform. This allows studying plasma turbulence in magnetic geometries of increasing complexity, starting with the simplest configuration of quasi-concentric flux surfaces. The initial exploration of the main plasma properties, including plasma production mechanisms and particle confinement time, is followed by a detailed spectral characterization of the measured electrostatic quasi-coherent fluctuations. Measurements of the toroidal and poloidal mode numbers reveal field-aligned modes. These present a poloidal localization indicating a clear ballooning feature that is in agreement with the results of a linear fluid code.

The first experimental measurements of plasma blobs in the presence of a single-null X-point are performed. Blobs propagating radially outwards across the X-point are conditionally sampled, which allows us to track and analyze in detail the corresponding dynamics. The  $\mathbf{E} \times \mathbf{B}$  drifts induced by the background potential gradients and the fluctuating potential dipole are both responsible for the measured blob acceleration in the X-point region. The contribution of the potential dipole is explained on the basis of an analytical model, in which the variation of the magnetic field intensity close to the X-point plays a key role. This results in a blob speed scaling that is in good agreement with the measured values.

**Keywords:** plasma physics, nuclear fusion, magnetic confinement, plasma turbulence, TORPEX, Langmuir probes, concentric magnetic flux surfaces, electrostatic fluctuations, ballooning modes, diverted plasmas, single-null X-point, plasma particle drifts, plasma blobs.



# Résumé

Le contrôle et le confinement des plasmas pour atteindre la fusion nucléaire sont limités par la compréhension des mécanismes qui déterminent l'évolution du transport turbulent des particules et de l'énergie. Les investigations directes de la turbulence du plasma dans les expériences de fusion nucléaire sont entravées par les températures et les densités très élevées. Les expériences de physique des plasmas de base sont une solution alternative pour conduire des études de la turbulence. De plus, elles offrent la possibilité de valider les codes numériques. TORoidal Plasma EXperiment (TORPEX) est une machine de ce type, qui a été utilisée au cours des dernières années pour explorer la turbulence du plasma en géométrie toroïdale, avec des lignes de champ ouvertes et suivant des trajectoires hélicoidales. Cette configuration contient les caractéristiques principales du *scrape-off layer* (SOL), qui est la région au bord des plasmas de fusion où les surfaces de flux sont ouvertes. La SOL joue un rôle central dans l'équilibre des dynamiques qui déterminent le confinement du plasma global.

La première étape de ce travail de thèse a été une amélioration technique de TORPEX, avec l'installation d'un conducteur toroïdal en cuivre dans la chambre à vide de TORPEX. Le passage d'un courant dans ce conducteur génère un champ magnétique poloidal, qui induit une transformée rotationnelle. Il nous est alors possible d'étudier la turbulence du plasma dans des configurations magnétiques simples, avec des surfaces de flux concentriques, ainsi que des géométries plus complexes. L'exploration initiale des principaux paramètres du plasma, comme les mécanismes de production du plasma et le temps de confinement, a été suivie par une caractérisation spectrale détaillée des fluctuations électrostatiques mesurées. Les mesures des modes poloidaux et toroidaux indiquent des modes alignés avec les lignes du champ magnétique. Par ailleurs, la localisation poloidale des modes indique un aspect de ballonnement (*ballooning*), qui est en accord avec les résultats d'un code fluid linéaire.

Les premières mesures expérimentales des blobs du plasma avec un point X ont été obtenues. La méthode du *conditional sampling* a été appliquée aux blobs qui se propagent radialement vers l'extérieur du plasma à travers le point X. Il nous a alors été possible de suivre et analyser en détail leur dynamique. L'accélération du blob dans la région du point X est due à la fois aux dérives  $\mathbf{E} \times \mathbf{B}$  qui sont induites par les gradients du potentiel plasma de fond, et par le potentiel fluctuant du dipole du blob. Cette dernière contribution peut être expliquée à partir d'un modèle analytique qui prend en compte la variation d'intensité du champ magnétique près du point X. Les valeurs de vitesse du blob calculées sont en accord avec les valeurs mesurées.

---

**Mots clefs:** physique des plasmas, fusion nucléaire, confinement magnétique, turbulence du plasma, TORPEX, sonde de Langmuir, surfaces de flux concentriques, fluctuations électrostatiques, modes de ballonnement, plasma avec diverteur, dérives des particules du plasma, blob du plasma.



# Sinossi

Attualmente, il controllo e il confinamento di plasmi da fusione sono principalmente limitati dalla comprensione dei meccanismi fisici che determinano l'evoluzione del trasporto turbolento di particelle ed energia. Le ricerche sulla turbolenza di plasma in esperimenti sulla fusione nucleare sono fortemente limitate dalle elevate temperature e densità raggiunte. Le macchine sviluppate per investigare la fisica dei plasmi di base, forniscono una soluzione alternativa per lo studio della turbolenza, con la possibilità di applicare una rigorosa validazione dei codici numerici. Uno di questi esperimenti è TORPEX, sul quale è stata condotta una completa caratterizzazione della turbolenza di plasma in presenza di linee di campo magnetico elicoidali. Questa configurazione riproduce le caratteristiche principali dello scrape-off layer (SOL) presente in un tokamak, che corrisponde alla regione esterna dove le superfici di flusso sono aperte. Il SOL ha un ruolo chiave nel bilancio delle dinamiche che determinano il confinamento complessivo del plasma.

Il primo obiettivo di questa tesi è un upgrade tecnico di TORPEX, che consiste nell'installazione di un conduttore toroidale di rame all'interno della camera da vuoto. La corrente che fluisce all'interno del conduttore genera un campo magnetico poloidale, con la conseguente introduzione di una trasformata rotazionale. Ciò permette di studiare la turbolenza di plasma in geometrie magnetiche di complessità crescente, a partire dalla configurazione più semplice, caratterizzata da superfici di flusso concentriche.

L'esplorazione iniziale delle principali proprietà del plasma, tra cui i meccanismi di produzione e il tempo di confinamento delle particelle, è seguita da una dettagliata caratterizzazione spettrale delle fluttuazioni elettrostatiche quasi coerenti misurate. Le misure dei numeri toroidale e poloidale del modo, rivelano la presenza di modi allineati con le linee di campo. La localizzazione poloidale di questi modi suggerisce una natura di tipo ballooning. Ciò è confermato numericamente da simulazioni lineari effettuate con un codice basato sulle equazioni fluide di plasma.

Inoltre, sono state eseguite le prime misure di blob di plasma in presenza di un punto X. I blob che si propagano radialmente verso l'esterno, attraversando il punto X, sono stati analizzati tramite il metodo del *conditional sampling*. Le corrispondenti dinamiche sono state seguite e analizzate in dettaglio. L'accelerazione misurata dei blob nella regione del punto X viene spiegata in termini di due meccanismi principali: il drift  $\mathbf{E} \times \mathbf{B}$  indotto dai gradienti del potenziale elettrostatico di fondo, e quello relativo al dipolo elettrico interno al blob. Quest'ultimo, in particolare, presenta un'evoluzione che può essere spiegata con un modello analitico, dove la variazione dell'intensità del campo magnetico vicino al punto X gioca un ruolo determinante. Ciò risulta in una stima della velocità del blob che è in buon accordo con i valori misurati.

---

**Parole chiave:** fisica del plasma, fusione nucleare, confinamento magnetico, turbolenza di plasma, TORPEX, sonde di Langmuir, superfici magnetiche di flusso concentriche, fluttuazioni elettrostatiche, modi ballooning, plasmi con divertore, punto a X, drift della particelle del plasma, blob di plasma.

# Contents

<b>1</b>	<b>Introduction</b>	<b>1</b>
1.1	Nuclear Fusion . . . . .	1
1.2	Plasma . . . . .	3
1.3	Fusion devices . . . . .	5
1.3.1	Magnetic Confinement Fusion . . . . .	6
1.4	Motivation and Outline . . . . .	9
<b>2</b>	<b>TORPEX</b>	<b>13</b>
2.1	Vacuum vessel . . . . .	13
2.2	Magnetic field . . . . .	15
2.3	Plasma production . . . . .	16
2.4	Diagnostics . . . . .	18
2.4.1	Langmuir probes . . . . .	18
	The new HEXTIP movable twins . . . . .	22
	The field-aligned probe array . . . . .	24
	The oblique field electrode . . . . .	25
2.4.2	Other diagnostics . . . . .	27
2.5	Previous turbulence studies . . . . .	28
2.6	Summary . . . . .	31
<b>3</b>	<b>In-vessel toroidal conductor</b>	<b>33</b>
3.1	Overview of the experimental set-up . . . . .	34
3.1.1	Toroidal copper conductor . . . . .	35
3.1.2	Current feed-through . . . . .	36
3.1.3	Circuit and control . . . . .	38
3.2	System requirements and design . . . . .	39
3.2.1	Accessible safety factor . . . . .	39
	Current ripple tolerance . . . . .	40
3.2.2	Conductor heating . . . . .	41
3.2.3	Stresses on the set-up . . . . .	43

## Contents

---

Vertical supports . . . . .	44
3.3 Accessible magnetic configurations . . . . .	45
3.3.1 Wall-limited configurations . . . . .	46
3.3.2 Diverted configurations . . . . .	47
Horizontal single-null X-point . . . . .	47
Vertical single-null X-point . . . . .	47
Vertical double-null X-point . . . . .	48
Second-order null-point (snowflake divertor) . . . . .	49
3.4 Magnetic field measurements . . . . .	49
3.4.1 Experimental set-up for the magnetic field measurements . . . . .	49
3.4.2 Measurements of magnetic field . . . . .	50
3.5 Summary . . . . .	52
<b>4 Plasma features in the closed field line configuration</b>	<b>53</b>
4.1 Time-averaged plasma profiles . . . . .	53
4.1.1 Ion saturation current profiles . . . . .	53
4.1.2 Plasma potential and temperature profiles . . . . .	56
4.1.3 Control parameter dependence . . . . .	56
Plasma profile sensitivity to $B_\theta$ - toroidal copper conductor (TC) current	57
$B_\phi$ - electron cyclotron (EC) layer radial position . . . . .	58
Magnetron power scan and the enhanced plasma production regime . .	60
Neutral pressure . . . . .	63
Ion mass - Gas type . . . . .	65
4.2 Plasma production . . . . .	66
4.2.1 Plasma breakdown dynamics . . . . .	67
4.2.2 Steady-state plasma source . . . . .	67
4.2.3 Enhanced plasma production regime . . . . .	70
4.3 Plasma particle confinement time . . . . .	71
4.4 Summary . . . . .	72
<b>5 Electrostatic fluctuations in the closed field line configuration</b>	<b>75</b>
5.1 Experimental studies of quasi-coherent modes . . . . .	76
5.1.1 Data analysis techniques . . . . .	76
Spectral analysis . . . . .	76
Statistical structure analysis . . . . .	79
Conditional average sampling . . . . .	81
5.1.2 Plasma scenario and experimental set-up . . . . .	82
5.1.3 Identification of quasi-coherent modes . . . . .	84
5.1.4 Wave number and mode number measurements . . . . .	88
5.1.5 Mode poloidal rotation . . . . .	92
$B_\phi$ inversion effects on the fluctuation dynamics . . . . .	95
5.2 Numerical studies of quasi-coherent modes . . . . .	96
5.2.1 Driving mechanism of the dominant quasi-coherent modes . . . . .	97

5.3 Summary . . . . .	98
<b>6 Electrostatic fluctuations in single-null X-point configurations</b>	<b>99</b>
6.1 Overview of the explored magnetic configurations . . . . .	99
6.2 Plasma flow dependence on the X-point position . . . . .	103
6.2.1 Background profiles . . . . .	104
6.2.2 Plasma particle fluxes . . . . .	105
6.3 Summary . . . . .	107
<b>7 The effect of the magnetic X-point on plasma blob dynamics</b>	<b>109</b>
7.1 Background plasma profiles . . . . .	110
7.2 Experimental blob dynamics from conditional sampling . . . . .	111
7.3 Analytical model for blob speed . . . . .	114
7.4 Comparison of experimental data with analytical predictions . . . . .	116
7.5 Summary . . . . .	117
<b>8 Conclusions</b>	<b>119</b>
<b>A Neutral pressure measurements</b>	<b>123</b>
A.1 TORPEX gauge calibration curves . . . . .	123
<b>B Toroidal conductor technical notes</b>	<b>127</b>
B.1 Procedure for the TC vertical displacement or disassembling . . . . .	127
B.2 Remote control system . . . . .	129
B.2.1 Activate . . . . .	130
B.2.2 Deactivate . . . . .	130
B.2.3 Operation . . . . .	131
B.2.4 Control word programming . . . . .	132
<b>C Magnetic snowflake</b>	<b>135</b>
<b>Acronyms</b>	<b>137</b>
<b>Repeatedly used symbols</b>	<b>141</b>
<b>Bibliography</b>	<b>153</b>
<b>Acknowledgements</b>	<b>155</b>
<b>Curriculum Vitae</b>	<b>157</b>



# Introduction

## 1.1 Nuclear Fusion

Nature constitutes a constant source of inspiration to overcome the problems that mankind faces. In particular, the global energy demand is increasing at such a rate that our generation is forced to look for alternatives to the current energy options. In the last 60 years, the scientific community has investigated a possible answer looking at the primary energy source of our planet: the Sun (Fig. 1.1).

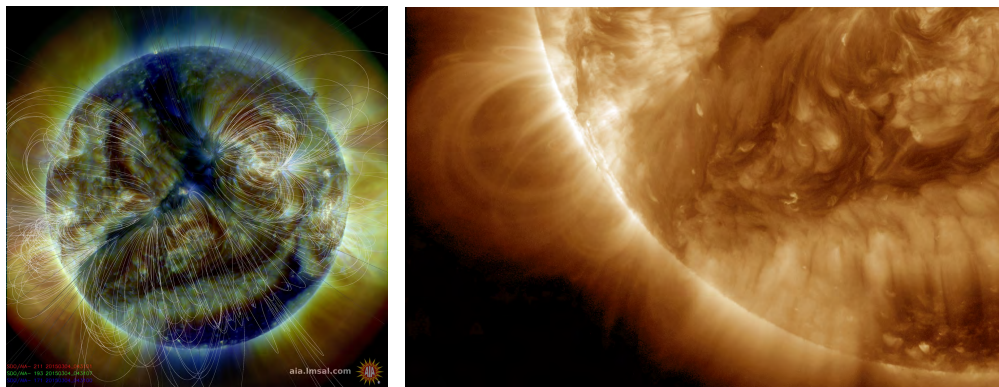


**Figure 1.1** | On the left, photograph of the Sun from the Atmospheric Imaging Assembly (AIA) of the Solar Dynamics Observatory (SDO), filtered for the [211, 193, 171] Å wavelengths. The white trajectories indicate the magnetic field lines [1]. On the right a detail for the 193 Å [2].

A power of  $10^{26}$  W is constantly emitted by the Sun [3], but only  $10^{11}$  W reach the Earth surface, corresponding to an average energy flux of  $1.37 \text{ kW/m}^2$ . Present technology allows producing electricity from it, but at the same time the efficiency of the implemented physical process poses severe constraints, both practical and economical: expensive photovoltaic panels covering an area comparable to that of the city to be powered would be necessary. A less direct and more challenging approach is to make a leap ahead and reproduce nuclear fusion

## Chapter 1. Introduction

reactions in controlled conditions. Nuclear fusion is the physical mechanism [4] responsible for the creation of all the known elements heavier than hydrogen ( $H_2$ ), and consists in the production of a new nucleus after two lighter ones fuse into an intermediate unstable nucleus. If the total mass of the final products,  $\sum_f M_f$ , is smaller than that of the reacting nuclei,  $\sum_i M_i$ , the nuclear reaction is exothermic. A quantity of energy proportional to the mass difference

$$\Delta M = \sum_i M_i - \sum_f M_f > 0 \quad (1.1)$$

is released in the form of kinetic energy of the produced particles according to Einstein's relation  $E = \Delta M c^2$ . This can be understood in terms of the strong nuclear force<sup>1</sup> acting on the nucleons (protons and neutrons), the elements constituting the nuclei. This interaction provides a binding energy  $B$  for the nucleus to be stable, resulting in a total mass  $M$  lower than the sum of masses of the single nucleons. This can be expressed as

$$M = Z m_p + (A - Z) m_n - \Delta m_B, \quad (1.2)$$

where  $A$  is the mass number,  $Z$  is the number of protons with mass  $m_p$ ,  $(A - Z)$  is the number of neutrons with mass  $m_n$  and  $\Delta m_B = B/c^2$  is the lack of mass transformed into binding energy. Consequently, eq. (1.1) and eq. (1.2) indicate that exothermic reactions correspond to those where  $\sum_f B_f > \sum_i B_i$ , or equally those where the final products have larger  $B/A$  than the reactants. We can identify these reactions from the dependence of the binding energy per nucleon versus the mass number. We see in Fig. 1.2 that fusion reactions are exothermic for  $A \lesssim 56$ , while for heavier nuclei the process has to be reversed to extract energy (fission).

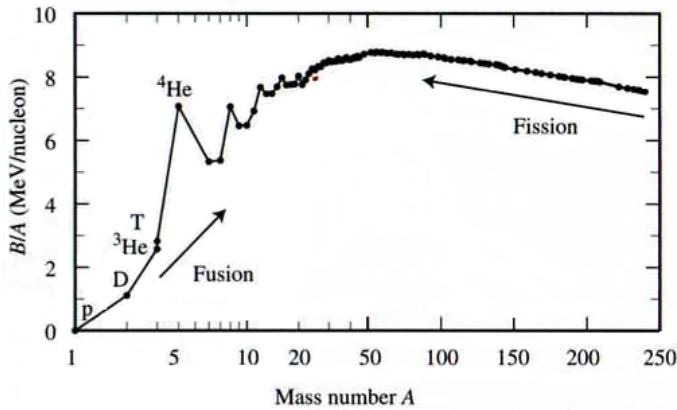


**Figure 1.2** | Binding energy per nucleon versus mass number  $A$  for the most stable elements [5].

In the Sun, several reactions resolve in a chain, starting with a proton-proton fusion  $p^+ + p^+ \rightarrow 2H + e^+ + \nu + 0.42 \text{ MeV}$ , where  $e^+$  is a positron,  $\nu$  is a neutrino and  $0.42 \text{ MeV}$  ( $1 \text{ eV} \approx 11.600 \text{ K}$ ) is the output kinetic energy.

<sup>1</sup>One of the four fundamental forces of nature: the gravitational, electromagnetic, strong nuclear, and weak nuclear forces.



## 1.2 Plasma

In an experiment designed to produce fusion reactions, as in the Sun, it is unavoidable to deal with highly energetic particles. Two or more particles with the same charge must get close enough to overcome the Coulomb potential barrier and fuse under the effect of the strong interaction. This process is facilitated by the quantum tunnelling, which allows a particle with an energy lower than the height of the barrier to pass through it. The required energy is at least of the order of  $10^4$  eV and in these conditions the natural state of the matter is called plasma, the fourth state of matter. The plasma state can be typically reached at about 10.000 K, when ionization processes start to occur and electrons are ripped off from the atoms. The partially or completely ionized gas constitutes a system susceptible to externally applied electromagnetic fields, dominated by long-range interactions and characterized by collective behaviors. For example, these generate the strong electric forces responsible for the plasma quasi-neutrality on macroscopic scales [6]. Plasma temperatures are generally too high to be compatible with the presence of life, which is the reason why on the Earth there are only a few examples of plasmas. Some of them are shown in Fig. 1.3. The most common manifestation of plasmas on our planet are flames, with temperatures of the order of 1.000 K, but much

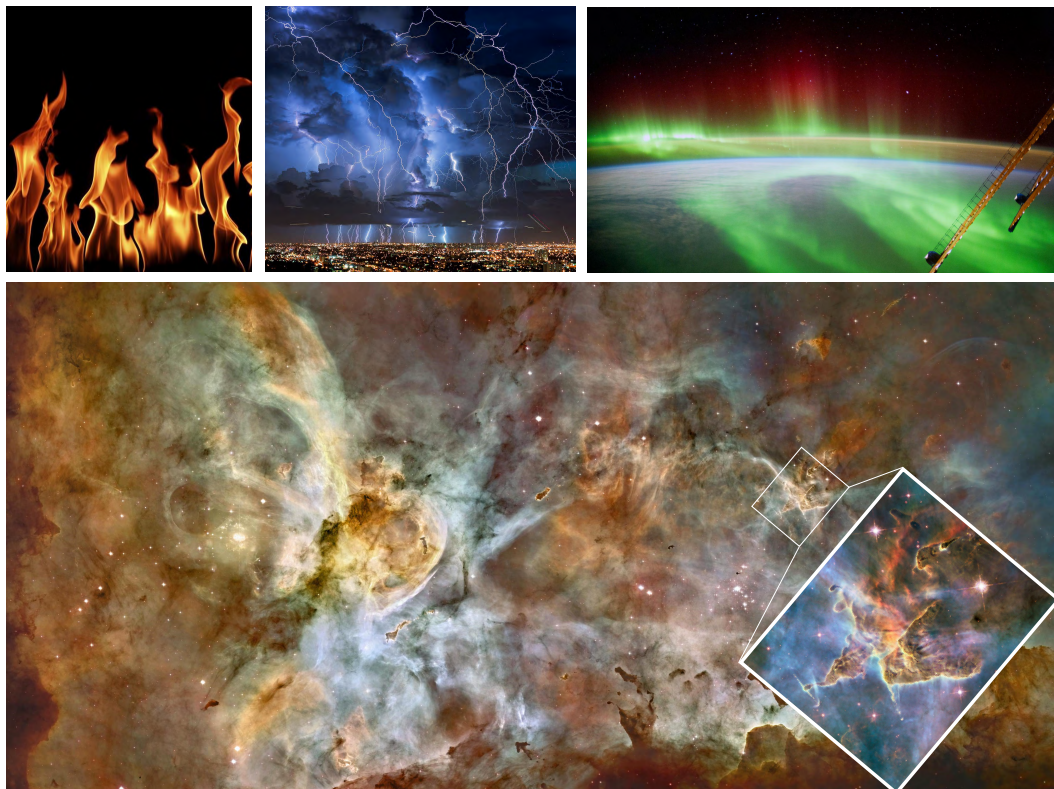


**Figure 1.3** | On the top, examples of plasmas on Earth: from the left a flame, a lightning storm and an aurora captured from the International Space Station. On the bottom, a photograph taken from the Hubble Space Telescope of the Carina Nebula (NGC 3372), 7.500 light-years away from Earth, with a detail of the "Mystic Mountain", a star forming region.

## Chapter 1. Introduction

higher temperatures are reached by lightnings ( $\sim 50.000\text{ K}$ ), which occur over time-scales of hundreds of milliseconds. However, as we start to leave the Earth atmosphere, most of the ordinary matter is in the form of a plasma. Already at 80 km of altitude, in the *ionosphere*, a plasma with a density of  $10^{11}\text{ m}^{-3}$  at 1.000 K is present. Plasma is constantly emitted by the Sun at supersonic speed, with densities and temperatures in the range of  $10^6\text{ m}^{-3}$  and  $10^5\text{ K}$ . This phenomenon, called *solar wind*, is responsible for the ionization of neutral particles in the Earth atmosphere at high latitudes, with the consequent emission of light resulting in auroras [7]. In the outer space, the region between celestial bodies, there is only a partial vacuum. Interstellar clouds (nebulae - Fig.1.3) and intergalactic space are filled with a low temperature and a low density plasma. The Sun itself, as all the stars, is a giant sphere of plasma with a temperature ranging from  $10^7\text{ K}$  in the core to 6.000 K on the surface [8]. Overall, the temperature and density ranges covered by plasmas span over several orders of magnitude, as indicated in Fig. 1.4 and Tab. 1.1. Low temperature plasmas are routinely implemented in industrial processing, from surface treatment (etching, cleaning) to the commonly used neon lamps and TV screens, or plasma thrusters for aerospace applications. The more we move towards the top right of Fig. 1.4, the higher is the effort required to handle the corresponding laboratory plasmas. In particular, those with a thermonuclear interest pose serious confinement problems for the required temperatures and densities.

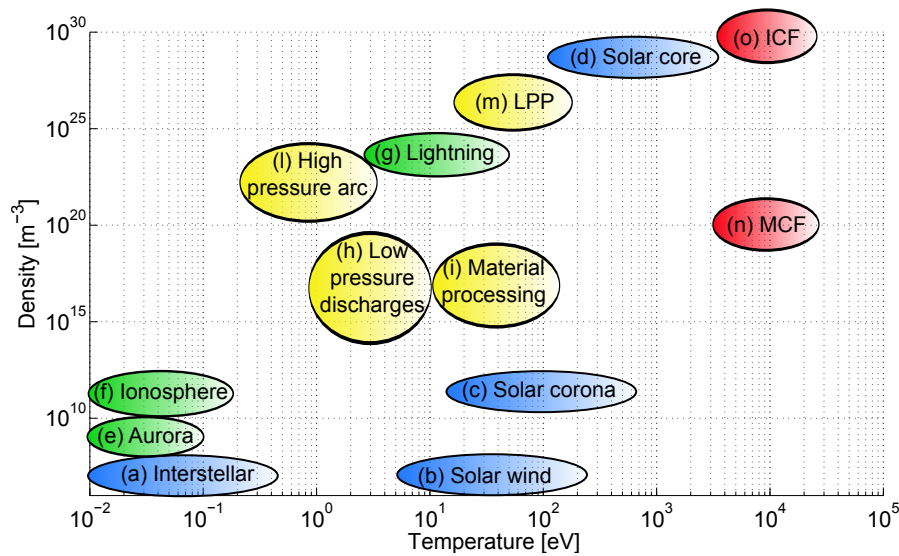


**Figure 1.4** | The plasma universe [8,9]. Examples of space (blue), geophysical (green), industrial (yellow) and fusion (red) plasmas. LPP refers to Laser Produced Plasmas, ICF to Inertial Confinement Fusion and MCF to Magnetic Confinement Fusion.

	(a)	(b)	(c)	(d)	(e)	(f)	(g)	(h)	(i)	(l)	(m)	(n)	(o)
$\log_{10}(n [\text{m}^{-3}])$	6	7	12	30	9	12	24	14-18	18	24	26	20	28
$\log_{10}(T [\text{eV}])$	-2	1	2	3	-2	-1	1	1-2	1-2	0	2	4	4

**Table 1.1** | Plasma parameters referring to the examples in Fig. 1.4.

### 1.3 Fusion devices

"It is a device within which appropriate isotopes of light elements could be caused to undergo nuclear fusion, the end result being the controlled production and extraction of useful quantities of energy, in excess of that required to operate the device". This is the answer to the question "What is a fusion reactor?" given in 1956 by R. Post [10], representing the ongoing effort of the scientific community to reproduce a small star on Earth to achieve a clean, safe and essentially inexhaustible source of energy.

First, the most promising reactions were identified in terms of output energy and required temperature for fusion reactions to be relevant in comparison to the other involved physical processes. We briefly report in Tab. 1.2 these reactions with the corresponding values of the cross sections<sup>2</sup> for relevant temperatures.

Reaction (values in MeV)	Cross section $\sigma$ [m <sup>2</sup> ]	Energy (keV)
$p+p \rightarrow D + e^+ + \nu_{(0.27)} + 1.17$	$3 \times 10^{-54}$	10
$D+D \rightarrow T_{(1.01)} + p_{(3.03)}$	$5 \times 10^{-32}$	64
$D+D \rightarrow He^3_{(0.82)} + n_{(2.45)}$	$5 \times 10^{-32}$	64
<b><math>D+T \rightarrow He^4_{(3.52)} + n_{(14.06)}</math></b>	<b><math>5 \times 10^{-30}</math></b>	<b>10</b>

**Table 1.2** | Examples of fusion reactions with the cross sections for the corresponding temperatures. D, T and He are, respectively, a nucleus of Deuterium, Tritium and Helium. p corresponds to a proton, n to a neutron,  $\nu$  a neutrino and  $e^+$  a positron. The values in the parenthesis indicate the kinetic energies of the particles in MeV.

The most convenient reaction involves the fusion of the nuclei of two isotopes of hydrogen, Deuterium and Tritium, releasing a neutron and one alpha particle (nucleus of Helium). Most of the output kinetic energy resulting from the mass difference between reactants and products is channeled into the neutron, according to the principle introduced in Sec. 1.1. An operational temperature of  $10^4$  eV is required and represents the first goal for the exploration of different experimental solutions. The simplest concept of accelerating a mono-energetic population of ions on a fixed target or towards a second beam (acceleration-based fusion [10]) would result in a process dominated by Coulomb collisions<sup>3</sup>, only heating the target. This is the reason why a high temperature plasma in thermal equilibrium is necessary. In the Sun, the balance between the plasma pressure and its own gravitational field provides the equilibrium for a stable fusion burning. On Earth, the challenge is to implement a different way to confine the mixture of highly energetic charged particles in a limited region where the first and fourth state of matter have to co-exist. The available technology and the limited thermal resistance of the known materials have led to the selection of two main alternatives that are under investigation today: Inertial Confinement Fusion (ICF) and Magnetic Confinement Fusion (MCF).

<sup>2</sup>This provides an estimate of the probability for a generic reaction to happen.

<sup>3</sup>Most of the particle energy is lost in the emission of Bremsstrahlung radiation.

## Chapter 1. Introduction

The ICF [5] (Fig. 1.5-left) is based on the idea of directing several high power lasers<sup>4</sup> on a small D-T fuel pellet. High precision timing and alignment allow an almost isotropic ablation of the pellet surface on nanosecond time scales, consequently compressing the inner core by momentum conservation ("rocket effect") and leading to fusion reactions in it [12]. The feasibility of a fusion reactor based on this concept is strongly hampered by the difficulty in handling the involved plasma instabilities, by the total efficiency of the process and by the high repetition rate of the pellet injection required to obtain relevant output energies. MCF (Fig. 1.5-right) aims at producing fusion relevant plasmas and keep them in steady state conditions by using magnetic fields.

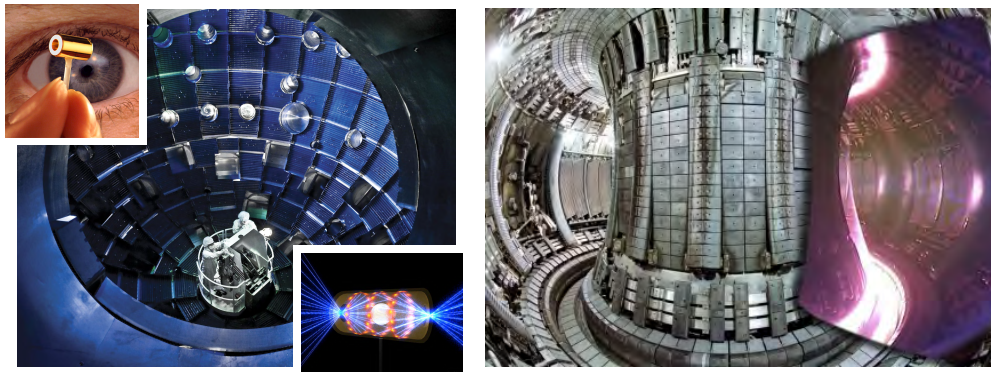


**Figure 1.5** | On the left, image of the laser chamber at NIF. On the top inset, photograph of the target cylinder containing the fuel pellet, while on the bottom inset, sketch of the fusion process [13]. On the right, interior of the Joint European Torus (JET) vacuum vessel, with a detail of the visible light emitted during a plasma discharge [14].

### 1.3.1 Magnetic Confinement Fusion

Charged particles respond to the presence of a magnetic field by feeling the Lorentz force, which modifies their trajectories in helices around the field lines. This suggests the possibility of using magnetic fields to trap the plasma energetic particles and avoid that they intercept the containing walls. Equilibrium considerations indicate that helical field lines wrapping around a torus provide an optimal magnetic field geometry (Fig. 1.6 green lines, Fig. 1.7 yellow lines): exploring both the upper and lower part of the torus, the particles cancel the  $\mathbf{B} \times \nabla B$  induced electric field that would result in an outward  $\mathbf{E} \times \mathbf{B}$  drift of the whole plasma column. This configuration can be attained mainly in two ways: the stellarator and the tokamak.

In a stellarator the total magnetic field is obtained using only external field coils (Fig. 1.6). A solution consists in a primary field generated by toroidal field coils, superimposed to a component resulting from helical field coils, like those shown in Fig. 1.6-left and implemented on Wendelstein 7-A. Present technology allows a different design approach, where a unique set of modular toroidal coils is manufactured to produce an optimized plasma shape, like that of Wendelstein 7-X [15] (Fig. 1.6-right).

A tokamak [17] is basically a transformer, exploiting the high plasma conductivity to induce

<sup>4</sup>The National Ignition Facility (NIF) contains a 192-beam, 1.8 MJ, 500 TW ultraviolet laser system [11].

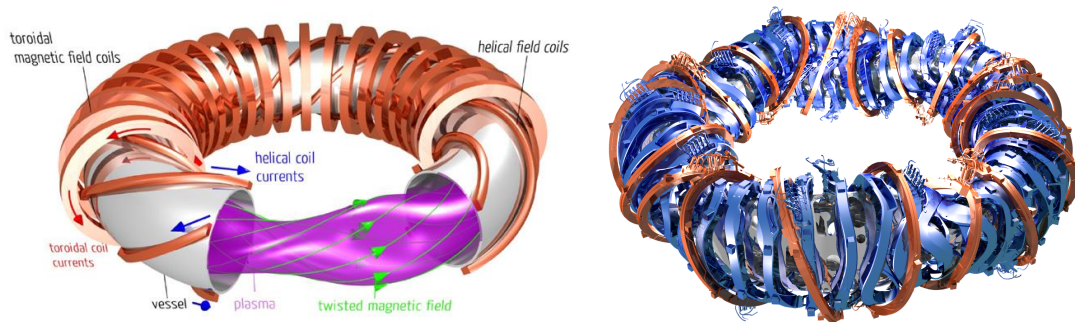


**Figure 1.6** | Left: schematic design of a stellarator [16]. Right: magnetic field coils of Wendelstein 7-X.

a toroidal plasma current (red arrows in Fig. 1.7) that has a twofold role: it generates the poloidal magnetic field that allows to nest the magnetic field lines together with the main toroidal component (obtained by external magnetic coils), and at the same time it heats the plasma. However, the temperature dependence upon the plasma resistivity ( $\eta \sim T^{-3/2}$ ) implies a decreasing efficiency of the Ohmic heating as  $T$  rises. Therefore, both stellarators and tokamaks require auxiliary heating techniques to increase the plasma temperature up to approximately  $10^4$  eV and achieve fusion conditions. The plasma heating systems generally implemented include the neutral beam injection (NBI) and radio-frequency (RF) waves<sup>5</sup>. In tokamaks, a major problem is posed by plasma disruptions, consisting in a global loss of the plasma confinement with the consequent deposition of a high power on the surrounding walls [18]. Stellarators are inherently disruption-free, since the required magnetic configurations are

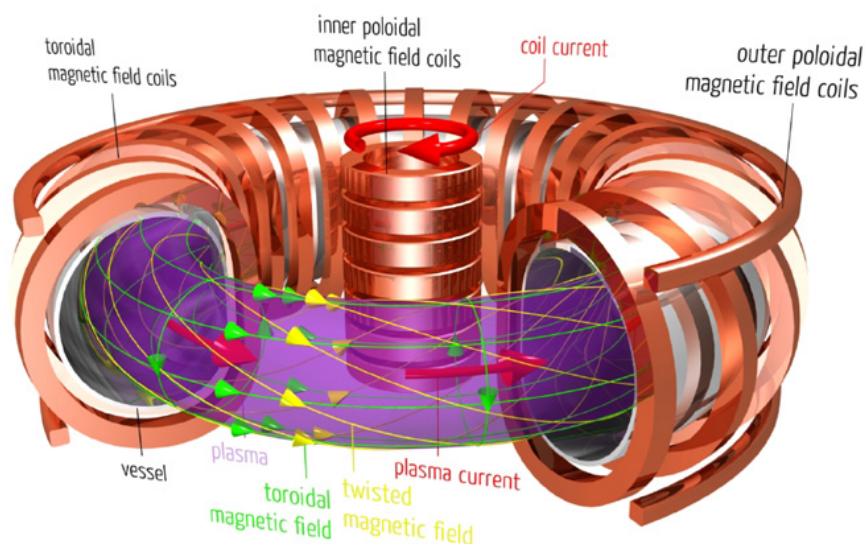


**Figure 1.7** | Schematic design of a tokamak [16].

<sup>5</sup>Electron cyclotron resonance heating (ERCH) or ion cyclotron resonance heating (ICRH).

generated without a toroidal plasma current. Moreover, the absence of any inductive process allows a much easier access to steady-state operations with respect to tokamaks. The first step to assess the success of one of the two options will be determined by the capability of reaching the breakeven, where more power  $P_{\text{out}}$  than that required as input for the system  $P_{\text{in}}$  is produced. The gain factor  $Q$ , defined as the ration  $P_{\text{out}}/P_{\text{in}}$ , quantifies the efficiency of the reactor. Investigations on the creation of an hot plasma and its thermal insulation by a toroidal magnetic field were initiated at the Kurchatov institute, where the first TMP tokamak was developed in 1956, with a plasma current of 200 kA [19]. After 42 years, JET established the present world record of  $Q \approx 0.63$ , where 16.1 MW of D-T fusion power were produced from 25.4 MW of input power [20]. The next step is ITER [21–23], a project born from a wide international cooperation to construct in Cadarache (France) an experimental reactor designed to reach  $Q = 10$ , which will become operational within the next decade. However, a gain factor even higher must be accessible for a realistic fusion power plant, taking into account that only the fusion alpha particles can be confined and exploited to keep a self-sustained plasma, as well as the efficiencies of the processes to obtain electricity for the grid.

The basic layout of a tokamak magnetic field is characterized, on most of the plasma volume, by field lines that define closed flux surfaces (Fig. 1.7). In the outer region of the plasma, called the scrape-off layer (SOL), the field lines intercept the surrounding walls, where a high amount of power can be deposited. This magnetic configuration has been optimized during the years to guarantee that the plasma facing components can withstand the output fluxes of particles and energy. One of the investigated solutions is the diverted geometry, meant to drive the plasma leaking out of the central confinement region in a well-defined exhaust area on the bottom of the vacuum vessel (Fig. 1.8). This allows both to remove waste material and to mitigate high power fluxes using impurity seeding and forcing the plasma to radiate most of its energy while limiting the perturbation of the central core [24, 25].

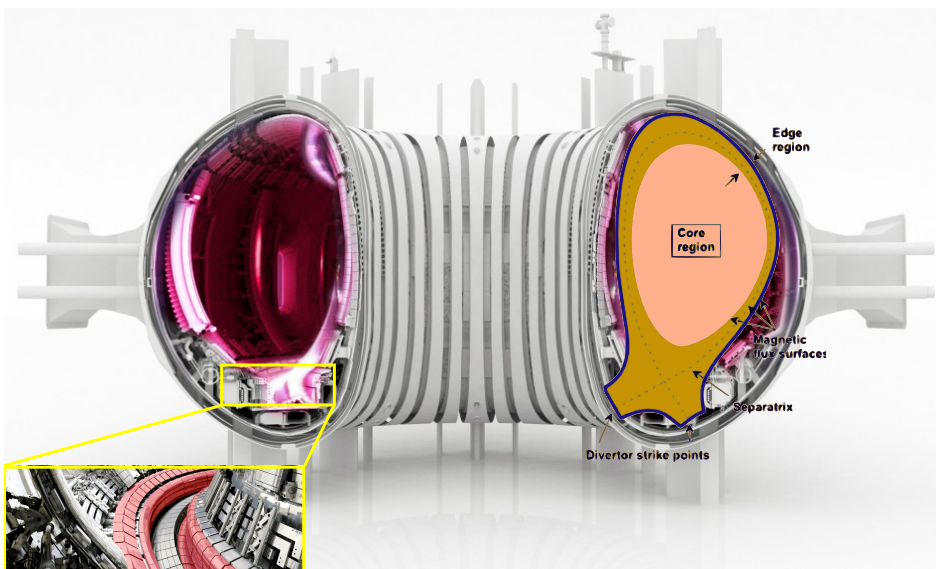


**Figure 1.8** | Cut of JET torus where a single null X-point configuration is implemented. On the bottom left, a detail of the divertor. Image adapted from [25, 26]

A comprehensive understanding of the global particle and energy transport in toroidal fusion devices constitutes one of the main open issues. Theory predicts a plasma cross-field diffusion, defined *neoclassical*, resulting from the combination of particle Coulomb collisions and complex orbits in toroidal geometry and with peculiar features according to the plasma collisionality. However, the estimated diffusion coefficients are two orders of magnitude lower than those obtained from experiments. This measured enhanced plasma transport is generally referred to as *anomalous* [27], and experimental investigations have pointed towards plasma turbulence as its major cause. At the edge, turbulence shows a convective behavior with intermittent energy bursts [28–30]. The associated power fluxes are so significant that they constitute a serious issue and constraint for the lifetime of ITER and future fusion reactors. Turbulence develops from the presence of free energy sources (e.g. pressure gradients), from which plasma instabilities extract energy that feed into turbulent fluctuations, leading to linearly unstable modes that subsequently evolve linearly. In the last decades, a strong effort has been dedicated by the fusion community to the investigation of plasma instabilities, from their linear evolution to the highly turbulent non-linearly saturated state [31–33]. However, the complexity of the problem is extremely challenging, involving multiple charged turbulent fluids coupled through electromagnetic fields. Further studies are therefore necessary to obtain a deeper understanding of the topic.

### 1.4 Motivation and Outline

The anomalous transport discovered in tokamaks has a key role in the performance and operation of a fusion reactor. This requires further experiments on plasma heat, momentum and particle transport processes. Investigations on tokamaks are hampered by the high temperatures and densities limiting the use of direct diagnostics. Probes can only be inserted for a very short time in the SOL [34, 35]. Fast cameras in the visible range [36] provide indirect measurements of edge-localized modes (ELM) and blobs, with gas puff imaging (GPI) in some cases [37]. Current experimental data about the structures and dynamics of the energy and particle losses during ELMs are not sufficient to verify the proposed models concerning either their origin [38] or their evolution [39]. Basic plasma physics experiments [40–45] offer an alternative solution for turbulence studies, allowing a much easier diagnostic access, due to lower temperature and density plasmas. One of these machines is TORPEX [46], a basic plasma physics device where important features of a tokamak SOL, namely density gradients in the presence of curvature and gradient of the magnetic field, are reproduced in the simple magnetized torus (SMT) configuration of open helical field lines. However, this configuration lacks a poloidal field component, which characterizes tokamak plasmas with closed flux surfaces.

In this thesis, we address the problem of plasma turbulence and electrostatic instabilities on TORPEX with a novel scheme to include a poloidal magnetic field component. This is produced by driving a toroidal current applying a voltage at the two extremes of an in-vessel toroidal conductor. The presented solution allows us to better mimic the tokamak SOL and to

reproduce more fusion relevant scenarios, including diverted configurations with first order (X-point) or second order (snowflake) magnetic null points. In particular, we focus on plasmas with quasi-concentric flux surfaces and magnetic configurations with an X-point. The latter has a central relevance in fusion research since diverted magnetic geometries are the leading candidates to handle the particle and energy outflow from the plasma core. A comprehensive understanding of the plasma dynamics in the X-point region and along the divertor legs is necessary.

The investigation of the mechanisms behind turbulent behaviors in magnetized plasmas has a much wider relevance than fusion-related applications, since the definition of a theoretical model to describe the statistics of a turbulent flow is one of the unsolved problem in physics [47–49]. Turbulence characterizes the fluid dynamics of many physical systems and the interplay between different fields has a crucial role in scientific progress. Examples of turbulence include the flow in many industrial equipment [50] as well as the external flow around all kind of vehicles [51]. Geophysical evidences of turbulence cover a wide range of spatial scales, from the size of small rivers [52] to terrestrial atmospheric circulation [53]. The understanding of many astrophysical phenomena is critically linked to their turbulent features [54], like in accretion disks [55] or in the solar corona [56]. Even the heart sounds reflect the turbulence created when the heart valves snap shut.

This thesis is structured as follows:

In **Chapter 2**, we present TORPEX focusing on the technical features of the device, including the pumping system, the production and confinement of the plasma and the main available diagnostics. We conclude with the main plasma properties during a typical discharge and with a summary of the results obtained in the last years on TORPEX operated as a simple magnetized torus (SMT). These provide the basis to deal with magnetic field configurations of increasing complexity.

**Chapter 3** overviews the toroidal copper conductor system installed on TORPEX, which is the key technical achievement of this thesis work. We start from its design optimization, taking into account several technical constraints, such as the Ohmic heating of the conductor, the required features of the power supply and the mechanical supports. We then move to the commissioning of the set-up and the poloidal magnetic field measurements, concluding with a description of the most relevant accessible magnetic field geometries.

**Chapter 4** is focused on the characterization of plasma features in the presence of a poloidal magnetic field with quasi-concentric flux surfaces. Plasma production mechanisms are analyzed, as well as measurements of the particle confinement time. Time-averaged and fluctuating plasma parameters are compared to those of the SMT configuration.

In **Chapter 5**, we present the results of the plasma electrostatic fluctuation studies in quasi-concentric flux surfaces. Ion saturation current fluctuations are characterized in terms of power spectral density to identify the dominant coherent modes and their spatial localization. A statistical approach is used to determine the mode spectral properties by computing the



statistical dispersion relation. The poloidal and toroidal wave numbers are obtained, as well as the corresponding mode numbers. A three-dimensional linear code based on the drift-reduced Braginskii equations is used to investigate the nature of the instabilities. The linear analysis suggests a dominant ballooning character of the modes.

In **Chapter 6**, we explore some of the accessible fusion relevant magnetic geometries, in particular in the presence of a single null X-point. A first insight into the electrostatic fluctuation dynamics is given. Plasma particle flows are analyzed varying the X-point position.

**Chapter 7** is dedicated to the study of plasma blob dynamics in the region of an X-point. The blob speed is obtained from conditionally sampled averaged data. A strong acceleration of the structure along its trajectory towards the X-point is observed. The  $\mathbf{E} \times \mathbf{B}$  drift contributions of the background plasma potential gradients and blob potential dipole are isolated, showing a time evolution that can explain the fast blob dynamics. An analytical model based on charge conservation is derived for the blob speed associated to the potential dipole, including the ion polarization currents, diamagnetic currents and parallel currents. A crucial role is played by the variation of the magnetic field intensity in the vicinity of the X-point. The predicted values displays a good quantitative agreement with the experimental data.

Finally, **Chapter 8** summarizes the presented studies, providing an outlook for further investigations that have become possible with the inclusion of the toroidal conductor system.



## TORPEX

TORPEX [46] is a basic plasma physics device at the *Centre de Recherches en Physique des Plasmas* (CRPP) of the *École polytechnique fédérale de Lausanne* (EPFL), in Switzerland. It constitutes the main tool of this thesis. A photograph of the experimental set-up is shown in Fig. 2.1. TORPEX was designed to provide a flexible environment for plasma turbulence studies addressing basic physics issues of fusion relevance. The main advantage with respect to large fusion devices consists in the low power fluxes, allowing to perform a comprehensive exploration over the entire plasma volume. Typical plasma parameters include a plasma density  $n_e \approx 10^{16} \text{ m}^{-3}$  and an electron temperature  $T_e < 10 \text{ eV}$ . The ion species are generally considered cold ( $T_i < 1 \text{ eV}$ ) for the lack of any relevant associated heating mechanism. The operational flexibility of TORPEX is maximized by the very high plasma reproducibility and the possibility to continuously sustain the plasma for several minutes by microwave injection, which assures the required statistics.

In this chapter, we detail the different aspects and components of the device starting from the vacuum vessel and the air evacuation before the gas injection, to the plasma production and confinement. We give an overview of the available diagnostics to investigate the plasma properties, concluding with a summary of the results achieved in the last years.

### 2.1 Vacuum vessel

A toroidal chamber with  $R_0 = 1 \text{ m}$  major radius and  $a_0 = 0.2 \text{ m}$  minor radius is obtained by assembling four electrically insulated sets. Each of them is composed of three stainless-steel sectors covering a toroidal angle of 30 degrees. The access to the inner volume of the vessel is guaranteed by 48 ports almost equally distributed on the top, bottom and side of the chamber. Four movable sectors, toroidally separated by 90 degrees from each other [57], are designed to allow the installation of components requiring a major access to the inner vessel. These sectors can be removed sliding on rails along the radial direction, as shown in the top-right inset of Fig. 2.1.

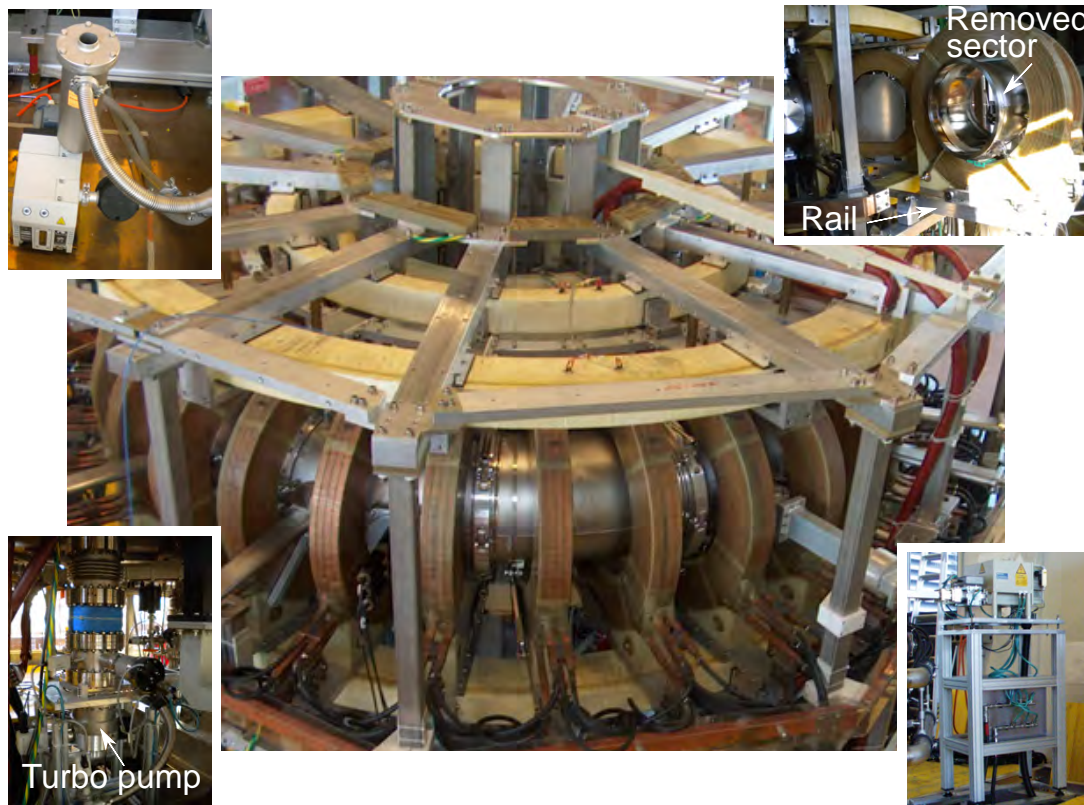


**Figure 2.1** | Photograph of TORPEX. Removed mobile sector on the top-right. A primary and a turbo-pump on the top-left and bottom-left inset, respectively. The high power magnetron on the bottom-right.

Before injecting the gas to be ionized, the evacuation of the air must be completed in two main steps. Once the vessel is sealed, two rotary pumps (Fig. 2.1, top-left inset) allow obtaining a primary vacuum pressure up to  $p \approx 5 \times 10^{-2}$  mbar. Consequently, four turbo-pumps<sup>1</sup> (Fig. 2.1, bottom-left inset), equally displaced along the toroidal direction and supported by an equal number of rotary pumps, are activated to reach the baseline vacuum of  $p \approx 4 \times 10^{-7}$  mbar. Several types of gas ( $H_2$ , deuterium (D), helium (He), neon (Ne), argon (Ar)) can then be injected from a single port to attain an equilibrium pressure in the range  $[10^{-5}, 10^{-4}]$  mbar for  $H_2$ . A differential pumping system is implemented where O-rings guarantee a vacuum safe displacement of the movable components installed on the TORPEX ports. This solution provides an intermediate vacuum region at the interface between the internal high vacuum and the external atmospheric pressure to avoid any severe stress on the turbo-pumps in case of leaks<sup>2</sup>.

<sup>1</sup>Nominal pumping speed of 345 l/s for nitrogen.

<sup>2</sup>In these circumstances, further safety measures are implemented, such as the automatic closure of the valve between the turbo-pumps and the TORPEX chamber.

## 2.2 Magnetic field

A wide variety of magnetic geometries can be obtained with the set of coils available on TORPEX. The main toroidal component  $\mathbf{B}_\phi$  is generated by 28 equally spaced water-cooled coils positioned along the toroidal direction (identified as toroidal field coils (TFC) - red coils in Fig. 2.2). The plasma production mechanisms<sup>3</sup> constrain its value in the range [70, 85] mT. A further small magnetic field can be produced using 10 poloidally distributed toroidal coils displaced around the vacuum vessel (yellow coils in Fig. 2.2), indicated from now on as vertical field coils (VFC). These can be combined in several ways, providing a high flexibility for the different accessible magnetic configurations. The simplest geometry is attained operating TORPEX as a SMT, where a vertical magnetic field  $B_z \leq 5$  mT is generated and superimposed to the toroidal one, resulting in open helical field lines, as shown in Fig. 2.2.

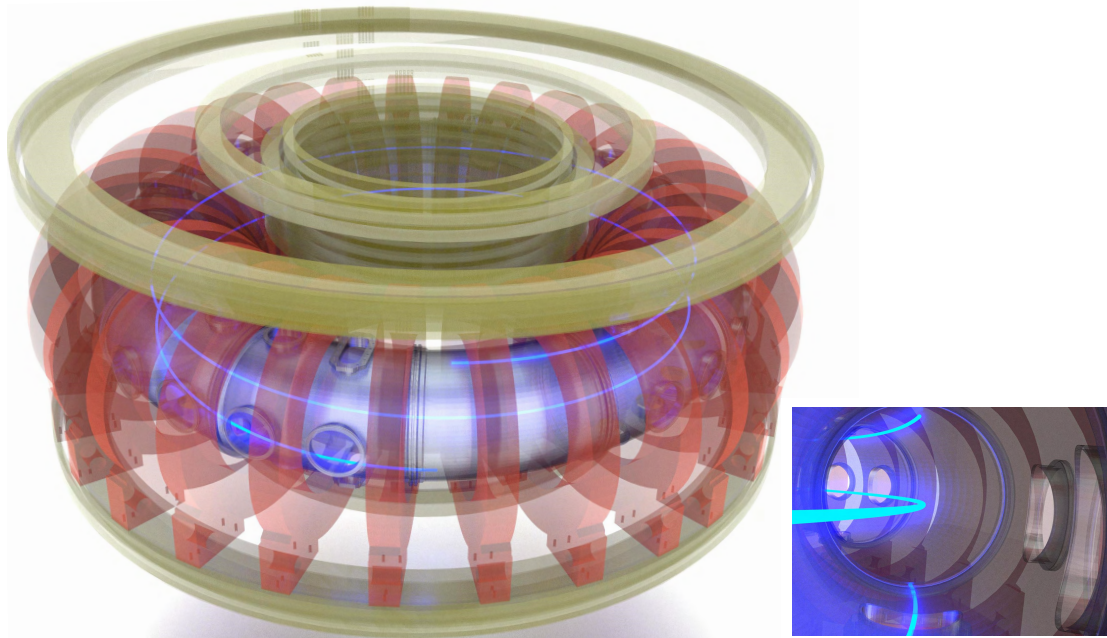


**Figure 2.2** | CAD drawing of TORPEX with an open helical magnetic field line (in blue) in the SMT configuration. In red, the toroidal field coils, while in yellow, the vertical field coils. A cut of the poloidal cross section is given in the inset.

The presence of a pure toroidal field leads to vertical charge-dependent  $\nabla B$  and curvature drifts. These generate a vertical electric field inducing an outward radial  $\mathbf{E} \times \mathbf{B}$  force. The inclusion of a vertical field  $B_z$  has two opposite effects. On one side, it allows short-circuiting the drift-induced electric field reducing the perpendicular losses. At the same time, it generates open field lines resulting in a much higher particle parallel loss channel towards the walls as  $B_z$  is increased (decreasing the connection length). Therefore, a trade-off can be found optimizing the vertical field intensity to maximize the particle confinement time [58]. The SMT is the main configuration used on TORPEX since the beginning of its operation in 2003 [59],

<sup>3</sup>Introduced in Sec. 2.3.

reproducing the main features of the tokamak SOL. It includes the magnetic field curvature, which is one of the driving mechanisms for plasma instabilities in the SOL, together with density and magnetic field gradients.

Some of the poloidal coils can also be operated in a ohmic configuration [60], generating an inductive plasma current for a time interval of  $\Delta t \approx 17$  ms. The short duration of the discharge is mainly due to the unstable condition of the plasma column in the presence of  $\mathbf{E} \times \mathbf{B}$  drifts, the magnetic pressure and the hoop force, with the consequent increase of its major radius moving towards the low field side (LFS).

More advanced magnetic geometries can be attained with the inclusion of a poloidal magnetic field  $\mathbf{B}_\theta$ , generated driving a current  $I_{TC} \leq 1$  kA through a 1 cm radius toroidal copper conductor recently installed on TORPEX [61]. The CAD drawing of the experimental set-up with an example of the resulting magnetic field line is shown in Fig. 2.3. A more detailed discussion of this system, which is one of the main technical achievements of this thesis, is given in Ch. 3.

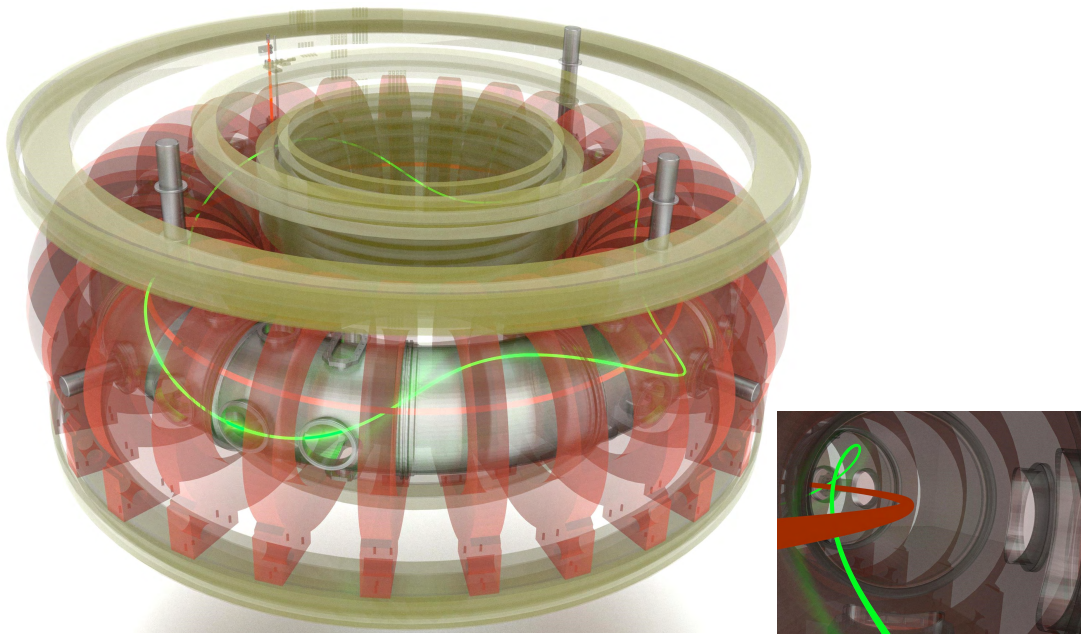


**Figure 2.3** | CAD drawing of TORPEX with the inclusion of the in-vessel toroidal copper conductor. In green, an example of a magnetic field line resulting from the superposition of  $B_\phi$ ,  $B_\theta$ .

### 2.3 Plasma production

The energy to generate the plasma is transferred to the neutral gas via microwave injection from the LFS. Electromagnetic (EM) waves with a frequency  $f_{RF} = 2.45$  GHz are directed through a wave-guide into the vacuum vessel in the direction perpendicular to the toroidal magnetic field. The injection antenna is constituted by a truncated wave-guide, designed to select the ordinary-mode (O-mode) of the RF fields<sup>4</sup>. A resonant acceleration of gas free

<sup>4</sup>Characterized by the direction of the RF electric field parallel to the TORPEX toroidal magnetic field.

electrons occurs at the EC layer, namely where the magnetic field is such that the electron gyro-motion resonates with the radiation frequency:

$$f_{CE} = \frac{eB}{2\pi m_e} = f_{RF} \Rightarrow B_{f_{RF}=2.45 \text{ GHz}} \approx 0.0876 \text{ T}. \quad (2.1)$$

This first energy transfer drives the impact ionization process responsible for the plasma breakdown. However, only a small fraction of the power is absorbed. Most of the radiation is reflected by the inner wall and the original O-mode polarization is partially lost, resulting in a mixture of O-mode and extraordinary-mode (X-mode). The initial increase of plasma density provided by the EC resonance introduces a further absorption of the X-mode polarization at the upper hybrid (UH) layer, defined by the location where the following resonant condition is satisfied:

$$f_{UH} \approx \sqrt{f_{CE}^2 + f_{pe}^2} = f_{RF} \quad \text{with} \quad f_{pe} = \sqrt{\frac{n_e e^2}{4\pi^2 m_e \epsilon_0}} \quad (\text{plasma frequency}). \quad (2.2)$$

Here  $n_e$  is the electron plasma density,  $e$  is the electron charge,  $m_e$  the electron mass and  $\epsilon_0$  the vacuum permittivity.

It was experimentally verified that after the first partial EC power transfer, most of the radiation energy is absorbed at the UH resonance, resulting in steady-state vertical slab-like plasma profiles radially located between the EC and the UH layers [62]. The EC layer radial position can be easily obtained from eq. 2.1 with the following approximation:

$$B \approx B_\phi \approx B_{\phi,0} R_0 / R \Rightarrow R_{EC} = \frac{R_0 e}{2\pi m_e f_{RF}} B_{\phi,0} \approx 11.42 B_{\phi,0} [\text{T}], \quad (2.3)$$

where  $B_{\phi,0}$  [T] is the toroidal magnetic field value measured in Tesla at  $r = 0$  cm. The UH resonance occurs more towards the LFS and its poloidal location depends on both the magnetic field and the plasma density. Using eq. 2.2 with the same approximation of eq. 2.3 for the magnetic field, we can obtain an estimate of the required density at each radial position  $R$  to resonate with the RF wave:

$$n_{UH} [10^{17} \text{ m}^{-3}] = \frac{(2\pi)^2 m_e c_0}{e^2} f_{RF} \left[ 1 - \left( \frac{R_{EC}}{R} \right)^2 \right] \approx \frac{f_{RF} [\text{GHz}]}{8} \left[ 1 - \left( \frac{R_{EC}}{R} \right)^2 \right]. \quad (2.4)$$

The direct injection of X-mode radiation from the LFS is avoided since, as the plasma is generated, the EM wave would first encounter a fluid cut-off [63] at  $f_R \approx \frac{1}{2} \left( |f_{CE}| + \sqrt{f_{CE}^2 + 4f_{pe}^2} \right)$ , corresponding to a density:

$$n_R [10^{17} \text{ m}^{-3}] = \frac{f_{RF} [\text{GHz}]}{8} \left( 1 - \frac{R_{EC}}{R} \right). \quad (2.5)$$

The resulting reflection and formation of a standing wave would greatly decrease the plasma production efficiency [63]. Two magnetrons are available to produce RF radiation. A high power magnetron inject the radiation from the LFS and provides a pulsed power in the range

$300\text{ W} \leq P_{\text{rf}}^{\text{HP}} \leq 40\text{ kW}$ , which can be modulated with different waveforms. A low power, steady-state operation is guaranteed by a second magnetron injecting the EM waves from the bottom of the vacuum vessel in the range  $200\text{ W} \leq P_{\text{rf}}^{\text{LP}} \leq 1\text{ kW}$ .

## 2.4 Diagnostics

TORPEX is equipped with a wide variety of diagnostics, supported for data acquisition by an electronic system<sup>5</sup> providing a sampling frequency of 250 kHz. The same electronic is used to store the relevant experimental parameters of the device, including the magnetic field coil currents, the injected and reflected magnetron power. Most of the measurements are performed using electrostatic Langmuir probes (LPs) to measure the main plasma parameters, namely plasma density  $n_e$ , electron temperature  $T_e$  and plasma potential  $V_{\text{pl}}$ . An overview of the other available diagnostics is given in Sec. 2.4.2.

### 2.4.1 Langmuir probes

Direct measurements of plasma parameters rely on the possibility of establishing an electrical contact between the plasma and a probing metallic object<sup>6</sup>, called Langmuir probe<sup>7</sup>. Many studies have been conducted on this topic and the development of a comprehensive theory is still an open issue [64]. The plasma response to the presence of a conductor is almost entirely concentrated in the *Debye sheath* [65, 66], an intermediate non-neutral layer with a thickness between 15 and 30 times the Debye length  $\lambda_D = \sqrt{\epsilon_0 T_e / (n e^2)}$  that is generated in front of the conducting surface. The sheath features are mainly determined by the interplay between the mobility of the different plasma species and the bias of the metallic surface  $V_{\text{pr}}$  with respect to the plasma potential  $V_{\text{pl}}$ . The latter is defined as the potential drop between the bulk plasma and the walls.

The sheath formation can most easily be understood if we consider a floating conductor inside a plasma, which is therefore electrically isolated and cannot draw any current in steady-state. Because of the extreme lightness of electrons with respect to ions, the surface rapidly charges up negatively repelling the negative particles. An equilibrium condition of *ambipolar flow* with equal ion ( $\Gamma_i$ ) and electron ( $\Gamma_e$ ) fluxes (no net electrical current) is reached at the floating potential  $V_{\text{fl}} (< V_{\text{pl}})$ . If we instead connect the conductor to a voltage source and apply a progressively lower voltage, less electrons are collected and a net positive ion current leaves the plasma, up to a saturation value  $I_{\text{sat}}^i$  where no electrons reach the collecting surface. At  $V_{\text{pr}} \simeq V_{\text{pl}}$ , the perturbations to the free ion and electron currents are small and there is no sheath formation. Further increasing  $V_{\text{pr}}$  we move into the regime of ion repulsion, up to the electron saturation current  $I_{\text{sat}}^e$  where no ions are collected.

The understanding of the sheath physics results in simplified analytical models that include

---

<sup>5</sup>With the exception of the fast imaging camera, supplied with its own acquisition system.

<sup>6</sup>Generally tungsten or graphite.

<sup>7</sup>The name refers to Irvin Langmuir, who conducted the first investigations on this topic in 1924.



the plasma parameters and allow to associate the measured LP currents to the corresponding applied voltages in the range of sheath existence, namely  $V_{pr} \lesssim V_{pl}$ . The simplest approach describes a collisionless plasma without magnetic field, where the dynamics are dominated by a Maxwellian population of electrons, with cold ions. This leads to the following expression for the collected probe current [65]:

$$I_{pr}(V_{pr}) = I_{sat}^i \left[ 1 - e^{e(V_{pr} - V_{fl})/T_e} \right] \quad \text{with} \quad I_{sat}^i = J_{sat} A_{pr}^{eff} = \frac{1}{2} e n_e c_s A_{pr}^{eff}, \quad (2.6)$$

where  $J_{sat}$  is the ion saturation current density,  $c_s = \sqrt{k_B T_e / m_i}$  is the ion sound speed and  $A_{pr}^{eff}$  is the effective surface of the probe at the sheath entrance. As previously anticipated, we can see that  $I_{pr}(V_{pr} = V_{fl}) = 0$ , while  $I_{pr} = I_{sat}^i$  is recovered for  $e(V_{pr} - V_{fl})/T_e \ll 1$ .

A straightforward regime of LP operation is the *ion saturation current* mode, which provides a convoluted information on the plasma density and temperature, referring to eq. 2.6 ( $I_{sat}^i \propto n_e \sqrt{T_e}$ ). The weaker dependence on temperature variations allows one to use this expression to get a qualitative insight of the plasma density. LP time-signals in  $I_{sat}^i$  are also regularly used to perform spectral investigations of plasma electrostatic fluctuations [67], as presented in Ch. 5. To fully exploit eq. 2.6, it is necessary to measure the LP current for the full range of voltages between  $I_{sat}^i$  and  $I_{sat}^e$ . This can be experimentally performed by applying to the LP a sweeping bias (Fig. 2.4 (b)) on time scales during which the plasma parameters can be considered approximately constant<sup>8</sup>. The corresponding measured values of  $I_{pr}$  (Fig. 2.4 (a)) are used to reconstruct the characteristic plasma I-V curve (Fig. 2.4 (c)). This could be analyzed using eq. 2.6 to obtain  $n_e$ ,  $T_e$ , and  $V_{fl}$  with a 3 parameter least-square fit. However, this requires the knowledge of the range of validity of eq. 2.6, namely the value of  $V_{pl}$ . Ideally, the latter could be extracted from a sharp "knee" that should appear in the I-V curve as the LP bias is increased

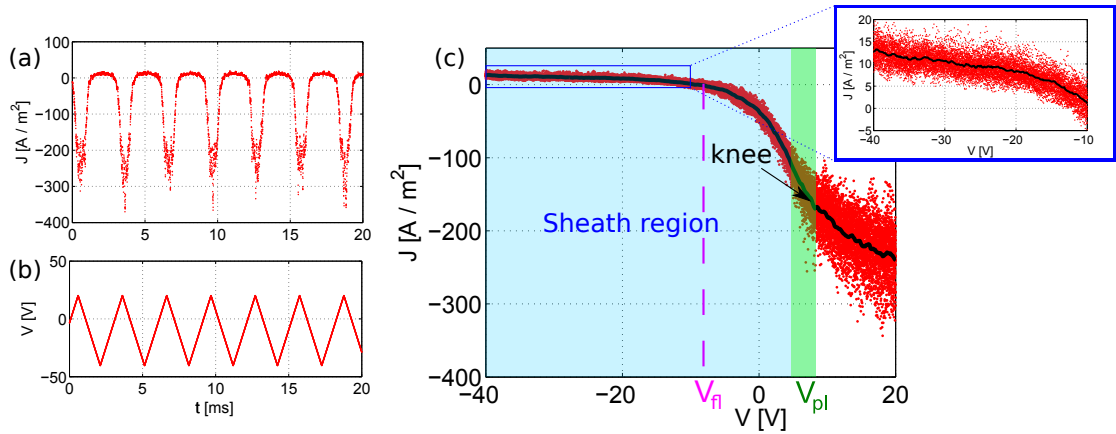


**Figure 2.4** | (a) LP measured current density time-trace in a window of 20 ms, without the capacitive effects, using a 330 Hz sweeping bias between -40 V and 20 V (b). In (c), the I-V curve corresponding to 100 ms of data is reconstructed, with the black curve indicating the average. The voltage range over which the sheath is generated is highlighted in light blue, while the shaded green region corresponds to where the plasma potential is indicatively located.

<sup>8</sup>On TORPEX the applied sweeping frequency is generally 330 Hz.

from the ion collection regime (approximate location indicated in Fig. 2.4 (c)). This "knee" would result for  $V_{pr}$  slightly higher than  $V_{pl}$ , when  $I_{sat}^e$  is reached and all the ions are repelled. Experimentally, neither  $I_{sat}^e$  (positive voltages in fig. 2.4 (c)) nor  $I_{sat}^i$  (negative voltages in the inset of Fig. 2.4 (c)) really saturate, which brings us to the following considerations.

The non saturated ion current for progressively negative biases is caused by the increasing width of the sheath (*Debye expansion*) and has to be taken into account for a correct estimate of the plasma parameters introducing the  $\alpha$  parameter in eq. 2.6 to add a linear dependence for negative voltages:

$$I_{pr}(V_{pr}) = I_{sat}^0 \left[ 1 - \alpha(V_{pr} - V_{fl}) - e^{e(V_{pr} - V_{fl})T_e} \right], \quad (2.7)$$

where  $I_{sat}^0$  is the  $I_{sat}^i$  value extrapolated at the floating potential. However, the non saturated electron current hampers the identification of the predicted "knee" at  $V_{pr} \simeq V_{pl}$ , and therefore the possibility to define the bias range of sheath existence where eq. 2.7 is valid. The *minimum temperature method* is generally implemented [68]. This consists in varying the upper value of the voltage range in which eq. 2.7 is applied, approximately in the shaded green region of Fig. 2.4 (c) where a "knee" can be identified. The fit providing the lower value of  $T_e$  is selected. Once  $n_e$ ,  $T_e$  and  $V_{fl}$  are known, a quantitative estimate of  $V_{pl}$  can be retrieved [64] from the ambipolar flow condition  $\Gamma_i = \Gamma_e$ :

$$V_{pl} = V_{fl} + \frac{\mu T_e}{e} \quad \text{with} \quad \mu \simeq \log \sqrt{\left( \frac{2m_i}{\pi m_e} \right)}. \quad (2.8)$$

The parameter  $\mu$  for a hydrogen plasma on TORPEX was measured to be [62]  $\mu_H = 3.1 \pm 0.6$ . We must underline that the analysis introduced in this section requires large data statistics, thus  $I_{pr}$ ,  $V_{pr}$  measurements averaged over many sweep cycles. The obtained values of  $n_e$ ,  $T_e$ ,  $V_{fl}$  and  $V_{pl}$  are therefore time-averaged quantities. The fluctuating components require more advanced experimental techniques (BOX-CAS [68, 69]) or more advanced model of LPs based on the triple probe concept [70].

The basic LP theory presented herein is valid for probe sizes  $a \gg \lambda_D$  and can be extended to magnetized plasmas with the magnetic field lines perpendicularly incident on the probe surface if the condition  $\rho_{e,i} \gg a$  is satisfied, where  $\rho_{e,i}$  is the electron/ion gyro-radius. For  $\rho_{e,i} < a$ , a complete theory is still missing. In this case, the practical approach consists in still using eq. 2.6 or eq. 2.7, but to calculate the effective collection area of the probe,  $A_{pr}^{eff}$ , as the projected surface in the direction of the magnetic field [64].

Several LP geometries have been developed in TORPEX. Most of them are installed on movable systems for one-dimensional (1D) radial or two-dimensional (2D) poloidal scans.

These scans can be performed on a shot-to-shot basis, taking advantage of the high reproducibility of TORPEX plasmas. In Fig. 2.5 some of them are presented, including simple probe designs such as the TWIN probes, with a 4.9 mm long single pin, a linear array of LPs separated by 1.8 cm (SLP) and the 2DSSLP, a 2D array of 8 cylindrical single-sided LPs with a radial separation of 1.5 cm. The MACH-probe [71, 72] is composed of 5 tungsten plates of 8 mm

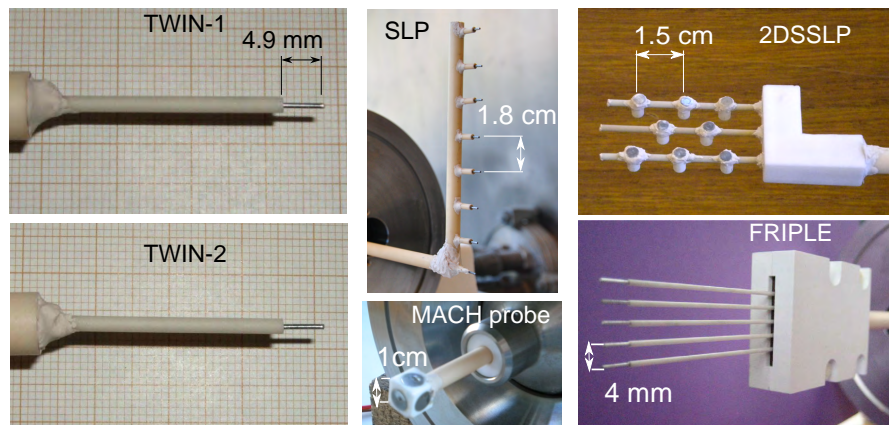


**Figure 2.5** | Movable LPs with different designs implemented on TORPEX.

diameter installed on five of the six faces of a 1 cm wide Teflon cube. Each electrode can be operated as a LP, but the chosen design allows computing the Mach number from the upstream and downstream currents, measured using plates on opposite faces. The five-tip triple probe (FRIPLE) [70] is a set of 5 LPs separated by 4 mm, based on the triple probe configuration [73]. This can be used to obtain fluctuating measurements of plasma density, temperature and potential.

Other LPs are installed on fixed arrays, in particular the hexagonal turbulence imaging probe (HEXTIP) (Fig. 2.6). This diagnostic was originally designed with 86 LPs welded on ceramic arms, arranged on four separate stainless steel rings, two for the measurements on the high field side (HFS) and two for those on the LFS. The rings are fixed on the inner walls of the chamber and toroidally separated by less than  $20^\circ$ . The superposition of the LP positions on the same poloidal plane, based on the assumption of toroidal symmetry, results in a hexagonal

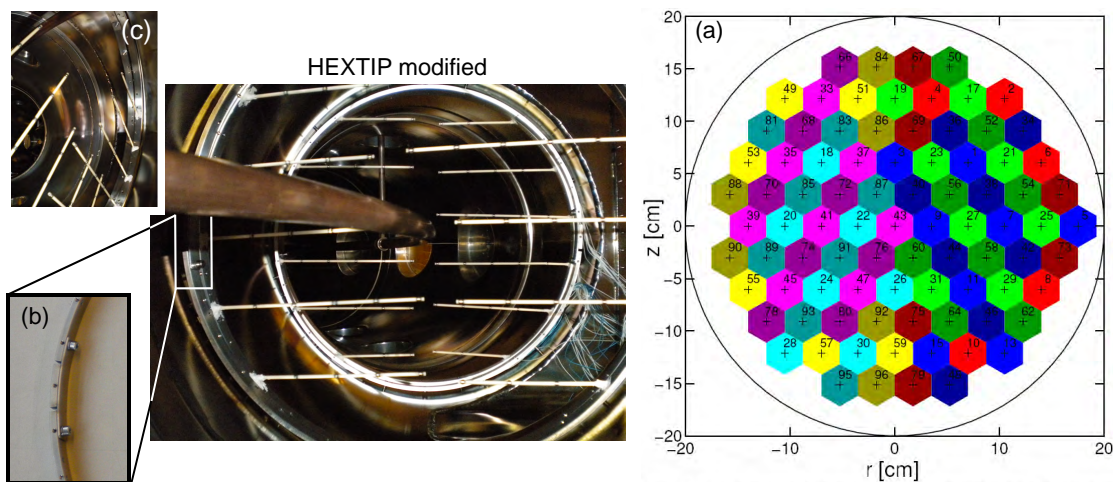


**Figure 2.6** | (a) 2D mapping of the HEXTIP LPs on the poloidal cross section, without the central probe at ( $r \approx 0, z \approx 0$ ) cm. HEXTIP modifications required for the compatibility with the TC in (b). (c) HEXTIP ring tilting during the TC lifting operations.

pattern covering the whole cross section (Fig. 2.6 (a)), providing an overview of the 2D plasma features with a spatial resolution of 3.5 cm. The inclusion of the TC inside the vacuum vessel posed problems of geometrical compatibility. First of all, the fragility of the HEXTIP ceramic arms required their removal during the TC installation procedure. Each of the stainless steel rings was consequently modified by cutting a small portion of the structure, to be able to insert them into the vessel once the TC was installed. Before clamping each ring against the vessel walls, the cut arc needs to be screwed back on its original position to keep the structure rigidity (Fig. 2.6 (b)). Moreover, the TC is designed<sup>9</sup> to be displaced and set at different vertical positions. The presence of HEXTIP strongly limits this operation due to the presence of LPs at  $r \approx 0$  cm, forcing to cut the tip at  $(r \approx 0, z \approx 0)$  cm as a temporary solution to be able to set the TC in the middle of the vacuum vessel. Experiments in the SMT configuration necessitate to move the TC up to the top of the chamber. This requires to free the TC vertical path from the LPs at  $(r \approx 0, z \geq 0)$  cm by rotating the stainless steel rings, as indicated in Fig. 2.6 (c). The difficulty of the procedure, together with the desirable improvement of the currently available HEXTIP spatial resolution, pushed towards an improved version of the diagnostic, as described below.

### The new HEXTIP movable twins

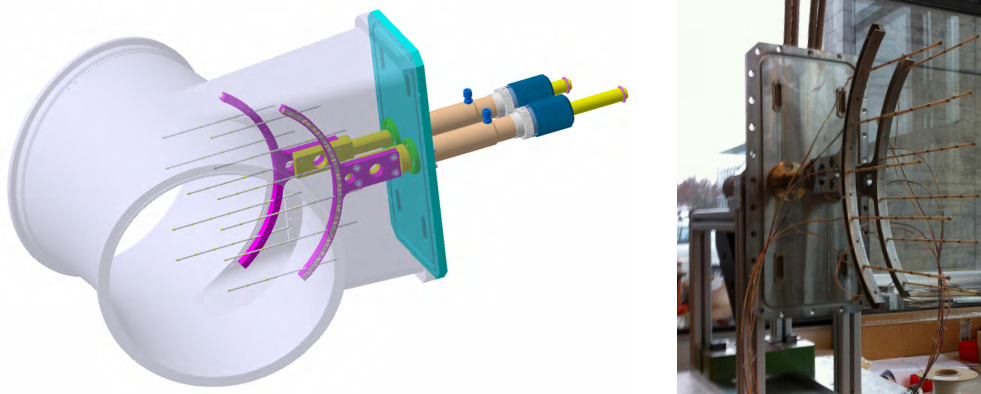


**Figure 2.7** | On the left, CAD drawing of the HEXTIP movable twins (HEX-MT) LFS parts inserted in a TORPEX sector. In magenta, the supporting stainless steel arcs. In yellow, the arms for the vacuum safe radial displacement obtained with the brown and blue components. Photograph of the diagnostic during the assembling on the right.

The HEXTIP movable twins (HEX-MT) constitutes the upgrade of HEXTIP and is designed to fulfil several requirements. To solve the issue of the vertical TC displacement, the LPs with  $|r| \leq 17.5$  mm are installed in the arms on the LFS, leading to longer ceramic tubes<sup>10</sup> with a maximum length of 269 mm. The corresponding supporting rings are substituted by stainless

<sup>9</sup>This will be discussed in more details in Sec. 3.

<sup>10</sup>Outer diameter  $\approx 3$  mm, inner diameter  $\approx 2$  mm.

steel arcs<sup>11</sup> installed on a movable radial system<sup>12</sup>. From the position corresponding to the original HEXTIP mapping, the LFS LPs can be rigidly moved 7 cm outwards or 3 cm inwards with a 1 mm accuracy. This allows the vertical displacement of the TC without tilting the rings supporting the probes and highly improves the HEXTIP radial resolution on a shot-to-shot basis. A differential pumping system guarantees the vacuum-safe radial movement of the structure. The HFS ring design was maintained the same, including the modification required for the installation introduced in Fig. 2.6 (b). The number of probes is increased to 95. The new ones are highlighted in Fig. 2.8 with a red contour.

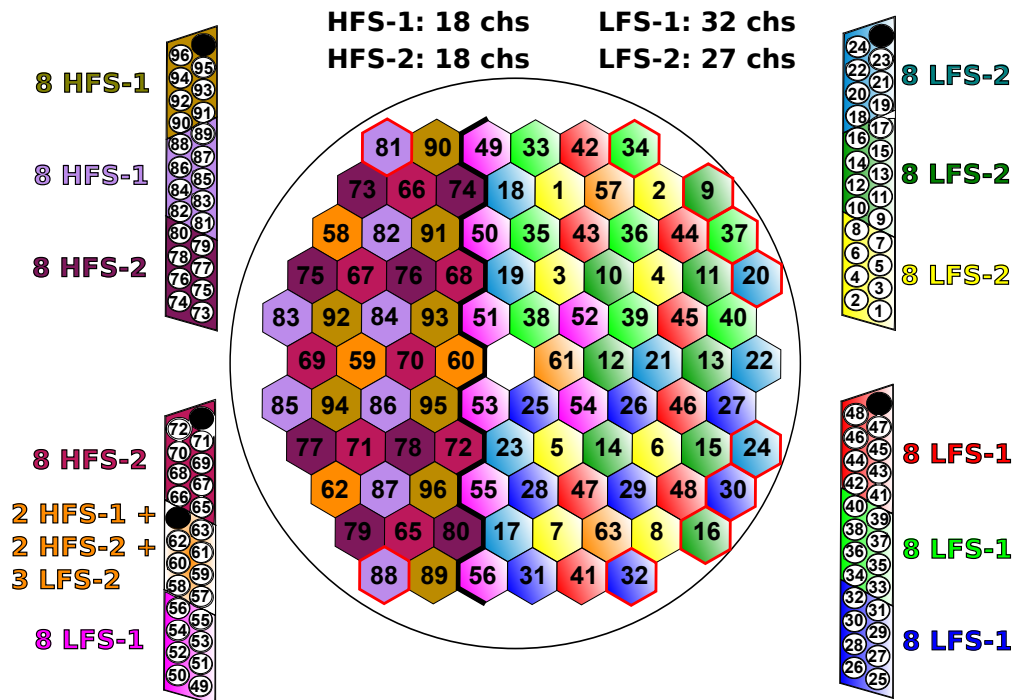


**Figure 2.8** | Mapping of the 95 LPs of the HEX-MT. The red contour indicates the new probes with respect to those of the original mapping (Fig. 2.6). The vertical black poly-line separates the fixed LPs from the movable ones. The numbers correspond to the channels of the acquisition card.

The vertical black polygonal chain separates the LPs installed on the LFS supports from those of the HFS rings. Contrary to the original HEXTIP design [74], one single type of stainless steel hollow cylinder was chosen for all the LPs, with a notch on the side. This facilitates the assembly for the spot welding on the laser drilled ceramic tubes, as illustrated in Fig. 2.9 (a). The inner diameter of 3.05 mm, wall thickness 0.5 mm, and height 2 mm, results in a projected area perpendicular to the magnetic field of  $A_{\perp} = 16.2 \text{ mm}^2$  (Fig 2.9 (a)).

The vacuum feed-through of the LP cables is guaranteed by 4 male-to-male SUBD plugs with 25 pin (Fig. 2.9 (b)), directly welded on the flange (cyan component in Fig. 2.7). Four corresponding female connectors in PEEK are used on the vacuum side [75] (Fig. 2.9 (c)), where the LP monopole wires are connected. Four shielded 25-pole cables transmit the measured

<sup>11</sup> Fig. 2.7, magenta elements on the left.

<sup>12</sup> Fig. 2.7, yellow, brown and blue components.

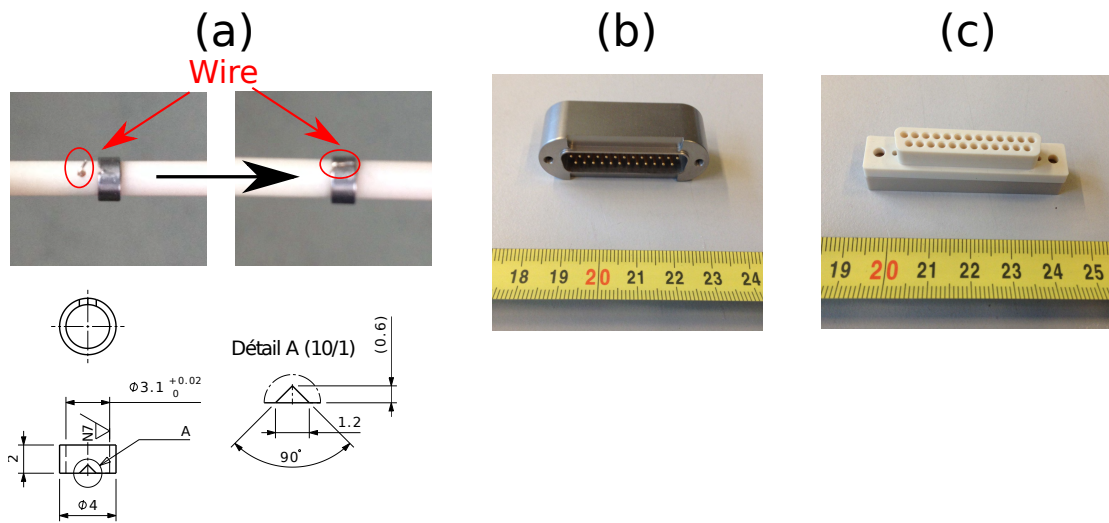


**Figure 2.9** | (a) Details of the stainless steel cylinder preparation for the spot-welding, with the corresponding technical drawing. (b) Male-to-male SUBD 25-pole feed-through connector. (c) Vacuum-side peek plug.

signals to the electronic units. To avoid a ground loop, the cable shielding is connected to the ground of the electronics unit, but not to the feed-through. As for the previous HEX TIP, the amplification electronics consists of 12 boards, each dedicated to 8 probes. These electronic cards can be remotely configured independently, operated in floating potential or ion current, applying a bias potential<sup>13</sup> among four values:  $[-54, -42, -30, -15]$  V. The amplified signals are acquired using a dt196 96-channel digitizer at 250 kHz with 16 bit of resolution [76]. With the aim of performing correlation measurements with LPs toroidally separated  $180^\circ$ , two identical models of this modified HEX TIP have been constructed and will be progressively installed the next months.

### The field-aligned probe array

The field-aligned probe array (FAPA) shown in Fig. 2.10-left is a 2D array of 44 LPs. This is designed to perform poloidally field-aligned measurements of plasma electrostatic fluctuations in quasi-concentric magnetic flux surfaces (Fig. 2.10-right). In particular, poloidal wave number ( $k_\theta$ ) measurements of quasi-coherent modes are presented in Sec. 5.1.4.

The LPs are poloidally aligned along five calculated flux surfaces, separated from each other by 1 cm, as sketched in Fig. 2.10-right. Cylinders with a 0.8 mm central hole, wall thickness 0.3 mm, length 1.2 mm and projected area perpendicular to the magnetic field of  $A_\perp = 8.76 \text{ mm}^2$  are used. These are supported by eleven ceramic tubes of variable lengths, fixed on a stainless steel structure installed on the bottom of TORPEX, as indicated in the lower inset of Fig. 2.10. This is also the best solution to keep the arms vertically and therefore more stable. The arms are held fix in place by screws pushing them against the metallic support. A small

<sup>13</sup>Typically  $-42$  V.

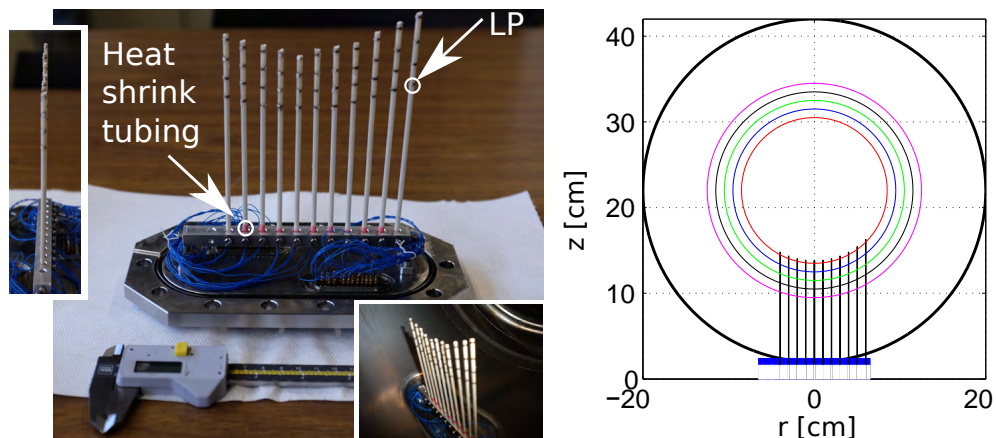


**Figure 2.10** | On the left, photographs of FAPA, before and after the installation on TORPEX. Design of the diagnostic on the right.

piece of heat shrink tubing (red in Fig. 2.10) surrounds each arm, where there is the contact with the screw, to better distribute the pressure and reduce the risk of breaking the ceramic. The electronic system of the old HEXTIP is used for the data acquisition. By connecting the FAPA radially inner connector to the input of the HEXTIP electronic card for the C-ring, and the outer to that for the D-ring, the channel correspondence shown in Fig. 2.11 results.

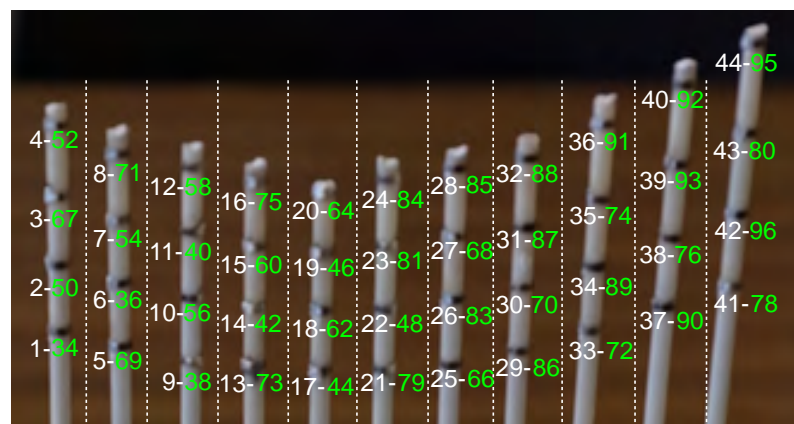


**Figure 2.11** | Correspondence of the FAPA LPs (white numbers) with the HEXTIP LPs (green number), connecting the FAPA radially inner connector to the electronic input for the C-ring, and that radially outward to the electronic input for the D-ring.

### The oblique field electrode

Plasma parameter measurements using LPs currently rely on a theory that loses validity as the magnetic field lines impinge the probe surface at shallow angles [77, 78]. Several models are under investigations to extend the LP theory to almost tangential field lines [79], but none of them has undergone a comprehensive validation against experimental data. This is of great

relevance for fusion-oriented devices, where flash-mounted Langmuir probes (FMLPs) are largely implemented [80]. FMLPs are wall-embedded LPs with an angle  $\theta_{in}$  between the probe surface and the field lines close to  $0^\circ$ , mainly constrained by the maximum tolerable power fluxes.

Deeper investigations can be performed on basic plasma physics devices such as TORPEX, owing to much lower power fluxes. The oblique field electrode (OFE) diagnostic was developed<sup>14</sup> to explore the LP behaviors in the presence of non-perpendicular magnetic fields, reproducing the FMLP design. Three electrodes are installed on a supporting plate in PEEK<sup>15</sup> and surrounded by a 1 mm thick conducting surface set at the TORPEX ground potential to reproduce the tokamak wall (Fig. 2.12).

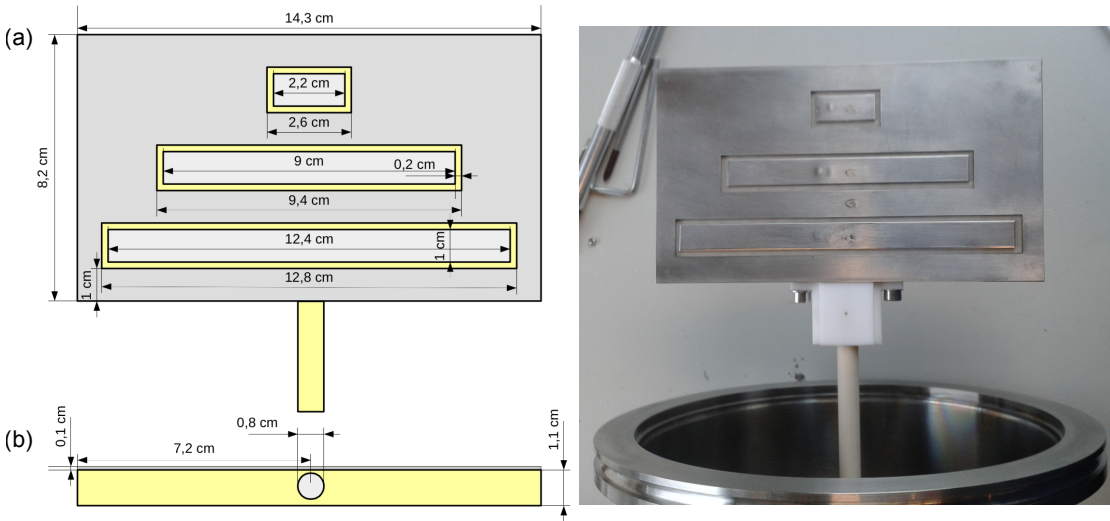


**Figure 2.12** | Technical drawing of OFE on the left. Photograph of OFE on the right.

The electrode lengths of 2.2 cm, 9 cm and 12.4 cm are chosen to vary the projected probe area focusing on the conditions of validity of the model presented in [79]. The whole system can be rotated  $360^\circ$  around its axis to change the field line incidence angle. The OFE was tested in the SMT configuration, choosing the poloidal position at ( $r \approx 13.7, z \approx 0$ ) cm in the source-free region of the plasma to limit the  $I_{sat}^e$  collected current. A sweeping bias between -40 V and 20 V (330 Hz) was applied. The incidence angle  $\theta_{in}$  was varied in the range  $[-6^\circ, 60^\circ]$ . When the sweeping voltage was applied on the electrode set at the desired radial position, the other two were kept at the ground potential like the surrounding plaque to avoid any interference between adjacent electrodes. In Fig. 2.13 (a) we report the first results of I-V measurements for several incidence angles  $\theta_{in}$ . As reported in previous works [81], if the projection of the LP area perpendicular to the field lines is considered, we observe an increasing  $J_{sat}^i$  and  $J_{sat}^e$  for smaller angles which can not be described with a standard LP theory. The ratio  $|J_{sat}^e|/|J_{sat}^i|$  changes with  $\theta_{in}$ , decreasing from the expected value  $\approx 34$  [65, 82]. A comparative study between the standard I-V curve analysis presented in Sec. 2.4.1 and the model of [79] is foreseen.

<sup>14</sup>In collaboration with the TP-IV student G. Willoud.

<sup>15</sup>Polyether ether ketone, a colorless organic thermoplastic polymer.



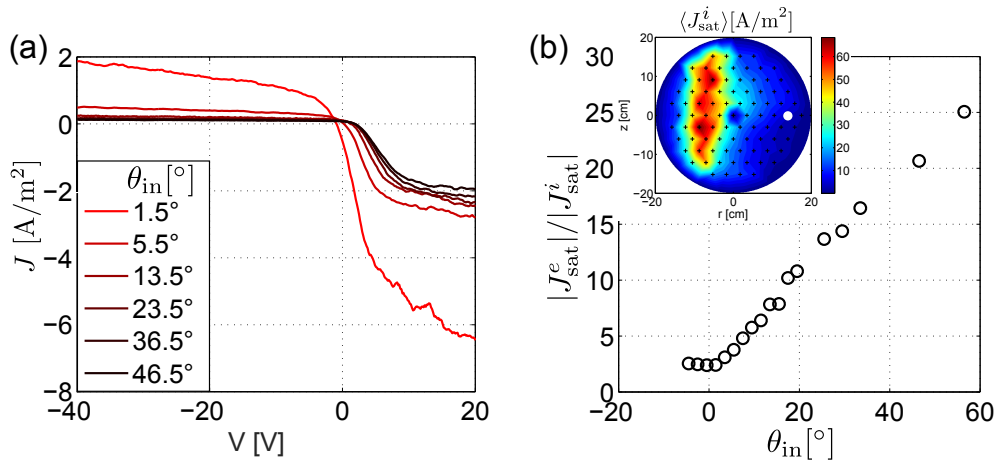


**Figure 2.13** | Measured I-V curves (a) and measured ratio of electron saturation current density over ion saturation current density (b) for several magnetic field incidence angles. In the inset, time-averaged  $J_{sat}$  plasma profiles with the position of the biased electrode indicated with a white dot on the LFS.

### 2.4.2 Other diagnostics

A comprehensive study of plasma features requires information that can not be provided by electrostatic probes, but can be obtained with the implementation of complementary diagnostics. Some of them are herein introduced and shown in Fig. 2.14.

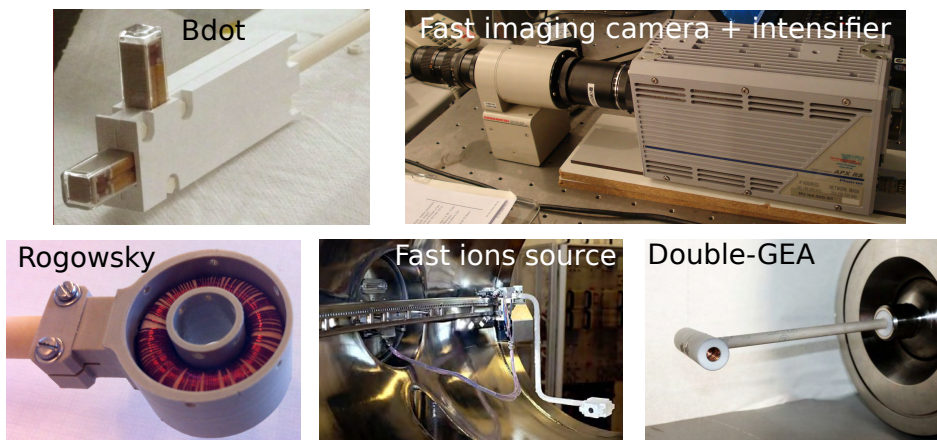


**Figure 2.14** | Some of the diagnostics available on TORPEX.

**Bdot** is a magnetic probe developed<sup>16</sup> to measure the fluctuating parallel current density  $\tilde{J}$  [83]. It consists of three pick-up coils separated 3.5 cm and arranged in an L-shaped array. This provides magnetic field measurements at three different locations, which allow to use the Ampere's law  $\tilde{J} = (\nabla \times \tilde{\mathbf{B}})/\mu_0$ .

A miniaturized current probe is also available for measurements of the single blob current filament [84]. The magnetic flux associated with the blob current is amplified winding a

<sup>16</sup>In collaboration with the group at the Reverse-Field eXperiment (RFX) in Padova, Italy.

**Rogowski** coil around a ferrite core.

A **fast imaging camera** (Photron Ultima APX-RS) in the visible range complements electrostatic measurements providing a non-perturbative approach with a high spatio-temporal resolution [85, 86]. A maximum framing rate of 250 kHz, together with a tomographic reconstruction, allows to measure 2D poloidal plasma fluctuations with frequencies up to 20 kHz and a spatial resolution of 2 cm. A low plasma emissivity is compensated with the implementation of the Hamamatsu C10880-03 image intensifier.

**Fast ions** can be injected and detected in TORPEX plasmas to study their interaction with turbulence [87, 88]. The suprathreshold ion source consists of a thermionic emitter coupled to a two-grid accelerating system to produce a current up to  $10\ \mu\text{A}$ . This is collected by a detector composed of two gridded energy analyzers (GEAs) facing opposite directions to perform differential measurements and reduce the background noise. A lock-in amplifier is used to further improve the signal-to-noise ratio. Three-dimensional (3D) measurements can be obtained with the ion source installed on a toroidal rail and the GEA mounted on a 2D poloidal movable system.

### 2.5 Previous turbulence studies

Most of the TORPEX scientific results have been obtained operating the device as a SMT. The first investigations were dedicated to the plasma production [62] and confinement [58], discussed in Sec. 2.2 and 2.3, respectively. The plasma is typically generated on the HFS, resulting in slab-like vertical profiles. A representative plasma is displayed in Fig. 2.15 (a), on the basis of HEX TIP  $J_{\text{sat}}$  data<sup>17</sup>. The time-averaged contours of  $J_{\text{sat}}$  for 40%, 60% and 80% of the maximum value are indicated with black, gray and white dashed lines.

Coherent modes develop on the region of density gradients [91], corresponding to the high fluctuating levels of  $\tilde{J}_{\text{sat}}$  visible on the HFS. Three-dimensional fluid simulations with the Global Braginskii Solver [92] led to the identification of three main instability regimes driving plasma turbulence [89] on TORPEX: drift wave (DW), ideal and resistive interchange modes. The onset of these modes can be controlled by varying the pitch angle of the magnetic field lines, corresponding to the number of toroidal turns  $N$  run by the helical field lines between the bottom and the top of the vessel walls ( $N = 2$  in Fig. 2.2). The main control parameter to change  $N$  is the vertical magnetic field, keeping the toroidal field constant to maintain the EC layer at the same radial position. Ideal interchange modes<sup>18</sup> dominate for  $N \lesssim 7$ , driving a strong radial transport for the high TORPEX collisionalities. This prevents the formation of the radial pressure gradients necessary for the onset of DWs, which are expected for high  $N$ . Increasing  $N$  allows accessing the resistive interchange wave regime, as verified with experimental measurements of the vertical mode number  $l = 1$ , corresponding to a vertical wave number  $k_v = 2\pi l$  [67]. These are reported in Fig. 2.15 (b) with black circles, together with the

---

<sup>17</sup>From now on, the regime of current saturation is always referred to that of ions.

<sup>18</sup>Characterized by a parallel wave number  $k_{\parallel} \approx 0$ , while a  $k_{\parallel} \neq 0$  correspond to resistive interchange modes.

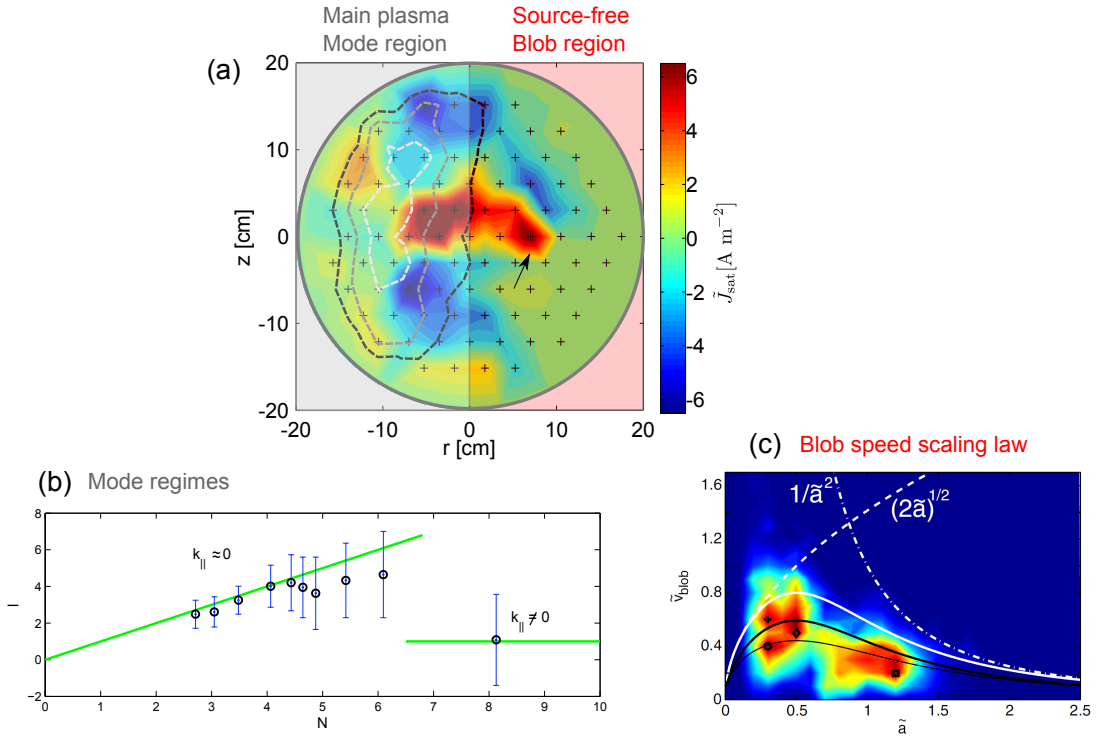


**Figure 2.15** | (a) Snapshot of 2D conditionally averaged  $\bar{J}_{\text{sat}}$  data obtained with HEX TIP LPs, indicated with black crosses. On the HFS the high  $J_{\text{sat}}$  fluctuations indicate a  $N = 2$  mode in the region of pressure gradients. These can be observed from the black, gray and white dashed contours reproducing the time averaged  $J_{\text{sat}}$  values at, respectively, 40%, 60% and 80% of the maximum. On the LFS, a blob detaching from a wave crest and propagating radially outward is indicated with a black arrow. (b) Experimental measurements (black circles) and simulations (green curves) of TORPEX turbulence regimes [89]. The transition from ideal ( $k_{\parallel} \approx 0$ ) to resistive ( $k_{\parallel} \neq 0$ ) interchange modes can be observed at  $N \approx 7$ . In (c), the blob speed scaling law for different parameters (white and black lines) is compared to the experimental measurements of the joint probability between the normalized blob speed  $\tilde{v}_{\text{blob}}$  and the normalized blob size  $\tilde{a}$  [90]. Different gases are indicated with the different symbols: H<sub>2</sub> ( $\square$ ), He ( $\diamond$ ), Ne (+) and Ar ( $\circ$ ).

simulations indicated by the green lines.

The source-free region on the LFS is characterized by a radial particle transport mainly dominated by intermittent events, commonly referred to as blobs [33,93]. These poloidally localized filamentary structures are ubiquitous in toroidal plasmas [36] and are commonly observed in fusion devices [94]. A comprehensive investigation on the blob birth [95], dynamics [90,96] and control [97] has been performed on TORPEX for the ideal interchange mode regime. Blobs originate from the crest of the interchange waves, where they are sheared-off by the  $\mathbf{E} \times \mathbf{B}$  drift resulting from the total pattern of fluctuating potential  $\tilde{V}$ . The outward radial propagation is then driven by the same drift mechanism, with the internal  $\nabla B$  and curvature induced electric field controlled by the balance of blob parallel and perpendicular currents. Fig. 2.15 (c) shows the blob speed scaling law compared to a statistical analysis of blob velocities. The dashed line is the expected blob velocity in the absence of parallel currents, while the dash-dotted line corresponds to the scaling where sheath currents are dominant. By varying the ion mass,

both regimes are obtained.

TORPEX electrostatic fluctuations in both the mode and blob regions show clear similarities with the statistical properties of tokamak SOL turbulence for a wide range of control parameters [98, 99].

Further studies addressed the interaction of suprathermal ions with TORPEX turbulence. The first experimental evidence of a superdiffusive and subdiffusive ion transport on the same background plasma for different values of ion energy was obtained (Fig. 2.16).

A key advantage of TORPEX investigations consists in the possibility of performing a rigorous validation procedure of numerical simulations by using high resolution experimental data [100, 101].

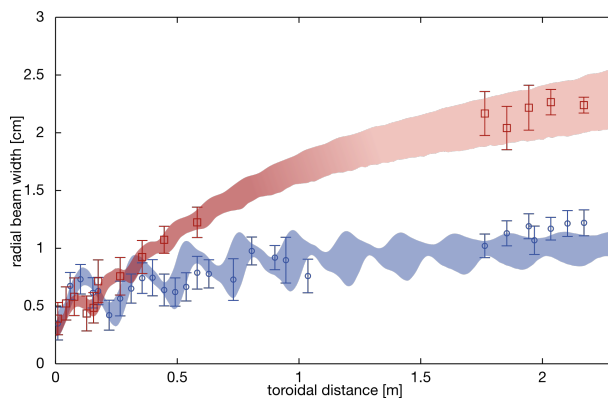


**Figure 2.16** | Measurements (red squares and blue circles) of the suprathermal ion beam radial width varying the traveled toroidal distance, compared to the numerical simulations (shaded regions). Red data correspond to 30 eV ions and indicate a superdiffusive behavior, while blue data are related to a subdiffusive regime.

## 2.6 Summary

A summary of the main TORPEX parameters is given in the following, including those of the device (Tab. 2.1) and the plasma-related ones (Tab. 2.2). We underline the electrostatic feature of TORPEX plasmas, for the extremely low  $\beta$ . Moreover, the charged particles are strongly magnetized having  $f_{CE} \gg \nu_{ee}, \nu_{eH}$  and  $f_{CI} \gg \nu_{iH}$ , as well as  $\rho_{e,i} \ll L_n$ .

Parameter	Value	Parameter	Value
$R$	1 m	$B_\phi$	$\approx [70 - 90]$ mT
$a_0$	0.2 m	$B_z$	$< 5$ mT
$P_{\text{rf}}^{\text{HP}}$	$\approx [0.3-40]$ kW	Gas	H <sub>2</sub> , D, He, Ne, Ar
$P_{\text{rf}}^{\text{LP}}$	$\approx [0.2-1]$ kW	$p_n (n_n)$	$\approx [1 - 10] \times 10^{-5}$ mbar ( $[10^{17} - 10^{18}] \text{ m}^{-3}$ )

**Table 2.1** | Device parameters.

Parameter ( <b>Gas independent</b> )	Value
$n_e$	$\approx 10^{16} \text{ m}^{-3}$
$x = n_e / (n_e + n_n)$	$\approx 0.01$ (1%)
$T_e$	$< 10$ eV
$T_i$	$< 1$ eV
$\beta = 2\mu_0 n_e T_e / B_\phi^2$	$\approx 10^{-5}$
$V_{\text{pl}}$	$\approx [10 - 20]$ V
$f_{CE} = eB / (2\pi m_e)$	$\approx 2.45$ GHz ( $B \approx B_\phi = 88$ mT)
$f_{pe} = \sqrt{n_e e^2 / (4\pi^2 \epsilon_0 m_e)}$	$\approx 900$ MHz
$v_{\text{th},e} = \sqrt{k_B T_e / m_e}$	$\approx 10^6$ m/s ( $T_e = 5$ eV)
$\rho_e = v_{\text{th},e} / (2\pi f_{CE})$	$\approx 0.07$ mm
$L_n$	$\approx 4$ cm
$\lambda_D = \sqrt{\epsilon_0 k_B T_e / (n_e e^2)}$	$\approx 0.17$ mm
Parameter ( <b>Gas dependent</b> )	Value ( <b>H<sub>2</sub></b> )
$f_{CI} = ZeB / (2\pi m_i)$	$\approx 1.3$ MHz ( $B \approx B_\phi = 88$ mT)
$\nu_{iH} \approx n_n \sigma_{iH} v_{\text{th},i}$ [68]	$\lesssim 50$ kHz
$\nu_{eH} \approx n_n \sigma_{eH} v_{\text{th},e}$ [68]	$\approx 1$ MHz
$\nu_{ee} = e^4 \ln \Lambda n_e Z^2 / [3(2\pi)^{3/2} \epsilon_0^2 \sqrt{m_e} T_e^{3/2}]$	$\approx 80$ kHz
$\lambda_{\text{mfp},ee} = v_{\text{th},e} / \nu_{ee}$	$\approx 10$ m
$v_{\text{th},i} = \sqrt{k_B T_i / m_i}$	$< 10^4$ m/s
$\nu_{ii} = e^4 \ln \Lambda n_i Z^4 / [12\pi^{3/2} \epsilon_0^2 \sqrt{m_i} T_i^{3/2}]$	$\gtrsim 7$ kHz
$\lambda_{\text{mfp},ii} = v_{\text{th},i} / \nu_{ii}$	$\lesssim 1$ m
$c_s = \sqrt{\gamma Z k_B T_e / m_i}$	$\approx 2.2 \times 10^4$ m/s ( $T_e = 5$ eV)
$\rho_i = v_{\text{th},i} / (2\pi f_{CI})$	$< 1.3$ mm
$\rho_s = c_s / (2\pi f_{CI})$	$\approx 3$ mm

**Table 2.2** | Plasma parameters.



## In-vessel toroidal conductor

The SMT configuration introduced in Sec. 2.2 allows performing basic investigations of plasma electrostatic instabilities of relevance for fusion experiments. The toroidal vacuum vessel with the toroidal field coils assures the presence of a magnetic field curvature and gradient, reproducing the main features of the field geometry in a tokamak SOL. However, the SMT configuration lacks a rotational transform  $\iota$ , which corresponds to the mean number of toroidal transits divided by the mean number of poloidal transits of a field line on a toroidal flux surface. This requires a further poloidal magnetic field to generate nested magnetic surfaces, bending the plasma particle paths in a loop around the cross section, like in a tokamak. A poloidal component of the magnetic field can be produced on TORPEX implementing the ohmic system on some of the toroidal coils to generate an inductive plasma current. It was experimentally verified that the duration of a stable plasma is limited to 17 ms without an active feedback system of the coil currents [60]. This is mainly determined by the natural tendency of the plasma column to increase its major radius for the presence of  $\mathbf{E} \times \mathbf{B}$  drifts, magnetic pressure and hoop force.

In this chapter, we present the design, development and commissioning of the alternative experimental set-up implemented in this thesis work [61] for the generation of a poloidal field. The system is based on a current-carrying toroidal copper conductor inside the TORPEX vessel, as indicated in Fig. 3.1. This possibility was initially investigated in the early 70's on several devices for the achievement of fusion conditions, with the in-vessel conductor either suspended through magnetically screened pairs of leads [102] or in levitating mode [103]. More recently, a layout with a vertically supported central conductor has been implemented on the MISTOR device [45]. An advantage of this solution with respect to an inductive current drive is the decoupling of the plasma from the poloidal magnetic field source. This represents a crucial step in producing tokamak-like configurations in TORPEX. It allows investigating plasma fluctuations addressing SOL physics issues, as well as the core region of closed flux surfaces or the topological transition between closed and open magnetic field lines. More advanced fusion relevant magnetic geometries are accessible, including single-null X-points and second-order nulls (magnetic snowflakes).

### 3.1 Overview of the experimental set-up

The toroidal copper conductor is composed of four similar plain copper sections of 1 cm radius, with angular extensions of  $90^\circ$ ,  $102^\circ$ ,  $90^\circ$  and  $78^\circ$ . These values are chosen according to the TORPEX port availability to limit the stress on the stainless steel junctions used to assemble them together, as shown in Fig. 3.1 (e).

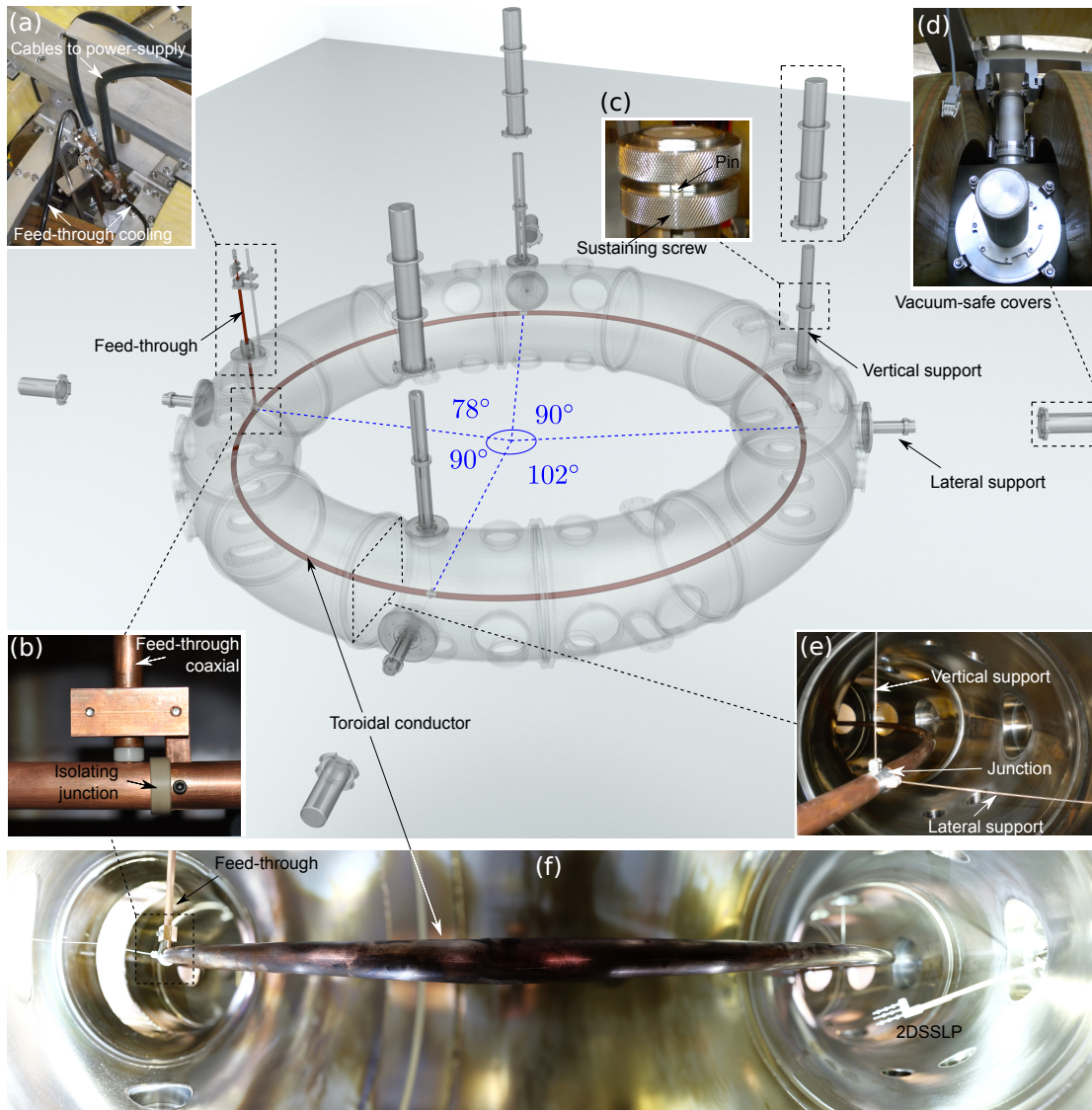


**Figure 3.1** | Design of the TC system with photographs of the main components. (a) Current feed-through top view, with indicated the connection to the water cooling system and the cables connected to the power supply. (b) Photograph of the feed-through connection to the TC. (c) Detail of one support, with the screw sustaining the pin were one of the vertical stainless steel wires is fixed. (d) Photograph of the vacuum-safe covers of the horizontal and vertical supports. (e)f) Photograph of the TC system installed inside TORPEX, with the details of some components.



### 3.1. Overview of the experimental set-up

The four sections are supported inside the TORPEX vacuum chamber at the junction points by four lateral and three vertical 1 mm stainless steel wires, as indicated in Fig. 3.1 (e). The seven supporting leads are electrically floating to reduce perturbations to the plasma and are fixed on a pin sustained by a screw, shown in Fig. 3.1 (c). This can be vertically moved, setting the TC at intermediate vertical positions with a precision of  $\pm 3$  mm. The possibility to move the TC along the full vertical length of the vessel (recovering the SMT configuration if required) constitutes a new feature with respect to other similar systems, such as that reported in Ref. [45]. This allows exploring more advanced magnetic configurations discussed in Sec. 3.3. The vacuum of the main chamber is guaranteed by reinforced stainless steel covers, indicated in Fig. 3.1 (d). The fourth vertical holder is the electrical feed-through, shown in Fig. 3.1 (a|b), consisting of a coaxial rod to minimize the magnetic field perturbations. An active cooling along the toroidal length of the TC is avoided to keep the system as simple as possible, while it is developed for the current feed-through. The corresponding cooling cables are indicated in Fig. 3.1 (a) and are described in more details in Sec. 3.1.2. In Fig. 3.1 (f), we show a photograph of the TC system installed inside TORPEX.

#### 3.1.1 Toroidal copper conductor

The useful copper (Cu) physical properties [104] are summarized in Tab. 3.1, while the structural parameters of the TC are reported in Tab. 3.2.

Density	Linear thermal expansion coefficient	Specific heat	Resistivity ( $T^* = 293$ K)	Resistivity thermal coefficient
$d_{\text{Cu}}$	$\alpha_{\text{Cu}}$	$c_{s,\text{Cu}}$	$\rho_{\text{Cu}}^*$	$k_{\text{Cu}}$
$8.96 \times 10^3 \text{ kg m}^{-3}$	$6.5 \times 10^{-6} \text{ K}^{-1}$	$385 \text{ J K}^{-1} \text{ kg}^{-1}$	$1.69 \times 10^{-8} \Omega \text{ m}$	$4.4 \times 10^{-3} \Omega \text{ m K}^{-1}$

**Table 3.1** | Cu physical properties.

Radius	Length	Section	Surface	Mass	Resistance	Inductance
$a$	$\ell = 2\pi R_0$	$S = \pi a^2$	$A = 2\pi a \ell$	$M = \ell S d_{\text{Cu}}$	$R = \rho_{\text{Cu}}^* \ell / S$	$L$
1 cm	6.28 m	3.14 cm <sup>2</sup>	0.39 m <sup>2</sup>	17.65 kg	0.35 m $\Omega$	$6 \times 10^{-6}$ H

**Table 3.2** | TC structural parameters.

The TC inductance is obtained from the expression for a current loop with a conductor radius  $a$  and curvature radius  $R$  [105]:

$$L(a, R) = \mu_0 R \left[ \ln \frac{8R}{a} - 2 + \frac{Y}{2} + O\left(\frac{a^2}{R^2}\right) \right] = \mu_0 R \left[ \ln \frac{8R}{a} - \frac{7}{4} \right] \simeq 6 \times 10^{-6} \text{ H}, \quad (3.1)$$

where the second order terms  $O(a^2/R^2)$  have been neglected and  $Y = 1/2$  is the contribution to the self-inductance given by the inner part of the conductor [106] for the direct current (DC) regime with a current uniformly distributed on the cross section. In alternating current (AC)  $Y = 0$  since the current is mainly distributed on the conductor surface (skin effect).

#### 3.1.2 Current feed-through

The design of the feed-through is shown in Fig. 3.2, along with a detailed view of the connection to the TC, on the lower part, and the vacuum-tight sliding seal. A coaxial solution is adopted to minimize the magnetic field perturbations. The internal rod has an inner and outer diameter of  $a_{ic}^i = 4$  mm and  $a_{ic}^o = 6$  mm, respectively, while those of the external one are  $a_{ec}^i = 10$  mm and  $a_{ec}^o = 12$  mm. These are indicated in red and orange in Fig. 3.2 (a). The dimensions are chosen to reduce the coaxial external surface and therefore its influence on the plasma. The effective cross sections are  $16 \text{ mm}^2$  and  $35 \text{ mm}^2$ , respectively, corresponding to the following radii:

$$\begin{cases} a_{ic}^{\text{eff}} = \sqrt{(a_{ic}^o)^2 - (a_{ic}^i)^2} \simeq 2.2 \text{ mm} \\ a_{ec}^{\text{eff}} = \sqrt{(a_{ec}^o)^2 - (a_{ec}^i)^2} \simeq 3.3 \text{ mm} \end{cases} \quad (3.2)$$

A nylon-based material (Polyamide 6 - PA6) is used to isolate the coaxial conductors in the upper and bottom parts (Fig. 3.2, in yellow). The vacuum is obtained with O-rings at several positions, as indicated in green in Fig. 3.2: on the bottom and on the top, between the PA6 and the conductor, as well as in the middle, where a region of intermediate pressure is obtained with a connection to the TORPEX differential pumping system. The coaxial conductor requires an active cooling along the whole vertical length to prevent the feed-through overheating and damaging of the both the PA6 and the O-rings<sup>1</sup>. The cooling system of the toroidal field coils is used for this purpose, forcing the circulation of demineralised water in the empty volume of the coaxial wire, as illustrated in Fig. 3.2. Water is injected from the top of the feed-through, circulating between the two conductors for most of the vertical length up to the lower point, where it passes through two holes flowing inside the internal conductor.

In the presence of currents  $\gtrsim 800$  A, the structure can undergo mechanical oscillations in the range of a few Hz that induce an intermittent short-circuit between the coaxial conductors. The reason for these vibrations is still not clear. A new modified version is under development to overcome this technical issue. The new design includes small pieces of insulators between the internal and external rods along the full vertical length of the feed-through to prevent the vibrations, with a design that allows the passage of the cooling water.

---

<sup>1</sup>Further details are given in Sec. 3.2.2.

### 3.1. Overview of the experimental set-up

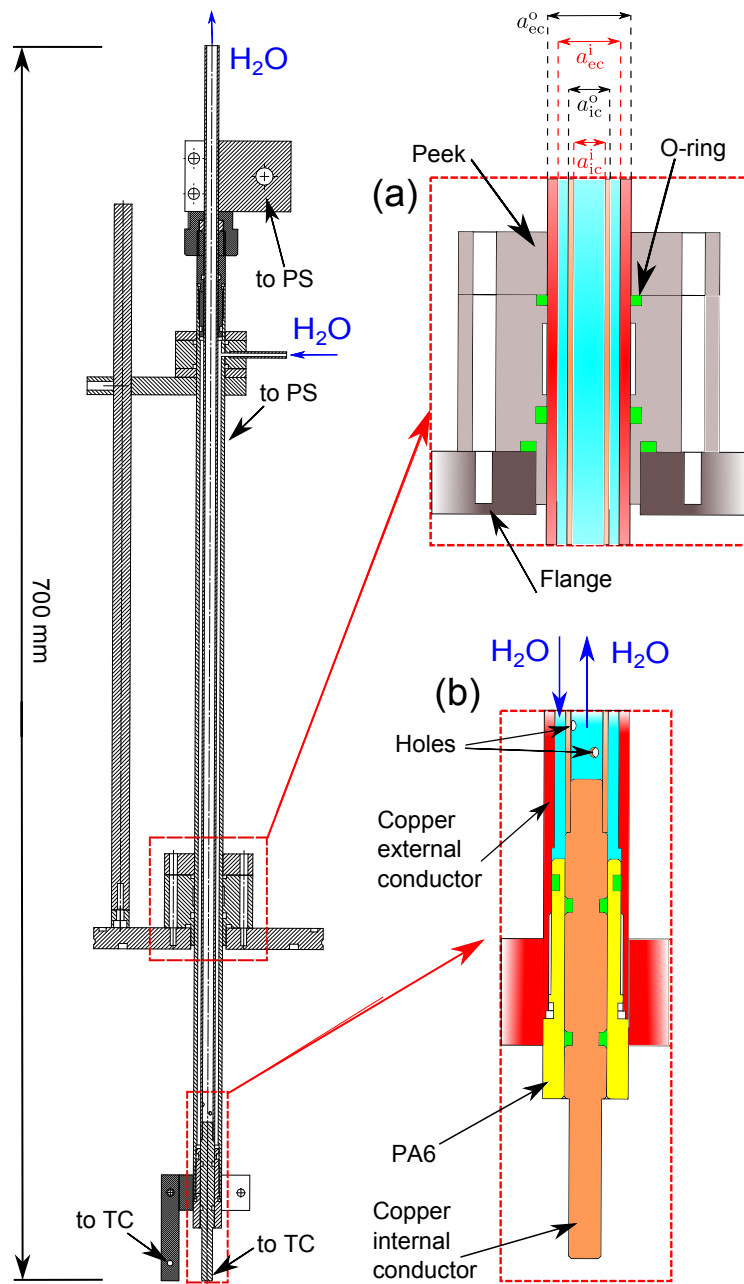


**Figure 3.2** | Drawings of the current feed-through for the TC. Demineralised water is injected from the top and flows between the internal (in orange) and external (in red) conductors down to the bottom of the feed-through. Here the water flows into the inner conductor through holes, as outlined in the zoomed inlet on the bottom right and is pumped out from the top. In yellow, the insulator in polyamide 6 (PA6) between the two conductors, used in a similar way on the top of the feed-through. On the top right, a zoomed view of the vacuum-tight sliding seal is provided. Vacuum sealing is insured by the component in PEEK shown in light gray, insulating the outer conductor from the vacuum vessel. The green parts correspond to the holes for the O-ring, to keep the vacuum. The indicated dimensions of the internal and external conductors are, respectively, [ $a_{ic}^i = 4 \text{ mm}$ ,  $a_{ic}^o = 6 \text{ mm}$ ] and [ $a_{cc}^i = 10 \text{ mm}$ ,  $a_{cc}^o = 12 \text{ mm}$ ].

### 3.1.3 Circuit and control

The TC circuit has a total resistance of approximately  $33\text{ m}\Omega$  and is fed by a three-phase DC power supply (PS) capable of delivering  $1.1\text{ kA}$  with  $1400\text{ A/s}$  nominal slew rate<sup>2</sup>. A closed loop Hall effect current transducer module is implemented for the measurement of the current (Fig. 3.3).

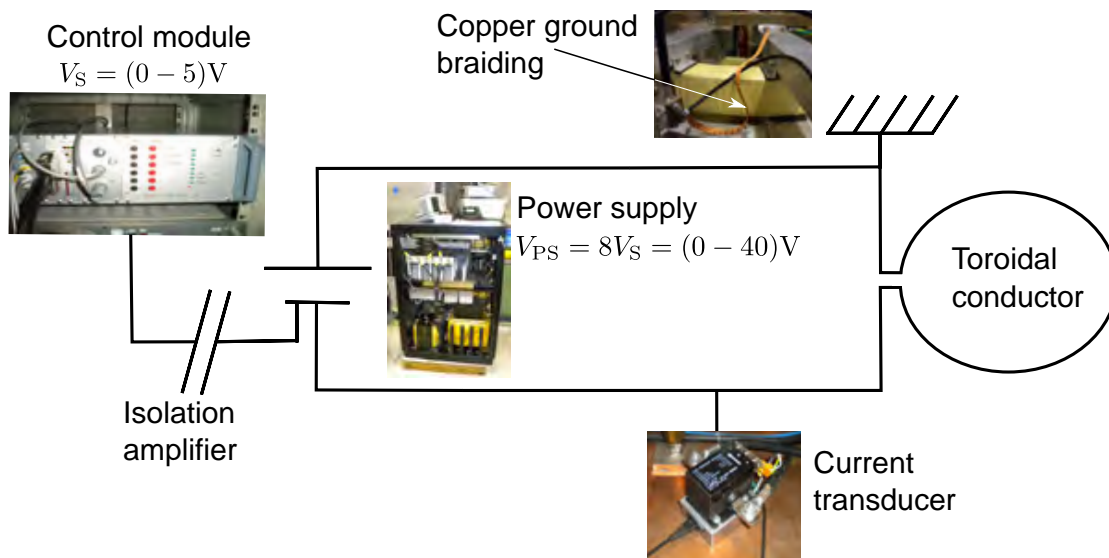


**Figure 3.3** | Schematic of the TC electrical circuit with the photographs of the main elements. The remote control module is electrically isolated from the PS with an isolation amplifier and provides a voltage signal between  $0\text{ V}$  and  $40\text{ V}$ . This drives a current in the circuit that is measured by a current transducer before entering in the TC, which can be set at a fixed potential with respect to the vessel using the indicated copper ground braiding.

The PS is remotely controlled using a dedicated electronic module, from which it is kept electrically isolated with an isolation amplifier. This allows changing the potential of the TC with respect to the TORPEX vacuum chamber, using the copper ground braiding shown in Fig. 3.3.

The control module is integrated in the TORPEX control software and it is at present programmed to work in ON-OFF mode, providing a single voltage step in the range  $0\text{--}5\text{ V}$ , which is amplified eight times. The electronic control module is designed to generate waveforms with multiple steps in the voltage signal, providing flexibility in the choice of the TC current time-trace. The voltage signal, in either ON-OFF or multi-step mode, can be triggered at different times with respect the beginning of the plasma discharge.

<sup>2</sup>The measured value is  $1700\text{ A/s}$ .

## 3.2 System requirements and design

### 3.2.1 Accessible safety factor

The safety factor  $q$  is equivalent to the rotational transform  $\iota = 2\pi/q$  and quantifies the wrapping of the helical field lines around the torus. It is defined as the rate of change of toroidal flux  $\Phi$  with poloidal flux  $\Psi$ :

$$q = \frac{d\Phi}{d\Psi} \quad \text{with} \quad \begin{cases} d\Psi = 2\pi R B_\theta dx \\ d\Phi = \oint (B_\phi dx) ds \end{cases}, \quad (3.3)$$

where  $dx$  is the infinitesimal separation between two flux surfaces, as indicated in Fig. 3.4.

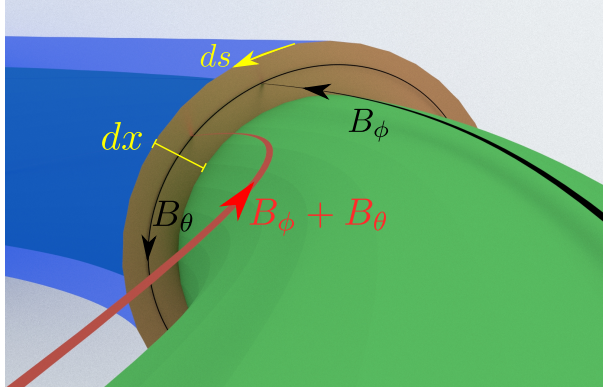


**Figure 3.4** | Sketch of poloidal and toroidal field fluxes in the region (orange) between two flux surfaces (indicated in blue and green).

It can be written in its integral form as:

$$q = \frac{1}{2\pi} \oint \frac{1}{R} \frac{B_\phi}{B_\theta} ds, \quad (3.4)$$

where the integral is calculated over a single poloidal turn around the flux surface.

The main technical features of the system are set by the requirement of obtaining a safety factor of the order of  $q \approx 5$  on a sufficiently large portion of the plasma volume to perform tokamak-relevant studies of plasma instabilities. An approximated expression can be obtained for a circular cross section using the limit of large aspect ratio [17], which is satisfied on TORPEX with  $A=R_0/a_0=5$ :

$$q \approx \frac{r}{R_0} \frac{B_\phi}{B_\theta}, \quad (3.5)$$

with  $r$  the minor radius. At this point,  $B_\theta$  can be calculated using the integral form of the Ampere's law applied on an infinite straight wire, neglecting the possible contribution of the vertical field coils:

$$\oint_C \vec{B}_\theta \cdot d\vec{\ell} = \mu_0 I_{TC} \quad \Rightarrow \quad B_\theta = \frac{\mu_0 I_{TC}}{2\pi r}, \quad (3.6)$$

### Chapter 3. In-vessel toroidal conductor

while the toroidal field can be written as  $B_\phi \sim B_{\phi,0}R_0/(R_0 + r)$ , leading to the following expression of the safety factor radial profile:

$$q(r) \approx \frac{r}{R_0} \frac{B_\phi(r)}{B_\theta(r)} \approx \frac{2\pi r^2}{(R_0 + r)} \frac{B_{\phi,0}}{\mu_0 I_{TC}} \approx 4 \times 10^5 \frac{r^2}{(1 + r) I_{TC}}. \quad (3.7)$$

Here we have considered a toroidal field at the center of the vacuum vessel  $B_{\phi,0} \approx 0.08$  T, corresponding to  $r_{EC} \approx -10$  cm. The calculated radial profiles of the safety factor for  $I_{TC} = [0.5, 1.0, 1.5, 2.0]$  kA are shown in Fig. 3.5. We chose 1 kA as the required current, which can be delivered by the PS available at the CRPP.

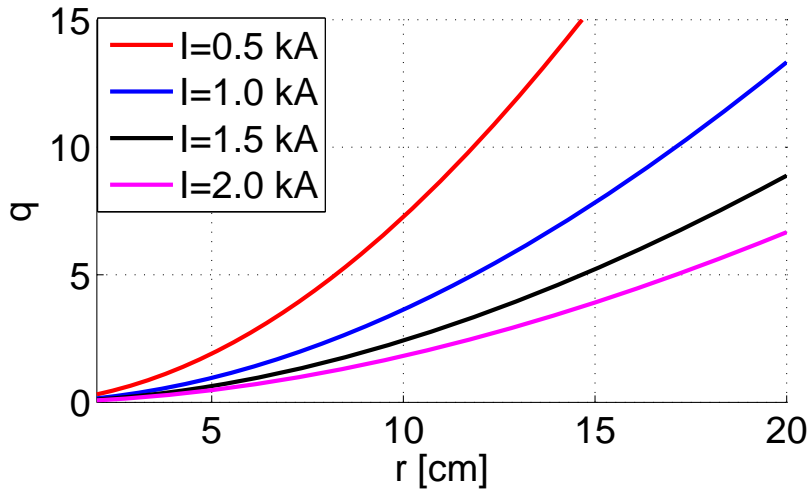


**Figure 3.5** | Simulated safety factor radial profile in the large aspect-ratio approximation for a toroidal magnetic field in the center of the vacuum vessel of 80 mT and a TC current of [0.5, 1.0, 1.5, 2.0] kA.

### Current ripple tolerance

We now provide an estimate of the tolerable TC current ripple for a basic configuration of concentric field lines where the VFC contribution to  $B_\theta$  can be neglected. A variation in the TC current determines the displacement of a flux surface, with the corresponding change in the radial position of a fixed safety factor value. As most of the plasma investigations are conducted with spatially localized measurements performed with LPs, the  $q$  radial displacement is required to be within the size of an HEXTIP LP ( $\Delta r_{LP} \approx 3$  mm). This implies that the maximum allowed percentage value of current ripple ( $\Delta I$ ), at the radial position  $r$ , is given by:

$$q(I_{TC}, r) = q(I_{TC} + \Delta I, r + \Delta r_{LP}) \quad \Rightarrow \quad \frac{\Delta I}{I_{TC}} = \left[ \frac{(r + \Delta r_{LP})^2 (1 + r)}{r^2 (1 + r + \Delta r_{LP})} - 1 \right], \quad (3.8)$$

where we have used eq. 3.7. The calculated values in the range  $r = [4 - 20]$  cm are shown in Figure 3.6. The available PS satisfies the chosen criterion, having a residual current ripple of 1%.

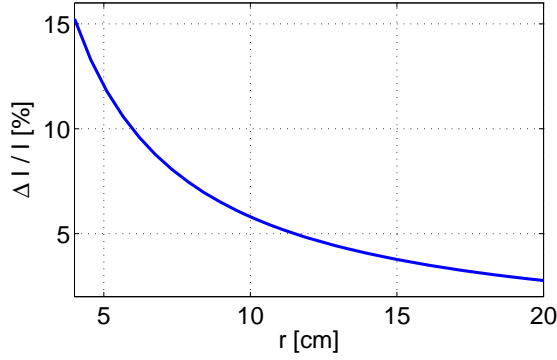


**Figure 3.6** | Maximum percentage current ripple  $\Delta I/I_{TC}$  vs. the radial position  $r$ .

### 3.2.2 Conductor heating

The Joule heating constitutes one of the main constraints on the design and operation of the TC. We focus on the temperature variation of the system during a single discharge in adiabatic conditions, with a continuous flow of current, which constitutes an upper limit as we neglect the temperature relaxation processes, such as conduction and radiation. A simplified time trace of the TC is considered, assuming a linear ramp-up until  $t_1$ , a flat-top between  $t_1$  and  $t_2$  at  $I_{ft}$  and a ramp-down up to  $t_3$ , as sketched in Fig. 3.7:

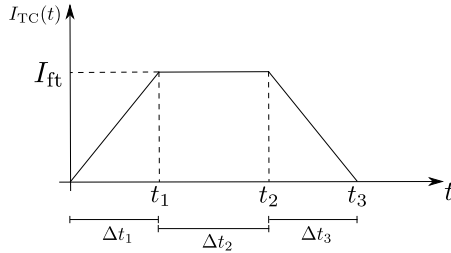


**Figure 3.7** | Current profile.

Time window	$I(t)$
$\Delta t_1$	$I = I_{ft} t / t_1$
$\Delta t_2$	$I = I_{ft}$
$\Delta t_3$	$I = I_{ft}(t_3 - t) / (t_3 - t_2)$

**Table 3.3** | Current evolution during a discharge.

The Cu resistivity temperature dependence is taken into account assuming the linear approximation of the complete Bloch-Grüneisen expression [107], which is an accurate estimate in the range of temperatures [200-800] K [108]. The resulting electric resistance for a conductor of length  $\ell$  and section  $S$  is:

$$R(T) = \rho_{Cu}(T) \frac{\ell}{S} = \rho_{Cu}^* [1 + k_{Cu}(T - T^*)] \frac{\ell}{S}, \quad (3.9)$$

with a corresponding Ohmic heating power  $W(T, t) = R(T)I^2(t)$ . This determines a temperature variation  $\dot{T}(t) = M c_{s,Cu} W(T)$ , which can be rewritten in the following linear first order differential equation:

$$\dot{T}(t) - B I^2(t) T(t) = B \left[ \frac{1}{k_c} - T^* \right] I^2(t) \quad \text{with} \quad B = \frac{\rho_{Cu}^* k_{Cu}}{d_{Cu} c_{s,Cu} S^2}. \quad (3.10)$$

### Chapter 3. In-vessel toroidal conductor

The solution is given by:

$$T(t) = T^* + \left\{ \frac{e^{C_t f(t)} [k_c (T_i - T^*) + 1] - 1}{k_c} \right\}, \quad (3.11)$$

with

	$C_t$	$f(t)$	$T_i = T(t_i)$
$t \in [0 \div t_1]$	$B I_{ft}^2 / 3 t_1^2$	$t^3$	$T_0$
$t \in [t_1 \div t_2]$	$B I_{ft}^2$	$t - t_1$	$T_1$
$t \in [t_2 \div t_3]$	$B I_{ft}^2 / 3 (t_2 - t_3)^2$	$(t - t_3)^3 - (t_2 - t_3)^3$	$T_2$

We underlined the high sensitivity of the result on the value of the conductor radius  $T(t) \sim \exp(Bt) \sim \exp(a^{-4}t)$ .

We analyze the conducting component of the TC system with the smallest cross section, namely the coaxial feed-through internal rod ( $a \approx 2.2$  mm). This is in contact with O-rings and PA6 components having a temperature tolerance of  $T \approx 80^\circ\text{C}$ , which sets the upper limit for the conductor heating. We can therefore evaluate the corresponding maximum allowed flat-top current duration  $\Delta t_2$ , assuming  $\Delta t_1 = \Delta t_3 = 0.6$  s for the measured slew rate of the implemented PS. The results for flat-top current values in the range [0.5 – 2] kA are shown in Fig. 3.8, assuming initially the system at the room temperature ( $T^* \approx 293$  K).

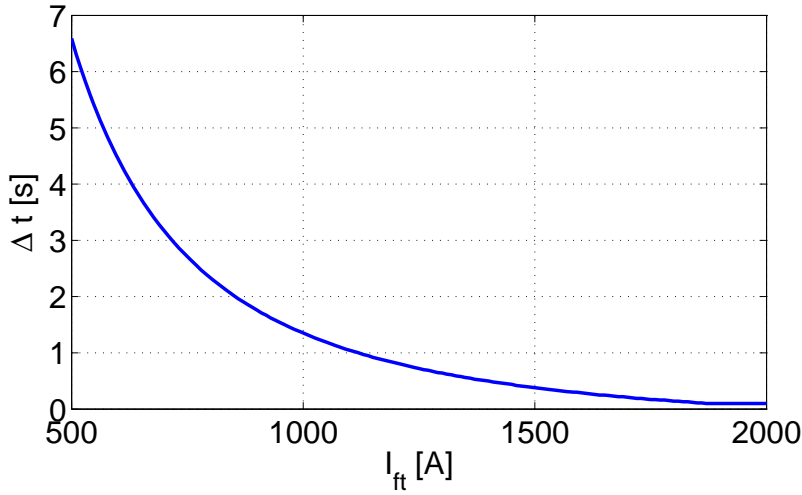


**Figure 3.8** | Maximum flat-top current duration for currents in the range [0.5 – 2] kA for the internal coaxial rod with a radius of  $a \approx 2.2$  mm.

For  $I_{ft} = 1$  kA, the time duration limit exceeds the  $\Delta t \approx 1$  s typically necessary to provide enough data statistics. However the conductor undergoes a sensitive heating that requires to be moderated with the cooling system introduced in Sec. 3.1.2 before the following discharge. In a *permanent current* regime of operation with consecutive discharges separated by a minimum time of  $\Delta t \approx 2$  minutes for the data acquisition, the current upper limit is mainly



given by the connection cables. These have a size ( $a \approx 5$  mm) smaller than the TC and a temperature limit of  $T \approx 70^\circ$  given by the isolating material (PVC). This corresponds to a maximum acceptable current intensity (ampacity<sup>3</sup>)  $I_{\max} \approx 200$  A that sets, for a given  $I_{\text{TC}}$ , the minimum required time interval  $\Delta t_{\text{OFF}}$  between the discharges. The current intensity can be obtained considering the Ohmic heating during the discharge  $\Delta Q = RI^2 \Delta t_{\text{ON}}$  and calculating the equivalent current  $I_{\text{eq}}$  corresponding to the same dissipated power for the total time  $\Delta t_{\text{ON}} + \Delta t_{\text{OFF}}$ . It follows:

$$I_{\text{eq}} = \sqrt{\frac{\Delta t_{\text{ON}}}{\Delta t_{\text{ON}} + \Delta t_{\text{OFF}}}} I_{\text{TC}} \leq I_{\max} \Rightarrow \Delta t_{\text{OFF}} \geq \left[ \left( \frac{I_{\text{TC}}}{I_{\max}} \right)^2 - 1 \right] \Delta t_{\text{ON}}, \quad (3.12)$$

where we have approximated the whole discharge with a current flat-top of 1.5 s. The results for a current range  $I_{\text{TC}} = [0.5 - 1]$  kA and flat-top durations  $\Delta t_{\text{ON}} = [0.5 - 6]$  s are shown in Fig. 3.9.

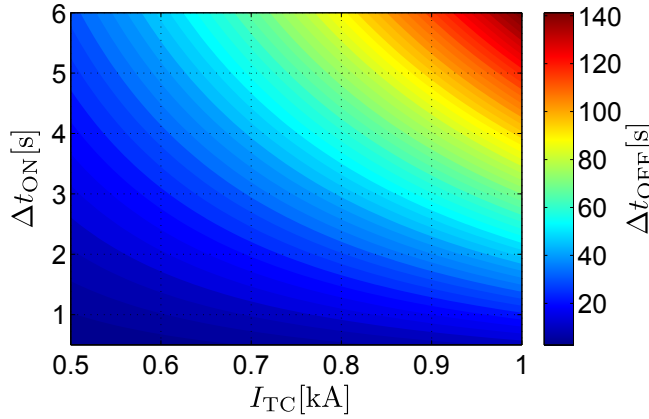


**Figure 3.9** | Minimum time window between consecutive discharges ( $\Delta t_{\text{OFF}}$ ) in a regime of permanent current, for different discharge durations ( $\Delta t_{\text{ON}}$ ) and TC currents ( $I_{\text{TC}}$ ).

The resulting minimum time between consecutive discharges for the accessible parameters shown in Fig. 3.8 is of the order of 40 s, which is much lower than the necessary  $\Delta t \approx 120$  s required by the acquisition system.

#### 3.2.3 Stresses on the set-up

We now introduce the analyzed stresses on the system, focusing in particular on the effect of the TC weight, which has defined the number of sustaining vertical supports in the final design.

A loop conductor with a loop radius  $R$ , section radius  $a$ , inductance  $L$  and carrying a DC current  $I$  is subject to a hoop force  $F_h$  along the radial direction given by the derivative of the

<sup>3</sup>The maximum amount of electrical current a conductor or device can carry before sustaining immediate or progressive deterioration.

### Chapter 3. In-vessel toroidal conductor

---

stored energy  $E = I^2 L/2$  with respect to the radial distance [109]:

$$|\mathbf{F}_h(a, R)| = \frac{dE(a, R)}{dR} \simeq \frac{1}{2} \mu_0 I^2 \left( \ln \frac{8R}{a} - \frac{7}{4} + \frac{a}{8} \right) \quad (3.13)$$

where eq. 3.1 is used. This corresponds to a force  $\mathbf{F}_h \simeq 1.2$  N for  $I \simeq 1$  kA.

The presence of a homogeneous vertical magnetic field adds a further radial Lorentz Force in the outward or inward direction, depending on the field sense if upward or downward:

$$|\mathbf{F}_L^{\mathbf{B}_v}| = I \oint_{\ell} \mathbf{ds} \times \mathbf{B} = 2\pi R I B_z \simeq 30 \text{ N}, \quad (3.14)$$

with  $B_z = 5 \times 10^{-3}$  T and  $I \simeq 1$  kA. Both the hoop force and the radial Lorentz Force are negligible compared to the yield strength of the structure.

#### Vertical supports

A solution with three vertical supports, including the feed-through, is explored. The port constraints the toroidal separation between the three sections to distribute the weight, indicated in Tab. 3.4. A finite element static study of the structure<sup>4</sup> excludes this design for the excessive vertical deflection of  $\sim 6$  mm and for the Von Mises stress<sup>5</sup> up to  $\sim 25$  MPa. The results are reported in Fig. 3.10. The same analysis is performed for 4 supports, including an isolating

	Number of supports	Toroidal angles
Blue	3	115.77°, 90°, 154.28°
Green	4 (ideal)	90°, 90°, 90°, 90°
Red	4 (viable)	90°, 90°, 78°, 102°

**Table 3.4** | Explored solutions for the TC vertical supports.

junction<sup>6</sup> between the conductors (indicated in Fig. 3.1 (d)) at the position of the feed-through to further reduce the mechanical stress. The viable solution revealed similar features with respect to the ideal one with a toroidal separation of 90° between the copper sections. The maximum vertical deformation results to be 1.2 mm, with much lower stresses, as it can be noticed in Fig. 3.10. A design with 4 supports and a junction in between the two conductor extremes is therefore chosen in particular for the weakness of the feed-through, as can be seen comparing Fig. 3.11 (a|b).

<sup>4</sup>Performed with the commercial engineering simulation software Ansys in collaboration with the CRPP drawing workshop.

<sup>5</sup>Also known as *maximum distortion strain energy criterion*, providing an estimate of the tensile stress on the conductor, reaching a critical value at 30 MPa for copper.

<sup>6</sup>Material: TECAPEEK GF 30.

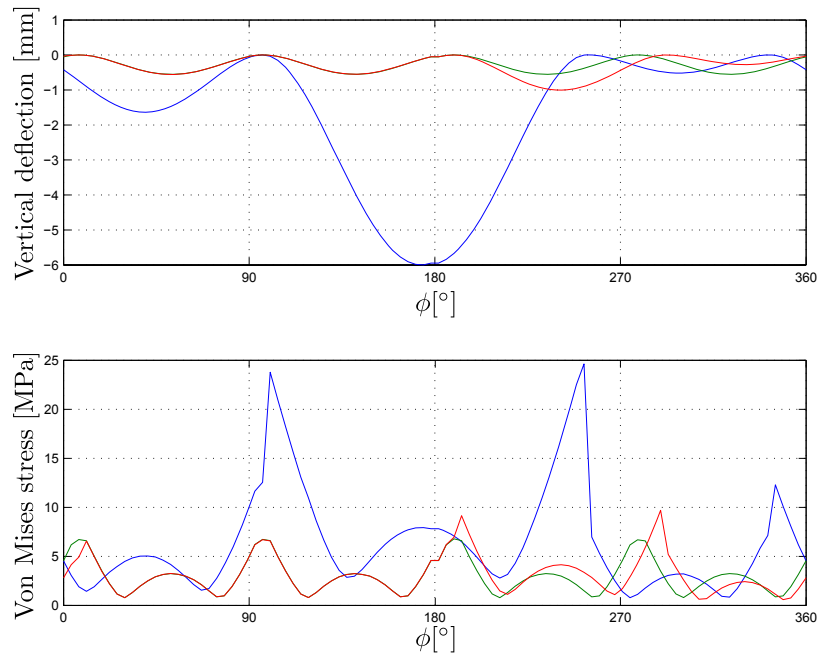


**Figure 3.10** | Study of the Von Mises stress on the TC at different toroidal angles. Blu: 3 supports; green: 4 supports-ideal; red: 4 supports-viable.

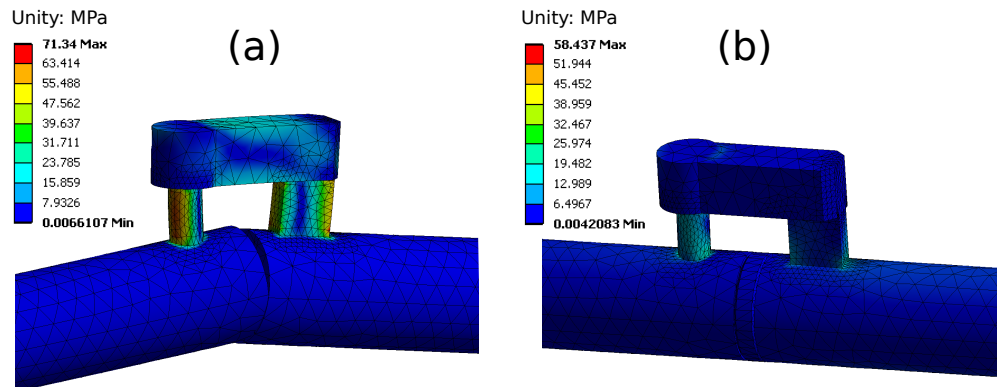


**Figure 3.11** | Von Mises stress on the vertical feed-through with 4 supports, without (a) and with (b) the isolating junction.

### 3.3 Accessible magnetic configurations

The poloidal field generated by the TC can be combined to the field  $B_z$  produced by the set of VFC introduced in Sec. 2.2 to obtain different magnetic configurations. These can be calculated using the measured currents in the TFC, TC and VFC. The TC is modeled with several discrete sources sharing the total current, computing for each source the analytical solution of the generated poloidal field using the electromagnetic Green's functions. The most relevant accessible configurations are presented in the following, identifying the external coils as A1, A2, B1, B2, C1, C2, D1, D2, E1, E2 and providing the corresponding current paths.

3.3.1 Wall-limited configurations

The poloidal magnetic field without any  $B_z$  is naturally wall limited on the LFS with a SOL about 10 cm width on the HFS. In Fig. 3.12 we show the poloidal magnetic field generated with  $I_{TC} = 1$  kA in the clock-wise direction from the top.

The implementation of the quasi homogeneous vertical magnetic field used for the SMT gives access to a wide range of magnetic configurations. A small  $B_z$  component to compensate the higher field intensity on the HFS allows to obtain quasi-concentric flux surfaces, shown in Fig. 3.13. The *ideal vertical field* with 12 A of current in the VFC is used. Keeping the same  $I_{TC}$  but with a higher  $B_z$ , a SOL originates on the LFS, as illustrated in Fig. 3.14. We should stress that wall-limited SOL presents an incidence angle of the field lines on the wall almost tangential.

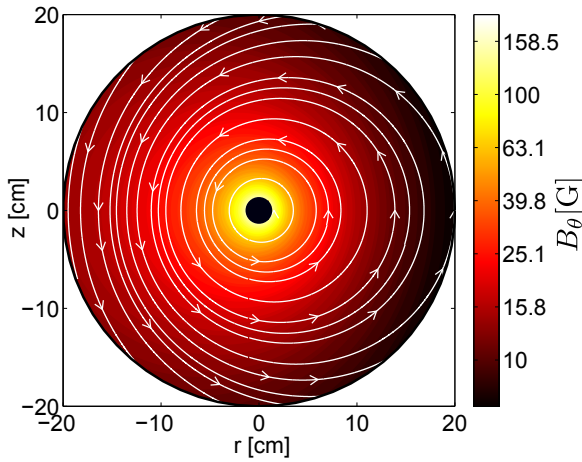


**Figure 3.12** | Poloidal magnetic field generated by the TC indicated with a black circle in the middle of the vacuum vessel, driving a current of  $I_{TC} = 1$  kA. The white arrows indicate the magnetic field lines.

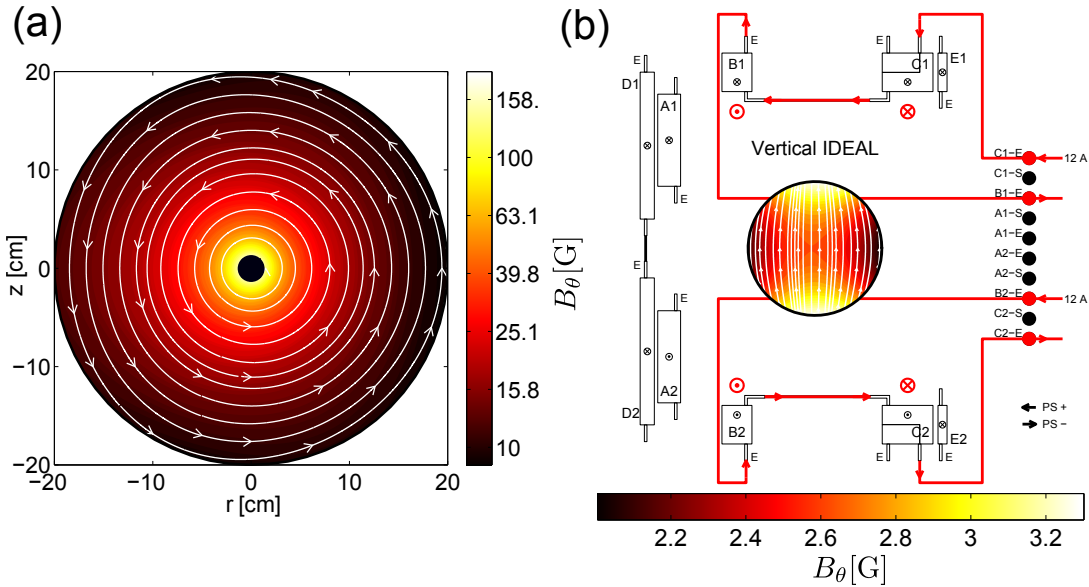


**Figure 3.13** | (a) Quasi-concentric flux surfaces obtained using the VFC in the *ideal vertical field* configuration with 12 A of current, indicated in (b).  $I_{TC} = 1$  kA.

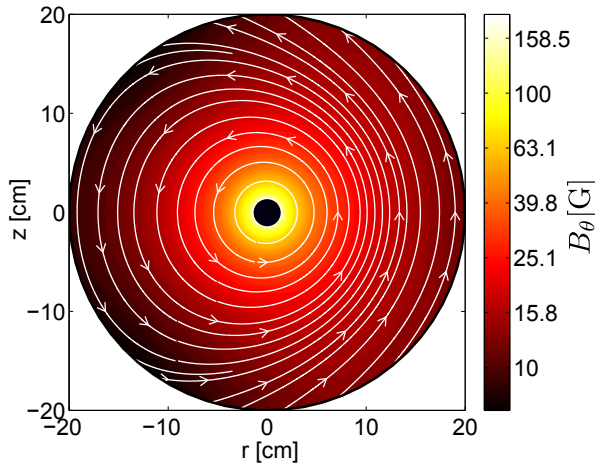


**Figure 3.14** | Wall-limited magnetic field geometry with a SOL on the LFS obtained with 30 A of currents in the VFC.

#### 3.3.2 Diverted configurations

In the following, we indicate some of the accessible diverted configurations.

##### Horizontal single-null X-point

Further increasing  $B_z$  allows to produce a single-null X-point on the HFS at  $z \approx 0$  cm. The results with a VFC current of 100 A are shown in Fig. 3.15. Inverting the direction of the VFC current, the single-null X-point can be moved to the LFS.

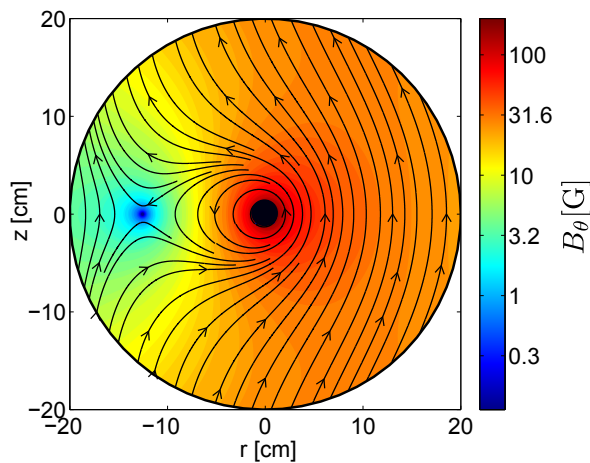


**Figure 3.15** | Magnetic configuration with a single-null X-point on the HFS at  $(r \approx -12.5, z \approx 0)$  cm. The field lines are indicated in black.

##### Vertical single-null X-point

To generate an X-point along the vertical axis at  $r \approx 0$  cm, a quasi-horizontal magnetic field has to be produced with the VFC. In Fig. 3.16, an example with  $I_{TC} = 1$  kA and VFC current of 140 A is shown.

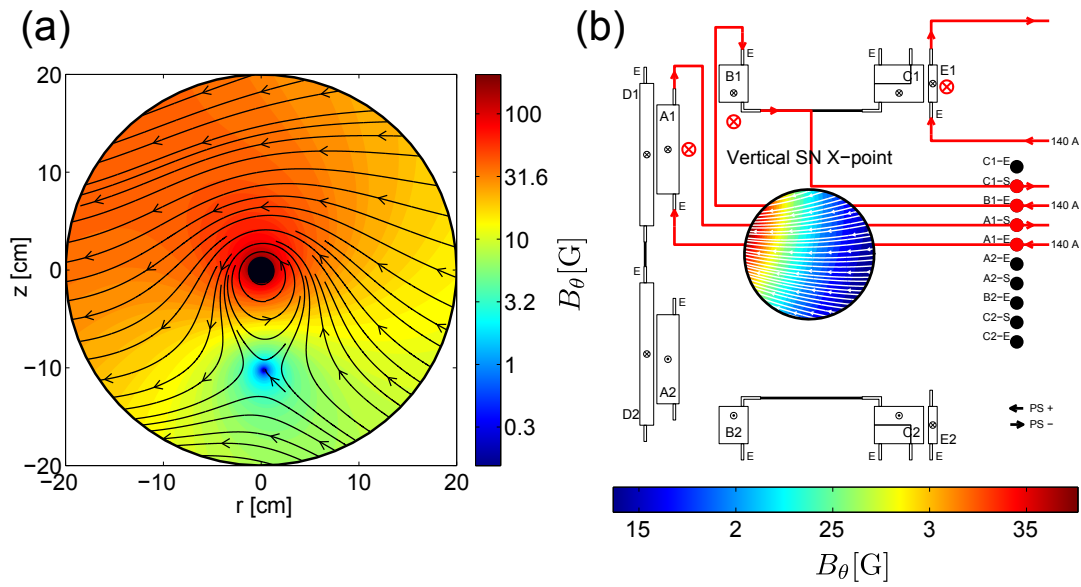


**Figure 3.16** | (a) Single-null X-point at  $(r \approx 0, z \approx -10)$  cm. (b) Current paths of the VFC to produce the required horizontal magnetic field.

### Vertical double-null X-point

The VFC current path can be changed to produce a vertical double-null X-point, together with the poloidal field generated by the TC. We show an example with the VFC current is 300 A, while  $I_{TC} = 500$  A.

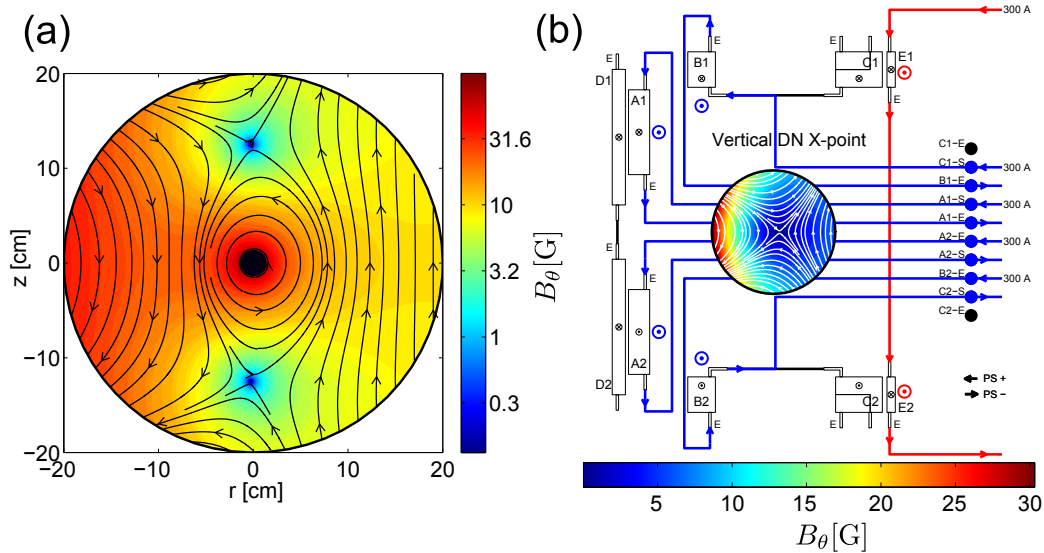


**Figure 3.17** | (a) Vertical double-null X-point at  $(r \approx 0, z \approx -12.5)$  cm and  $(r \approx 0, z \approx 12.5)$  cm. (b) Current paths of the VFC to produce an horizontal magnetic field of opposite directions on the lower and upper part of the poloidal cross section.

**Second-order null-point (snowflake divertor)**

The possibility to move the TC on the upper part of the vacuum chamber gives the possibility to generate a second-order null point, also known as snowflake divertor, at almost the center of the poloidal cross section. An example is indicated in Fig. 3.18 setting the TC at  $z \simeq 16.5$  cm, with the corresponding configuration of the VFC requiring three different power supplies (current values). The simulated TC current is 1 kA.

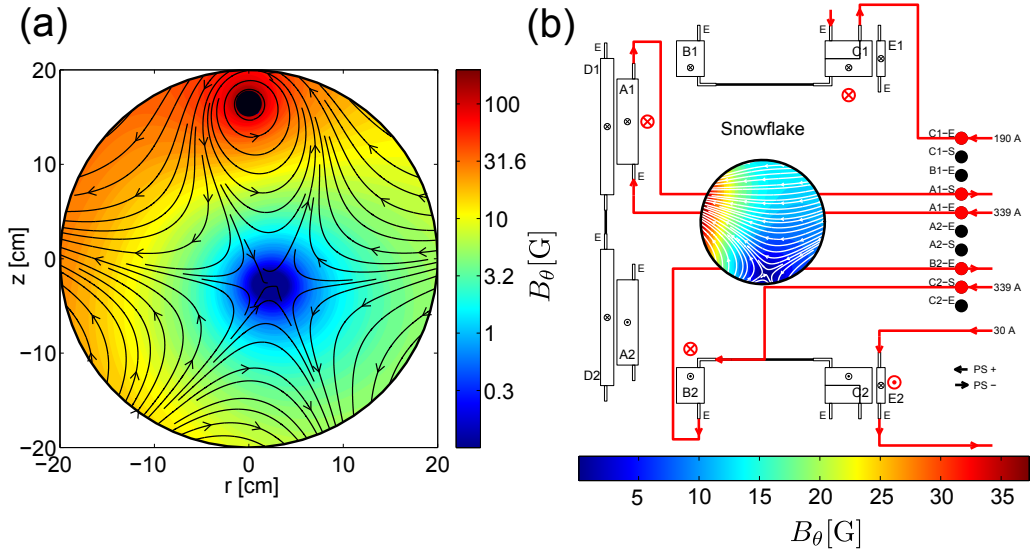


**Figure 3.18** | (a) Second-order null point (snowflake divertor) at  $(r \simeq 2, z \simeq -2)$  cm. (b) Current paths of the VFC with three power supplies.

**3.4 Magnetic field measurements**

The calculated magnetic field configurations are used to choose the experimental current values of the magnetic field coils (TFC, VFC) and TC to obtain the required magnetic geometries. The computed poloidal component is validated measuring the magnetic field generated by the TC without the plasma.

**3.4.1 Experimental set-up for the magnetic field measurements**

A single axis Hall transducer, Sentron Model ZS150 3-5-2I [110] is used for the measurements. It is powered by a standard  $\pm 12V$  laboratory power supply. A Lakeshore Model 340 Temperature Controller provides temperature stability at about  $40^\circ$ . The active volume of the probe head has a size of  $1.0 \times 0.3 \times 0.2 \text{ mm}^2$ , as shown in Fig. 3.19. The probe sensitivity of  $1.1 \text{ V/T}$  leads to measured signals of  $V_{\text{sig}} \approx 1 \text{ mV}$ , which are amplified by the TORPEX Langmuir amplifiers. The nominal amplification factor of 100 was tested with a Voltmeter resulting to be correct within 1%. The non-linearity of the probe response is negligible in the magnetic field range of interest.

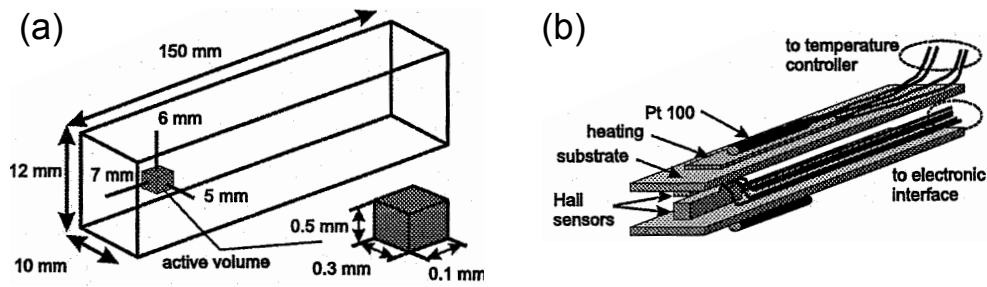


**Figure 3.19** | (a) Layout of the probe head with details of the position and volume of the active part. (b) Details of the probe head. Two Hall sensors are mounted on ceramic supporting plates. The heating foils are fixed on the outside and the 100W RTD platinum temperature sensors are fixed on top of these [110].

The TC is positioned at ( $r \approx 0, z \approx 0$ ) cm and the Hall probe is mounted on a stainless steel arm setting the sensor at  $z \approx 0$  cm with respect to the TORPEX poloidal cross section. A 90 degree holder is used to keep the probe vertical and to align the sensor axis with the vertical direction of the magnetic field, as indicated in Fig. 3.20 (a). The other extreme of the arm is fixed to a radial movable system (slide) with a sensitivity of 0.5 mm per turn of the knob. The slide is fixed to the TORPEX port and maintained horizontally verifying the alignment with an electronic level (Fig. 3.20 (b|c)). The uncertainty on the probe position according to the measured sizes of the implemented components is 2 mm, using the TORPEX port as reference. This is verified from the probe relative distance with respect to the TC.

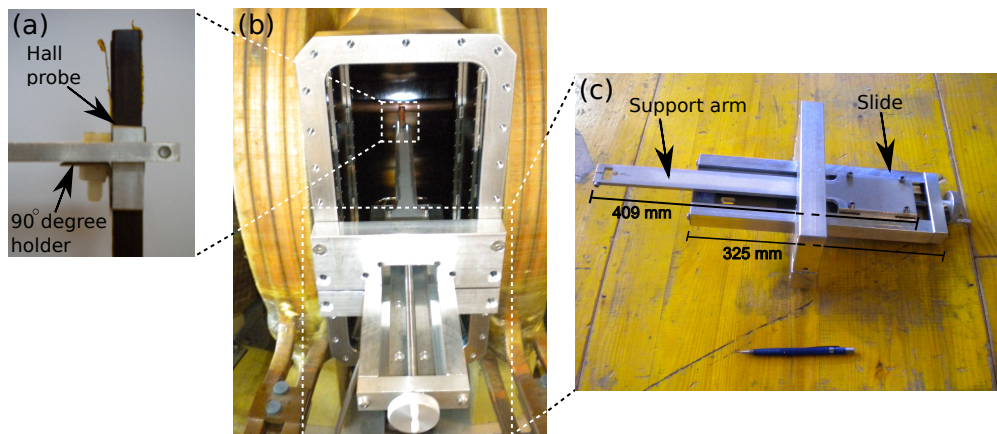


**Figure 3.20** | (a) Photograph of the probe fixed on the arm extreme and kept vertically with a try square. (b) Photograph of the experimental set-up installed on the TORPEX port. (c) Photograph of the system for the radial displacement of the Hall probe, with the supporting stainless steel arm fixed on a slide.

### 3.4.2 Measurements of magnetic field

The measurements are performed with a spatial step of 5 mm in the range  $r = [1.5 - 20]$  cm on the LFS. At each radial position, the TC magnetic field signal is maximized driving a current



### 3.4. Magnetic field measurements

$I_{TC} \approx 1025$  A, which is measured ( $I_{meas}$ ) with the current transducer introduced in Sec. 3.1.3. The first part of the signal with  $I_{TC} = 0$  is used for background removal. The flat-top values are averaged over a time window of about 200 ms. The magnetic field value corresponding to the same measured current is then calculated and compared to that simulated. The results are shown in Fig. 3.21, indicating a good agreement within the error bars between the computed and measured poloidal magnetic field. The absolute difference between measured and simulated magnetic field is given in Fig. 3.22 (a) and is less than 0.5 Gauss on most of the LFS, corresponding to a relative error below 3%, as shown in Fig. 3.22 (b). This confirms the reliability of the simulations of the magnetic field configurations, which can therefore be used to design future experimental scenarios.

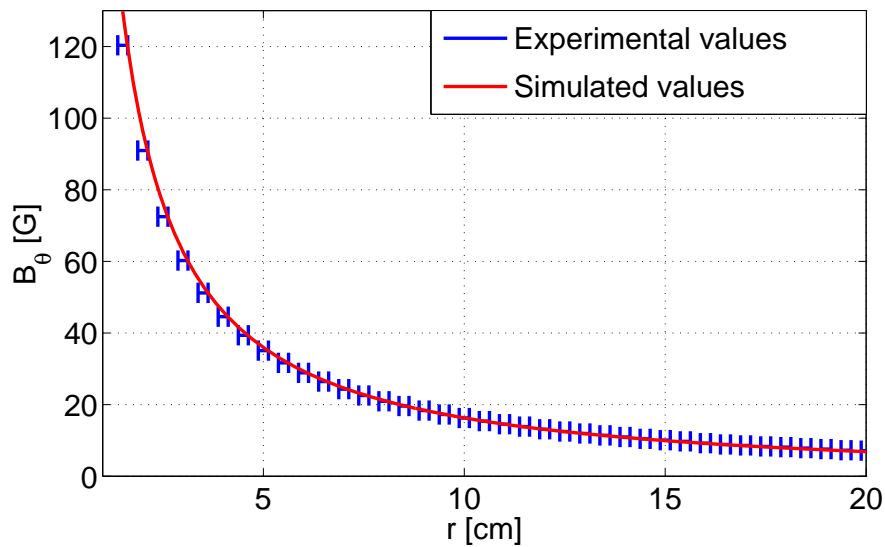


Figure 3.21 | Comparison of measured and simulated magnetic field.

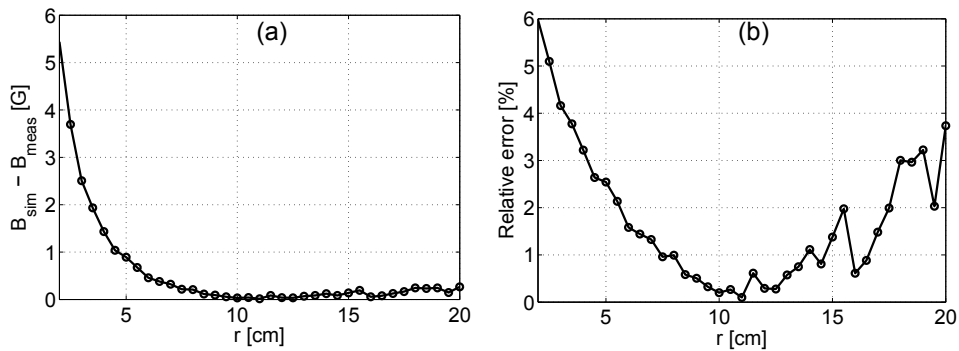


Figure 3.22 | Absolute (a) and relative (b) difference between the measurements and simulations.

### 3.5 Summary

In this chapter, the new toroidal copper conductor recently installed on TORPEX has been introduced. The current driven in the TC generates a poloidal magnetic field that combines with the toroidal component, closing the magnetic field lines and introducing a rotational transform. This allows to perform turbulence studies in more fusion relevant magnetic geometries.

The main technical features of the system are reported, together with the design requirements, including the accessible safety factor, the ohmic heating and the stresses on the structure. An overview of the magnetic configurations that can be explored is given, focusing in particular on wall-limited and diverted solutions. The commissioning of the system has been completed with the measurements of the poloidal magnetic field, which have been compared to the simulated values. This provides a quantitative estimation of the simulated magnetic field reliability.

# Plasma features in the closed field line configuration

In this chapter, we present a preliminary investigation of the main plasma features in the presence of a poloidal magnetic field. In particular, we focus on quasi-circular magnetic flux surfaces analyzing the plasma response to the variation of control parameters. These are the externally controlled quantities that are not modified by the plasma feedback action. The TORPEX control parameters are the neutral pressure ( $p_n$ ), the injected magnetron power ( $P_{\text{mag}}^{\text{inj}}$ ), the toroidal magnetic field ( $B_\phi$ ), which determines the radial location of the EC resonance layer ( $r_{\text{EC}}$ ), and the poloidal magnetic field ( $B_\theta$ ), changed by varying the TC current ( $I_{\text{TC}}$ ). Plasmas generated from different gases, such as H<sub>2</sub>, He and Ar, are characterized with  $p_n$  in the range  $[10^{-5} - 10^{-4}]$  mbar, increasing  $P_{\text{mag}}^{\text{inj}}$  up to 3 kW and varying  $r_{\text{EC}}$  between -15 cm and the center of the vacuum vessel. The first investigations on plasma production properties with closed flux surfaces are presented, as well as an estimate of the particle confinement time. Some of these results are included in [61].

## 4.1 Time-averaged plasma profiles

In the following, we investigate the background plasma profiles of density, temperature and plasma potential in closed flux surfaces. The differences with respect to the SMT configuration are highlighted and the plasma reproducibility is verified. The time-averaged 2D density profiles are explored for a wide range of control parameters, identifying a regime of enhanced plasma production.

### 4.1.1 Ion saturation current profiles

The 2D  $J_{\text{sat}}$  profiles obtained interpolating the HEX TIP measurements are analyzed. A current with a flat-top duration of 500 ms at  $\approx 900$  A is driven in the TC, as indicated in Fig. 4.1. The reported time-trace presents the typical dynamics of the TC current, with a slew-rate of  $dI/dt \approx 1700$  A/s. A vertical field component  $B_z$  of approximately 3 Gauss, shown in Fig. 4.2 (a|b), is added to obtain quasi-concentric flux surfaces over most of the plasma volume during

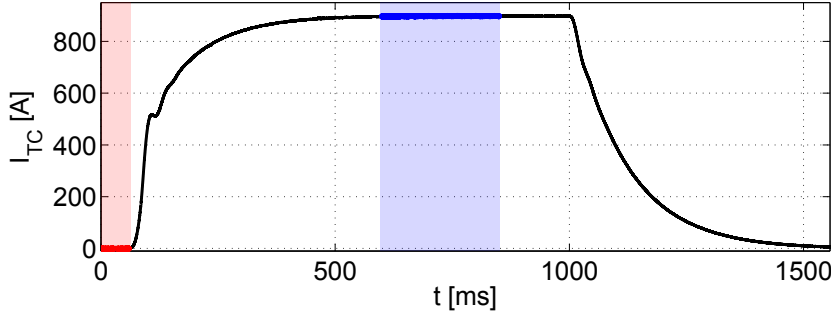


**Figure 4.1** | Measured TC current signal for the discharge #55066 with the red and blue time traces corresponding to the time windows analyzed.

the flat-top, as illustrated by the simulated field lines in Fig. 4.2 (c|d). From a top view, the toroidal magnetic field is counterclockwise, while the TC current is clockwise. These are the standard directions used throughout this work unless otherwise specified.  $\text{H}_2$  gas with a neutral pressure  $p_n \approx 1.8 \times 10^{-4}$  mbar is ionized by injecting an almost constant RF power of 340 W. The toroidal magnetic field is set to  $B_{\phi,0} \approx 79$  mT at the center of the vacuum vessel, corresponding to the EC resonance layer at  $r_{\text{EC}} \approx -10$  cm. In Fig. 4.2 we show the 2D interpolated data corresponding to the two temporal windows before the start of the current ( $t = [0 - 60]$  ms) and during ( $t = [600 - 850]$  ms) the current flat-top highlighted in Fig. 4.1. The radial cuts resulting from the LPs at  $z \approx 0$  cm and  $z \approx -3$  cm are illustrated in Fig. 4.2 (e).

Clear differences with respect to the phase of no-TC current are observed in the time-averaged ion saturation current density profiles ( $\langle J_{\text{sat}} \rangle$ ) in Fig. 4.2. During the current flat-top, the plasma profiles change, resulting in almost constant  $\langle J_{\text{sat}} \rangle$  along the flux surfaces. Moreover, the  $\langle J_{\text{sat}} \rangle$  maximum increases, peaking in the region of higher poloidal field close to the TC. A maximum electron plasma density of  $\langle n_e \rangle = 2\langle J_{\text{sat}} \rangle / (ec_s) \approx 6 \times 10^{16} \text{ m}^{-3}$  can be calculated from eq. 2.6, assuming the peak temperature of approximately 5 eV indicated in Fig. 4.3. The effective geometrical surface  $A_{\text{pr}}^{\text{eff}}$  of HEXTIP probes given in [74] is used, with an adiabatic index  $\gamma=1$  and a charge state  $Z_i=1$ . The intensity of plasma fluctuations, quantified by the standard deviation of the measured  $J_{\text{sat}}$  signals, decreases from a maximum of  $18 \text{ A/m}^2$  to less than  $10 \text{ A/m}^2$  in the presence of the poloidal field (a reduction of approximately 50%), as can be seen in Fig. 4.2 (b|c). This feature is also observed in other experiments [45].

We note that the power absorbed by the plasma ( $P_{\text{mag}}^{\text{abs}}$ ) in the two analyzed time-windows does not change. This can be obtained from the difference between the measured injected magnetron power ( $P_{\text{mag}}^{\text{inj}}$ ) and that traveling backward along the injection waveguide after being reflected by the inner wall ( $P_{\text{mag}}^{\text{ref}}$ ).

The plasma reproducibility is verified for a set of typical experimental parameters ( $I_{\text{TC}} \approx 760$  A,  $p_n \approx 1.8 \times 10^{-4}$  mbar,  $r_{\text{EC}} \approx -10$  cm,  $P_{\text{mag}} \approx 300$  W) with  $\text{H}_2$  gas, repeating the same discharge three times. For each discharge, a time window of about 600 ms during the current flat-top is used to calculate the time average and the standard deviation on the HEXTIP  $J_{\text{sat}}$  signals. The

#### 4.1. Time-averaged plasma profiles

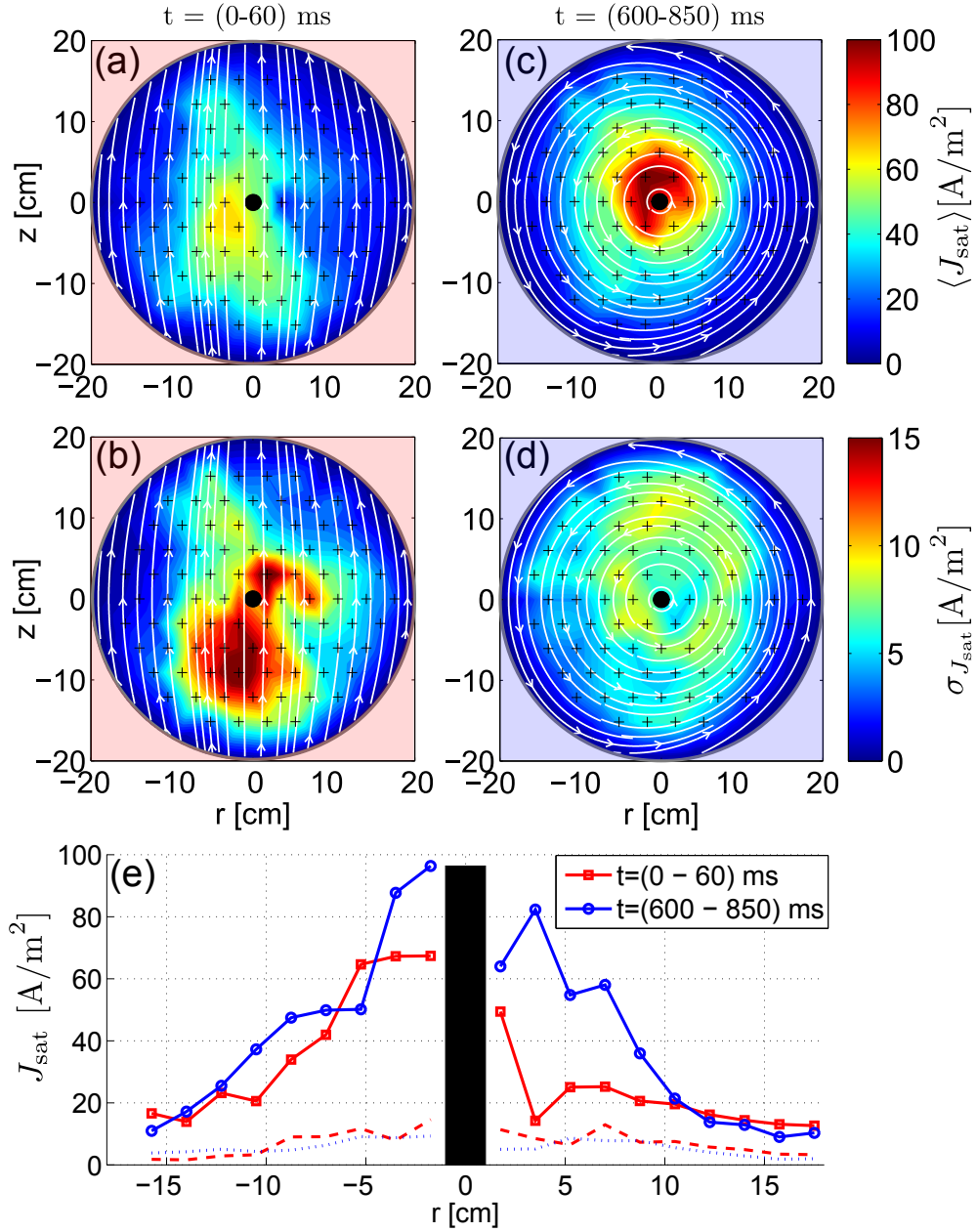


**Figure 4.2** | (a|c) 2D profiles of the HEXTIP time-averaged  $J_{\text{sat}}$  data, with the corresponding standard deviation displayed, respectively, in (b) and (d). (e) radial cuts of the measurements shown in (a|c) (continuous lines) and (b|d) (dashed lines), using the LPs at  $z \approx 0$  cm and  $z \approx -3$  cm. In white on (a|b|c|d) the simulated magnetic field lines on the poloidal cross section. The black central circle represents the TC while the black crosses correspond to the HEXTIP probe positions. Discharge #55066.

variation of  $\langle J_{\text{sat}} \rangle$  between the analyzed discharges is within 10 % for all probes and below 5 % for most of them. The variation of the  $J_{\text{sat}}$  standard deviation is within 20 % for all the LPs and below 10 % for most of them.

### 4.1.2 Plasma potential and temperature profiles

The background radial profiles of plasma temperature ( $T_e$ ) and potential ( $V_{pl}$ ) are measured on the LFS at  $z \simeq 0$  cm for the  $I_{TC}$  values of (460, 530, 610, 680, 750) A. Using the procedure introduced in Sec. 2.4.1,  $T_e$  and  $V_{pl}$  are extracted from the I-V curves obtained with the 2DSSLP (see Sec. 2.4.1). A sweeping voltage at a frequency of 330 Hz between  $-40$  V and  $20$  V is used to cover both the ion and electron saturation regimes. The measurements are performed with a spatial resolution of  $0.5$  cm, radially moving the probe between discharges. The results are shown in Fig. 4.3 for the different currents.

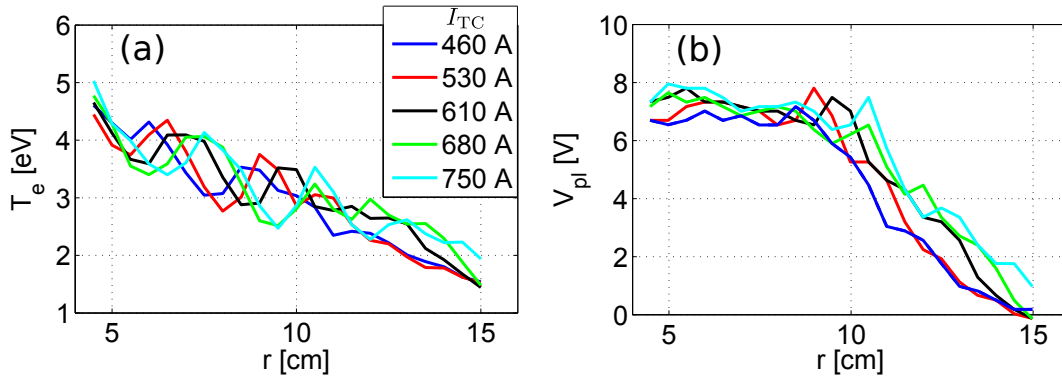


**Figure 4.3** | LFS radial profiles at  $z \simeq 0$  cm of: (a)  $T_e$  and (b)  $V_{pl}$  calculated from the measured I-V curves using the probe #08 of the 2DSSLP for the five values of TC current.

The plasma potential reaches approximately  $8$  V in the center and the maximum electron temperature is about  $5$  eV, as for the SMT configuration [74]. Both  $T_e$  and  $V_{pl}$  peak toward the region of higher poloidal magnetic field, at the center of the poloidal cross section.

From now on, the 2D  $n_e$  plasma profiles are computed assuming a constant temperature of  $5$  eV. Taking into account the influence of the temperature profile on the poloidal cross section does not significantly modify the qualitative features of the presented  $n_e$  profiles.

### 4.1.3 Control parameter dependence

We investigate the dependence of the time-averaged 2D  $n_e$  profiles upon  $I_{TC}$ ,  $r_{EC}$ ,  $P_{mag}^{inj}$ ,  $p_n$  and the gas type. We report the plasma profile variations taking place gradually and directly linked to the modified control parameter, without any significant change in the absorbed magnetron power. However, for most of the control parameters we identify a threshold value above which a step-like transition is observed in the LP  $J_{sat}$  time traces, corresponding to a sudden increase in the absorbed magnetron power and modification of the plasma source intensity and, in some cases, location. In the following, we refer to this condition as enhanced plasma production. This regime is analyzed in more details in Sec. 4.1.3, which is devoted to the  $P_{mag}^{inj}$  exploration.

**Plasma profile sensitivity to  $B_\theta$ - TC current**

$H_2$  plasmas are considered with control parameters defined in Tab. 4.1. We explore four values of accessible  $I_{TC}$ , and therefore intensity of  $B_\theta$ . The vertical magnetic field is adjusted for each value of TC current to produce quasi-circular flux surfaces. The  $J_{sat}$  data are averaged on a time-window of  $\Delta t \approx 600$  ms. The results are illustrated in Fig. 4.4.

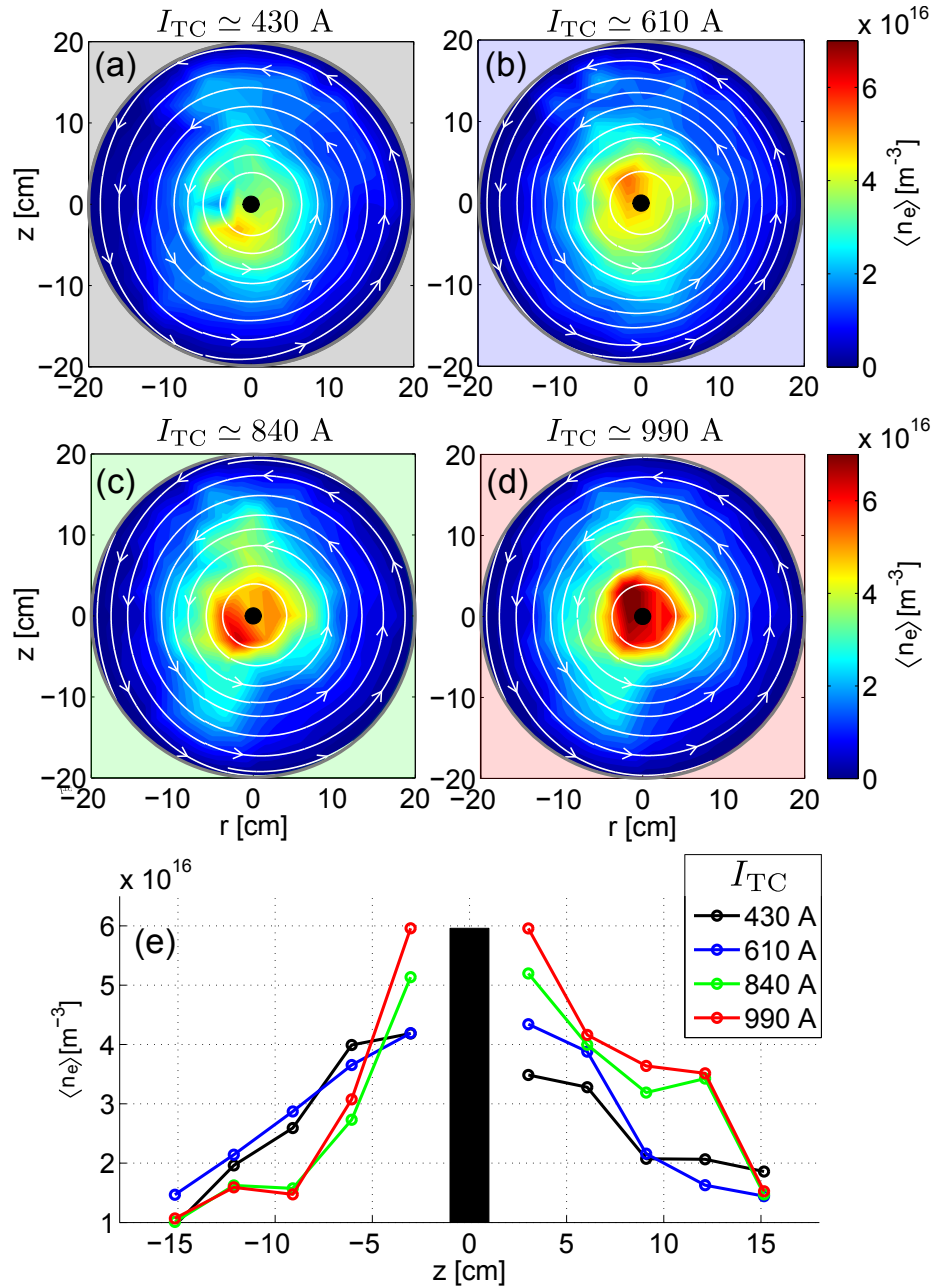


**Figure 4.4** | 2D time-averaged density profiles for four values of TC current, namely 430 A (a), 610 A (b), 840 A (c) and 990 A (d). The corresponding discharges are the #59790, #59819, #63346, and #63301 respectively. A vertical cut using the LPs data at  $r \approx 0$  cm and  $r \approx -1.8$  cm are illustrated in (e).

Gas	$I_{TC}$	$r_{EC}$	$P_{mag}^{inj}$	$p_n$
H <sub>2</sub>	[430, 610, 840, 990] A	-10 cm	300 W	$1.8 \times 10^{-4}$ mbar

Table 4.1 | Control parameters for the TC current scan.

The peak density progressively increases close to the TC in the region of high  $B_\theta$  up to a value of  $n_e \approx 6 \times 10^{16} \text{ m}^{-3}$ . This reduces the characteristic length of the density gradients, defined as  $L_n = n/\nabla n$ . For  $I_{TC} \approx 1 \text{ kA}$ , we observe on the HFS a minimum  $L_n \approx 1.5 \text{ cm}$ . A slight density asymmetry can be observed along the poloidal direction also for higher currents. The origin of this asymmetry is not clear but we should note that our experiment includes potential sources of poloidal asymmetries, such as the lateral and vertical TC supports, as well as the TC feed-through. As observed for the other control parameters, also the TC current presents a threshold value for the activation of the enhanced plasma production. Doubling the value of injected magnetron power, a fast decrease in the absorbed magnetron power is observed during the current ramp-up, as indicated<sup>1</sup> in Fig. 4.5. The transition starts at  $t \approx 300 \text{ ms}$  and is completed at  $t \approx 400 \text{ ms}$ , with the plasma entering in the enhanced plasma production regime previously mentioned. The impossibility to control the TC current dynamics limits the investigations of the changes in the plasma poloidal profiles, which are analyzed in more details in Sec. 4.1.3 by continuously varying the injected RF power.

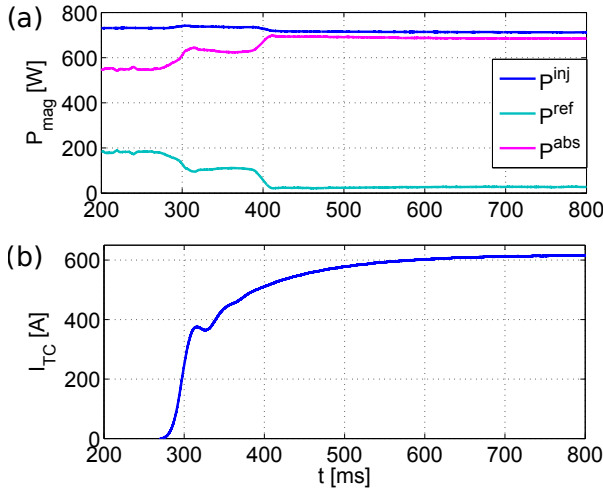


Figure 4.5 | Smoothed (a) injected ( $P^{inj}$ ), reflected ( $P^{ref}$ ) and absorbed ( $P^{abs}$ ) magnetron power signals. (b) TC current ramp-up. Discharge #58248.

### $B_\phi$ - EC layer radial position

The intensity of the toroidal magnetic field  $B_\phi$  determines the radial position of the EC resonance layer, which is required to be inside the vacuum vessel for the plasma breakdown, as discussed in Sec. 2.2. The EC resonance position at the inner edge of the vacuum vessel, namely  $r_{EC} \approx -20 \text{ cm}$ , sets the lower limit of the toroidal field. This corresponds to a magnetic field at the center of the vacuum vessel of  $B_{\phi,0} \approx 70 \text{ mT}$ . Starting from the discharge at

<sup>1</sup>The presented magnetron data are smoothed with a 20 ms moving average. From now on this type of filter is applied on the presented magnetron time-traces, if not stated otherwise.



$I_{TC} \approx 610$  A, discussed in the previous section, we perform a scan of the EC resonance position at  $r_{EC} \approx (-15, -5, 0)$  cm, corresponding to  $B_{\phi,0} \approx (74, 83, 88)$  mT. Fig. 4.6 shows the 2D profiles of the time-averaged density for the indicated discharges. In Fig. 4.6 (d) the radial profiles at  $z \approx 0$  cm are given. The location of the resonance responsible for the plasma breakdown

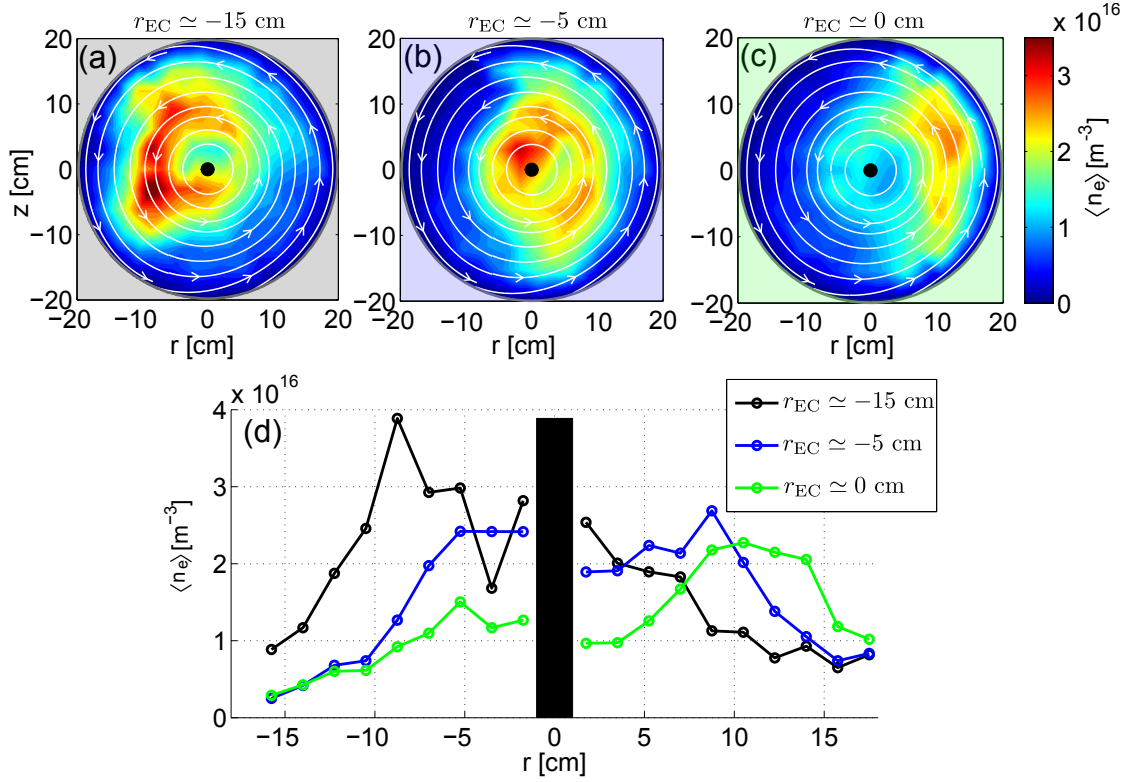


**Figure 4.6** | Poloidal profiles of plasma density with the EC resonance layer at  $r_{EC} \approx -15$  cm (a),  $r_{EC} \approx -5$  cm (b) and  $r_{EC} \approx 0$  cm (c), injecting  $P_{mag} \approx 300$  W. The corresponding cuts are  $z \approx 0$  cm are given in (d). The analyzed discharges are the #55043, #55040 and #55042.

influences the steady state profiles, which are displaced towards the LFS, as indicated by previous studies [111]. We can notice for  $r_{EC} \approx 0$  cm that most of the plasma occupies a volume at  $r \geq 10$  cm, even in the presence of  $B_{\theta}$ . The poloidal symmetry of the profiles is therefore optimized with  $r_{EC} \approx -10$  cm, with the plasma peaking in the central region of high  $B_{\theta}$ .

The effects of inverting the toroidal field ( $B_{\phi}$ ) direction have also been investigated. In Fig. 4.7 (a)(b), an example of plasma with  $B_{\phi}$  in the counterclockwise direction from the top view and with the direction inverted is given. The control parameters indicated in Tab. 4.1 are used, with the exception of  $I_{TC} \approx 740$  A and  $P_{mag}^{inj} \approx 500$  W. The time-averaged density and standard deviation contours at 40%, 60% and 80% of the maximum are illustrated. Changes in the time-averaged profiles and the fluctuation properties are observed. This could be due in part to the up-down symmetry breaking resulting from the introduction of the TC system, mainly for the presence of the vertical supports, including the current feed-through. The plasma fluctuating features can be affected by the inversion of the  $\mathbf{E} \times \mathbf{B}$  drifts. Further observations are provided in Sec. 5.1.5.

## Chapter 4. Plasma features in the closed field line configuration

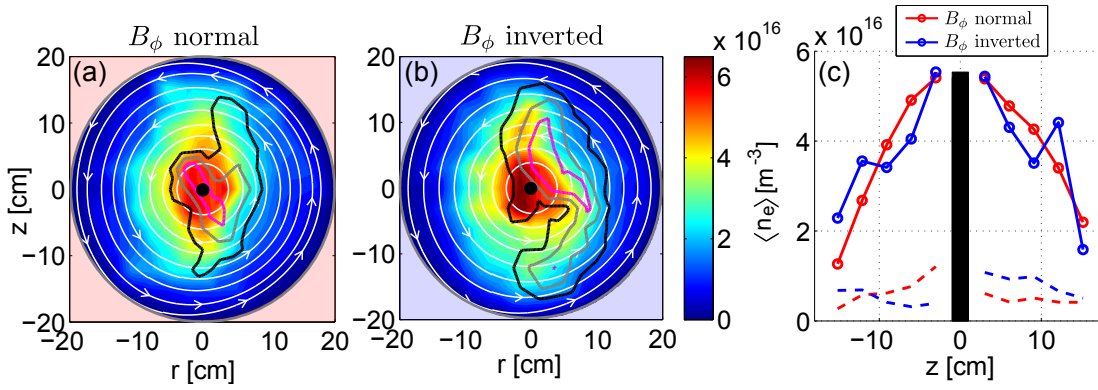


**Figure 4.7** | Time-averaged 2D density profiles on a 100 ms time window. (a) counterclockwise  $B_\phi$  from the top view of TORPEX, corresponding to the usually implemented direction (discharge #62984). (b) Same control parameters, inverting the direction of  $B_\phi$  (discharge #63055). (c) Vertical profiles at  $r \approx 0$  cm of the time-averaged density (continuous lines) and standard deviation (dashed lines).

### Magnetron power scan and the enhanced plasma production regime

We consider the same plasma conditions as in Fig. 4.6, but with approximately twice the injected power  $P_{\text{mag}} \approx 700$  W. The effects on the time-averaged profiles are shown in Fig. 4.8. A higher magnetron power increases the plasma density, affecting in turn the location of the

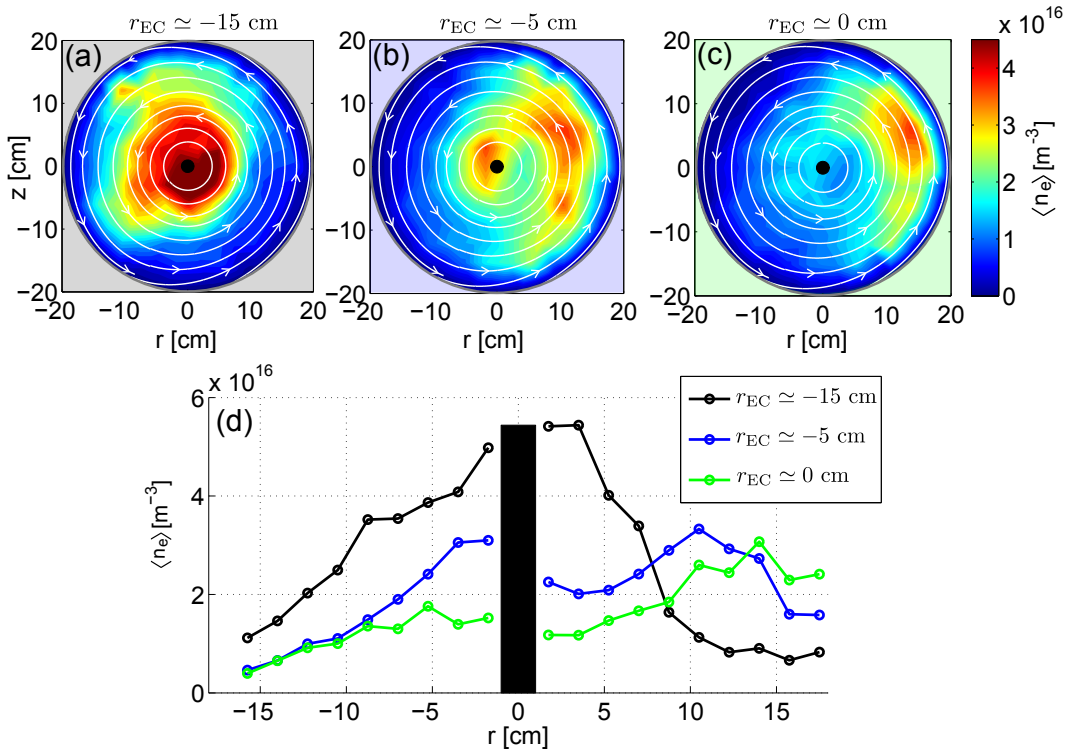


**Figure 4.8** | Poloidal profiles of plasma density with the EC resonance layer at  $r_{\text{EC}} \approx -15$  cm (a),  $r_{\text{EC}} \approx -5$  cm (b) and  $r_{\text{EC}} \approx 0$  cm (c), injecting  $\approx 700$  W. The corresponding cuts at  $z \approx 0$  cm are given in (d).

UH resonance location. This leads to the displacement of the peak density towards the LFS. This is evident comparing the profiles corresponding to the same  $r_{EC}$  of Fig. 4.6 and Fig. 4.8.

Increasing the microwave power further, the plasma enters in the previously mentioned enhanced plasma production. The sharp transition can be observed during the magnetron power ramp-up, analyzing the absorbed magnetron power and the LP time traces. An example of triangular modulation of the injected magnetron power for a  $H_2$  plasma with a neutral pressure  $\simeq 1 \times 10^{-4}$  mbar,  $r_{EC} \simeq -12.5$  cm and  $I_{TC} \simeq 400$  A is shown in Fig. 4.9.

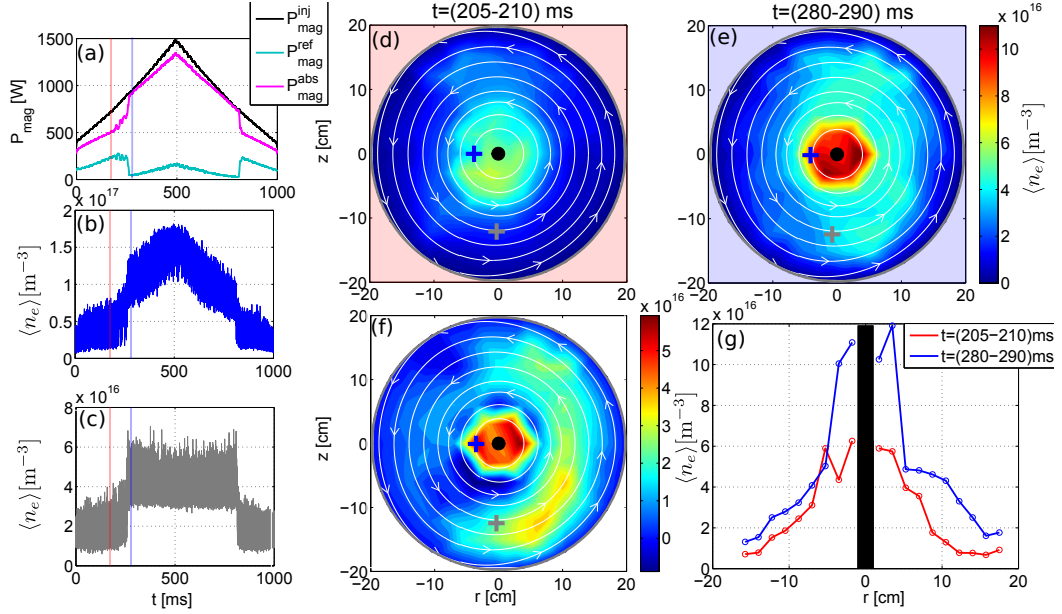


**Figure 4.9** | (a) Injected, reflected and resulting absorbed magnetron power in black, green and magenta, respectively. (b)(c)  $n_e$  time traces of two HEX TIP LPs indicated with the crosses of the corresponding colors in (d)|(e). The 2D poloidal density profiles before and after the transition are illustrated in (d)|(e), corresponding to the time-averaged data of HEX TIP LPs in the red and blue shadowed regions indicated in (b)|(c). (f) shows the difference between the data of (e) and (d). The radial cut at  $z \approx 0$  cm are reported in (g). Data for the discharge #58326, with  $r_{EC} = -12.5$  cm and  $I_{TC} = 400$  A.

During the injected power ramp-up, a jump in the reflected power occurs at  $t \approx 200$  ms, when  $P_{mag}^{inj} \simeq 750$  W, as shown in Fig. 4.9 (a). As the magnetron power rises, the measured reflected power drops to almost zero in  $\Delta t \approx 50$  ms, corresponding to an almost complete RF power absorption. Then, the injected power is progressively reflected in a fraction similar to that measured before the transition. However, during the power ramp-up the absorption mechanism is fully activated with an injected power of  $\simeq 870$  W, while during the power ramp-down the plasma starts to leave the enhanced production regime at a lower power ( $\simeq 800$  W). In Fig. 4.9 (b)(c) the time traces of two HEX TIP LPs are given, with their poloidal location indicated with the crosses of the corresponding color in Fig. 4.9 (d)|(e). The 2D poloidal time-averaged profiles of  $n_e$  before and after the transition are illustrated in Fig. 4.9 (d)|(e), with the difference reported in Fig. 4.9 (f). A higher value of  $n_e$  is visible in the region close to the TC as well as on the LFS along the flux surfaces at  $r \simeq 10$  cm. This appears also from the data radial cut

## Chapter 4. Plasma features in the closed field line configuration

at  $z \approx 0$  cm in Fig. 4.9 (g). The density of  $n_e \approx 1.2 \times 10^{17} \text{ m}^{-3}$  for the data shown in Fig. 4.9 (e) corresponds to an absorbed power  $\leq 1$  kW. The same density value is reached in the SMT with an absorbed power  $\geq 2.5$  kW [111]. Steep gradients of plasma density are attained with a minimum value of characteristic length  $L_n \approx 1$  cm.

Setting the EC resonance layer more towards the HFS, at  $r_{\text{EC}} \approx -15$  cm, the plasma can enter the enhanced plasma production regime increasing the plasma production in the region close to the TC but without the activation of the plasma source on the LFS. The transition occurs at  $P_{\text{mag}}^{\text{inj}} \approx 750$  W, as with the previous value of  $r_{\text{EC}}$ . In Fig. 4.10 (a|b|c) we show the time-averaged density before, after the transition and their difference, respectively. Fig. 4.10 (d) illustrates the profiles at  $z \approx 0$  cm.

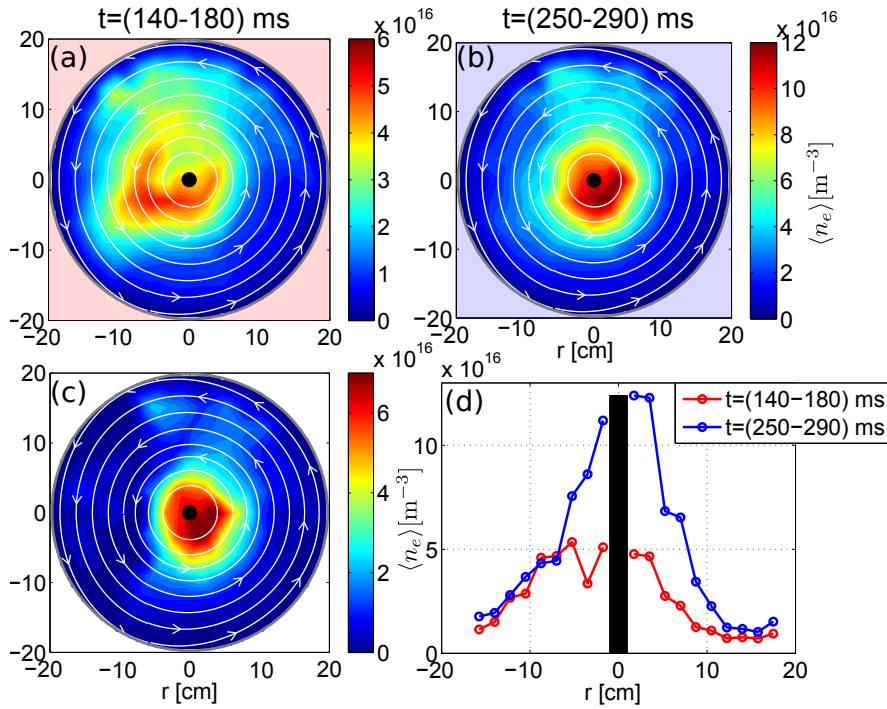


**Figure 4.10** | The 2D poloidal profiles before (a) and after (b) the transition. (c) illustrates the difference between the data of (a) and (b). The radial cut at  $z \approx 0$  cm are reported in (d). Data for the discharge #58301 with  $r_{\text{EC}} \approx -15$  cm and  $I_{\text{TC}} \approx 400$  A.

A sudden change in the visible light emitted by the plasma can be observed during the transition with the fast framing camera described in Sec. 2.4.2. An example for a discharge with  $I_{\text{TC}} \approx 620$  A is given in Fig. 4.11. The increase in the RF absorption is indicated in Fig. 4.11 (a), with the transition taking place at  $P_{\text{mag}}^{\text{inj}} \approx 750$  W. Two snapshots of the collected light before and after the transition are shown in Fig. 4.11 (b|c). A frame-rate of 50 kHz is used here. A filter is applied for the noise removal to the measured data averaging the values of each pixel with its surrounding elements fitting in a matrix  $3 \times 3$ . The camera provides a tangential view on a lateral port of TORPEX, with the TC in the middle, the LFS on the left-hand side and the HFS on the right-hand side, as illustrated in Fig. 4.11 (d).

The peak value of the intensity is observed to double after the transition in the region close

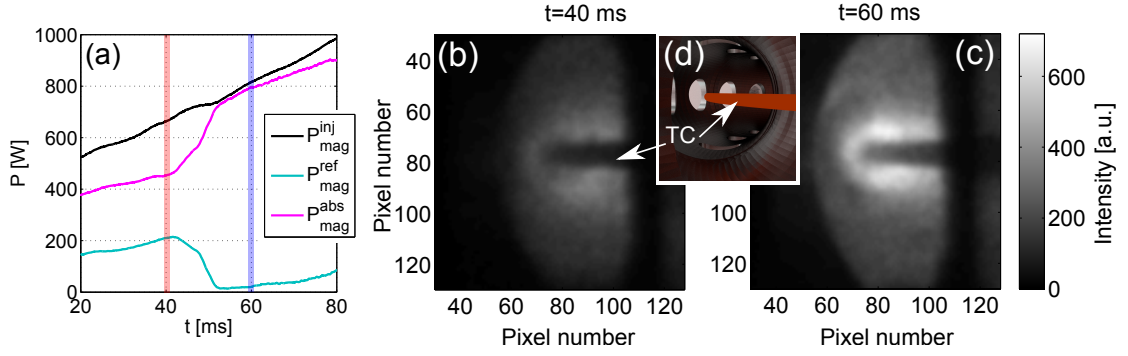


**Figure 4.11** | Filter data of visible light measured with the fast imaging camera. (a) Magnetron power time traces with highlighted in red and blues the times of the acquired visible light shown in the two frames (b|c). (d) sketch of the camera view, with the TC indicated in the middle of the vacuum vessel. Discharge #55328.

to the TC. We remark that the possible in-situ activation of the plasma production on the LFS at  $r \approx 10$  cm is not visible, since the maximum accessible radial position is  $r \approx 5$  cm for the geometrical constraints of the implemented mirror and the TORPEX port, on which the camera is installed.

### Neutral pressure

To investigate the effect of varying the neutral gas pressure  $p_n$ , the EC resonance layer is set at  $r_{EC} \approx -15$  cm, injecting  $P_{mag} \approx 600$  W, with a flat-top current  $\approx 610$  A. The time-averaged 2D profiles of  $n_e$  for three values of  $p_n$  are shown, in Fig. 4.12. We can identify the two main competing effects of the  $p_n$  variation. In Fig. 4.12 (a|b), an increase of  $p_n$  from low values leads to a higher peak density, displaced towards the center of the vacuum vessel in the region of higher  $B_\theta$ , where the UH resonance condition is satisfied. This can be explained with a higher plasma production efficiency, reducing the fast-electron mean free path  $\lambda_{mfp}$  and increasing the collision probability. However, in Fig. 4.12 (b|c) the plasma density is observed to decrease since, for density values too high, a too-low  $\lambda_{mfp}$  could result in a insufficient energy gain of the free electrons to maintain the plasma production rate.

The lowest pressure for which the breakdown is reached in  $H_2$  is  $p_n \approx 2 \times 10^{-5}$  mbar, similar to that of the SMT. Injecting a power of  $P_{mag} \approx 600$  W, with  $I_{TC} \approx 620$  A and  $r_{EC} \approx -10$  cm, a peak density of  $n_e \approx 8 \times 10^{16} \text{ m}^{-3}$  is reached with circular plasma profiles, as illustrated in Fig. 4.13. This value corresponds to a plasma with a peak ionization fraction of approximately 10%.

Changing  $p_n$  can trigger the enhanced plasma production. The results for a  $H_2$  plasma with  $r_{EC} \approx -12.5$  cm and  $I_{TC} \approx 620$  A are presented in Fig. 4.14 (a), where the absorbed magnetron power  $P^{abs}$  is given for different values of neutral pressure<sup>2</sup> and injected power. In Fig. 4.14 (b) the corresponding volume integrated density is calculated ( $N_{tot}$ ). The enhanced plasma production regime corresponds to the jumps in the reported curves. We can observe that for a fixed injected-RF power, the transition occurs only with a minimum neutral pressure value  $p_n$ .

<sup>2</sup>Obtained using the Compact Capacitance Gauge CMR 275, which provides gas independent values.

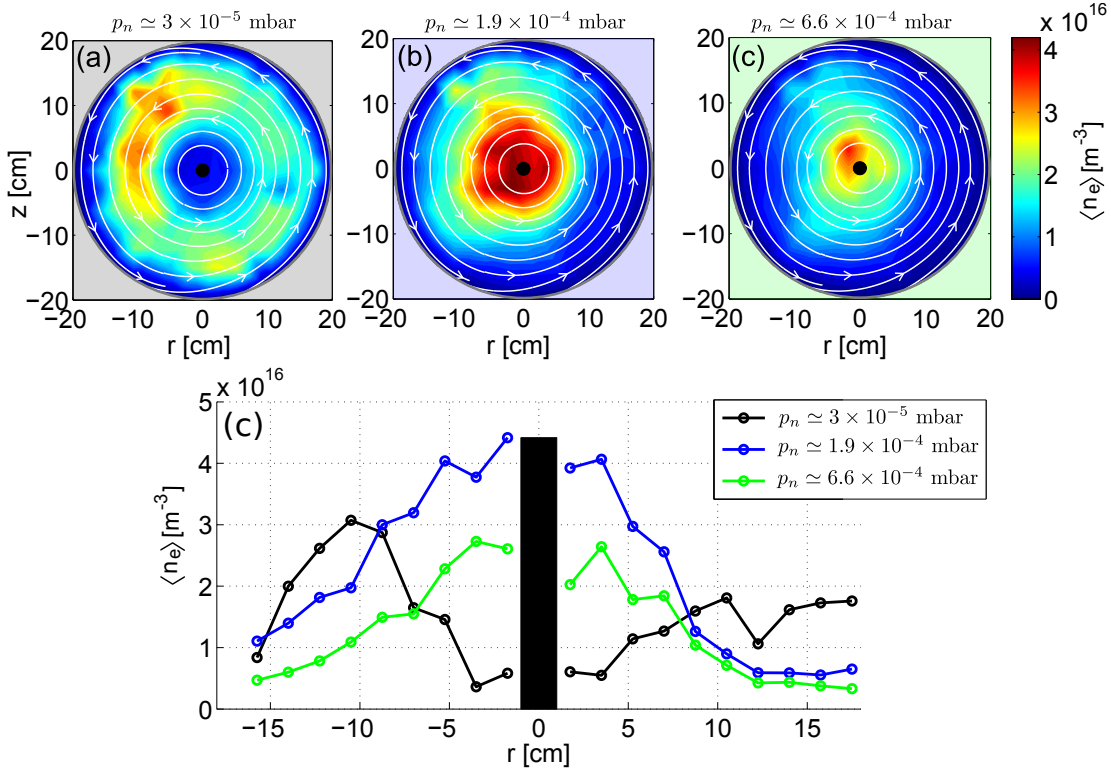


**Figure 4.12** | 2D time-averaged density for  $p_n \approx (0.3, 1.9, 6.6) \times 10^{-4}$  mbar, in (a)|b|c) respectively. The corresponding profiles at  $z \approx 0$  cm are given in (c). Discharges #57835, # 57839, #57847.

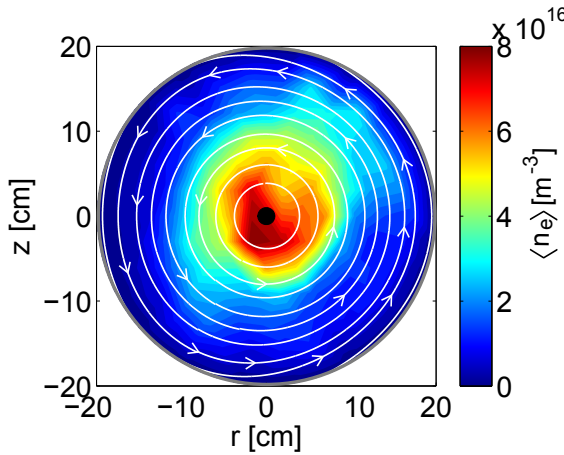


**Figure 4.13** | 2D time-averaged density profiles for the  $p_n \approx 2 \times 10^{-5}$  mbar. Discharge #57390.

The higher  $P_{\text{mag}}^{\text{inj}}$ , the lower the  $p_n$  threshold. We speculate that this correlation can be linked to a minimum required value of  $n_e$  referring to the role of  $p_n$  previously discussed, therefore the possible implication of the UH resonance. This is in agreement with the curve of 560 W, where the transition occurs only for intermediate values of  $p_n$ . For all the analyzed data the increase of  $P^{\text{abs}}$  and  $N_{\text{tot}} \approx 30\%$ , as can be inferred from Fig. 4.14 (c|d), where the data normalized to the values just before the transitions are illustrated.

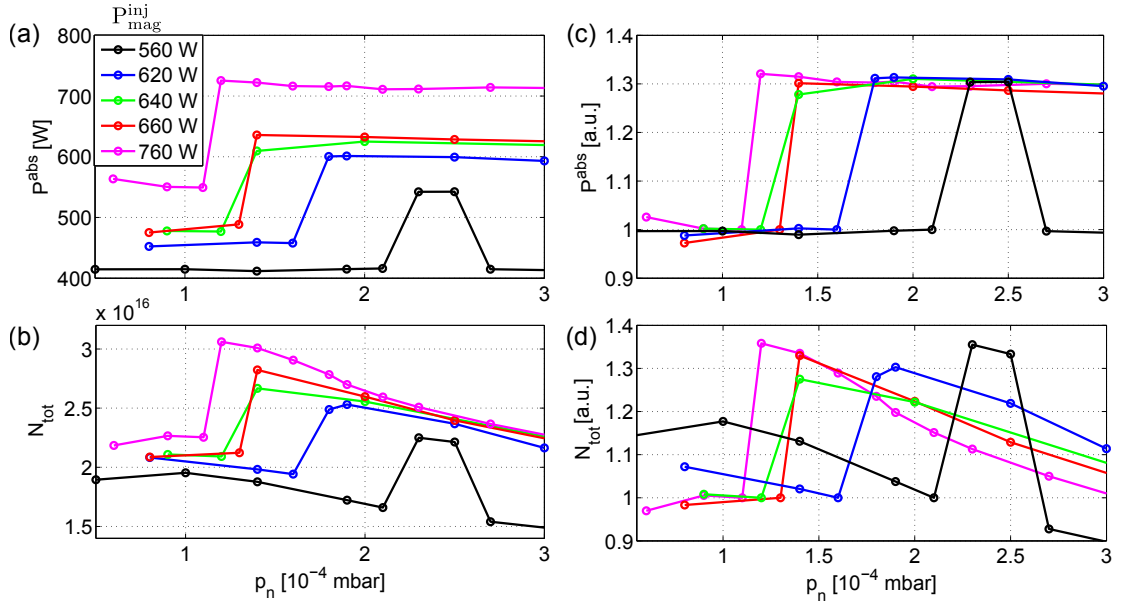


**Figure 4.14** | (a|b) Absorbed magnetron power and volume integrated plasma density as a function of the neutral pressure for different values of injected magnetron power. (c|d) Same data normalized to the corresponding value before the transition.

### Ion mass - Gas type

The choice of the neutral gas has the direct effect of changing the ion mass once the plasma is formed. Moreover, more complicated effects related to the atomic physical properties of the gas could play a role, such as the collision cross sections in the ionization processes.

In Fig. 4.15 we show the 2D profiles of the  $n_e$  time average and standard deviation for  $H_2$ , He and Ar, with  $I_{TC} \simeq 610$  A,  $P^{inj} \simeq 600$  W,  $r_{EC} \simeq -12.5$  cm and  $p_n \simeq 2 \times 10^{-4}$  mbar<sup>3</sup>. We can

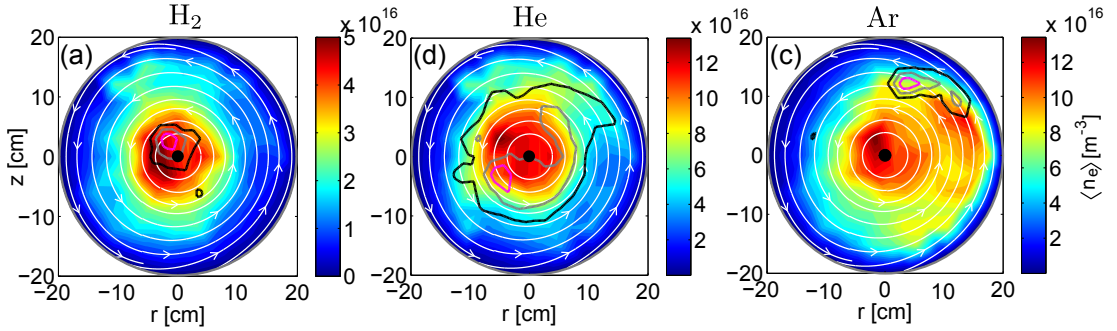


**Figure 4.15** | Time-averaged density for a  $H_2$  (a), He (b) and Ar (c) plasma. Density standard deviation contours at 40% (black), 60% (gray) and 80% (magenta) of to the maximum value. Discharges #57873, #57626, #57262.

<sup>3</sup>The neutral pressure is measured using the Compact Full Range Gauge PKR 251, which provides gas-dependent values. The calibration curves provided in the APPENDIX are used to obtain the presented  $p_n$  values from those measured. For measured pressures  $p_{meas} \leq 4 \times 10^5$  mbar, a constant calibration coefficients can be used ( $p_n = K p_{meas}$ ) for  $H_2$  ( $K = 2.4$ ), He ( $K = 5.9$ ) and Ar ( $K = 0.8$ ).

observe for He and Ar a density more than twice higher that in H<sub>2</sub>, for the same control parameters. With a higher ion mass, the background profiles get broader and the poloidal location of plasma fluctuations changes. The black, gray and magenta curves in Fig. 4.15 indicate the iso-lines at 40%, 60% and 80% of the peak value. It must be remarked that a high level of plasma fluctuations does not necessarily correspond to the location of quasi-coherent electrostatic modes. This is analyzed in details in chapter 5.

The enhanced plasma production regime is accessible by He and Ar plasmas too. Injecting a magnetron power of  $P_{\text{mag}} \approx 560$  W and varying the neutral pressure for a He plasma, we report the transition dependence on the TC current . We can observe in Fig. 4.16 that the neutral pressure threshold decreases for higher values of  $I_{\text{TC}}$ .

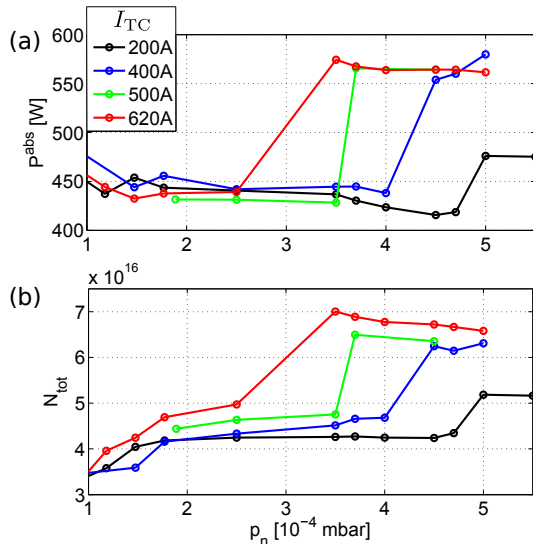


**Figure 4.16** | (a|b) Absorbed magnetron power and volume integrated plasma density as a function of the neutral pressure for different values of  $I_{\text{TC}}$ .

## 4.2 Plasma production

In the new closed field line configuration, we investigate whether the steady state plasma profiles are different if the plasma is generated by the microwaves before or during the current flat-top, when the closed field line geometry is obtained. In Fig. 4.17, we show the results for  $I_{\text{TC}} \approx 620$  A and  $r_{\text{EC}} \approx -10$  cm. Fig. 4.17 (a) illustrates the current time trace of a discharge where the magnetron is triggered during the TC current flat-top at about 700 ms, as can be seen in Fig. 4.17 (c). The time-averaged density values in the range [1100 – 1250] ms are provided in Fig. 4.17 (e). Figure 4.17 (b|d) shows an example where the current is driven at about 80 ms, when the magnetron low power phase is already started, while the corresponding densities time averaged between [700 – 850] ms are visible in Fig. 4.17 (f). The relative difference of the time-averaged signals of 83 out of 85 probes between the two discharges is less than 10%, which is comparable to the value given by the plasma reproducibility. This is verified for the following control parameters:  $I_{\text{TC}} \approx (400, 620)$  A,  $r_{\text{EC}} \approx (-15, -12.5, -10, -7.5)$  cm,  $P_{\text{mag}} \approx 300$  W and  $p_n \approx 1.8 \times 10^{-4}$  mbar.



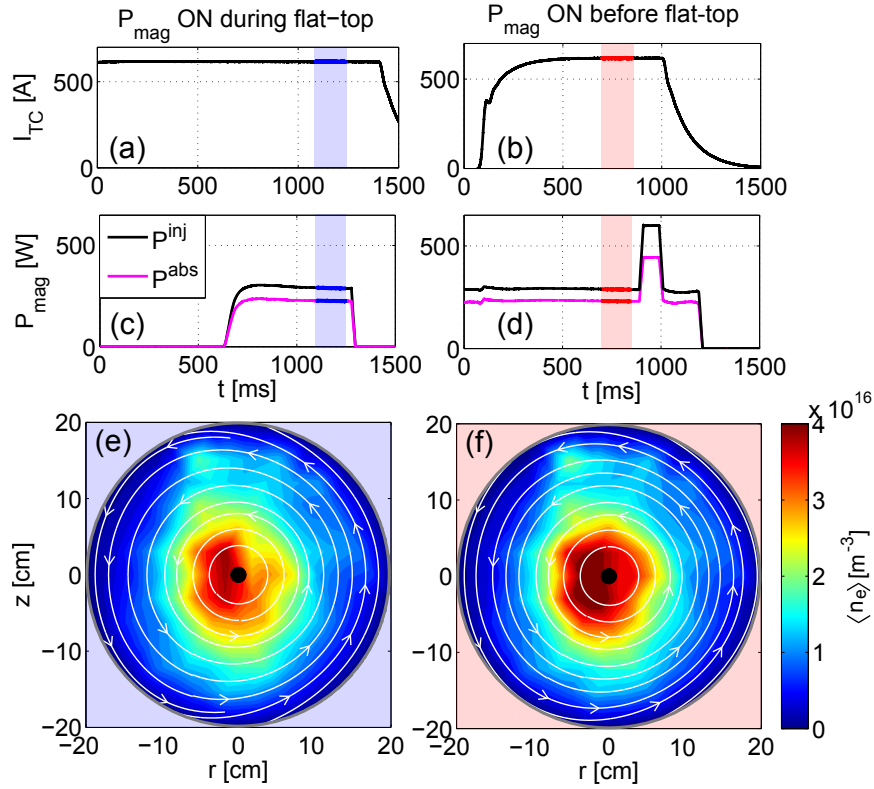


**Figure 4.17** | (a)(b) TC current time traces for the discharges #58397 and #58839, corresponding to the magnetron triggered, respectively, during and before the current flat-top. (c)(d) Injected and absorbed (black-magenta) magnetron power signals; in blue and red the time windows when the  $n_e$  time average shown in (e)(f) has been performed.

### 4.2.1 Plasma breakdown dynamics

A discharge with the magnetron trigger during the current flat-top at  $I_{TC} \simeq 620$  A is analyzed to obtain the plasma density time evolution from the breakdown to the steady state condition, in a time window of  $\Delta t \simeq 30$  ms. HEX TIP data are averaged on consecutive time windows of 1 ms. The 2D results for four different snapshots are shown in Fig. 4.18.

The EC layer is set at  $r_{EC} \simeq -12.5$  cm on the HFS and indicated in magenta, while the density layer corresponding to the UH resonance is indicated in gray<sup>4</sup>. This is calculated using eq. 2.4. We can notice initially the breakdown taking place at the EC layer location, with a fast plasma transport along the corresponding flux surfaces. Then, the density increase activates the UH resonance progressively moving the plasma source towards the center of the vacuum vessel.

### 4.2.2 Steady-state plasma source

Once the plasma has reached the steady-state equilibrium, the source location can be investigated with the same procedure implemented in [111]. The magnetron power is modulated

<sup>4</sup>We should keep in mind this is only indicative, since we have assumed a constant  $T_e = 5$  eV.

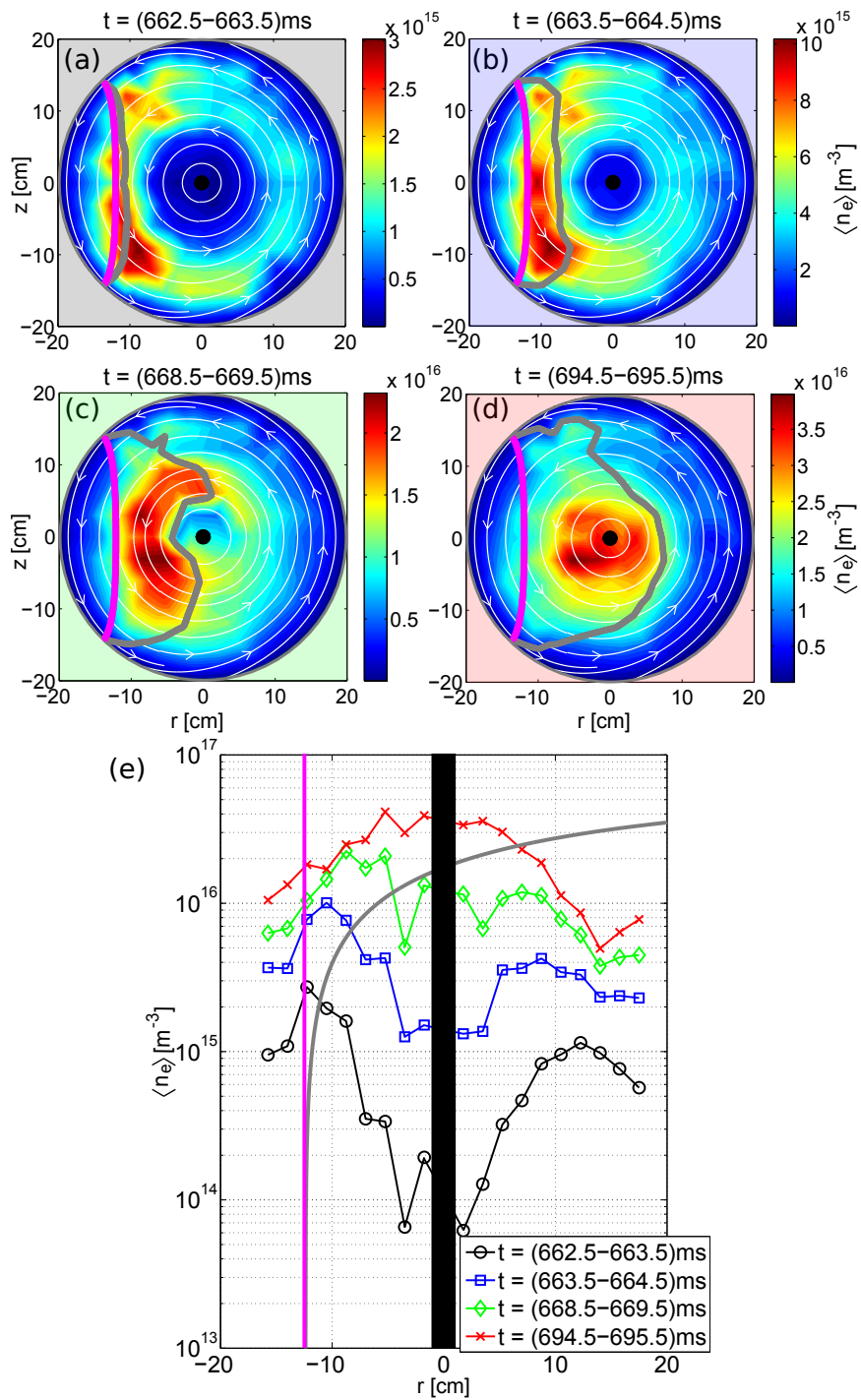


**Figure 4.18** | (a)|b|c|d) Time averaged 2D plasma density at different times during the plasma formation. (e) Radial cuts at  $z \approx 0$  cm for the four chosen times with the central conductor in black at  $z = 0$  cm. The EC resonance layer and the upper hybrid resonance layer correspond, respectively, to the magenta and gray curves. Discharge #58396.

with a frequency of 250 Hz during the TC current flat-top, with a maximum power of  $P_{\text{mag}}^{\text{inj}} \approx 1.1$  kW and a duty cycle of 10%, as shown in Fig. 4.19 (a). The conditional average sampling (CAS) technique is applied on the measured power signal detecting the power rises, indicated with red circles in the inset of Fig. 4.19 (a). Time windows of  $800 \mu\text{s}$  around the identified events ( $\tau = 0 \mu\text{s}$ ) are selected and averaged together for the injected and absorbed magnetron power time-traces and LP data. The resulting time evolutions provide information on the characteristic plasma response to a fast variation of RF power, indicating the plasma production location. The CAS injected and absorbed magnetron signals are represented in Fig. 4.19 (b) using a dashed and a continuous line. Fig. 4.19 (c) shows the LP density fractional variation  $\delta n$  obtained from the conditionally averaged signals for four different LPs, defined as:

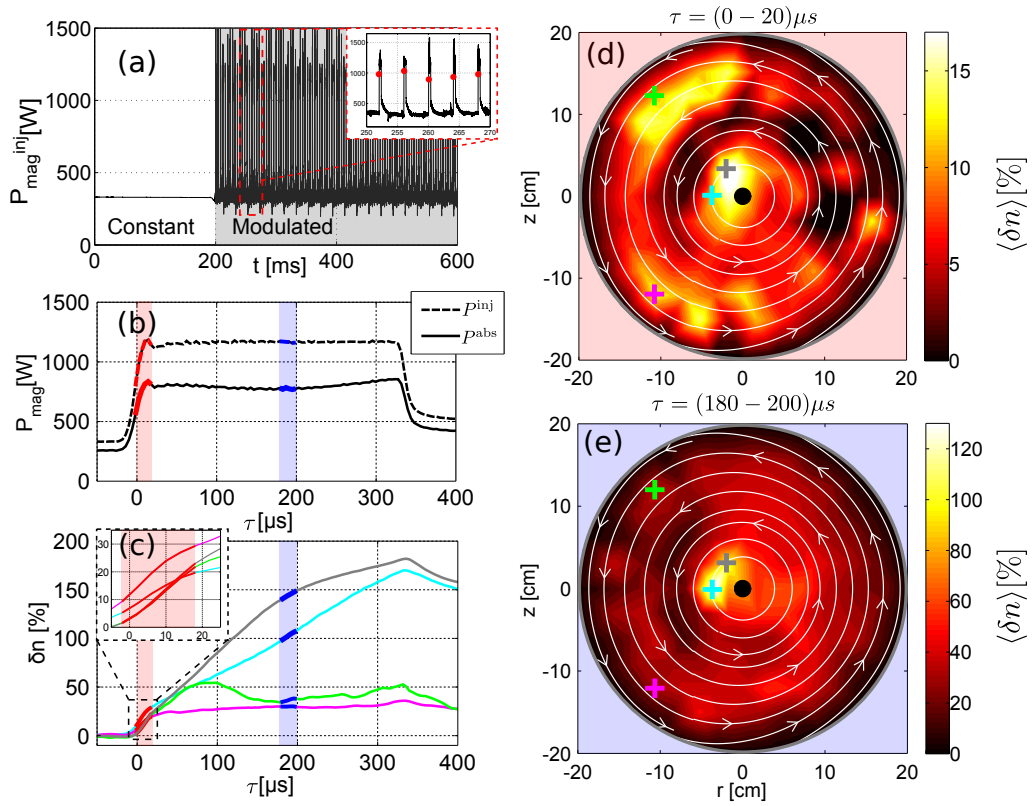


**Figure 4.19** | (a) Magnetron power modulation with the detected trigger obtained from the CAS analysis indicated with red dots in the inset. (b) Injected and absorbed CAS magnetron power in dashed and continuous black lines, respectively. (c) CAS fractional variation  $\delta n$  for the LPs indicated with crosses of the corresponding colors in (d) and (e). (d) and (e),  $\delta n$  time averaged on the windows indicated with red and blue shadowed regions in (b) and (c). Discharge #58179.

$$\delta n = \frac{n(\tau) - \langle n^{\text{low}} \rangle}{\langle n^{\text{low}} \rangle}, \quad (4.1)$$

where  $\langle n^{\text{low}} \rangle$  is the CAS density averaged in the time window  $\tau = [-120, -40] \mu\text{s}$ . The spatial locations of the analyzed LPs are indicated with crosses of the corresponding colors in Fig.

4.19 (d|e), where two snapshots of time averaged  $\delta n$  calculated for all the HEX TIP LPs on the red and blue shadowed regions in Fig. 4.19 (b|c) are shown.

The average profiles during the constant power phase before the beginning of the modulation are compared with the 2D profiles obtained from the  $\langle n^{\text{low}} \rangle$  data, resulting in a difference lower than 5% for all LPs. This allows the density to relax to the steady-state profiles during the low power phase of the modulation.

We can observe in the time interval  $\tau = [0 - 20] \mu\text{s}$  a fast plasma response in the region close to the EC layer ( $r_{EC} = -12.5 \text{ cm}$ ), as well as close to the TC, suggesting the activation of both the EC and UH resonances. After the initial transient phase, the plasma source starts to be mainly localized close to the TC, as can be seen in Fig. 4.19 (e) from the  $\delta n$  averaged in the time window  $\tau = [180 - 200] \mu\text{s}$  and from the cyan and gray LP time traces in Fig. 4.19 (c). This is presumably related to the UH layer, suggesting a dominant efficiency of the ionization mechanism associated with the UH resonance mechanism, in agreement to the previous studies on TORPEX with the SMT configuration.

### 4.2.3 Enhanced plasma production regime

In this section we analyze in detail the dynamics of the transition to the enhanced plasma production regime. To get an insight of the LFS  $n_e$  profile evolution during the transition, a plasma marginally stable with respect to the enhanced plasma production is investigated. A constant RF power close to the previously measured threshold value of  $P^{\text{inj}} \approx 750 \text{ W}$  is injected, as indicated in Fig. 4.20 (b). The HEX TIP  $n_e$  time traces and the reflected magnetron power reveal the presence of a limit-cycle, as illustrated in Fig. 4.20 (a|b), with intermittent drops and rises indicate the activation of an enhanced plasma source. The CAS technique is applied to select the transition events from the measured reflected magnetron power, as shown in Fig. 4.20 (b). The variations of the obtained CAS  $n_e$  data with respect to the values before the beginning of the transition ( $\tau = 0 \mu\text{s}$ ) are calculated. Two snapshots are given in Fig. 4.20 (d|e), indicating the location of the plasma source activation on the lower part of the poloidal cross section. The plasma production progressively increases on the LFS moving along the corresponding flux surfaces in the counterclockwise direction. The  $n_e$  increase on the probe close to the TC at ( $r \approx -1.8, z \approx 3$ ) cm can also be noticed. An interesting feature is the sudden drop in  $J_{\text{sat}}$  for the LP at ( $r \approx 3.5, z \approx 0$ ) cm. The presence of a plasma source on the LFS and close to the TC, as indicated in Fig. 4.9 (f) and Fig. 4.20 (e), is confirmed performing the same power modulation technique presented in Sec. 4.2.

One possible explanation for the enhanced plasma production is the formation of a density profile with more than one maximum, corresponding to multiple UH layers, as suggested in [111]. At the plasma source location indicated in Fig. 4.20 (d|e), namely ( $r \approx 0, z \approx -12$ ) cm, the required density for the UH resonance is  $n_e \approx 2 \times 10^{16} \text{ m}^{-3}$ , which is comparable with the measured value. However, the reasons for the step-like nature of the transition are still unclear, as well as the location of the initial plasma production on the bottom of the LFS shown in Fig. 4.20.

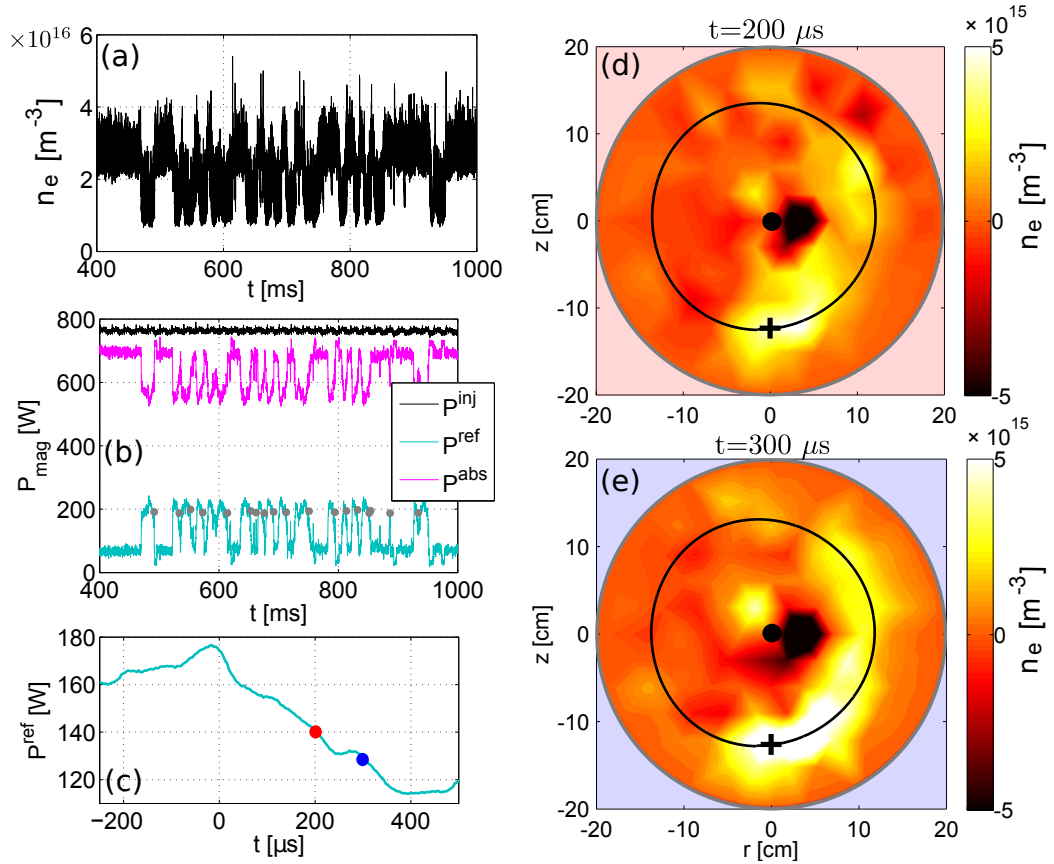


**Figure 4.20** | (a)  $n_e$  time trace of the probe indicated with a black cross in (d)e). (b) Injected, reflected and absorbed magnetron power, with the gray dots on the  $P^{\text{ref}}$  signal indicating the selected events for the CAS analysis. (c) CAS time-trace of the reflected magnetron power, with the red and blue dots indicating the times of the CAS  $n_e$  data shown in (d)e). A simulated flux surface is indicated with a black curve. Discharge #57938.

### 4.3 Plasma particle confinement time

The particle confinement time  $\tau$  can be evaluated by switching off the power source and fitting the decaying probe signals for a variety of conditions with an exponential:

$$J_{\text{sat}}(t) = A \exp(-t/\tau). \quad (4.2)$$

An  $\text{H}_2$  plasma with a neutral pressure in the range  $[0.4 - 7] \times 10^{-4}$  mbar is explored, fixing  $P_{\text{mag}} \simeq 600$  W,  $r_{\text{EC}} \simeq -15$  cm and  $I_{\text{TC}} \simeq 620$  A. The measured signal time-decay is characterized by a few general features, as it can be seen in Fig. 4.21 for the case at  $1.9 \times 10^{-4}$  mbar.

Two characteristic times can be inferred, based on two different exponential fits performed on two separate time-windows. The first, just after the switching off of the magnetron (zero of the time-axis of Fig. 4.21), provides a value in the range  $\tau_1 = [0.3 - 0.4]$  ms. The second, after about 0.50 ms, gives  $\tau_2 = [1.2 - 1.6]$  ms. As we are acquiring  $J_{\text{sat}}$ , both density and temperature are responsible for the signal decay and they could vary on different time-scales. In particular, as

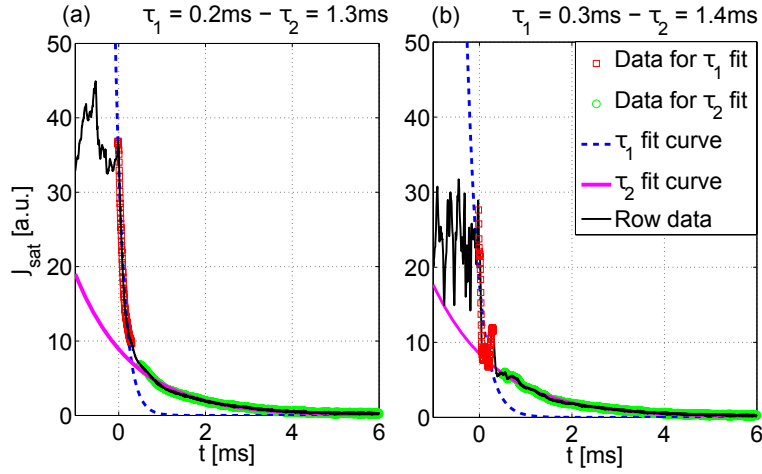


**Figure 4.21** |  $J_{\text{sat}}$  time signals taking the switching off of the magnetron as zero of the time axis. (a|b) signals of probes located, respectively, at  $(r \approx 3.5, z \approx 0)$  cm and  $(r \approx 7, z \approx 0)$  cm. In red and green the data corresponding to the two time windows where different exponential fits are performed. Discharge #57838.

reported for the SMT [111], a fast cooling of the plasma could be responsible for the fast decay of  $\tau_1$ . Increasing the toroidal current to  $I_{\text{TC}} \approx 920$  A, with  $r_{\text{EC}} \approx -10$  cm,  $P_{\text{mag}} \approx 300$  W and  $p_n \approx 1.8 \times 10^{-4}$  mbar has not given any significant improvement on  $\tau_1$  and  $\tau_2$ . In conclusion, the measured particle confinement time for the explored parameters results to be of the same order of magnitude as observed for the optimized SMT [111].

Considering the Bohm time  $\tau_B$  for a cylindrical column of radius  $a$ , defined as [6]:

$$\tau_B = \frac{a^2}{2D_B} = \frac{8a^2 eB}{k_B T_e} \approx 5.1 \text{ ms}, \quad (4.3)$$

where  $T_e \approx 5$  eV and  $B_\phi \approx 80$  mT were used, we find that  $\tau_B$  is factor of five larger than the experimental  $\tau$ . In a weakly ionized plasma, other processes such as recombination could play a significant role in the losses. The TC surface, which amounts to 1/20 the vacuum chamber surface, constitutes a further loss channel, as well as the system supports, even if electrically floating. It is worth mentioning that we did not try to optimize the particle confinement time, since it is sufficient to be comparable with the inverse of the growth rate of the expected plasma instabilities for the sake of turbulence studies. This is satisfied for the instabilities investigated in Ch. 5, characterized by dynamics varying on time scales  $\sim f_{\text{inst}}^{-1} \approx 10^{-4}$  s (Sec. 5.1.3), with an expected growth-rate of  $\sim c_s / \sqrt{L_p R} \approx 10^5 \text{ s}^{-1}$  (ideal interchange modes).

## 4.4 Summary

In this chapter, the first 2D measurements of plasma profiles in the new TORPEX configuration of concentric flux surfaces were presented. The plasma shape changes when the poloidal component is included in the magnetic geometry. For typical values of control parameters,

such as H<sub>2</sub> plasmas with  $p_n \simeq 1.8 \times 10^{-4}$  mbar,  $P_{\text{mag}}^{\text{inj}} \simeq 340$  W and  $r_{\text{EC}} \simeq -10$  cm, the resulting density profiles peak at the center of the vacuum chamber, close to the TC where the poloidal field is higher. However, although the presence of closed magnetic field lines eliminates the parallel losses, the plasma density is of the same order of magnitude as in the SMT, since a number of particle sinks are still present. Comparable values of plasma potential and temperature are also observed.

The measurements indicate that the steady-state plasma profiles are determined by the interplay of several control parameters. Profiles with almost constant density along the flux surfaces can be obtained with different values of injected magnetron power, EC resonance position, neutral gas pressure and TC current.

The first investigations on the plasma production mechanisms are provided. As for the SMT configuration [112], the injected microwaves at  $f_{\text{rf}} = 2.45$  GHz in O-mode provide the plasma breakdown at the EC layer, accelerating the free electrons, which ionize part of the neutrals. The partial change to X-mode of the wave polarization after multiple reflections on the chamber wall allows the activation of the UH resonance, where most of the microwave power is subsequently absorbed. Similarly to the SMT case [111], the density peak of the resulting plasmas is located between the EC and UH resonance layers. However, a regime with the activation of a further plasma source on the LFS is observed. A volumetric plasma density increase of approximately 30% corresponds to a RF power absorption enhancement of 30%. In the range of the explored control parameters in the new closed flux surface configuration, the measured particle confinement time results to be comparable with that of the optimized SMT.

This systematic exploration of plasma profiles, modified by varying a number of control parameters over most of their accessible range, has allowed us to identify the optimal configuration for the plasma turbulence studies that constitutes the main goal of this thesis. These will be presented in Ch. 5, where further details will be provided.





## Electrostatic fluctuations in the closed field line configuration

Energy and particle radial transport, which occurs at rates much higher than those predicted by simple collisional diffusion, is an issue affecting all fusion magnetic devices [32, 113]. Investigations are still necessary to develop the required understanding of plasma instabilities responsible for this anomalous process, from the development of linear instabilities to the highly turbulent non-linearly saturated state. Turbulence spans over a wide range of spatio-temporal scales, but in fusion devices a key role is typically played by plasma fluctuations with a frequency lower than the ion cyclotron frequency. The implementation of probes to study these turbulent phenomena in tokamaks, as well as in stellarators, is hampered by the high values of temperature and density. For example, direct measurements with fast reciprocating LPs can be performed only in a narrow region at the edge of the plasma volume. Basic plasma physics experiments [41–45] offer an alternative for turbulence studies, allowing a much easier diagnostic access due to the lower temperatures and densities.

In the past, a comprehensive study of plasma fluctuations has been conducted on TORPEX in the SMT geometry [84], as introduced in Sec. 2.5. The SMT exhibits the main features of the tokamak scrape-off layer, namely pressure gradients, curvature and gradients of the magnetic field. The topics covered range from the investigation of electrostatic instabilities [46], to the birth and dynamics of intermittently generated blobs [90] and supra-thermal ion interactions with turbulence [87]. Numerical simulations validated on experimental data [101] have revealed that different instability regimes can be obtained on TORPEX by varying the amplitude of the vertical magnetic field. Ideal interchange modes develop for a high vertical magnetic field value, corresponding to a short connection length for the magnetic field lines. As the number of toroidal turns performed by the open helical field lines is increased, resistive interchange modes start to dominate [89].

This chapter describes the first systematic investigations of TORPEX plasma turbulence in the presence of a poloidal magnetic component. In particular, we focus on electrostatic fluctuations with quasi-concentric flux surfaces. Quasi-coherent modes are observed on the LFS of the poloidal cross section. The techniques implemented for the spectral characterization of the modes are introduced. A particular set of control parameters is chosen for the investigation of the electrostatic modes, and a scan in the poloidal field intensity is conducted. The measurements of the background plasma density are followed by the investigation of the spatial localization of the dominant quasi-coherent modes. These are identified from the power spectral density (PSD) of the ion saturation current density fluctuations  $\tilde{J}_{\text{sat}}$  measured using HEX TIP LPs. The statistical dispersion relation is obtained from the measured signals. This allows quantifying the mode spectral features, namely the poloidal and toroidal wave numbers,  $k_\theta$  and  $k_\phi$ , and the corresponding poloidal ( $m$ ) and toroidal ( $n$ ) mode numbers. The mode dynamics is investigated, with focus on its poloidal rotation. Observations of the effect of the toroidal field inversion on the mode features are reported.

To assess the nature of the dominant instabilities, a first step in the experiments-simulations comparison is performed using a linear drift-reduced Braginskii solver [100].

## 5.1 Experimental studies of quasi-coherent modes

### 5.1.1 Data analysis techniques

We provide here an overview of the implemented data analysis technique, namely the Fourier approach, the statistical structure analysis and the conditional average sampling, with an introduction of the theoretical background.

#### Spectral analysis

A spectral Fourier approach allows decoupling the space and time dependence of a physical fluctuating quantity  $\tilde{J}(x, t)$ <sup>1</sup>, and therefore to independently analyze the frequency spectrum and the spectral wave-number of the fluctuations. This has a great relevance for experiments, where the study of the frequency representation is much more accessible. Measuring a time-trace of a physical quantity in a fixed position  $x$ , with a sampling time  $\delta t$ , is much easier than obtaining measurements at several spatial points for the wave-number representation. This allows estimating from a finite record of stationary data sequence, how the total power is distributed over frequency up to the Nyquist frequency [114]  $f_N = 1/(2\delta t)$ , calculating the PSD  $P(f)$  of the signal:

$$P(f) = J(x, f)J^*(x, f). \quad (5.1)$$

---

<sup>1</sup>We consider a 1D problem.

## 5.1. Experimental studies of quasi-coherent modes

The  $J(x, f)$  coefficients can be obtained from the discrete-time Fourier transform (DTFT):

$$J(x, f) = \sum_t \tilde{J}(x, t) e^{i2\pi f t}. \quad (5.2)$$

For experimental measurements with a sufficiently high data statistics, the typical procedure consists in dividing the signal in  $N$  finite time-windows, evaluating  $P(f)$  for each of them. The ensemble average is then calculated as:

$$P(f) = \langle J(x, f) J^*(x, f) \rangle = \frac{1}{N} \sum_{n=1}^N J^{(n)}(x, f) J^{*(n)}(x, f). \quad (5.3)$$

In Fig. 5.1 (a), we show an example of the procedure applied to the first 12 ms of the fluctuating component of the ion saturation current density time-trace  $\tilde{J}$  measured with a LP. The data are analyzed in three separate time windows, computing for each the PSD depicted in the lower insets. The complete analysis on the full time trace of 700 ms leads to the PSD of Fig. 5.1 (b). This quantifies the power associated to each spectral component over the accessible frequency spectrum, which results to be concentrated around  $f \approx 30$  kHz. The presence of quasi-coherent oscillations can be noticed in the inset of Fig. 5.1 (b).

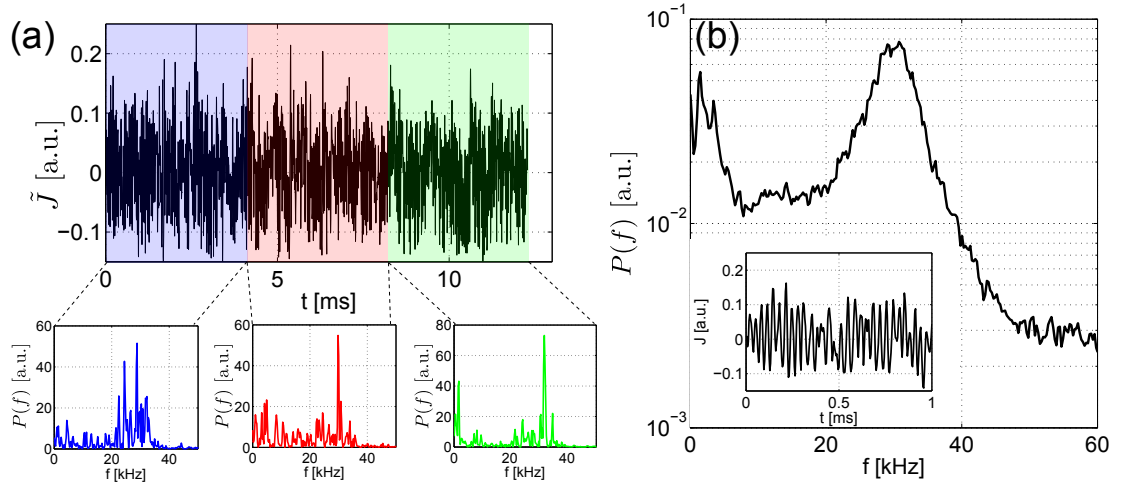


**Figure 5.1** | (a) Example of PSD calculation of the quantity  $\tilde{J}$  during the first 12 ms of a discrete time signal. (b) PSD resulting from the analysis over the total 700 ms length of the signal, with the associated quasi-coherent oscillations shown in the inset.

Time traces located at different positions are necessary to extract the spatial features of the mode, calculating the wave-vector  $k$  from the phase variation in space:

$$k(x, f) = \frac{\partial \Phi(x, f)}{\partial x}. \quad (5.4)$$

Assuming the wave-vector is spatially constant, it can be calculated as  $k = \Delta\Phi/\Delta x$ , using two probes at a relative distance  $\Delta x$ . This procedure is called **two-point correlation technique** [115, 116] and it's introduced in the following. The relative phase shift  $\Delta\Phi$  can be obtained from

## Chapter 5. Electrostatic fluctuations in the closed field line configuration

the argument of the cross-power spectral density  $P_c(f) = \langle J_1(x, f) J_2^*(x, f) \rangle$ , which is obtained from the DTFT of the cross-correlation between the two signals:

$$\Delta\Phi = \arg[P_c(f)] = \text{atan} \left\{ \frac{\Im[P_c(f)]}{\Re[P_c(f)]} \right\}, \quad (5.5)$$

where  $\Im[P_c(f)]$  and  $\Re[P_c(f)]$  are the imaginary and real parts of  $P_c(f)$ .

However, in a weakly turbulent regime, the power spectrum can be peaked in  $f$ , with a broad dispersion in  $k$ . To take this into account, the conditional wave number spectral density  $P(k, f) = P(f)\delta(k(x) - k(x, f))$  is calculated binning the space-phase  $(k, f)$ , counting for each bin the times the corresponding  $k$  has occurred. The discretization of this expression, with the application of the ensemble average, leads to:

$$P(k, f) = \frac{1}{N} \sum_{n=1}^N \bar{P}^{(n)}(f) I_{\Delta k}(k - k^{(n)}(f)), \quad (5.6)$$

with:

$$\bar{P}^{(n)}(f) = \frac{P_1^{(n)}(f) + P_2^{(n)}(f)}{2}, \quad I_{\Delta k}(k - k^{(n)}(f)) = \begin{cases} 1 & k \leq k^{(n)}(f) < k + \Delta k \\ 0 & \text{elsewhere} \end{cases}, \quad (5.7)$$

where:

$$k^{(n)}(f) = \frac{\arg[\langle J_1^{(n)}(x, f) J_2^{*(n)}(x, f) \rangle]}{\Delta x}. \quad (5.8)$$

An example is given in Fig. 5.2 (a).

The information on the spectrum broadening in  $k$  can be introduced in the estimate of the **statistical dispersion relation**  $\bar{k}(f)$  with the following procedure [117]. The conditional wave-number power spectrum is defined as:

$$p(k|f) = \frac{P(k, f)}{\sum_k P(k, f)}. \quad (5.9)$$

The value  $p(k|f)\Delta k$  represents the fraction of power at frequency  $f$  due to fluctuations with wave-numbers in the range  $[k, k + \Delta k]$ . The mean wave-number weighted over  $p(k|f)$  can thus be calculated:

$$\bar{k}(f) = \sum_{m=1}^{N_k} k^m p(k^m|f), \quad (5.10)$$

where  $N_k$  is the number of grid points along the  $k$ -dimension. The result for the data of Fig. 5.2 (a) is shown in Fig. 5.2 (b). Similarly, the mean wave-number spectral width can be obtained from:

$$\bar{\sigma}_k^2(f) = \sum_{m=1}^{N_k} p(k^m|f) [k^m - \bar{k}(f)]^2, \quad (5.11)$$

illustrated in Fig. 5.2 (c). We observe that the spectral width reaches a minimum at the dominant frequency ( $f \approx 30$  kHz), indicating the enhanced coherence with respect to the more turbulent state of the fluctuations over the rest of the spectrum. Consequently,  $P(f)$  is obtained by summing  $P(k, f)$  over the  $k$ -space, as shown in Fig. 5.2 (d).  $\bar{k}(f)$  and  $\bar{\sigma}_k^2(f)$  are averaged over a frequency window corresponding to the FWHM of the Gaussian fit over  $P(f)$ . The values used for the average are indicated in Fig. 5.2 (b)(c) by the red data.

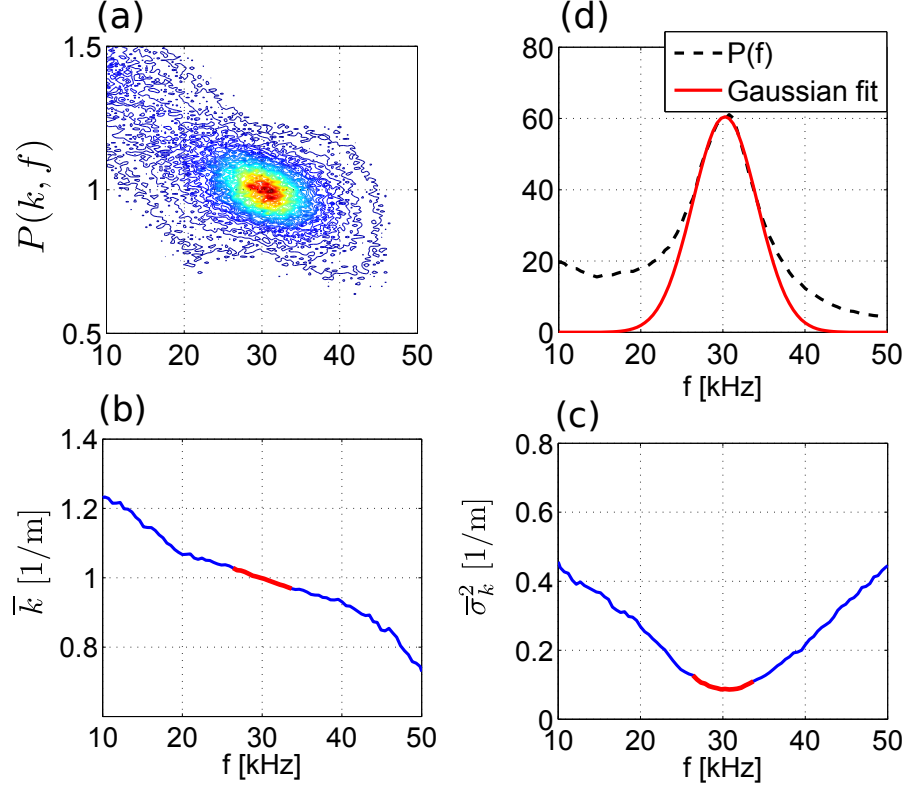


**Figure 5.2** | Example of the statistical dispersion relation (SDR) from the data shown in Fig. 5.17 (b).

### Statistical structure analysis

The propagating plasma structures can be investigated in the space domain by applying a statistical structure analysis on spatially distributed time traces [74, 118]. In the following, this is implemented on HEX TIP data. At each time  $i$ , the fluctuating component  $\delta n_e^i(\mathbf{r})$  of the 2D density matrix  $n_e^i(\mathbf{r})$  is obtained by interpolating the data on a triangulated grid. Structures are defined with a bounding polygon  $P_k$  that surrounds the data above a certain density threshold  $\delta n_e^{\text{th}}$ . The identified observables are subsequently followed in time, obtaining a series of trajectories. Integral-moment definitions can then be applied over the structure bounding polygon  $P_k$  along each trajectory, such as the center of mass  $\bar{\mathbf{r}}_{ik}$  of the  $k^{\text{th}}$  structure at the time frame  $i$ :

$$\bar{\mathbf{r}}_{ik} = \frac{1}{S_{ik}} \int_{\mathbf{r} \in P_{ik}} \mathbf{r} \delta n_e^i(\mathbf{r}) d^2 r, \quad (5.12)$$

$$S_{ik} = \frac{1}{A_{ik}} \int_{\mathbf{r} \in P_{ik}} \delta n e^i(\mathbf{r}) d^2 r, \quad (5.13)$$

$$A_{ik} = \int_{\mathbf{r} \in P_{ik}} d^2 r, \quad (5.14)$$

with  $S_{ik}$  and  $A_{ik}$  corresponding to the mass and area occupied by the structure, respectively. We note that the resulting centers of mass are not constrained by the spatial points of the physical measurements characterizing the hexagonal mapping of HEXTIP. A spatial grid of  $60 \times 60$  bins is defined for this analysis. The sequence of positions of the center of mass at subsequent times constitutes the structure trajectory. The trajectory realizations in each bin are counted, resulting in the data of Fig. 5.3 (a), where the structures are identified with the density threshold of  $4 \times 10^{15} \text{ m}^{-3}$ .

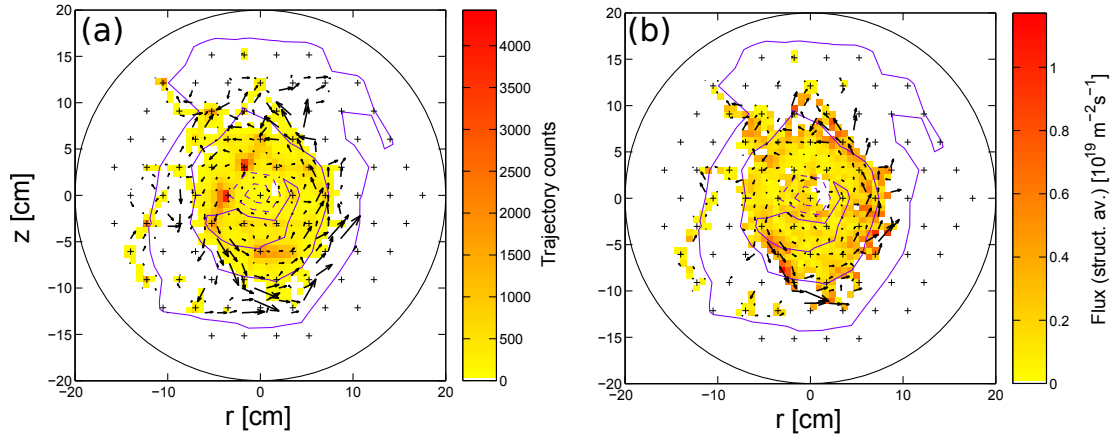


**Figure 5.3** | Example of the total number of trajectory on TORPEX poloidal cross section, for a discharge in closed flux surfaces.

Once the trajectory is defined, several structure observables can be statistically analyzed along the trajectory. For example, the structure velocity is defined as:

$$\mathbf{v}_i = \frac{\mathbf{r}_{i+1} - \mathbf{r}_{i-1}}{2\Delta t}, \quad (5.15)$$

with  $\Delta t$  the sampling period. Both the modulus and the direction of the resulting velocity field are first averaged over each trajectory in each bin, and then averaged over the trajectory realizations (ensemble average). The velocity field is depicted in Fig. 5.3 (a) with the black arrows. The ensemble-averaged structure-induced flux density  $\langle |\delta n \mathbf{v}| \rangle$  is a further observable that can be calculated to obtain information on the poloidal location of the main particle fluxes. The results are shown in Fig. 5.3 (b).

### Conditional average sampling

The almost complete absence of deterministic predictability constitutes the main difficulty in the investigations of turbulence. However, turbulent fluctuations can present coherent features underlying the dominant incoherent component. The conditional average sampling is a technique originally developed in fluid physics [119] to characterize turbulent flows by extracting the coherent patterns or structures, and has found a wide application in plasma physics [95, 120].

Let's consider the fluctuating component of the ion saturation current density  $\tilde{J}_{\text{sat}}(\mathbf{x}, t)$  that is measured on a 2D grid of LPs. A reference probe at the position  $\mathbf{x}_r$  is used to detect events whose amplitude is above a chosen threshold  $\tilde{J}_{\text{sat}}^{\text{th}}(\mathbf{x}_r, t)$ , indicated with the black dots above the dashed magenta line in Fig. 5.4 (a). We set a  $\tilde{J}_{\text{sat}}$  threshold of  $0.5\sigma_{\tilde{J}_{\text{sat}}}$ .

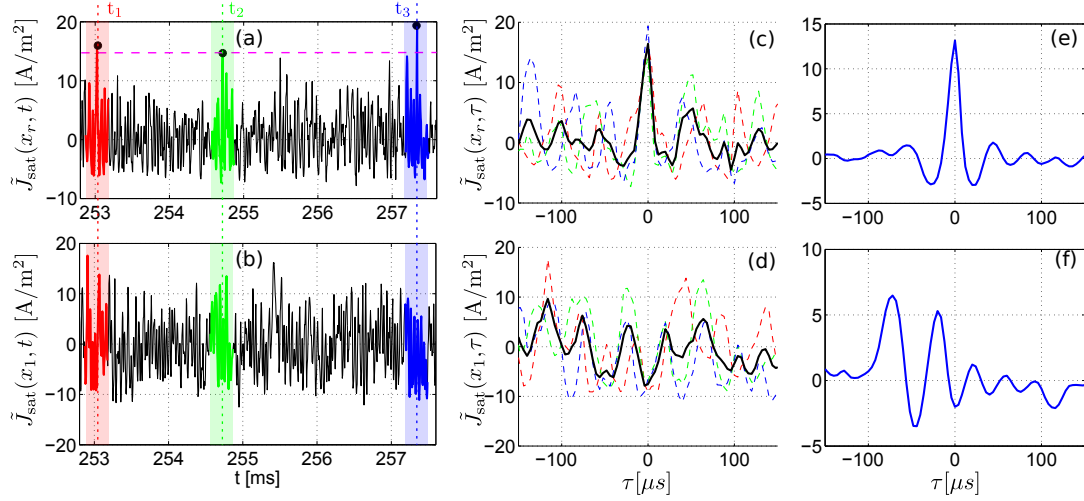


**Figure 5.4** | Example of CAS analysis on two LPs time traces (a|b). The signal in (a) is used for the detection of the events, indicated with black dots, above the chosen threshold (dashed magenta line). The data of the three selected time windows at  $t_1, t_2, t_3$  are shown in (c|d), with the corresponding average in black. (e|f) Results of the ensemble-averaging over the entire 800 ms of data.

Around each detected event at  $t_i$ , a time window of width  $\delta t$  is selected for all the probes, defining  $\tau = 0 \mu\text{s}$  the time of the event detection:

$$\tilde{J}_{\text{sat}}(x_p, t_i + \tau) \quad \text{with} \quad p = 1 : \text{number of probes}, \quad \tau \in [-\delta t/2, \delta t/2]. \quad (5.16)$$

We note that  $\delta t$  has to be of the order of the auto-correlation time of the signal, which quantifies the level of turbulence. The time trace of a second probe is illustrated in Fig. 5.4 (b), with highlighted three selected time windows with the chosen width of  $\delta t = 300 \mu\text{s}$ . This procedure results in a collection of  $N$  conditionally chosen time series that can be considered as independent realizations and ensemble-averaged:

$$\tilde{J}_{\text{sat}}(x_p, \tau) = \langle \tilde{J}_{\text{sat}}(x_p, t_i + \tau) \rangle = \frac{1}{N} \sum_{i=1}^N \tilde{J}_{\text{sat}}(x_p, t_i + \tau). \quad (5.17)$$

## Chapter 5. Electrostatic fluctuations in the closed field line configuration

This procedure is illustrated in Fig. 5.4 (c|d), where three examples of the selected data are superimposed, with the black curve indicated the corresponding ensemble-average. The conditional sampling over 800 ms of time trace results in the detection of approximately 500 events, which constitutes a sufficiently large set of samples for the convergence of the statistical ensemble average. The final CAS signals for the two LPs are shown in Fig. 5.4 (e|f), respectively. The signal in Fig. 5.4 (f) has a maximum at  $\tau \approx -70 \mu\text{s}$ , which indicates a time correlation with respect to the reference probe that is consistent with the spatial distance between the two probes of  $\Delta s \approx 11 \text{ cm}$  and the mode poloidal rotation analyzed in Sec. 5.1.5. This technique, applied to the complete set of HEX TIP LPs, allows isolating the dynamics of coherent structures over the poloidal region surrounding the reference probe. The complete analysis is shown in Fig. 5.5 for three snapshots at  $\tau = -44 \mu\text{s}$ ,  $\tau = -16 \mu\text{s}$  and  $\tau = 12 \mu\text{s}$ .

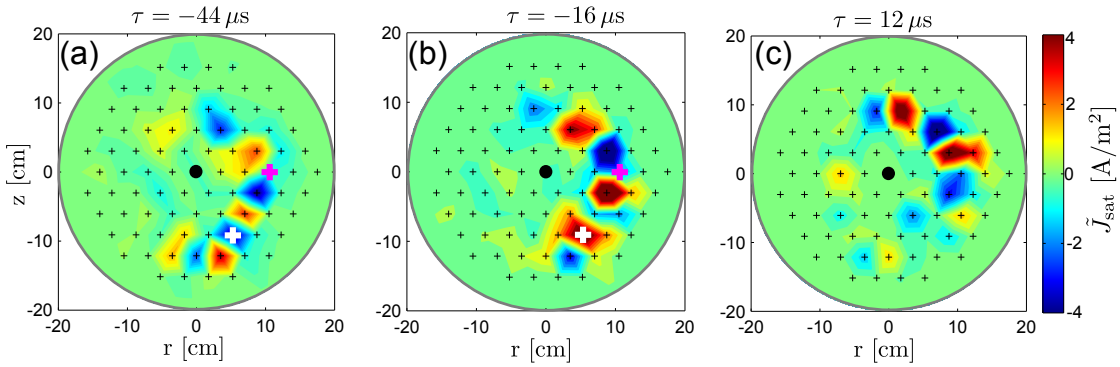


**Figure 5.5** | Example of CAS with three snapshots at  $\tau = -44 \mu\text{s}$ ,  $\tau = -16 \mu\text{s}$  and  $\tau = 12 \mu\text{s}$ . The magenta and white crosses correspond to the LP time traces shown in Fig. 5.4 (a|b), respectively.

However, the real strength of this method resides in the possibility of highly increasing the spatial resolution of the measurements, if highly reproducible plasmas are investigated. Using a fixed LP for the event detection, a second probe can be moved on a shot-by-shot basis over the spatial region of interest. This procedure is implemented in Ch. 6.

### 5.1.2 Plasma scenario and experimental set-up

Hydrogen plasmas are chosen for the study of plasma electrostatic modes, optimizing the scenario with respect to the presence of quasi-coherent fluctuations in poloidally symmetric density profiles. Low RF power discharges with typically  $P_{\text{mag}}^{\text{inj}} \approx 300 \text{ W}$  are investigated, as indicated in Fig. 5.6 (a). This allows avoiding the presence of the plasma source related to the enhanced plasma production regime, which is located on the LFS at  $r \approx 10 \text{ cm}$ , as shown in Fig. 4.20.

The toroidal field is oriented in the counterclockwise direction from a top view, with a value of  $B_{\phi,0} \approx 78.7 \text{ mT}$  corresponding to a position of the EC resonance layer  $r_{\text{EC}} \approx -10 \text{ cm}$ . A neutral gas pressure of  $1.8 \times 10^{-4} \text{ mbar}$  is implemented. In Fig. 5.6 (b), the  $I_{\text{TC}}$  time trace is shown, maintaining a flat-top phase for approximately 1 s with a current ripple within 1%. The analysis of the probe signals is limited to a time window of about 800 ms when all the



## 5.1. Experimental studies of quasi-coherent modes

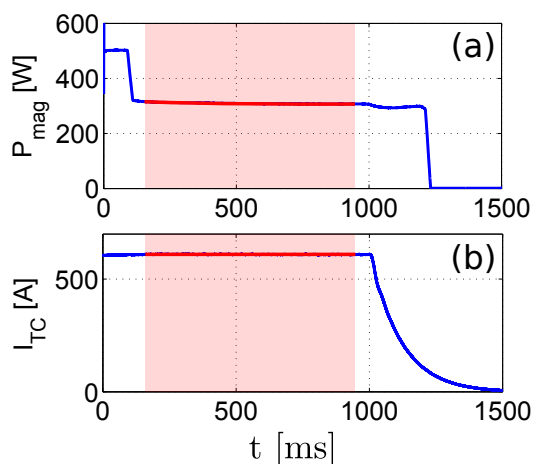


**Figure 5.6** |  $P_{inj}$  (a), and  $I_{TC}$  (b) time traces. The analyzed time window is highlighted in red.

control parameters are approximately constant, indicated in Fig. 5.6 with the red-shaded region. A range of  $I_{TC}$  between 400 A and 800 A is explored, corresponding to the range of safety factor values shown in Fig. 5.7. These are calculated, according to eq. 3.4, averaging the local safety factor over a poloidal turn along the magnetic field lines computed on the basis of the measured coil currents.

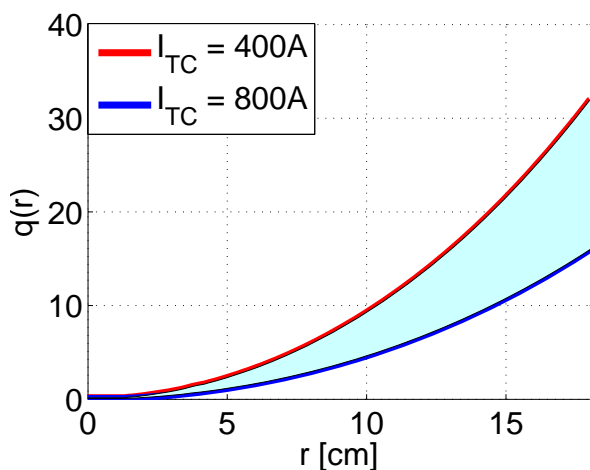


**Figure 5.7** | In light blue the region of values of the explored safety factor radial profiles  $q(r)$  is indicated.

For each current, a small vertical field component is added to obtain quasi-concentric flux surfaces on most of the plasma volume, as shown in Fig. 5.8(a|b). We note that for the present experiments, the copper ground braiding introduced in Sec. 3.1.3 was connected to the feed-through to minimize the potential difference between the TC and the vacuum vessel. However, an additional resistance of  $R \approx 4 \text{ m}\Omega$  is introduced in series between the copper braiding (which is grounded) and the TC. This results in a potential difference in the range  $\Delta V \approx [2, 3] \text{ V}$ , depending on the applied voltage for the explored values of  $I_{TC}$  current.

The measurements presented in this chapter are mainly performed with an extensive set of LPs with different arrangements that allow capturing two-dimensional features of modes on the poloidal cross section or performing more refined radial scans. The movable LPs

include TWIN-1, 2DSSLP, SLP and FRIPLE, illustrated in Fig. 2.5. A spectral analysis with correlation-based techniques can be performed setting these diagnostics at different toroidal positions. The fixed LPs include the FAPA, shown in Fig. 2.10, and the HEXTIP (Fig. 2.6). The former allows measuring the poloidal wave number  $k_\theta$  with 44 LPs poloidally aligned along the concentric flux surfaces at four different radial positions with 1 cm separation. HEXTIP is mainly used to obtain the 2D poloidal  $J_{\text{sat}}$  measurements. Two examples of the time-averaged density profiles are shown in Fig. 5.8 (a|b) for the discharges with  $I_{\text{TC}} \approx 460$  A and  $I_{\text{TC}} \approx 530$  A, respectively.

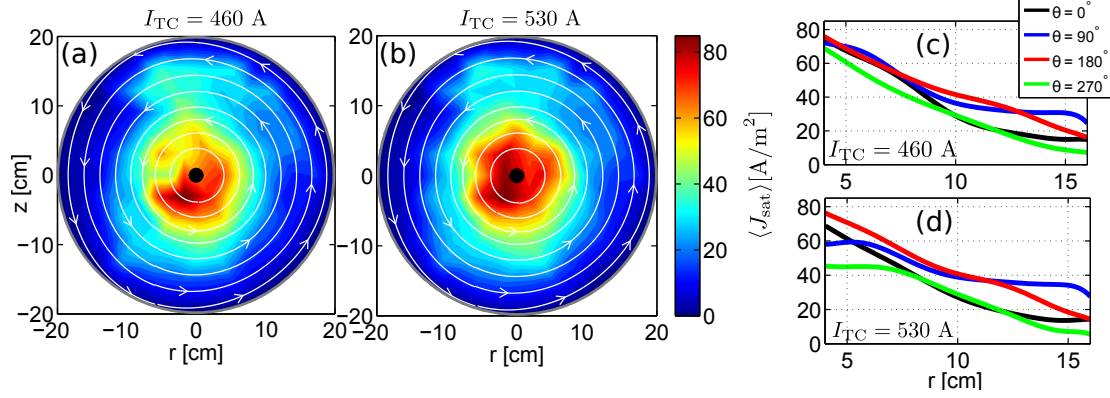


**Figure 5.8** | Time-averaged 2D density profiles calculated from the HEXTIP  $J_{\text{sat}}$  signals, for the discharge with (a)  $I_{\text{TC}} \approx 460$  A and (b)  $I_{\text{TC}} \approx 530$  A; the simulated magnetic field lines are shown in white and the toroidal conductor is represented with a full black circle in the middle of the cross section. (c|d)  $J_{\text{sat}}$  radial cuts for different poloidal angles.  $\theta = 0^\circ$  correspond to the profile at  $z = 0$  cm on the LFS, moving in the counterclockwise direction. Discharges #59809 and #59800.

The plasma shape matches qualitatively the simulated magnetic flux surfaces. However, a slight asymmetry can be observed in Fig. 5.8 (a|c) along the poloidal direction, as discussed in Sec. 4.1.3. In Fig. 5.9 we show the corresponding 2D profiles of floating potential, in which a slight poloidal asymmetry is observed.

The 2DSSLP is displaced on a shot-to-shot basis on the LFS at  $z \approx 0$  cm, with a spatial resolution of 0.5 cm, to obtain more detailed profiles of the background plasma profiles. A voltage swept at a frequency of 330 Hz between  $-40$  V and  $20$  V is applied to cover both the ion and electron saturation regimes. The  $n_e$  value in Fig. 5.10 (a) is extracted from the resulting I-V curves and combined to the  $T_e$  data of Fig. 4.3 to obtain the pressure profiles in Fig. 5.10 (b). We note the outward radial displacement of the position of the maximum density gradients by increasing the TC current.

### 5.1.3 Identification of quasi-coherent modes

The spatial localization of the plasma fluctuations on the poloidal cross section is determined by investigating the fluctuating component of  $J_{\text{sat}}$  signals ( $\tilde{J}_{\text{sat}}$ ). In particular, the higher order moments of the probability distribution function (PDF), namely the standard deviation  $\sigma_{J_{\text{sat}}}$  (second order-moment) and the skewness (third order-moment), are calculated. These are

## 5.1. Experimental studies of quasi-coherent modes

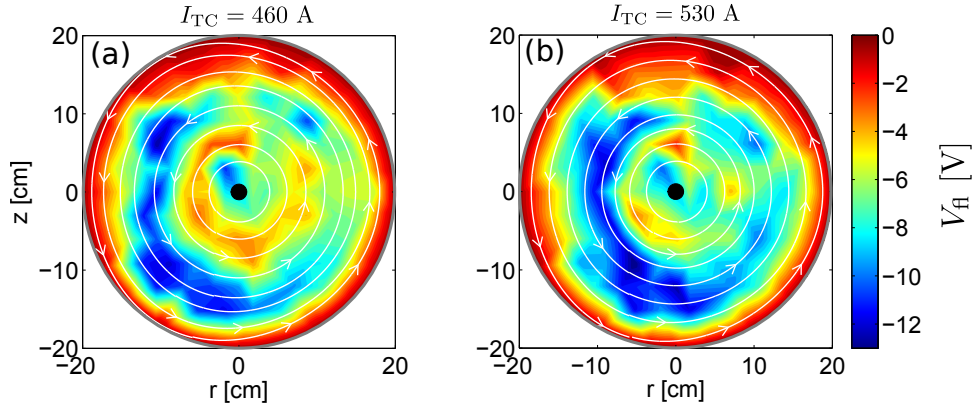


**Figure 5.9** | Time-averaged 2D floating potential profiles  $V_{fi}$  with (a)  $I_{TC} \approx 460$  A and (b)  $I_{TC} \approx 530$  A. Discharges #59812 and #59805.

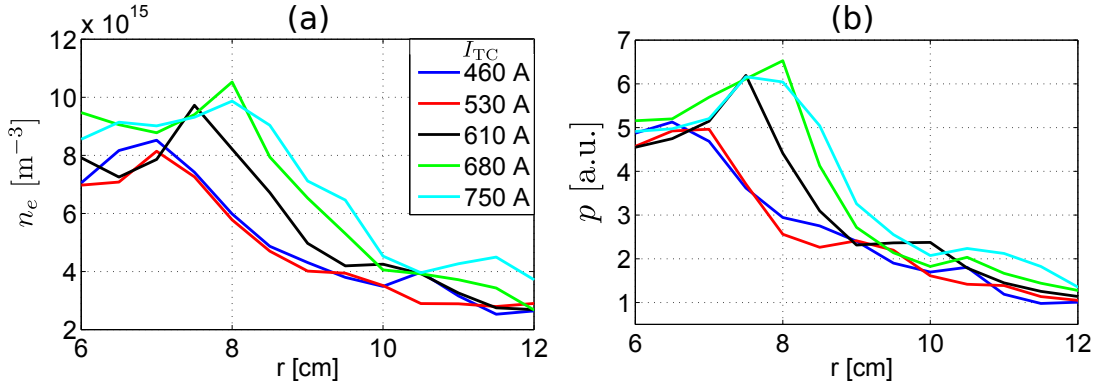


**Figure 5.10** | LFS radial profiles at  $z \approx 0$  cm of plasma density (a) and pressure (b) calculated from the measured I-V curves using the probe #07 of the 2DSSLP for the five values of  $I_{TC}$ . For the pressure values, the temperature data in Fig. 4.3 are used.

shown in Fig. 5.11 (a|b) for the discharge at  $I_{TC} = 460$  A, which is considered in the following analysis if not otherwise specified. A positive value of skewness indicates the passage of blobs. We can observe in Fig. 5.11 (b) a region of positive skewness on the LFS, with an example of the time-trace measured at  $(r \approx 10, z \approx -7)$  cm (black cross) in Fig. 5.12 (a). We note that the corresponding PDF in Fig. 5.12 (b) is not symmetrically distributed between positive and negative events.

The measured  $\sigma_{J_{sat}}$  indicates high fluctuations localized close to the TC on the HFS, as well as on the LFS at an almost fixed radial position  $r \approx 10$  cm. However, this does not discriminate broad-band fluctuations from quasi-coherent modes. An example of an LP signal measuring an electrostatic mode is given in Fig. 5.12 (c), with quasi-sinusoidal oscillations. The corresponding PDF is given in Fig. 5.12 (d), with a clear quasi-symmetric feature. The PSD is calculated for each LP time trace.

In Fig. 5.13 (a) we illustrate the PSDs of four LPs, indicated in Fig. 5.11 by the crosses of

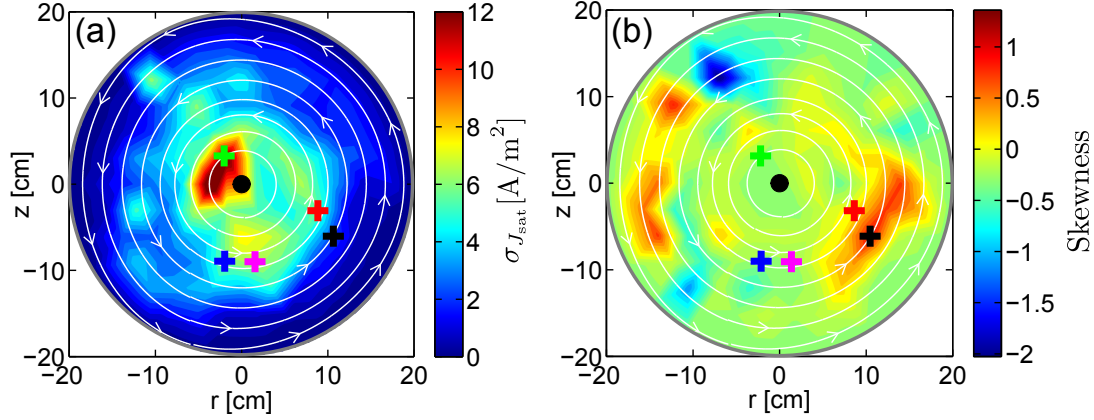


**Figure 5.11** | HEXTIP data for  $I_{TC} = 460$  A. Standard deviation (a) and skewness (b) of the measured  $J_{sat}$  time traces. The colored crosses refer to the probes analyzed in more details in Fig. 5.12 and Fig. 5.13. Discharge #59809.

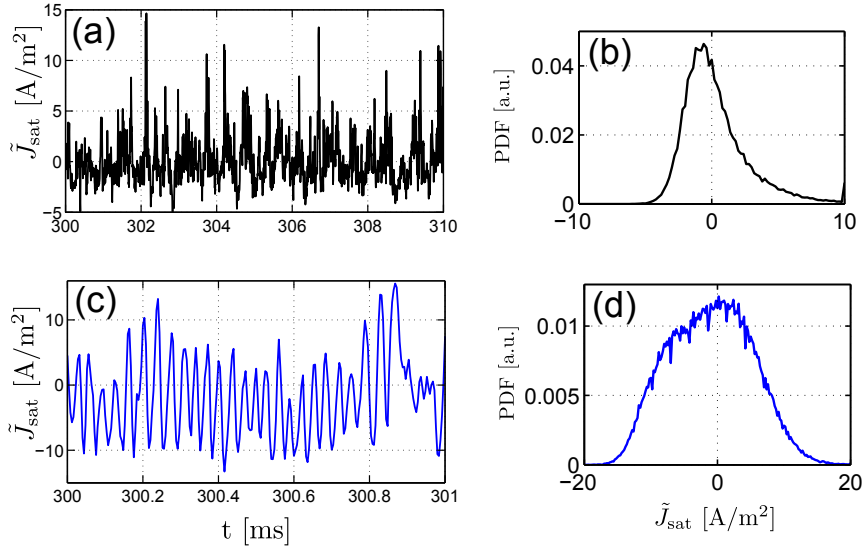


**Figure 5.12** | (a)(c) Examples of fluctuating  $J_{sat}$  time traces of the LPs indicated by the same colors in 5.11. The corresponding PDFs are shown in (b)(d).

the same color. The observed dominant quasi-coherent mode at a frequency of  $f \approx 30$  kHz constitute the main focus of our investigations, as it is the dominant feature of the fluctuation spectrum on an extended poloidal region. The stronger fluctuations measured by the LP close to the TC at  $(r \approx -3.5, z \approx 0)$  cm indicated in Fig. 5.11, present a much broader spectra without any coherent peak at  $f \approx 30$  kHz, as can be seen in Fig. 5.13 (a).

A qualitative identification of the mode poloidal position is given by the mode intensity calculated by averaging the PSDs of all HEXTIP signals on a window of  $\pm 3$  kHz around the dominant frequency. The result is shown in Fig. 5.13 (b), indicating that the mode is poloidally asymmetric with a clear ballooning character, as it is mainly localized on the LFS. The same features

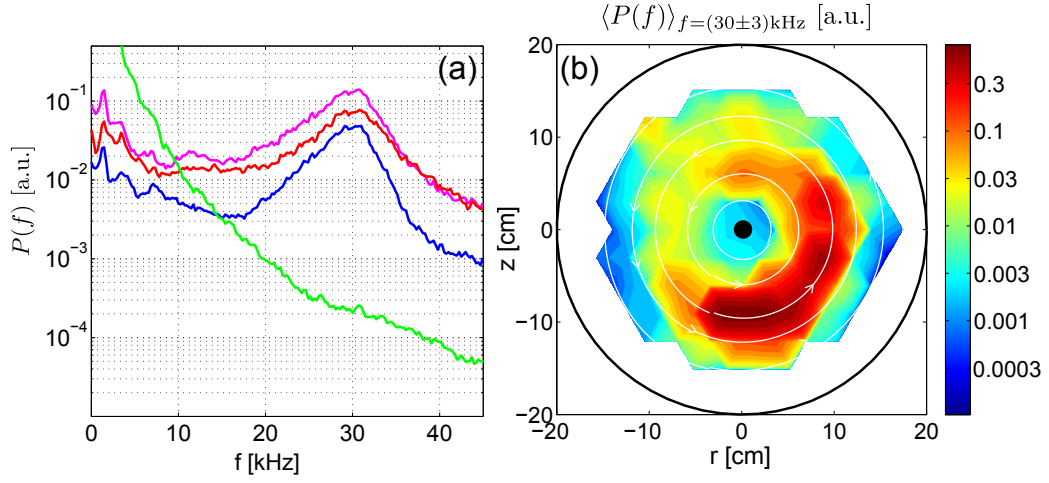


**Figure 5.13** | (a) PSDs of four LPs, indicated in Fig. 5.11 with crosses of the corresponding colors. (b) Mode intensity averaged on a frequency window of 3 kHz around the dominant mode frequency at 30 kHz.

are observed for all the current values explored. The Gaussian fit of the PSD with the highest mode intensity provides a first indication of the mode frequency  $f$  and spectral width  $\sigma_f$ , as illustrated in Table 5.1 for the different TC currents.

$I_{TC}$ [A]	$f$ [kHz]	$\sigma_f$ [kHz]	$r_m$ [cm]	$\sigma_{r_m}$ [cm]
460	29.8	2.4	9.0	1.2
530	29.1	2.9	9.8	1.1
610	26.8	2.4	10.5	1.0
680	23.2	2.2	10.9	1.3
750	22.8	1.0	11.2	0.9

**Table 5.1** | Frequency  $f$ , spectral width  $\sigma_f$ , radial position  $r_m$  and radial width  $\sigma_{r_m}$  of the dominant mode for different TC currents.

A more precise estimate of the mode radial position at  $z \simeq 0$  cm ( $r_m$ ) is obtained using the movable probes to evaluate at each radial position the maximum of the PSD fitted with a Gaussian. The radial width  $\sigma_{r_m}$  is given by the full width at half maximum (FWHM) of a Gaussian fit performed on the radial profile of the PSD maxima (Fig. 5.14). The results are summarized in Table 5.1. The data indicates that the mode moves slightly outward when the TC current is increased. This is consistent with the shift of the position of the maximum pressure gradient shown in Fig. 5.10 (b).

Complementary fully non-perturbative measurements of plasma fluctuations are performed with the fast imaging camera introduced in Sec. 2.4.2 with 100 kHz frame-rate on the portion of the LFS indicated in Fig. 5.15 (a). We report in Fig. 5.15 (b)(c) the standard deviation  $\sigma_I$  and skewness of the measured visible light intensity. For the noise removal, the data are

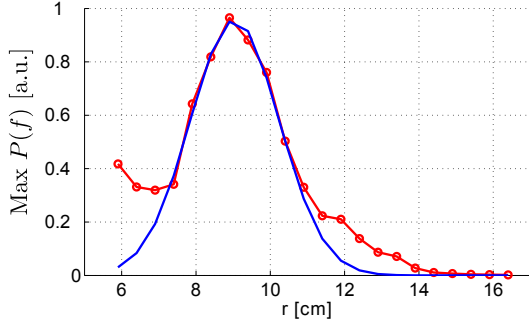


**Figure 5.14** | Radial scan of the PSD maximum on  $J_{\text{sat}}$  signals (red), fitted with a Gaussian function (blue), for  $I_{\text{TC}} = 460$  A.

filtered averaging the value of each pixel with its surrounding elements fitting in a  $3 \times 3$  matrix. Keeping in mind that the data are line integrated, we can observe the same poloidal position of the fluctuations and skewness on the lower part of the LFS. As in Fig. 5.11, positive values of skewness are located outward with respect to the high fluctuations region, indicating the propagation of structures. We remark that the position where  $\sigma_I$  undergoes a sudden decrease (at the vertical pixel number 25) coincides with that of the probe that is used as a spatial reference.

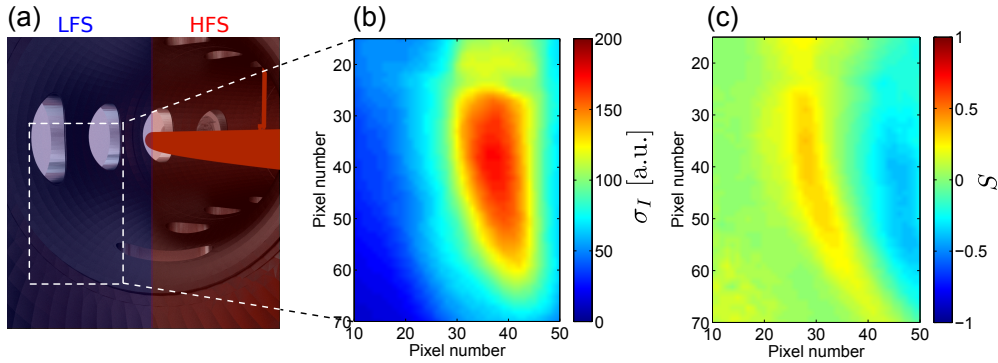


**Figure 5.15** | (a) Sketch of the poloidal location of the fast imaging camera measurements of visible light standard deviation and skewness shown in (b)(c), respectively. Discharge #59093.

### 5.1.4 Wave number and mode number measurements

To measure the toroidal wave number  $k_\phi$ , the four movable LPs introduced in Sec. 2.4.1 are placed at different toroidal locations indicated by the toroidal angle  $\phi$ , but at the same radial position of the maximum mode intensity  $r_m$ , as schematically sketched in Fig. 5.16. Starting from FRIPLE ( $\phi = 0$ ), in the clock-wise direction follow 2DSSLP ( $\phi_1 \approx 90^\circ$ ), TWIN-1 ( $\phi_2 \approx 193^\circ$ ) and SLP ( $\phi_3 \approx 296^\circ$ ).

Based on the results of Table 5.1, the chosen values are  $r_m = [9.5, 10, 10.5, 11, 11.5]$  cm for the values of current, respectively,  $I_{\text{TC}} = [460, 530, 610, 680, 750]$  A. In Fig. 5.17 (a) the  $J_{\text{sat}}$  signals of FRIPLE and TWIN-1 are shown for  $I_{\text{TC}} = 460$  A. We can already note that they have opposite phase ( $\Psi \approx 180^\circ$ ), suggesting a toroidal mode number  $n \approx 1$ . The two-point correlation tech-

## 5.1. Experimental studies of quasi-coherent modes

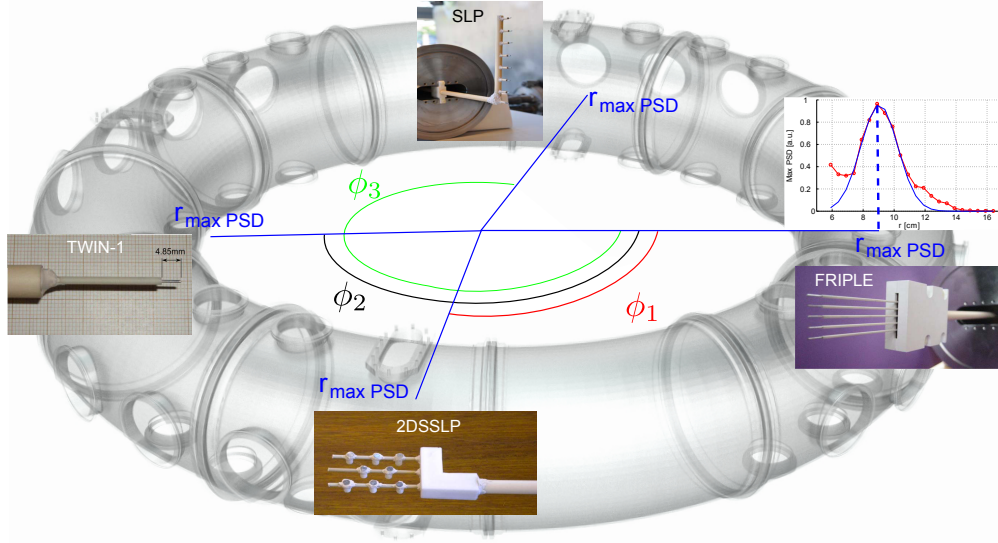


**Figure 5.16** | Schematic view of the LP locations around TORPEX to perform the measurements of the parallel dispersion relation.

nique is applied between FRIPLE and the other probes to calculate the statistical dispersion relation (SDR) that provides the relative phase shift  $\Psi$ . The power spectrum  $P(k, f)$  of the SDR resulting from FRIPLE and TWIN-1 signals is shown in Fig. 5.17 (b). A dominant frequency at 30 kHz is observed and consistent with the PSDs of Fig. 5.13 (a), as well as the toroidal wave number  $k_\phi \approx 1 \text{ m}^{-1}$ .  $k_\phi$  is computed as the angular coefficient of the linear fit on  $\Psi(x)$ :

$$k_\phi = \frac{d\Psi(x)}{dx}, \quad (5.18)$$

where  $x = R\phi$  is the distance of each probe from the reference one (FRIPLE) along the toroidal direction (Fig. 5.16). The results of this analysis for  $I_{TC} = 460 \text{ A}$  are shown in Fig. 5.17 (c), indicating a clear linear dependence of the phase shift  $\Psi$  of the measured signal with respect to the toroidal position.

The calculated wave numbers  $k_\phi$  are shown in Tab. 5.2. The  $\sigma_{k_\phi}$  are the uncertainties of the fit results with 95% confidence level. The corresponding mode numbers  $n$  are evaluated from the radial position  $R$  of the probes as:

$I_{TC}$ [A]	$k_\phi \text{ m}^{-1}$	$\sigma_{k_\phi} \text{ m}^{-1}$	$n$
460	1.05	0.22	$1.15 \pm 0.22$
530	1.17	0.86	$1.29 \pm 0.86$
610	1.14	0.20	$1.26 \pm 0.20$
680	1.14	0.38	$1.27 \pm 0.38$
750	1.27	0.87	$1.42 \pm 0.87$

**Table 5.2** | Toroidal wave number  $k_\phi$  and mode number for the explored values of TC current.

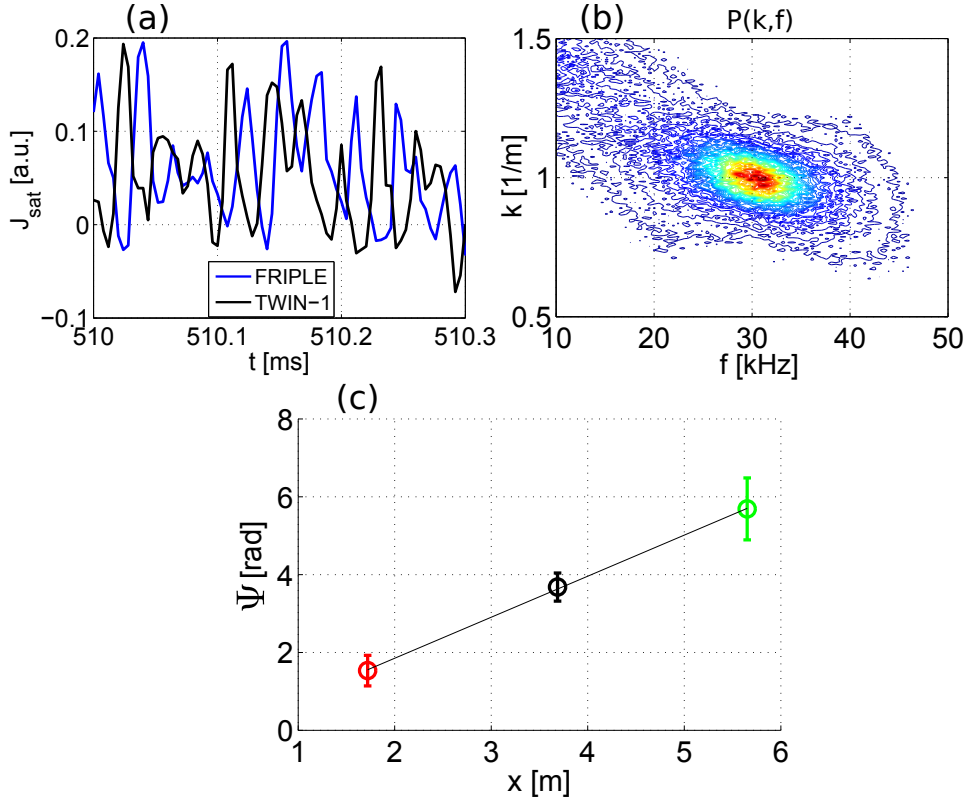


**Figure 5.17** | Data for  $I_{\text{TC}} = 460$  A. (a)  $J_{\text{sat}}$  time-traces of FRIPLE (blue) and TWIN-1 (black). (b) SDR computed between the signals shown in (a). (c) Linear fit on the phase shift  $\Psi$  between FRIPLE and the other LPs for the  $k_{\phi}$  estimate.

$$n = \frac{2\pi R}{\lambda_{\phi}} = Rk_{\phi}, \quad (5.19)$$

with the uncertainties obtained by statistically propagating the errors. The results illustrated in Fig. 5.18 indicate modes with  $n = 1$  within the experimental uncertainties.

The poloidal mode number  $m$  is measured using the FAPA diagnostic presented in Sec. 2.4.1. We note that the explored values of TC current, namely  $I_{\text{TC}} = [450, 500, 550, 600, 650]$  A, cover a smaller range with respect to those in Tab. 5.2. This is due to the fact that for currents larger than 650 A, the quasi-coherent mode is localized outside the spatial region covered by FAPA, which is composed of fixed LPs. For each value of current, the poloidal row of LPs with the largest mode intensity is selected, as can be seen in Fig 5.19 for the case  $I_{\text{TC}} \approx 450$  A, where the mode is localized on the third poloidal row starting from the bottom. For the cases in which two adjacent rows have comparable mode intensities, we select the row where the mode appears first on the poloidal cross section, namely the row with the first probe detecting it having the smaller radial position. The phase-shift with respect to the first LP on the HFS is computed from the statistical dispersion relation on consecutive couples of LPs. Since the



## 5.1. Experimental studies of quasi-coherent modes

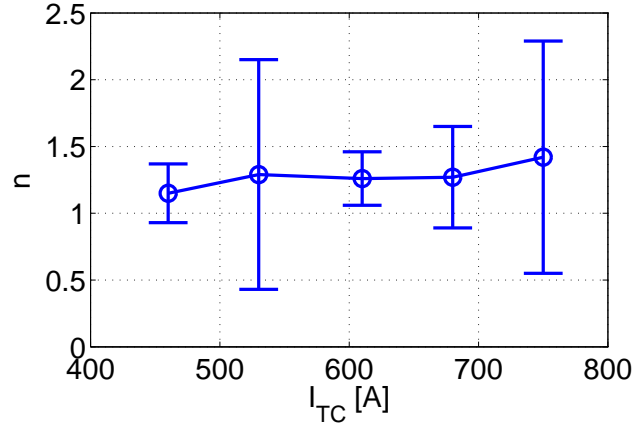


**Figure 5.18** | Toroidal mode number  $n$  as a function of the current  $I_{TC}$ .

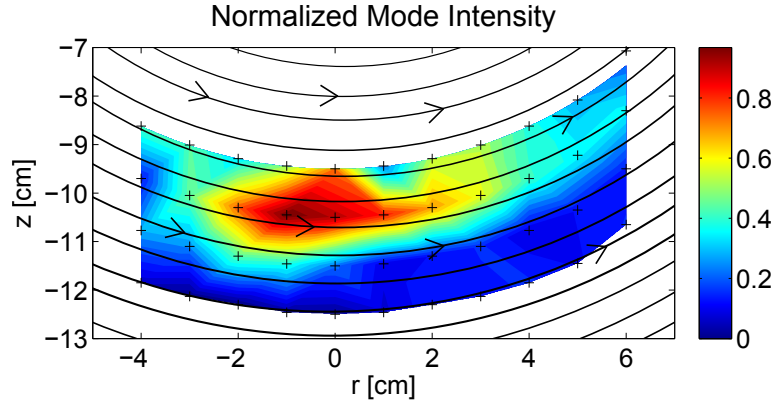


**Figure 5.19** | Normalized mode intensity on the FAPA for a discharge with  $I_{TC} \approx 450$  A. The black crosses correspond to the FAPA probes, while the black lines and arrows are the simulated magnetic field lines. Discharge #63268.

LP locations range from -4 cm to 6 cm, the transformed poloidal angle  $\theta^* = \theta - \epsilon \sin \theta$  value is computed [121] to take into account the toroidal magnetic field variation along the LP to the first order of the inverse aspect ratio  $\epsilon$ . The poloidal mode number is given by a linear fit of the phase shift  $\Psi(\theta^*)$ . We note that the LP position corresponding to the maximum mode intensity radially moves outwards as the TC current is increased, in agreement with the mode radial position measured at  $z \approx 0$  from the toroidally displaced LPs (Table 5.1). Table 5.3 and Fig. 5.20 summarize the results of this analysis.

To verify the field aligned character of the analyzed coherent modes, we calculate the safety factor values  $q(z_C)$  at the position of the analyzed poloidal row, averaged on the corresponding flux surface, for each value of  $I_{TC}$ . However, the estimate of the  $q$  values to be compared to the measured  $m$  is affected by several factors: the mode spatial width, the uncertainty on the LP positions and on the TC position. The  $q$  error-bars have been estimated as the range of value the safety-factor takes moving  $\pm 1$  cm radially from the poloidal row (PR) radial position.

$I_{TC}$ [A]	$z_C$ [cm]	$m$	$\sigma_m$	$q$	$\sigma_q$
450	10.5	10.54	0.22	9.5	1.8
500	10.5	10.37	0.27	8.6	1.7
550	11.5	10.87	0.52	9.3	1.6
600	11.5	9.86	0.32	8.6	1.5
650	12.5	11.46	0.59	9.5	1.5

**Table 5.3** | Poloidal mode number  $m$  and flux-surface averaged safety factor  $q$  for the explored values of TC current.

In conclusion, the field-aligned character of the investigated instability has been measured experimentally, as indicated by the results shown in Fig. 5.20.

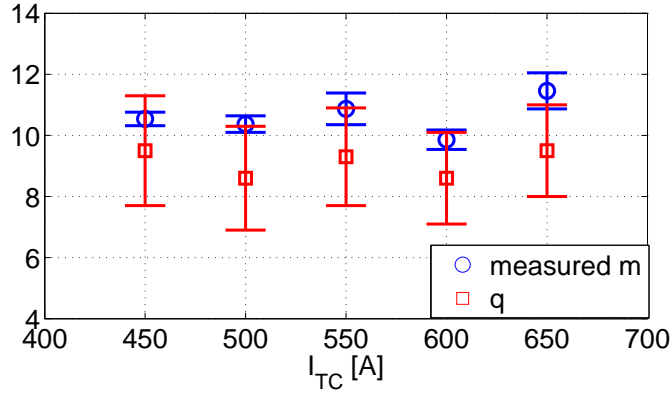


**Figure 5.20** | Poloidal mode number  $m$  (blue circles) and corresponding flux-surface averaged safety factor (red squares) for the investigated toroidal conductor currents  $I_{TC}$ .

### 5.1.5 Mode poloidal rotation

Complementary information on the investigated modes is provided by the study of their poloidal dynamics. The presence of propagating structures, either isolated blobs or quasi-coherent modes, can be identified with the statistical tracking technique presented in Sec. 5.1.1. The poloidal distributions of structure trajectories and speed for  $I_{TC} = 610$  A are shown in Fig. 5.21 (a|b). A density threshold of  $n_e = 2 \times 10^{15} \text{ m}^{-3}$  is used for the structure selection, which corresponds to the value of  $\sigma_{n_e}$  at the radial position  $r \approx 10$  cm. The black arrows, whose size is proportional to the detected velocity, provide a further representation of the structure speed. We can observe structures moving at a maximum speed of 2 km/s on almost circular trajectories between the indicated circular contours at 25% and 50% of the maximum  $\langle n_e \rangle$  value. The preferential spatial localization on the LFS region of bad curvature is confirmed, suggesting the ballooning character of the measured modes.

Further insight into the mode dynamics is obtained by applying the conditional average

## 5.1. Experimental studies of quasi-coherent modes

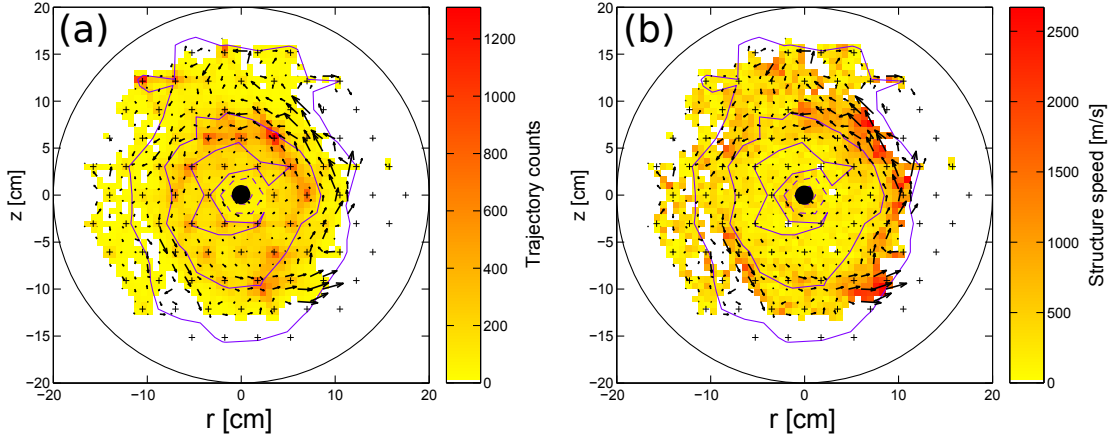


**Figure 5.21** | (a) number of structure trajectories and (b) average velocity field for  $I_{TC} = 610$  A. The black arrows indicate the structure preferential direction, with their size quantifying the structure speed. The contours correspond to the time-averaged  $n_e$  profiles at 25% (outermost), 50% and 75% of the maximum.

sampling to the HEXTIP data. The HEXTIP probe at ( $r \simeq 10.5, z \simeq 0$ ) cm is used as trigger to investigate the mode dynamics on the LFS, by selecting a time window of  $100 \mu\text{s}$  around the detected events. The poloidal rotation of the mode is evident in Fig. 5.22, which displays a few snapshots for the discharge with  $I_{TC} = 610$  A.

We note that the mode peak covers in a time  $\Delta t = 20 \mu\text{s}$  a spatial distance  $\Delta x \simeq 3.5$  cm, rotating in the poloidal counter clock-wise direction, which corresponds to the two HEXTIP probe tips indicated by the white crosses in Fig. 5.22 (c|d). This results in a poloidal mode phase velocity of:

$$|\mathbf{v}| = \frac{\Delta x}{\Delta t} = \frac{3.5 \text{ cm}}{20 \mu\text{s}} \simeq 1.75 \text{ km/s}, \quad (5.20)$$

which is in agreement with the values indicated in Fig. 5.21.

A second more precise estimate of the mode poloidal velocity in the laboratory frame  $v$  can be obtained from the measured frequency  $f = (26.8 \pm 2.4)$  kHz and poloidal mode number  $k_\theta$ :

$$|\mathbf{v}| = \frac{2\pi f}{k_\theta} = (1.78 \pm 0.24) \text{ km/s}, \quad (5.21)$$

where  $k_\theta$  is calculated from the poloidal mode number  $m = (9.86 \pm 0.32)$  for  $I_{TC} = 600$  A:

$$k_\theta = \frac{m}{r} = (93.9 \pm 9.4) \text{ m}^{-1}. \quad (5.22)$$

The two methods provide similar results.

We can now calculate the electron diamagnetic velocity  $v_{de}$  (clockwise) and the  $\mathbf{E} \times \mathbf{B}$  velocity

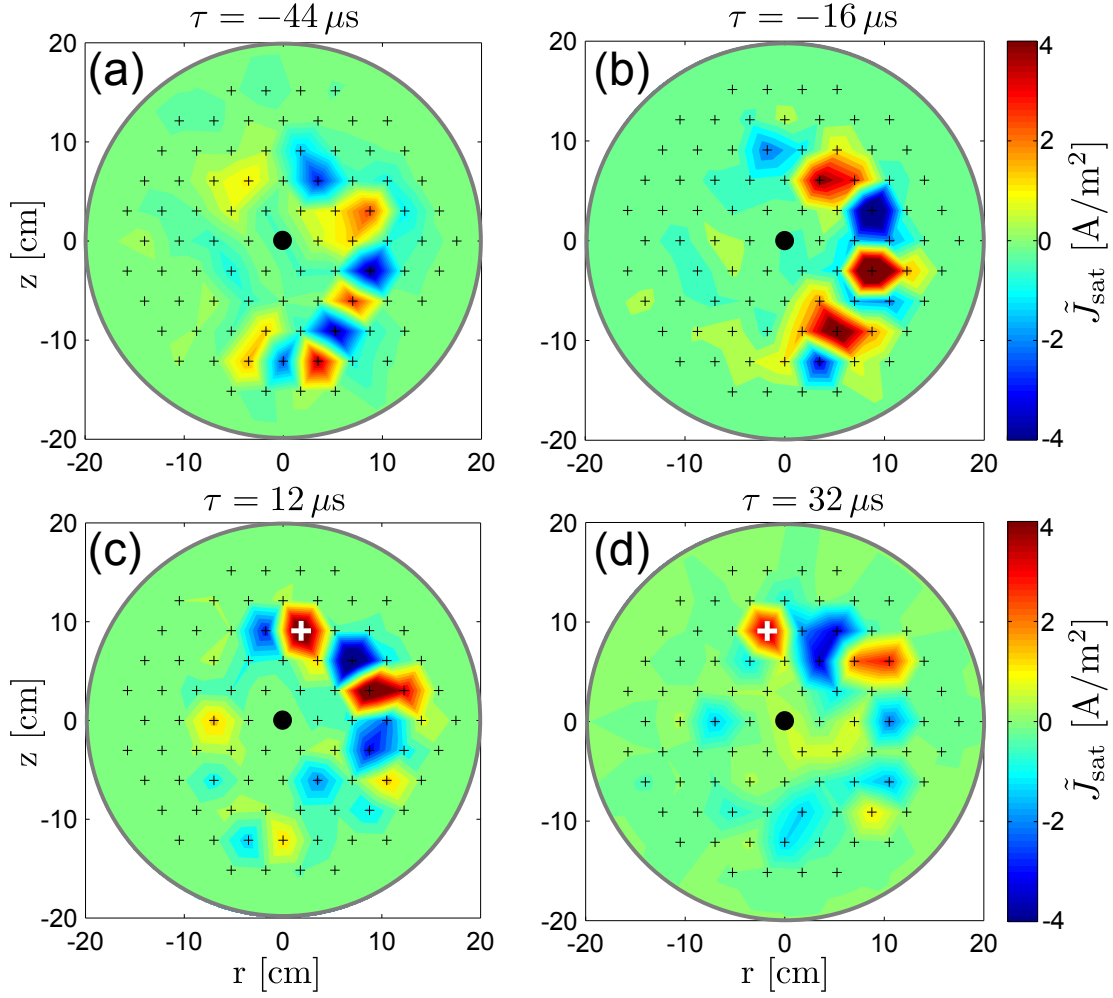


**Figure 5.22** | Snapshots of conditionally sampled HEXTIP data for  $I_{TC} = 610$  A, taking as reference the probe at  $(r \simeq 10.5, z \simeq 0)$  cm.  $\tau = 0 \mu\text{s}$  corresponds to the detection time of the events above the chosen threshold. Discharge #59819.

$v_{\mathbf{E} \times \mathbf{B}}$  (counterclockwise), defined as:

$$\mathbf{v}_{\mathbf{E} \times \mathbf{B}} = \frac{\mathbf{E} \times \mathbf{B}}{B^2} \quad \mathbf{v}_{\text{de}} = \frac{T_e}{eB_\phi^2} \frac{\nabla n_e}{n_e} \times \mathbf{B}_\phi. \quad (5.23)$$

An electron temperature  $T_e \simeq 3$  eV and a magnetic field  $B_\phi \simeq 78.7$  mT are considered. From the density radial profiles (Fig. 5.10) and plasma potential radial profiles (Fig. 4.3) we can obtain a density scale length  $L_n = |\nabla n_e / n_e|^{-1} \simeq 4$  cm and an electric field  $E = -\nabla V_{pl} \simeq 240$  V/m at the radial position of the mode. It follows that:

$$|\mathbf{v}_{\mathbf{E} \times \mathbf{B}}| = \frac{E}{B_\phi} \simeq 3 \text{ km/s}, \quad |\mathbf{v}_{\text{de}}| = \frac{T_e}{B_\phi L_{n_e}} \simeq 1 \text{ km/s}. \quad (5.24)$$

This confirms within the experimental uncertainties that the velocity in the laboratory frame

is affected by the Doppler shift:

$$|\mathbf{v}| = |\mathbf{v}_{\mathbf{E} \times \mathbf{B}}| - |\mathbf{v}_{\mathbf{de}}|. \quad (5.25)$$

We note that  $|\mathbf{v}_{\mathbf{de}}|$  and  $|\mathbf{v}_{\mathbf{E} \times \mathbf{B}}|$  are comparable, while the latter had a dominant role with respect to the modes measured with the SMT [67].

### $B_\phi$ inversion effects on the fluctuation dynamics

We now present the first qualitative studies of the effect of changing the toroidal field direction on plasma quasi-coherent fluctuations. According to eq. 5.23, reversing  $B_\phi$  from counter clock-wise to clock-wise from a top view implies the inversion of both  $\mathbf{v}_{\mathbf{E} \times \mathbf{B}}$  and  $\mathbf{v}_{\mathbf{de}}$ . This is valid if the direction of plasma potential and density gradients do not change, which is a reasonable assumption if the background  $J_{\text{sat}}$  profiles are similar, as can be noted in Fig. 4.7. In the following, we investigate the plasma configuration introduced in Fig. 4.7 (b), with  $B_\phi^{\text{inv}}$ . The clock-wise mode poloidal rotation in the laboratory frame is indicated by the statistical structure analysis shown in Fig. 5.23 (a). The analysis of the PSD of HEX TIP LPs indicates a quasi-coherent mode mainly localized in the upper region of the LFS, as illustrated in Fig. 5.23 (b), with a frequency  $f \approx 15$  kHz, in the same range of that for  $B_\phi^{\text{nor}}$  ( $f \approx 18$  kHz). The PSD of the probe indicated in Fig. 5.23 (b) with a blue cross is shown in Fig. 5.23 (c). These results confirm the ballooning feature of the measured modes and the relevance of the magnetic field line curvature drive on the LFS.

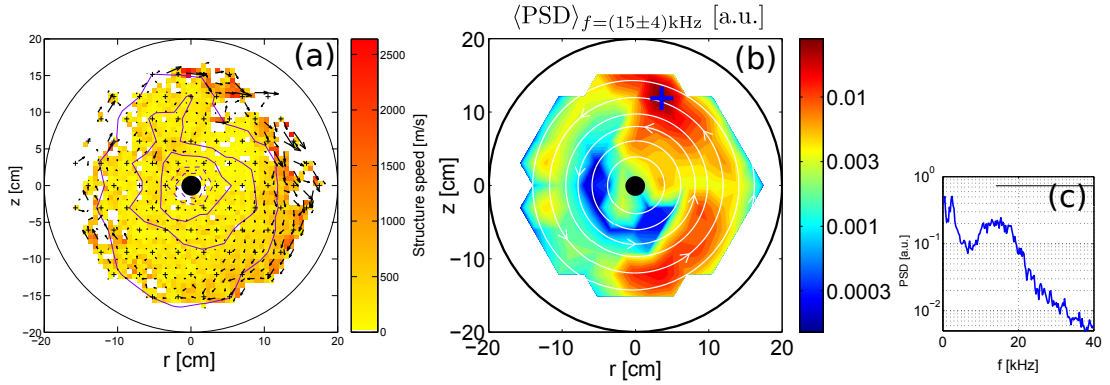


**Figure 5.23** | (a) Structures average velocity field. (b) Mode intensity averaged on a frequency window of 4 kHz around the dominant frequency at 15 kHz. (c) PSD of the LP  $J_{\text{sat}}$  time trace indicated with a blue cross in (b).

## 5.2 Numerical studies of quasi-coherent modes

We investigate the nature of the linear modes that are unstable in the considered configurations using a fluid approach. In TORPEX plasmas, the high particle collisionality assures the thermodynamic equilibrium that allows us to neglect kinetic effects. For electrons, the collision frequency is higher than the characteristic frequency of the observed fluctuations (referring to Tab. 2.2):

$$f_{\text{inst}} \lesssim 30 \text{ kHz} < \nu_{ee} \approx 80 \text{ kHz}. \quad (5.26)$$

As the ion temperature is not measured, we can only provide an approximate estimate of the ion-ion collision frequency assuming that they are cold:

$$T_i < 1 \text{ eV} \Rightarrow \nu_{ii} > 7 \text{ kHz}. \quad (5.27)$$

This is justified by the absence of any ion heating mechanism, so that we do not expect relevant kinetic effects. Moreover, the validity of the fluid approach is justified when the characteristic length of the macroscopic quantities is longer than the distance traveled by particles between collisions. For the magnetized plasmas investigated in TORPEX, this condition can be separately considered for the direction parallel and perpendicular to the magnetic field. For the former, the presence of closed field lines assures the variation of macroscopic quantities on spatial scales much longer than the collision mean-free path of both the electron and ion species ( $\lambda_{\text{mfp},ee} \approx 10 \text{ m}$ ,  $\lambda_{\text{mfp},ii} < 1 \text{ m}$ ), while along the transverse direction, the step-size between collisions is given by the Larmor radius:

$$L_{\perp} = L_n \approx 4 \text{ cm} \gg \rho_{e,i} (\lesssim 1 \text{ mm}). \quad (5.28)$$

A complete set of fluid transport equations was derived by Braginskii [122], starting from the first three moments of the particle distribution function  $f(t, \mathbf{x}, \mathbf{v})$ , corresponding to the continuity equation, the equation of motion and the heat-balance equation. This set of equations describe the evolution of the particle density, velocity and temperature, but it requires a closure scheme for the coupling of the fluid moments to those of higher order. This can be done phenomenologically or by kinetic methods. The latter are used in the Braginskii closure, which consists in finding the expression of the perturbed distribution function  $f_1(\mathbf{v})$  and substituting it in the higher order moments<sup>2</sup>. The resulting set of equations can describe time scales from  $f_{\text{CE}}^{-1} \approx 10^{-10} \text{ s}$  to the confinement time. Taking into account that the instability characteristic time is at intermediate values ( $f_{\text{inst}}^{-1} \approx 10^{-4} \text{ s}$ ), the problem can be further simplified by separating the particle motion between parallel and perpendicular components. The latter are eliminated as characterized by the fastest time-scales of the particle gyro-motions, keeping the time evolution of the parallel drift term. This procedure results in the drift-reduced equations. We note that this model does not take into account the collisions with neutrals, which are dominant in TORPEX plasmas ( $\nu_{eH} \approx 10^6 \text{ Hz}$ ,  $\nu_{iH} \approx 10^4 \text{ Hz}$ )

---

<sup>2</sup>We refer the reader to the Braginskii paper [122] for the details.

where a low ionization fraction is reached ( $\approx 1\%$ ). However, the almost elastic nature of the involved collisions suggests that they do not significantly influence the electron thermalization. Investigations of the drift-reduced Braginskii equations including the effect of neutrals are ongoing [123].

In this work, we focus on a set of linearized drift-reduced Braginskii equations. In the limit of cold ions ( $T_i = 0$ ), neglecting the stress tensor and the electromagnetic effects, the equations for the perturbed electron density,  $n_e$ , electron parallel velocity  $V_{\parallel e}$ , potential,  $\Phi$ , electron temperature  $T_e$ , and ion parallel velocity  $V_{\parallel i}$  can be written as [124]:

$$\frac{\partial n_e}{\partial t} = \frac{R}{L_n} \frac{\hat{P}^L(\Phi)}{B} + 2 \frac{\hat{C}^L}{B} (T_e + n_e - \Phi) - (\nabla_{\parallel} + \nabla \cdot \mathbf{b}) V_{\parallel e}, \quad (5.29)$$

$$\frac{1}{B^2} \frac{\partial \nabla_{\perp}^2 \Phi}{\partial t} = 2 \frac{\hat{C}^L}{B} (n_e + T_e) + (\nabla_{\parallel} + \nabla \cdot \mathbf{b}) (V_{\parallel i} - V_{\parallel e}), \quad (5.30)$$

$$\frac{m_e}{m_i} \frac{\partial V_{\parallel e}}{\partial t} = \nu (V_{\parallel i} - V_{\parallel e}) + \nabla_{\parallel} (\Phi - n_e - 1.71 T_e), \quad (5.31)$$

$$\frac{\partial T_e}{\partial t} = \frac{\eta}{B} \frac{R}{L_n} \hat{P}^L(\Phi) + \frac{4\hat{C}^L}{3B} \left( \frac{7}{2} T_e + n_e - \Phi \right) + \frac{2}{3} (\nabla_{\parallel} + \nabla \cdot \mathbf{b}) (0.71 V_{\parallel i} - 1.71 V_{\parallel e}), \quad (5.32)$$

$$\frac{\partial V_{\parallel i}}{\partial t} = -\nabla_{\parallel} (n_e + T_e). \quad (5.33)$$

Here,  $R$  is the major radius,  $\eta = L_n/L_T$ ,  $L_n$  and  $L_T$  are the radial scale lengths of the background density and temperature, respectively,  $B$  the modulus of the magnetic field and  $\nu$  is the normalized parallel resistivity.  $\hat{P}^L$  and  $\hat{C}^L$  are, respectively, the linearized Poisson bracket and curvature operator (see Ref. [124] for the complete expressions). These equations are solved with the numerical code presented in [125, 126].

### 5.2.1 Driving mechanism of the dominant quasi-coherent modes

For our calculations, we consider the radial position of the mode,  $a = 0.1$  m, the density and temperature scale lengths, respectively,  $L_n = 4$  cm and  $L_T = 10.5$  cm, plasma resistivity  $\nu = 6 \times 10^{-3}$  in  $c_s/R_0$  units, toroidal mode number  $n = 1$ , magnetic shear  $\hat{s} = 2$  and safety factor  $q = 9$ , as obtained from the experimental measurements.

The dominant linear growth rate  $\gamma$  is evaluated using several physical models. First, the complete set of eq. (5.29) (Full model) is implemented. Then, the same analysis is performed using four reduced models [125] where  $n_e$ ,  $\Phi$ ,  $V_{\parallel e}$  and  $T_e$  are evolved, neglecting the parallel ion velocity  $V_{\parallel i}$ , and therefore the coupling with the ion sound waves. These models include

## Chapter 5. Electrostatic fluctuations in the closed field line configuration

---

the resistive and inertial branches of the ballooning modes (BM) and of the drift waves (DW). In the BM models,  $\hat{C}^L$  is only kept in the vorticity equation,  $\nabla_{\parallel} n_e$  and  $\nabla_{\parallel} T_e$  are neglected in the electron velocity equation and  $V_{\parallel e}$  is neglected in both the density and temperature equations. In the DW models,  $\hat{C}^L$  is set to zero for all the fields. For both BM and DW, the resistive (RBM, RDW) and inertial (InBM, InDW) branches are obtained by neglecting, respectively, the inertial term ( $m_e/m_i \partial V_{\parallel e} / \partial t$ ) and the resistive one ( $-\nu V_{\parallel e}$ ). The results for the linear growth rate are shown in Tab. 5.4 and suggest the dominant character of the curvature term in determining the mode linear growth-rate.

Model	Full	RBM	InBM	RDW	InDW
$\gamma$	3.2	3.5	3.4	0.1	0

**Table 5.4** | Growth rate for a toroidal wave number  $n = 1$ ,  $m = 9$  using the following models: full model (Full), Resistive and Inertial Ballooning model (respectively RBM and InBM), Resistive and Inertial Drift Waves model (respectively RDW and InDW).

We can therefore infer the ballooning feature of the instabilities for the investigated plasma parameters, which is consistent with the measured poloidal localization of the mode mainly on the LFS, where the curvature plays a destabilizing effect. However, we can not discriminate between the resistive and the inertial branch. Non-linear simulations should be further developed to address the precise nature of the instability.

### 5.3 Summary

The investigation of plasma fluctuations and coherent modes in the quasi-circular, closed flux surface configuration of the TORPEX device was presented in this chapter. The poloidal field intensity is changed by varying the toroidal conductor current in the range 450 – 750 A. The dominant frequencies of coherent plasma fluctuations are identified and localized on the poloidal cross section. A spectral analysis of the coherent modes is performed, measuring the poloidal and toroidal wave numbers and mode numbers. The field-aligned feature of the mode is verified. The asymmetric poloidal localization of the plasma coherent structures suggests a ballooning character, which is confirmed by the theoretical analysis. Further investigations are envisaged to explore the dependence of plasma fluctuations on experimental parameters, such as different neutral pressures or gases. The use of the non-linear simulations is also foreseen.



## Electrostatic fluctuations in single-null X-point configurations

In the past decades, much effort has been devoted by the fusion community to the investigation of diverted magnetic geometries [127], where significant part of the plasma output power is driven through parallel transport to material surfaces, referred to as target plates. Heat deposition on the target plates is crucial in future fusion devices, such as ITER [23]. In this chapter, we present the first plasma fluctuation studies on TORPEX in diverted magnetic configurations. These are now accessible by superposing the magnetic field generated with the vertical field coils on the poloidal component produced with the toroidal copper conductor system, as discussed in Sec. 3.3, together with the main toroidal magnetic field. In particular, we focus on H<sub>2</sub> plasmas with a single null X-point, at a constant neutral pressure of  $p_n \approx 1.8 \times 10^{-4}$  mbar. An overview of the explored magnetic geometries is provided, together with preliminary results on the dynamics of the plasma modes observed in them. We then investigate a particular magnetic configuration, identifying the effects of the X-point position on the plasma background profiles and particle flow patterns.

This exploration of plasmas with different magnetic geometries was performed to define the optimal configuration to investigate the X-point effects on the dynamics of coherent structures.

### 6.1 Overview of the explored magnetic configurations

An example of a diverted configuration with a single-null X-point on the LFS at  $z = 0$  cm is shown in Fig. 6.1. The neutral gas is ionized by injecting  $P_{\text{mag}} \approx 800$  W and setting the EC resonance at  $r_{\text{EC}} \approx 1$  cm. The poloidal magnetic field is obtained driving a TC current of  $I_{\text{TC}} \approx 880$  A and a vertical field coil current of  $I_{Bv} \approx -54$  A, using the *ideal vertical field* configuration. The resulting poloidal field lines are indicated in white in Fig. 6.1, with a single-null X-point at  $(r \approx 12.5, z \approx 0)$  cm. The HEXTIP  $n_e$  data shown in Fig. 6.1 (a) are time-averaged over a time window of  $\Delta t \approx 300$  ms, when all the control parameters are kept constant, while the density standard deviation is illustrated in Fig. 6.1 (b). The plasma fluctuations are

## Chapter 6. Electrostatic fluctuations in single-null X-point configurations

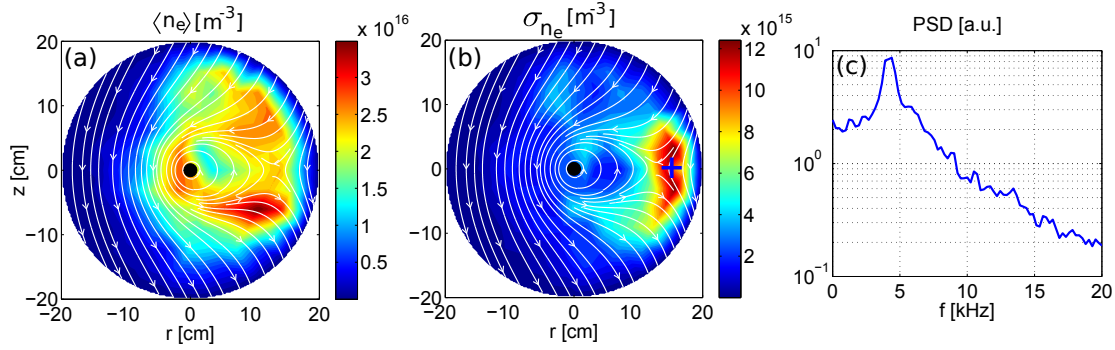


**Figure 6.1** | Example of a single-null X-point on the LFS at  $z = 0$  cm. (a)  $n_e$  time averaged profiles. (b)  $n_e$  standard deviation. (c) PSD of the probe indicated with a blue cross. Discharge #59929.

observed to be concentrated around the X-point region. The PSD of the LP indicated with a blue cross in Fig. 6.1 (b) is shown in Fig. 6.1 (c), indicating quasi-coherent oscillations at a frequency of approximately 4 kHz.

The magnetic configuration introduced in Fig. 3.16 is investigated in the following, with a single-null X-point at  $(r \simeq 0, z \simeq -9)$  cm. The poloidal field obtained driving a TC current of approximately 840 A is superimposed to that generated with 126 A in the vertical field coils. The plasma source is localized outside the confined region, positioning the EC resonance at

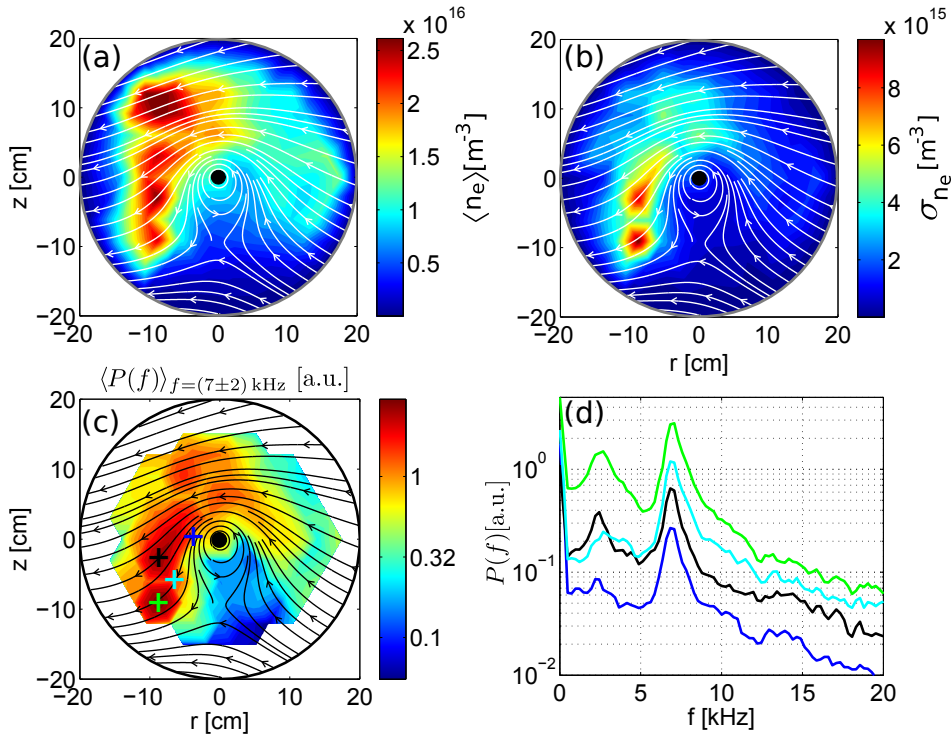


**Figure 6.2** | (a,b) time-averaged density and standard deviation. (b) PSD average in a frequency window of  $7 \pm 2$  kHz, with four crosses indicating the LPs with the PSDs of the corresponding color shown in (d). Discharge #63404.

## 6.1. Overview of the explored magnetic configurations

$r_{\text{EC}} \simeq -15$  cm. The resulting plasma covers mainly the poloidal region of open flux surfaces, as can be seen from the time-averaged density profiles in Fig. 6.2 (a). The density standard deviations in Fig. 6.2 (b) indicate high fluctuations localized just outside the confined region. These are associated with a quasi-coherent mode with a frequency  $f \approx 7$  kHz, as can be seen in Fig. 6.2 (c), where the PSDs of HEX TIP LPs are averaged over a frequency window of 4 kHz around the peak value. In Fig. 6.2 (d), the four PSDs are related to the LPs indicated in Fig. 6.2 (c) with crosses of the corresponding colors.

A qualitative understanding of the mode dynamics is obtained by applying the CAS technique on HEX TIP  $\tilde{J}_{\text{sat}}$  data. The probe at  $(r \simeq -1.2, z \simeq 3)$  cm is selected for the detection of the events above the threshold of  $0.5\sigma_{\tilde{J}_{\text{sat}}}$ . In Fig. 6.3, three snapshots at  $\tau = -36 \mu\text{s}$ ,  $\tau = 0 \mu\text{s}$  and  $\tau = 24 \mu\text{s}$  are shown.

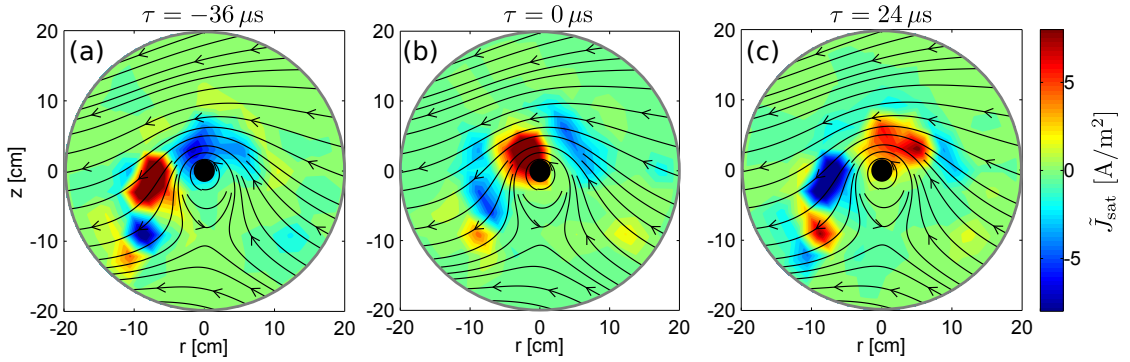


**Figure 6.3** | Conditionally sampled HEX TIP data at  $\tau = -36 \mu\text{s}$  (a),  $\tau = 0 \mu\text{s}$  (b) and  $\tau = 24 \mu\text{s}$  (c). The probe at  $(r \simeq -1.2, z \simeq 3)$  cm is used to detect the events.

The mode is observed to rotate in the clock-wise direction, at the edge of the confined region. This direction of propagation qualitatively agrees with the background  $\mathbf{E} \times \mathbf{B}$  drift pattern indicated with blue arrows in Fig. 6.4 (b), obtained in first approximation from the gradients of the background profiles of floating potential given in Fig. 6.4 (a). In Fig. 6.4 (c), we note that the  $V_{\text{fl}}$  fluctuations are localized around the confined region, similarly to those of  $n_e$ .

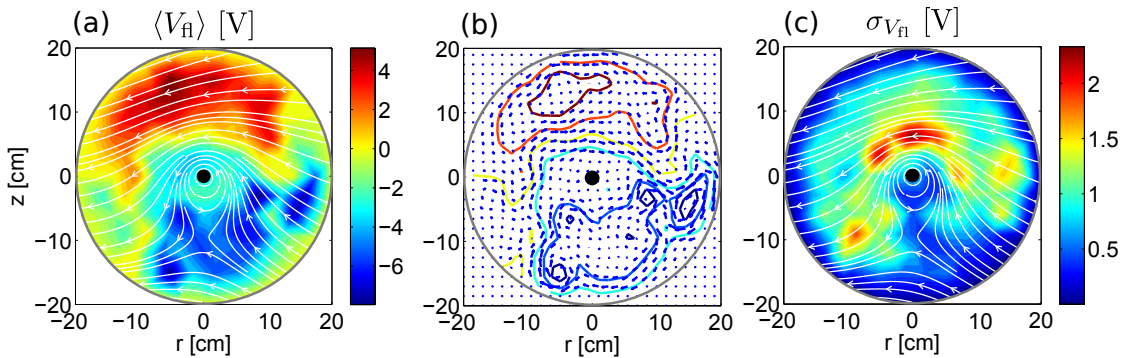


**Figure 6.4** | (a) time averaged  $V_{\text{fl}}$  data, with the associated  $\mathbf{E} \times \mathbf{B}$  drift indicated in (b) with blue arrows. These are tangential to the potential iso-lines indicated with colored curves. (c) Standard deviation of  $V_{\text{fl}}$ . Discharge #63407.

## Chapter 6. Electrostatic fluctuations in single-null X-point configurations

We now analyze the same magnetic configuration, but with the EC layer positioned at  $r_{EC} \simeq -10$  cm, to obtain the steady state density profiles mainly localized in the confined region, as shown in Fig. 6.5 (a). A lower current of  $I_{TC} \approx 100$  A is driven in the vertical field coils to increase the size of the confined region, setting the X-point at  $(r \simeq 0, z \simeq -11)$  cm.

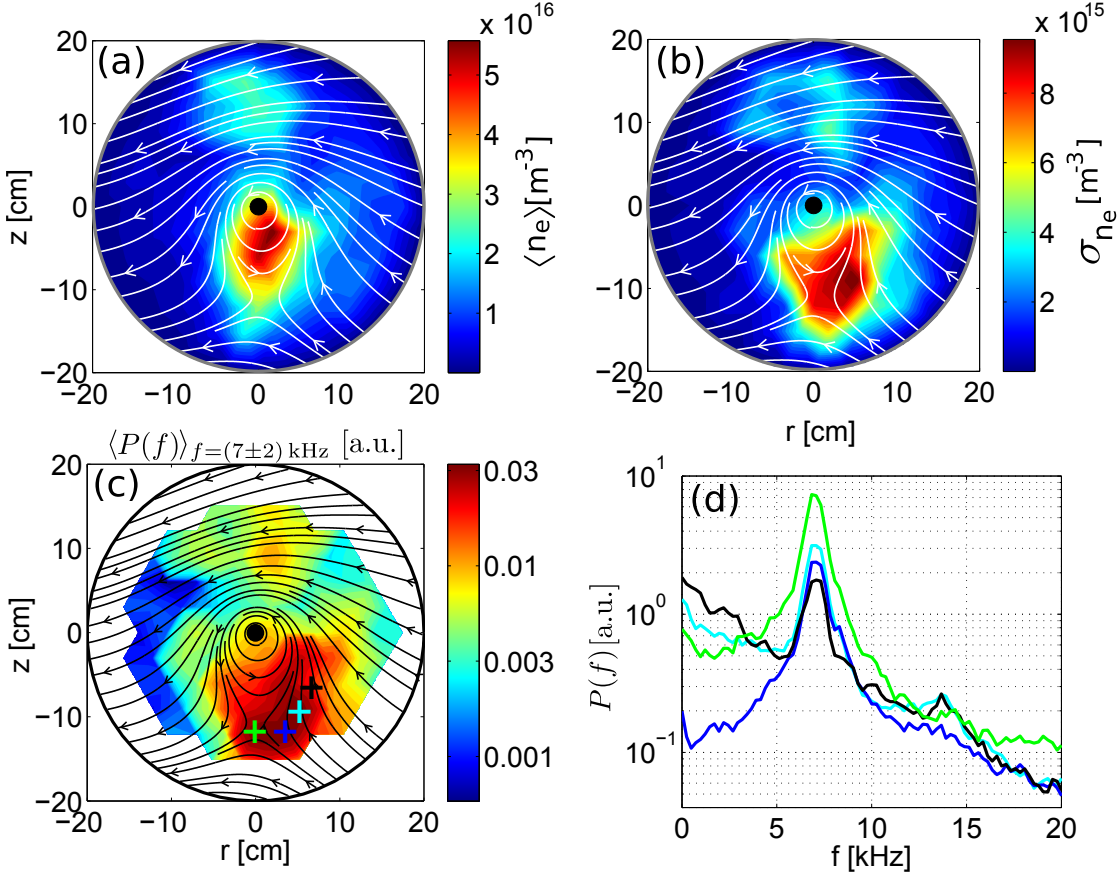


**Figure 6.5** | (a) time-averaged density and standard deviation. (b) PSD average in a frequency window of  $7 \pm 2$  kHz, with four crosses indicating the LPs with the PSDs of the corresponding colors shown in (d). Discharge #63984.

The plasma fluctuations are concentrated over the region of density gradients around the X-point, on the LFS, as indicated in Fig. 6.5 (b). These are associated with a quasi-coherent mode at  $f \approx 7$  kHz, as shown in Fig. 6.5 (c), where the PSDs of HEX TIP signals are averaged on a frequency window of 4 kHz around the dominant spectral component. The four colored crosses indicate the LPs with the PSDs of the corresponding color illustrated in Fig. 6.5 (d).

The poloidal region of high fluctuations is investigated in detail, performing a 2D scan with the 2DSSLP in ion saturation current on a shot-to-shot basis. A radial step of  $\Delta r = 1$  cm and a poloidal angle resolution of at least  $\Delta \theta = 2^\circ$  are chosen. The FAPA LP positioned in  $(r \simeq 1, z \simeq -10.5)$  cm, in the region of high fluctuations, is used to select the mode peaks above a density threshold of  $2\sigma_{n_e}$ . Quasi-coherent modes are observed to propagate around the X-point region, as shown in Fig. 6.6. In Fig. 6.6 (a), a peak of the mode starts to stretch radially at  $\tau = -48 \mu s$  as it propagates upward in the counter clock-wise direction. In Fig. 6.6 (b)(c), the

## 6.2. Plasma flow dependence on the X-point position

blob is observed to progressively detach, while in Fig. 6.6 (d) at  $\tau = 24 \mu\text{s}$ , it is clearly separated from the mode and propagates radially outward. This is confirmed by the PDFs of the ion saturation signals, showing a sensitive change in the measured skewness close to the X-point. The PDF of the probe at  $(r \approx 12, z \approx -6)$  cm indicated with a magenta circle in Fig. 6.6 (d) is shown in the inset and displays a skewed profile towards positive events. The value of the corresponding skewness is  $S \approx 1.2$ .

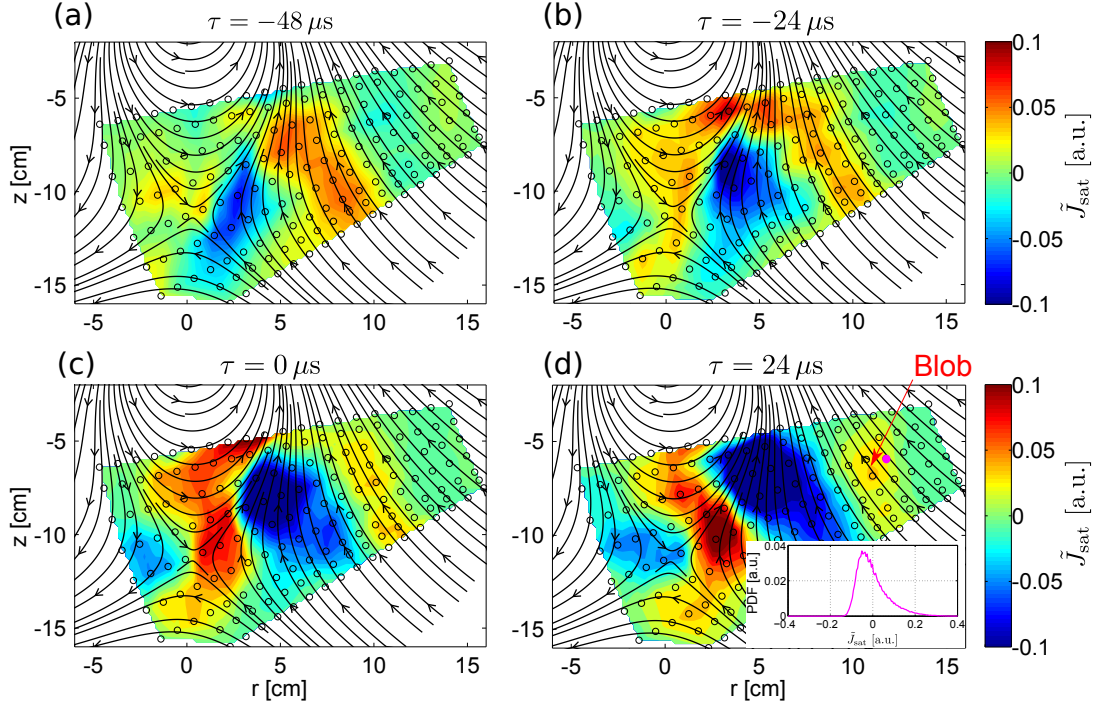


**Figure 6.6** | Conditionally sampled data obtained from 2D measurements with the 2DSSLP, using the FAPA probe at  $(r \approx 1, z \approx -9.5)$  cm for the event detection. Snapshots at  $\tau = -48 \mu\text{s}$  (a),  $\tau = -24 \mu\text{s}$  (b),  $\tau = 0 \mu\text{s}$  (c) corresponding to the event trigger, and  $\tau = 24 \mu\text{s}$  (d).

## 6.2 Plasma flow dependence on the X-point position

In this section, we analyze plasmas with the TC vertical position optimized for diverted magnetic configurations, suspended at  $r = (0 \pm 0.50)$  cm,  $z = (16.50 \pm 0.50)$  cm, as indicated with the black circle in Fig. 6.7(a). We aimed at producing almost vertical field lines outside the last closed flux surface on the HFS, and an X-point on the LFS, as indicated in Fig. 6.7 (a). This configuration has a key role for the studies of the blob dynamics in the presence of an X-point presented in Ch. 7. The total poloidal magnetic field results from the superposition of the component generated with the TC to a quasi-horizontal magnetic field produced using the vertical field coils, which are connected according to the current path displayed in Fig. 6.7(b).

## Chapter 6. Electrostatic fluctuations in single-null X-point configurations

The example presented in Fig. 6.7 is calculated with  $I_{TC} \simeq -1 \text{ kA}$ <sup>1</sup>, and 150 A in the vertical field coils. The current in the vertical field coils is varied to change the X-point position. The three explored values are  $I_{VFC} = [130, 150, 170] \text{ A}$ . The investigated plasmas are produced by injecting 300 W of RF power. The electron cyclotron resonance layer is set at  $r_{EC} = -14 \text{ cm}$  by setting the toroidal magnetic field at  $B_T \simeq 750 \text{ Gauss}$ . Discharges of about 1 s are performed, maintaining constant all the control parameters.

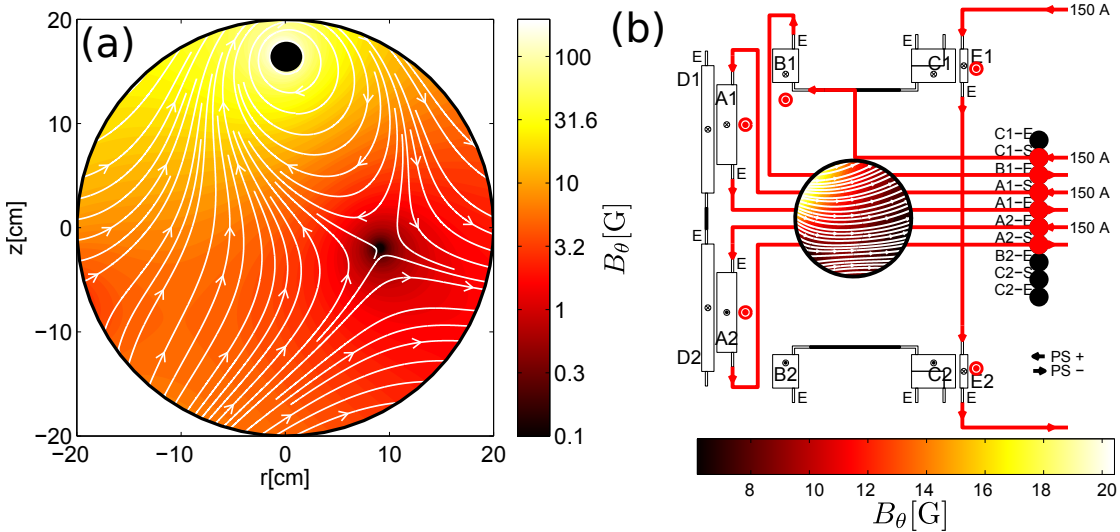


**Figure 6.7** | (a) Poloidal magnetic field of a diverted magnetic configuration, with an X-point on the LFS and the confined region cover the upper region of the poloidal cross section. (b) Circuit of vertical field coils used to add an almost horizontal component to the magnetic field generated by the toroidal conductor, indicated with a black circle in b), in order to obtain a single null X-point.

### 6.2.1 Background profiles

The 2D time-averaged density profiles obtained with HEXTIP are shown in Fig. 6.8 (a|c|e), for the three explored values of  $I_{VFC}$ . In Fig. 6.8 (b|d|f), the corresponding standard deviations are depicted. The X-point is vertically moved by varying the vertical field coil current. Both the time-averaged densities and the standard deviation profiles are modified. Quasi-coherent modes are identified with a dominant frequency between 5 kHz and 10 kHz in the high fluctuation region, which is elongated towards the X-point on the LFS. These can be compared to the measurements of floating potential, shown in Fig. 6.9. The region of closed flux surfaces present an almost constant electrostatic potential close to zero. Potential gradients appear just outside the last closed flux surface, generating a background electric field and a corresponding  $\mathbf{E} \times \mathbf{B}$  flow along the potential iso-lines.

<sup>1</sup>The sign indicates a counterclockwise direction seen from above, which is reversed with respect to the typical direction.

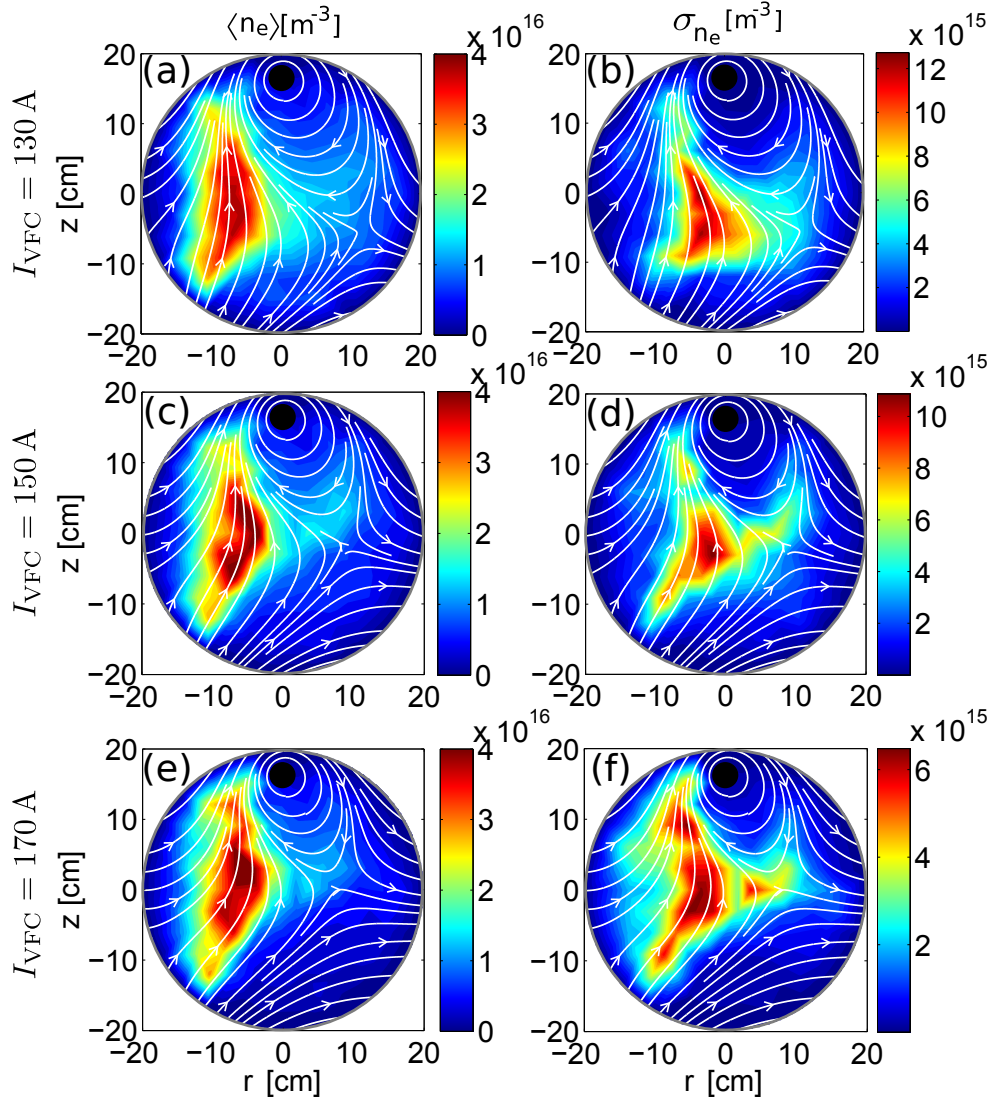


**Figure 6.8** | 2D time-averaged density (a|c|e), and standard deviation (b|d|f) with  $I_{TC} \simeq 1 \text{ kA}$  and  $I_{VFC} = [130, 150, 170] \text{ A}$ . The toroidal conductor is indicated with a black circle on the top of the cross section, the white lines reproduce the calculated magnetic field lines. Discharges #65530, #65528 and #65534.

### 6.2.2 Plasma particle fluxes

The statistical structure analysis introduced in Sec. 5.1.1 is performed on HEX TIP data to measure the plasma particle flows. The results of the analysis are shown in Fig. 6.10, with the ensemble-averaged structure flux  $|\langle \delta n \vec{v} \rangle|$ . The corresponding vector field is indicated by the superimposed black crosses.

The continuous lines represent the contours of the time-averaged density profiles at 25%, 50% and 75% of the maximum. If we compare Fig. 6.10 with Fig. 6.9, we can notice that the particle flow is advected towards the region of the X-point, where high gradients of electrostatic potential are located. This indicates the contribution of the background  $\mathbf{E} \times \mathbf{B}$  drift in deter-

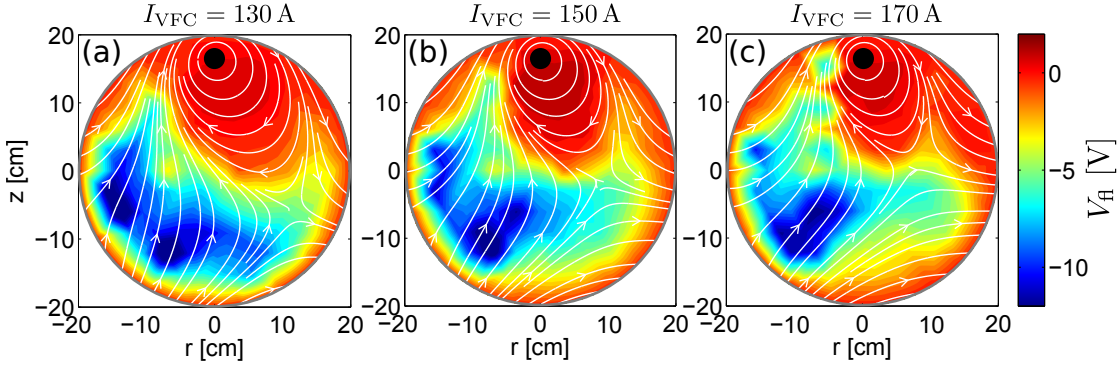


**Figure 6.9** | Two-dimensional time-averaged floating potential profiles with  $I_{VFC} = [130, 150, 170]$  A. Discharges #65531, #65529 and #65536.

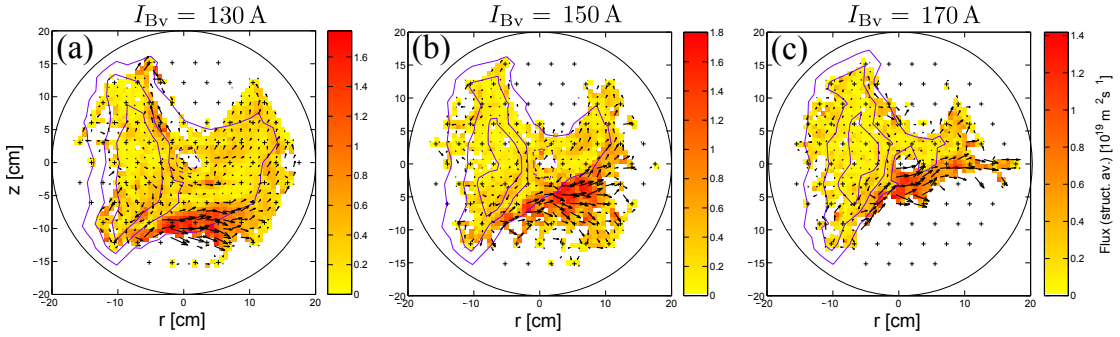


**Figure 6.10** | Plasma particle flows with  $I_{VFC} = [130, 150, 170]$  A. The black arrows indicate the ensemble-averaged vector field  $\langle \delta n \vec{v} \rangle$ , while the continuous lines correspond to the contours of the time-averaged density profiles at 25%, 50% and 75% of the maximum.

mining the particle fluxes. A quantitative analysis is performed for  $I_{VFC} \simeq 150$  A, calculating the number of particles per second  $\dot{N}$  advected outward by  $\mathbf{v}_{E \times B}$  through a surface defined by the rotation about the major axis of a curve  $C$ , limited by the potentials  $V_1$  and  $V_2$  [128]:

$$\dot{N} = \int_1^2 2\pi R n v_e (\hat{\mathbf{e}}_\phi \times d\mathbf{s}) \approx \frac{2\pi}{R_0 B_0} \langle n R^2 \rangle (V_1 - V_2) \simeq 6.7 \times 10^{18} \text{ s}^{-1}. \quad (6.1)$$

In eq. 6.1, the chosen integration path is a straight vertical line at  $r = 4$  cm, from  $z_1 = 0$  cm to  $z_2 = -4$  cm. Along this curve, we consider constant  $B_T$ ,  $R$  and  $n$ , using  $R = R_0 = 1.04$  cm,  $B_0 \simeq 730$  Gauss,  $\langle n \rangle \simeq 1.25 \times 10^{16} \text{ m}^{-3}$ ,  $V_1 = -1.3$  V and  $V_2 = -7.3$  V.

The obtained value of  $\dot{N}$  corresponds to a particle flux:

$$\Gamma = \frac{\dot{N}}{2\pi R(z_1 - z_2)} \simeq 2.5 \times 10^{19} \text{ m}^{-2} \text{ s}^{-1}, \quad (6.2)$$

which is comparable with the average value  $\Gamma \simeq 1.2 \times 10^{19} \text{ m}^{-2} \text{ s}^{-1}$  presented in Fig. 6.10 for the chosen region. The consistency of the result has been verified for different values of density threshold used to identify the structures, namely  $n_e^t = [1, 10] \times 10^{15} \text{ m}^{-3}$ . This indicates that the background drift has a significant role in the structure flow, but more refined analysis to



take into account the drift associated with the fluctuating component of the plasma potential are presented in Ch. 7.

Analyzing the plasma with  $I_{\text{VFC}} \simeq 170$  A, we observe that the PSDs on the  $n_e$  time traces indicate quasi-coherent fluctuations on the HFS. In Fig. 6.11, the PSDs averaged over a spectral window of 3 kHz around dominant frequency of 4 kHz is shown. The presence of a mode on the HFS is verified for the others value of  $I_{\text{VFC}}$ .

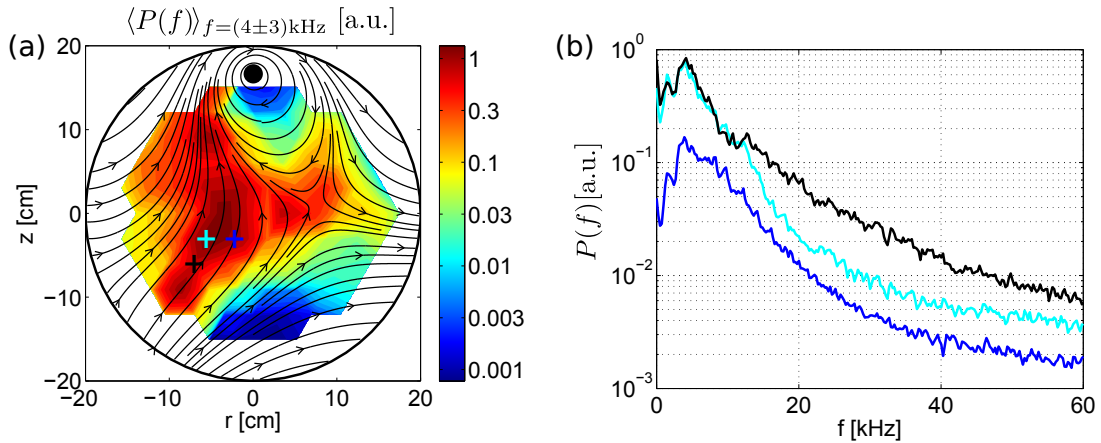


**Figure 6.11** | (a) Mode intensity averaged on a frequency window of 3 kHz around the dominant mode frequency at 4 kHz. (b) Three examples of PSDs, evaluated at the positions indicated with the crosses of the corresponding colors in (a).

### 6.3 Summary

In this chapter, we have provided an overview of the plasma features for the main accessible magnetic configuration on TORPEX with a single null X-point. The time-averaged density profiles are measured for different positions of the plasma source, outside or inside the confined region. Clear changes are observed in the poloidal position of the electrostatic fluctuations, which show quasi-coherent modes in a frequency range below 10 kHz. In particular, modes in the X-point region are observed for the discharge where the plasma is produced in the closed flux surface region, with the consequent detachment of blobs on the LFS.

First investigations on the influence of the X-point position on the plasma profiles and particle fluxes have been carried out. The background patterns of density and plasma flows are clearly influenced by the vertical displacement of the X-point position. Measurements of the 2D time-averaged floating potential profiles suggest a contribution of the background electric field to establish  $\mathbf{E} \times \mathbf{B}$ -induced drifts. The presented investigation of different magnetic configurations has allowed us to identify the best conditions to perform further studies on the effective role of the X-point in determining the plasma dynamics. The results on this topic are given in Ch. 7.



## The effect of the magnetic X-point on plasma blob dynamics

The high power fluxes that must be exhausted by the plasma facing materials constitutes a critical issue for future fusion power plants. The possibility of reaching high density regimes is in fact hampered by the limited heat fluxes that present divertor configurations can tolerate ( $P \approx 10 \text{ MW/m}^2$ ). Advective phenomena have been proven to give a significant contribution to the particle and heat flux from the plasma core across the last closed flux surface. Comprehensive experimental, numerical and analytical investigations indicate that a large portion of this transport takes the form of intermittent ejections of coherent structures, named blobs [36, 93, 129]. In the presence of diverted magnetic configurations, the understanding of blob dynamics in the X-point region and along the divertor legs remains an open question. The necessity to include electric fields and drifts in the divertor modeling has been identified [128], together with the importance of  $\mathbf{E} \times \mathbf{B}$  particle flows close to the X-point, both numerically [130] and experimentally [131]. However, the high temperatures and densities in fusion plasmas limit the diagnostic accessibility, making it difficult to directly measure blob features in the vicinity of X-points. This issue can be overcome in basic plasma physics devices, where measurements with the required spatial resolution can be performed over the whole plasma volume.

In this chapter, we detail the first experimental in-situ measurements of plasma blob dynamics in the X-point region. Blobs generated from the mode region on the HFS and radially propagating outwards across the X-point on the LFS are tracked and analyzed in detail. The blob speed is obtained from conditionally averaged data. A significant acceleration of the blobs in the region close to the X-point is observed. The background  $\mathbf{E} \times \mathbf{B}$  drift contribution is isolated from the blob electric potential dipole drive. The latter shows a time evolution that can explain the fast blob dynamics. An analytical model based on charge conservation is derived for the blob characteristic velocity  $v_b$ , similar to that presented in [90], including ion polarization, diamagnetic and parallel currents. A crucial role is played by the variation of magnetic field

intensity in the vicinity of the X-point. This determines the value of the geometrical parameter expressing the length of the current path parallel to the magnetic field, along which the blob dipole is short-circuited. The analytical results show a good quantitative agreement with the experimental data.

## 7.1 Background plasma profiles

The poloidal magnetic field geometry depicted in Fig. 6.7 is used for these experiments. This is obtained by driving a current of  $I_{TC} = -640$  A in the TC and 110 A in the toroidal coils. Hydrogen plasmas are produced by injecting 300 W of RF power with an average neutral pressure of  $1.8 \times 10^{-4}$  mbar. A toroidal magnetic field of 750 Gauss localizes the EC resonance at  $r_{EC} \simeq -14$  cm. This allows producing quasi-vertical field lines outside the last closed flux surface on the HFS, similarly to the SMT, as shown in Fig. 7.1 (a). A first order magnetic null point results on the LFS at  $(r \simeq 7, z \simeq 0)$  cm. Two-dimensional HEXTIP time-averaged signals of ion saturation current density  $J_{sat}$  are shown in Fig. 7.1 (a). The black, blue and cyan contours refer, respectively, to 80%, 60% and 40% of the standard deviation of the time-traces. These indicate the high fluctuation region where quasi-coherent modes are identified with a

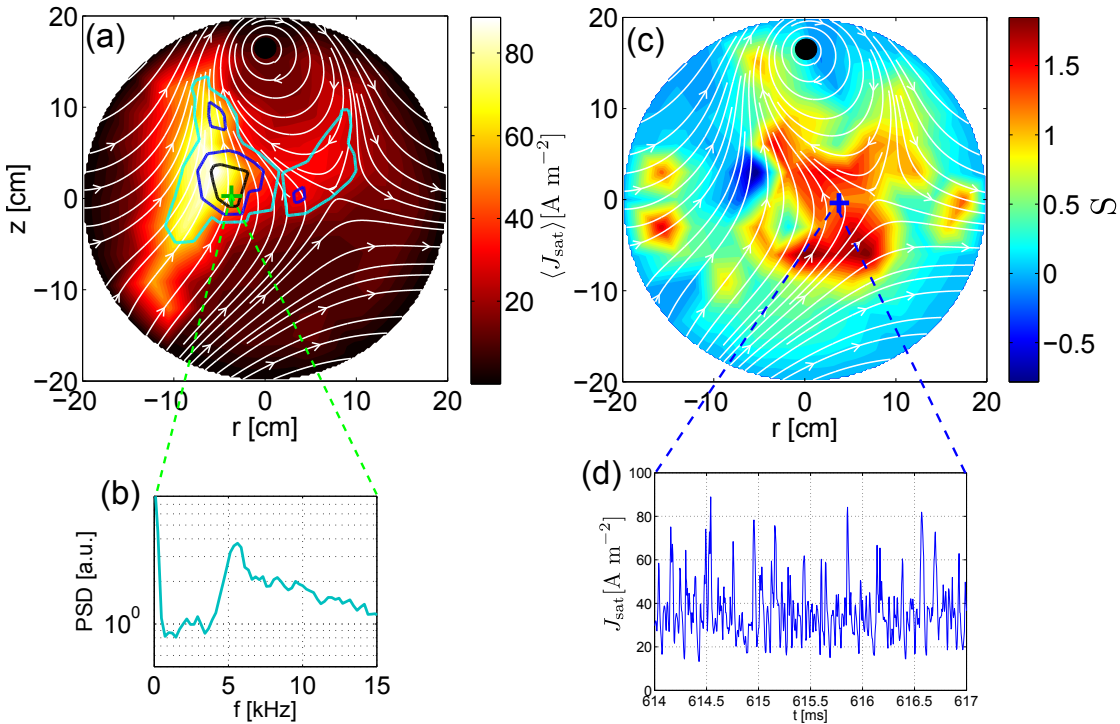


**Figure 7.1** | Two-dimensional time-average (a), and skewness (c) of HEXTIP  $J_{sat}$  time-traces. The black, blue and cyan contours correspond to the  $J_{sat}$  standard deviation iso-lines at 80%, 60% and 40% of the maximum value. The PSD of the probe indicated with the green cross at  $(r \simeq -3.5, z \simeq 0)$  cm is shown in (b), indicating a dominant frequency  $f \simeq 5$  kHz. In (d), the time trace of the HEXTIP probe indicated with a blue cross is reported. Discharge #65100.

## 7.2. Experimental blob dynamics from conditional sampling

dominant frequency  $f \approx 5$  kHz, as shown by the PSD in Fig. 7.1 (b) for the probe indicated with a green cross. In Fig. 7.1 (c), the values of the signal skewness indicate the presence of blobs in the X-point region, where a detailed analysis is performed. In Fig. 7.1 (d) we show the time trace of the LP indicated with a blue cross in Fig. 7.1 (c), which displays a large level of intermittency associated with blobs. The background plasma potential profiles are obtained with a refined poloidal scan using three LPs of the 2DSSLP (#1, #3, #7) with a sweeping bias at 330 Hz between -40 V and 20 V to cover both the ion and electron saturation current regimes. The electron temperature ( $T_e$ ) and floating potential ( $V_{fl}$ ) values are extracted from the I-V curves to evaluate the electrostatic plasma potential  $V_{pl} = \mu T_e / e + V_{fl}$ , with  $\mu = 3.1$  [62]. The resulting 2D profiles for the electrode #7 are shown in Fig. 7.2. We observe in Fig. 7.2 (a) that the high temperature region corresponds to the high density region of Fig. 7.1 (a).

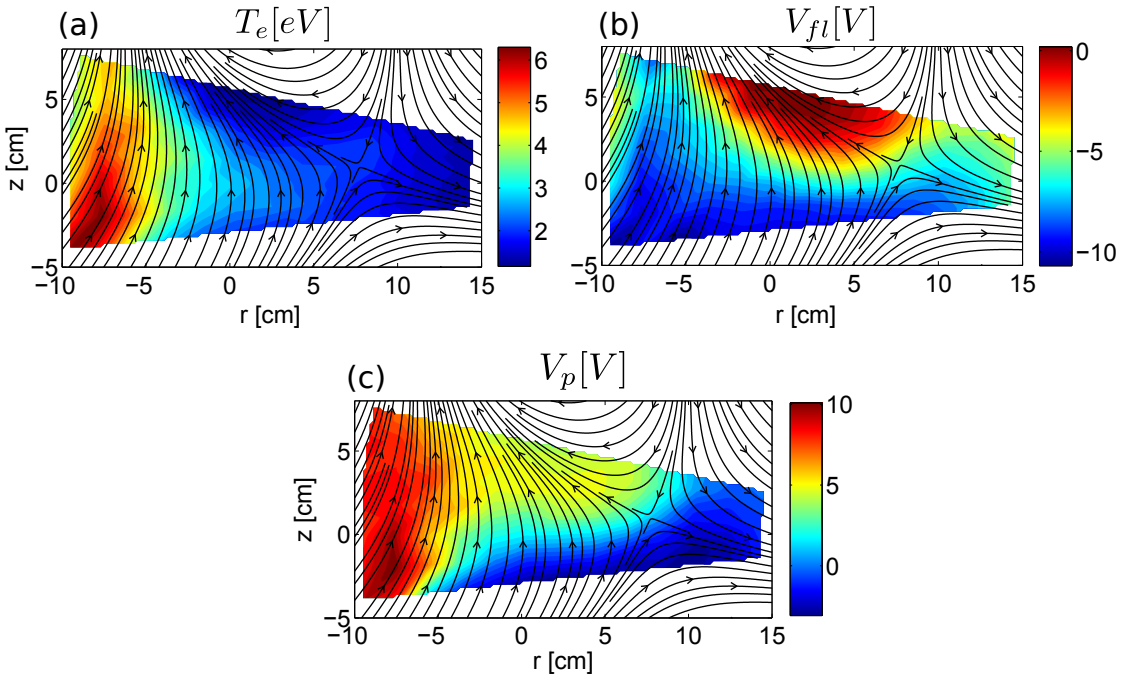


**Figure 7.2** | 2D profiles of electron temperature (a), floating potential (b) and plasma potential (c).

## 7.2 Experimental blob dynamics from conditional sampling

To investigate the blob motion, 2D measurements are performed with the 2DSSLP measuring separately the ion saturation current and the floating potential. These data are conditionally sampled and averaged around the blob detection time ( $\tau = 0 \mu\text{s}$ ) over a time window of 100  $\mu\text{s}$ , which is of the same order of magnitude of the  $J_{\text{sat}}$  signal auto-correlation time in the blob region. The events are detected using the HEX TIP LP located at ( $r \approx 7, z \approx 0$ ) cm, close to the X-point. This allows selecting the blobs that originate in the mode region and propagate radially outward passing through the X-point, therefore experiencing along their trajectory the variation of the poloidal field from  $B_z \approx 3$  Gauss to zero. An amplitude threshold corresponding to four times the standard deviation of the  $J_{\text{sat}}$  signals is chosen for the structure detection.

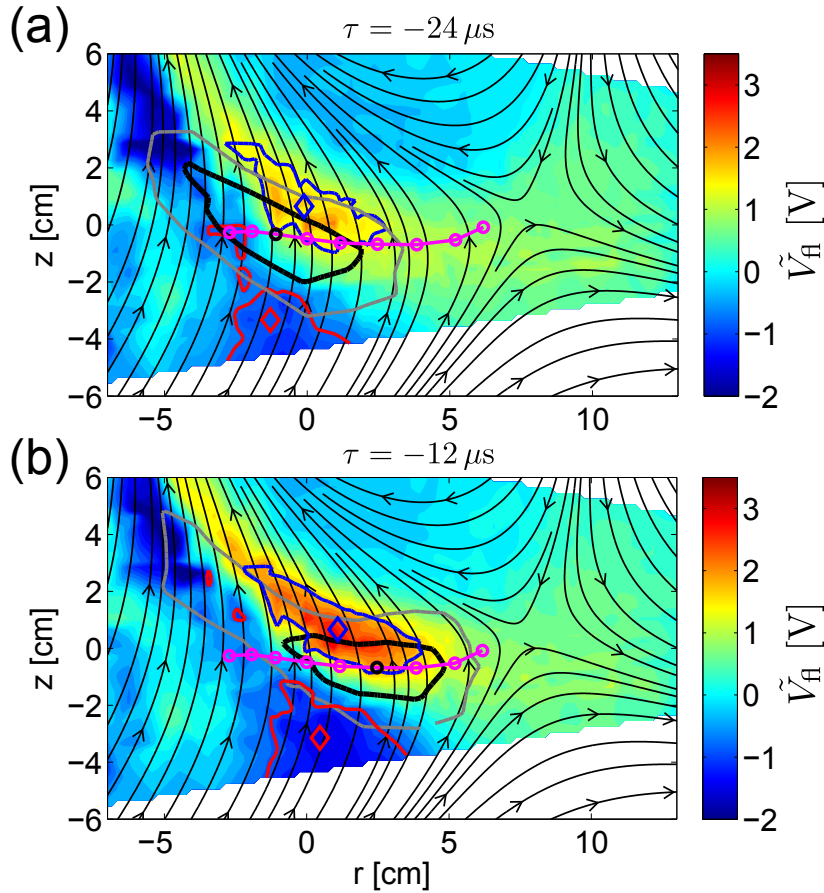


**Figure 7.3** | Fluctuating floating potential  $\tilde{V}_f$  at  $\tau = -24 \mu\text{s}$  and  $\tau = -12 \mu\text{s}$  obtained from CAS data of the 2DSSLP, using as trigger the HEXTIP probe at  $(r \approx 7, z \approx 0)$  cm. The blue and red contours indicate the floating potential values at 60% of the positive and negative peaks, with the weighed centers shown by the colored diamonds. The gray and black lines correspond to the  $\tilde{J}_{\text{sat}}$  contours at 20% and 60% of the structure amplitude, respectively. The magenta curve indicates the blob trajectory, with in black the position of the center of mass.

The same analysis is performed with a lower threshold, corresponding to two times the standard deviation, without any significant changes in the obtained blob dynamics. In Fig. 7.3 we show two snapshots of the CAS analysis on the measured fluctuating floating potential at  $\tau = -24 \mu\text{s}$  and  $\tau = -12 \mu\text{s}$ . The floating potential values at 60% of the positive and negative peaks are indicated with the blue and red contours. The colored diamonds correspond to the weighed centers. The gray and black lines represent the  $\tilde{J}_{\text{sat}}$  contours at 20% and 60% of the structure amplitude. The blob trajectory is indicated by the magenta curve and the black circle represents the instantaneous position of the blob center of mass. The blob position is evaluated at each time step from the center of mass of the structure calculated on the interpolated data inside the 60%  $\tilde{J}_{\text{sat}}$  contour. The corresponding speed in the time window between  $-28 \mu\text{s}$  and  $0 \mu\text{s}$  is obtained from the derivative of a fifth order polynomial fit on the displacement of the blob center of mass. The results are shown in Fig. 7.4 by the blue

## 7.2. Experimental blob dynamics from conditional sampling

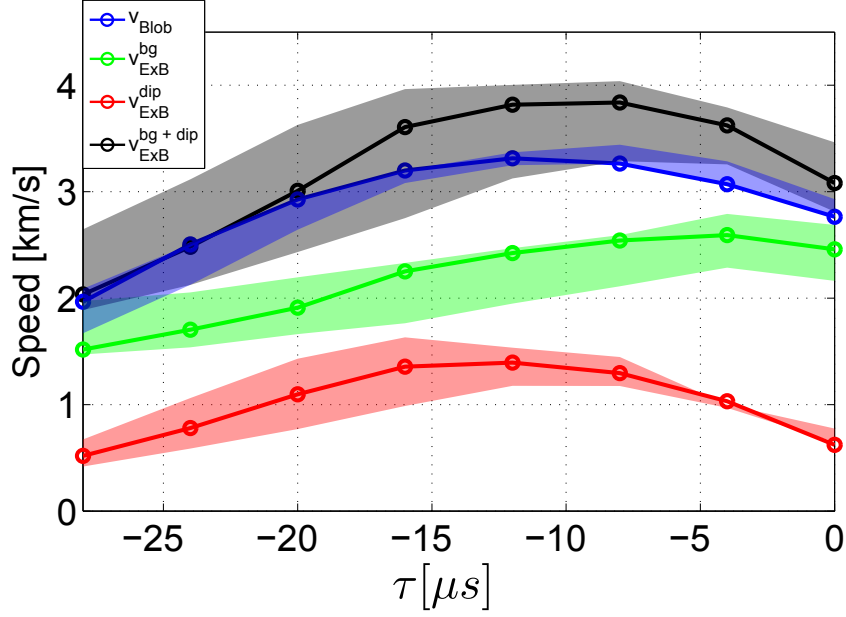


**Figure 7.4** | In blue, experimental blob speed obtained from the blob displacement. In black, total blob speed calculated as the sum of the drift associated to the background plasma potential gradients (in green) and that originating from the blob dipole electric field (in red).

curve, while the shaded region gives an estimate of the uncertainty on the calculated speed, applying the same procedure on the interpolated data inside the 40% and 80%  $\tilde{J}_{\text{sat}}$  contours. To obtain quantitative insight into the mechanisms determining the blob speed, the  $\mathbf{E} \times \mathbf{B}$  drift is evaluated by decomposing the total electric field into two main contributions:

$$\mathbf{E}_{\text{tot}} = \bar{\mathbf{E}}_{\text{bg}} + \tilde{\mathbf{E}}_{\text{dip}}. \quad (7.1)$$

$\bar{\mathbf{E}}_{\text{bg}} = -\nabla V_{\text{pl}}$  corresponds to the background plasma potential gradients, while  $\tilde{\mathbf{E}}_{\text{dip}}$  is the electric field originating from the blob fluctuating potential dipole  $\tilde{V}_{\text{fl}}$ . Both are calculated by smoothing the measured data and averaging the gradients over the values inside the 60%  $\tilde{J}_{\text{sat}}$  contour. We neglect in a first approximation the fluctuating temperature contribution to the plasma potential dipole. The two corresponding components of the blob speed are calculated as  $v_{E \times B}^{\text{bg}} = \bar{E}_{\text{bg}}/B$  and  $v_{E \times B}^{\text{dip}} = \tilde{E}_{\text{dip}}/B$ , indicated in Fig. 7.4 by a green and red curve. The shaded regions provide an estimate of the uncertainty on the estimated curves, obtained by averaging the electric fields inside the 40% and 80%  $\tilde{J}_{\text{sat}}$  contours. The speed associated with the blob dipole plays a crucial role in the first 16  $\mu\text{s}$ , contributing with 0.8 km/s to the total variation of the blob speed  $v_{E \times B}^{\text{bg} + \text{dip}}$ . This is indicated in Fig. 7.4 with the black curve, and is in good agreement with the measured blob speed  $v_{\text{Blob}}$ .

### 7.3 Analytical model for blob speed

To explain the time variation of the blob dipole, the magnetic field shear along the blob trajectory is considered in the following way. The vertical magnetic field in the region of the blob detachment from the original mode, namely at  $(r \simeq -2, z \simeq 0)$  cm, is approximately 3 Gauss. This value and the associated magnetic geometry allows us to refer to the previously studied SMT resistive interchange regime to infer the toroidally uniform feature of the fluctuations ( $k_{\parallel} \neq 0, k_{\text{tor}} = 0$ ) [67, 89]. This is supported by the vertical distance covered by a field line after a toroidal turn ( $\sim 2$  cm), which is comparable to the blob vertical size at 60% of its  $\tilde{J}_{\text{sat}}$  maximum, indicated in Fig. 7.3. These observations suggest that the detached blob is not a 2D field aligned sheath connected structure, but that it closes on itself [132], which is compatible with the measurements of the coherence between LPs positioned at different toroidal angles. Under these assumptions, the magnetic field provides a path  $L_{\parallel}$  for the parallel currents to short-circuit the vertical potential dipole. A schematic of this situation is shown in Fig. 7.5, in which the vertical, radial and toroidal coordinates are indicated with  $\hat{z}$ ,  $\hat{r}$  and  $\hat{y}$ .

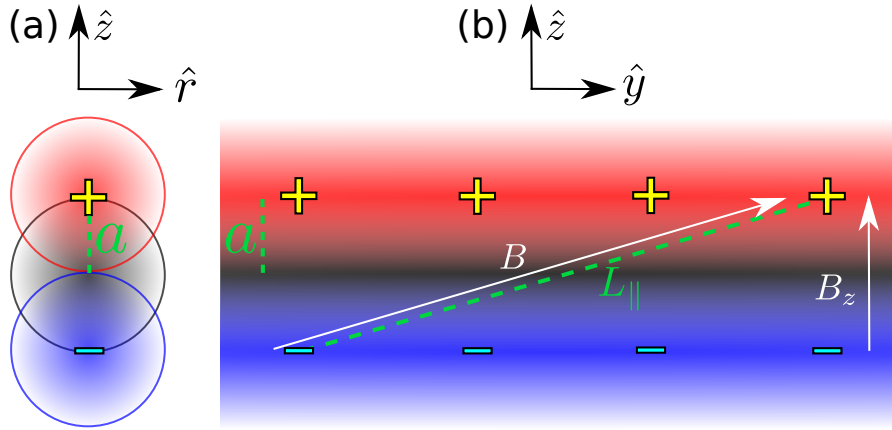


**Figure 7.5** | Schematic of blob density profile (black) with the associated potential dipole (red and blue) on the poloidal cross section (a) and along the toroidal direction (b), with the parallel connection length  $L_{\parallel}$  and the blob size  $a$  indicated.

As the blob approaches the X-point, the parallel connection length  $L_{\parallel}$  increases. This effect can be taken into account by evaluating the blob speed  $v_b$  starting from charge conservation:

$$\nabla \cdot \mathbf{J} = \nabla_{\perp} \cdot \mathbf{J}_{\perp} + \nabla_{\parallel} J_{\parallel} = 0, \quad (7.2)$$

in a way similar to the previously reported scaling laws [90, 129]. The main difference is the replacement of the parallel current to the sheath with the parallel current short-circuiting the blob dipole inside the plasma. We focus on this term using the hypothesis of axisymmetry ( $k_{\text{tor}} = k_y = 0$ ) by writing the parallel gradient as:

$$\nabla_{\parallel} = b_z \frac{\partial}{\partial z} + b_y \frac{\partial}{\partial y} = \frac{B_z}{B} \frac{\partial}{\partial z}, \quad \text{with} \quad b_z = \frac{B_z}{B}, \quad (7.3)$$



where  $B_z$  is the poloidal magnetic field and  $B$  the total magnetic field. It follows that:

$$\nabla_{\parallel} J_{\parallel} = \frac{B_z}{B} \frac{\partial J_{\parallel}}{\partial z}. \quad (7.4)$$

The parallel electric field can now be evaluated to obtain the parallel current  $J_{\parallel} = \sigma E_{\parallel}$ , with  $\sigma$  the effective plasma conductivity:

$$E_{\parallel} = \mathbf{E} \cdot \mathbf{b} = E_y b_y + E_z b_z = -\frac{\partial \tilde{\phi}}{\partial z} \frac{B_z}{B}. \quad (7.5)$$

Here  $\tilde{\phi}$  is the fluctuating blob potential. We therefore obtain:

$$\nabla_{\parallel} J_{\parallel} = -\sigma \frac{B_z}{B} \frac{\partial}{\partial z} \left( \frac{B_z}{B} \frac{\partial \tilde{\phi}}{\partial z} \right) \approx -\sigma \left( \frac{B_z}{B} \right)^2 \frac{\partial^2 \tilde{\phi}}{\partial z^2}. \quad (7.6)$$

The perpendicular current density contribution of eq. (7.2) is very similar to that in [90], where we consider the ion polarization and the electron diamagnetic currents. We finally get:

$$-\sigma \left( \frac{B_z}{B} \right)^2 \frac{\partial^2 \tilde{\phi}}{\partial z^2} + \frac{2c_s^2 m_i}{RB} \frac{\partial n}{\partial z} - \frac{m_i n}{B^2} \frac{d}{dt} \left( \nabla_{\perp}^2 \tilde{\phi} \right) = 0, \quad (7.7)$$

where  $c_s = \sqrt{T_e/m_i}$  is the ion sound speed and  $R$  the major radius. We can proceed with the same estimates performed in [90]:

$$\frac{\partial^2 \tilde{\phi}}{\partial z^2} \sim -\frac{2\tilde{\phi}}{(2a)^2}, \quad \nabla_{\perp}^2 \tilde{\phi} \sim -\frac{\tilde{\phi}}{a^2}, \quad \frac{\partial n}{\partial z} \sim -\frac{\delta n}{a}, \quad \frac{d}{dt} \sim \frac{\sqrt{2}c_s}{\sqrt{Ra}}. \quad (7.8)$$

In addition, we write:

$$\frac{B_z}{B} \sim \frac{2a}{L_{\parallel}}, \quad (7.9)$$

where  $L_{\parallel}$  is the parallel connection length along the magnetic field between the two peaks of the blob dipole, sketched in Fig. 7.5. The following expression is obtained:

$$\frac{2c_s^2 m_i}{RB} \frac{\delta n}{a} = \sigma \frac{2\tilde{\phi}}{L_{\parallel}^2} + \frac{m_i n}{B^2} \frac{\sqrt{2}c_s}{\sqrt{Ra}} \frac{\tilde{\phi}}{a^2}. \quad (7.10)$$

The blob speed can be estimated from  $\tilde{\phi} \sim B v_b a$  and  $\sigma = C n$ , where  $C$  indicates the proportionality coefficient between the plasma conductivity and the plasma density:

$$v_b = \frac{\delta n}{n} \sqrt{\frac{2a}{R}} c_s \left( \frac{1}{1 + A/L_{\parallel}^2} \right), \quad A = \frac{CB^2 a^{5/2} \sqrt{2R}}{m_i c_s} \quad (7.11)$$

For  $L_{\parallel} \rightarrow \infty$ , the inertial scaling  $v_b = \delta n/n \sqrt{2a/R} c_s$  is retrieved [129].

## 7.4 Comparison of experimental data with analytical predictions

We now compare the experimental values of the blob drift induced by the fluctuating potential dipole with the predictions of the derived analytical model. Since, experimentally, the blob size does not perfectly coincide with half of the distance between the dipole peaks entering in eq. (7.9), an intermediate value  $a = 1.5$  cm between the blob size contour at 60% and the dipole width is chosen. Deriving a scaling law with a different blob size and distance between the dipole peaks does not introduce significant changes in the results. Referring to the temperature  $T_e \approx 5$  eV measured in the mode region, we estimate  $c_s \approx 2.2 \times 10^4$  m/s. The velocity  $v_b$  can then be evaluated at each time step considering  $\delta n/n$  and  $B$  (hence  $L_{\parallel}$ ) the only position-dependent variables. We note that  $L_{\parallel}$  is the most significant parameter in the spatial variation of the estimated speed, increasing in the range [7 – 14] m, while  $\delta n/n$  is almost constant for most of the trajectory. The coefficient  $C$  is determined by assuming that the analytically estimated speed coincides with the experimental value at  $\tau = -28 \mu\text{s}$ . We note that we find  $C \approx 2 \times 10^{-13} \text{ C}^2 \text{ kg}^{-1} \text{ s}$ , which is three times the value we would obtain by calculating the conductivity as  $\sigma = \frac{ne^2}{m_e v_{eH}}$ , with  $v_{eH} = n_n \sigma_{eH} \sqrt{T_e/m_e} \approx 5 \times 10^5 \text{ s}^{-1}$ , considering a neutral density  $n_n \approx 5 \times 10^{18} \text{ m}^{-3}$ , an electron-neutral collision cross section  $\sigma_{eH} = 10^{-19} \text{ m}^2$  and a temperature  $T_e = 5$  eV.

The resulting values are indicated by the blue curve in Fig. 7.6 for the time window between  $-28 \mu\text{s}$  and  $-12 \mu\text{s}$ . Good agreement is found between the model and the experimentally measured contribution of the fluctuating potential dipole,  $v_{E \times B}^{\text{dip}}$  (red curve). We note that after  $\tau = -12 \mu\text{s}$ , the conditionally averaged sampled blob slows down, possibly because it breaks apart.

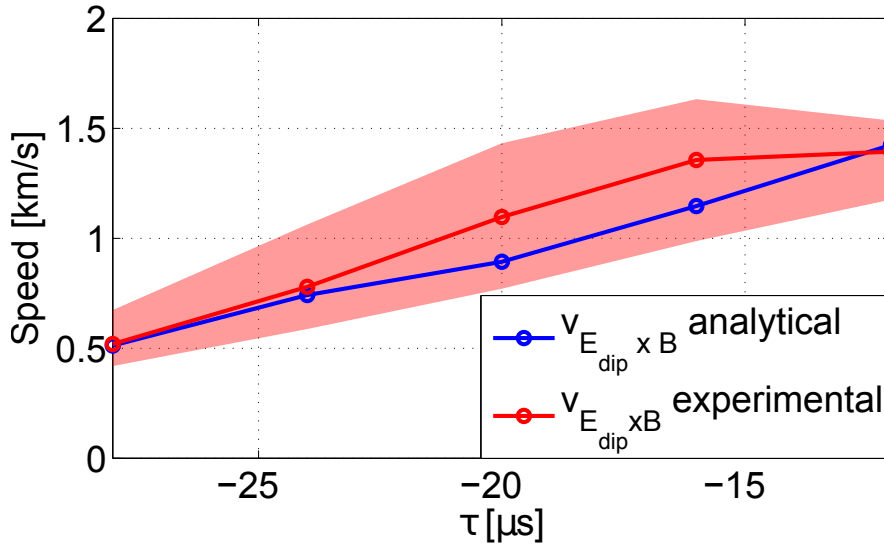


**Figure 7.6** | In blue, blob scaling speed evaluated during the acceleration phase with the introduced analytical model. In red, the measured contribution of the fluctuating blob dipole at the corresponding times.

## 7.5 Summary

The dynamics of plasma blobs in the proximity of a single null X-point has been investigated in this chapter. The experimental conditions suggest the presence of blobs that are not field aligned, nor connected to any material surface. The blob radial motion is determined by the  $\mathbf{E} \times \mathbf{B}$  flows associated to both the background electric field and the blob potential dipole. Their variation along the blob trajectory can explain the measured acceleration. An analytical model based on charge conservation has been developed to explain the potential dipole variation contributing to the blob speed. A crucial role is played by the field line geometry providing a parallel path for the short circuit of the blob vertical dipole, whose importance varies as the blob moves towards the X-point. A good quantitative agreement is found between the measured blob velocities and the blob speed scaling evaluated at the same time-steps. The analyzed data show that the blob dynamics is strongly influenced by the presence of an X-point. These results offer for the first time the possibility of benchmarking numerical simulations with experimental measurements of blob dynamics in the presence of X-point. Numerical studies on this topic are currently under development, focusing on the evolution of blobs in the presence of the same magnetic configuration implemented for our experiments [133].



## Conclusions

This thesis work is devoted to the investigation of plasma fluctuations in the TORPEX device, in magnetic field configurations of increasing complexity. These studies are motivated by the necessity of improving our understanding of turbulence dynamics in magnetically confined toroidal plasmas.

The design and installation of the in-vessel toroidal conductor on TORPEX was necessary to obtain a magnetic field configuration in which to perform plasma turbulence studies both in the presence of open field lines and closed flux surfaces. In the past years, TORPEX was operated as a simple magnetized torus (SMT), where open magnetic field lines result from the superposition of a small vertical magnetic component to the main toroidal field. Despite the presence of density gradients, magnetic field gradients and curvature, the SMT lacks a rotational transform. This was obtained in this work by introducing a poloidal magnetic field, generated driving a current in the toroidal conductor. The presence of a set of external toroidal coils available on TORPEX opens the possibility of exploring several magnetic configurations, from wall-limited and diverted plasmas, on which our studies are focused, to more advanced solutions with a second order null-point, corresponding to the snowflake divertor configuration investigated in recent years in tokamaks. The main technical considerations that led to the final design of the toroidal conductor system are introduced, including the range of accessible safety factors, the ohmic heating and the mechanical stresses on the system. A good quantitative agreement between measured and simulated poloidal magnetic field confirms the reliability of the new magnetic configurations that are accessible on TORPEX by implementing the toroidal conductor.

The main plasma features are detailed in the presence of quasi-concentric flux surfaces, obtained by setting the toroidal conductor at the center of the poloidal cross section. A clear change in the plasma shape is observed as the poloidal magnetic field is produced. Similarly to the SMT, the plasma breakdown is obtained by the acceleration of free electrons

at the electron cyclotron (EC) layer by injecting radio-frequency (RF) waves in the O-mode polarization scheme. As the first ionization of the neutral gas occurs, most of the power is absorbed by the fluid upper hybrid (UH) resonance, whose activation is guaranteed by the change in the polarization as the RF wave is reflected by the vacuum chamber walls. The density of the resulting plasmas is concentrated between the EC and the UH resonance layers, typically peaking in the region of higher poloidal field, close to the toroidal conductor.

A comprehensive exploration of the 2D profiles of ion saturation current indicates that the resulting steady-state plasma profiles are determined by the interplay of several control parameters, including the injected magnetron power, the EC resonance position, the neutral gas pressure and the toroidal conductor current. We also found the possibility to reach a regime of enhanced plasma production, with the activation of a further plasma source on the LFS, in which we observe an enhanced microwave power absorption of  $\approx 30\%$ , leading to a volumetric increase in the density of about 30%.

In the range of the explored control parameters, the orders of magnitude of the plasma density, temperature and particle confinement time are comparable to those measured in the optimized SMT. This can be ascribed to the presence of a number of particle loss channels, even if the closed magnetic field lines mitigate the parallel losses to the walls. We note that the optimization of the particle confinement time was not necessary for our purposes, as the measured value is comparable to the characteristic time of the measured plasma instabilities.

Electrostatic fluctuations are investigated in wall-limited plasmas with quasi-concentric flux surfaces, maximizing the poloidal symmetry of the resulting density profiles. The poloidal field intensity is varied by changing the toroidal conductor current in the range 450 – 750 A. Measurements of the power distribution on the spectral components of the coherent plasma fluctuations allows us to determine their spatial localization on the poloidal cross section. These present a clear ballooning feature, resulting to be poloidally asymmetric and concentrated over the bad magnetic field curvature region of the LFS. The identification of the dominant frequencies, in the  $\approx 20 - 30$  kHz range, is followed by a comprehensive characterization of the spectral features of the quasi-coherent modes. An extensive set of Langmuir probes is implemented to measure the poloidal and toroidal wave numbers, with the corresponding mode numbers. The results indicate field-aligned modes within the experimental uncertainties.

The first steps in the theoretical analysis of the nature of the measured quasi-coherent fluctuations are performed using a linear fluid code. For the explored range of experimental parameters, this indicates a much larger growth-rate for the ballooning modes with respect to drift waves, confirming the role of the magnetic field curvature as driving mechanism for the dominant instability.

The first explorations of TORPEX plasmas in magnetic geometries with a single null X-point are conducted. Several scenarios are tested, varying the toroidal magnetic field intensity to place the EC layer either inside or outside the confined region. The measured time-averaged density profiles show sensible changes that are consistent with the calculated poloidal field lines. Quasi-coherent modes with a dominant frequency below 10 kHz are identified in both

---

cases. Different dynamics of the fluctuations are observed according to the location of the plasma source. In particular, for the discharges in which the plasma is produced inside the closed flux surfaces, a more refined poloidal analysis is carried out in the X-point region. Quasi-coherent modes propagate in the counterclockwise direction around the last closed flux surface, where blobs detach and propagate radially outwards on the LFS.

The first investigations of the influence of the X-point position on the plasma profiles and particle fluxes are conducted in a particular magnetic configuration, optimized for the study of the dynamics of coherent structures in the presence of an X-point. The toroidal conductor is vertically moved close to the top of the vacuum vessel. The resulting poloidal field, together with the component obtained with the set of poloidal coils, produces an X-point on the LFS at  $z \approx 0$ , and a region of almost vertical field lines on the HFS. Here, the plasma is produced, with the consequent formation and radial propagation of poloidally localized structures. The vertical position of the X-point clearly influences the background patterns of plasma flows. 2D measurements of the time-averaged floating potential suggest a contribution of the background electric field in establishing  $\mathbf{E} \times \mathbf{B}$  drifts.

A detailed analysis of the propagation of plasma blobs is performed in the X-point region. The low values of vertical magnetic field suggest the presence of blobs that are not field aligned and not connected to any material surface. The measured blobs exhibit a fast acceleration while propagating towards the X-point. This can be explained in terms of the  $\mathbf{E} \times \mathbf{B}$  flow due to the background electric field, and to that associated with the blob potential dipole.

An analytical model based on charge conservation is developed to quantify the electric potential dipole contribution to the total blob speed. A crucial role is played by the change in the intensity of the poloidal field component along the blob trajectory close to the X-point. This results in a variation of the length of the parallel path for the short circuit of the blob vertical dipole. The measured blob velocities and the estimated blob speed scaling are in good quantitative agreement. This constitutes the first direct observation of the effect of a single-null X-point on plasma blob dynamics and offers for the first time the possibility of benchmarking numerical simulations against experimental measurements. The presented results can contribute to the understanding of transport processes in fusion relevant plasmas with diverted configurations.

Complementary experiments could be carried out in the future to obtain deeper insight into the topics studied during this thesis. It would be worth investigating in more details the enhanced plasma production observed during the exploration of the control parameters, of interest for a complete determination of the plasma production mechanisms. The understanding of the physical mechanism behind this regime could open new plasma scenarios, in a range of control parameters still unexplored, where turbulence presents different features with respect to those reported herein. The characterization of electrostatic fluctuations in concentric flux surfaces can be completed by varying control parameters, such as the neutral pressure and the gas type. The benchmarking of the non-linear version of the implemented fluid code against the experimental results is foreseen.

More generally, the installation of the toroidal conductor on TORPEX opens a wide range

## **Chapter 8. Conclusions**

---

of research lines that can be pursued. Among these, we just mention the study of plasma fluctuations in the presence of a second-order null magnetic snowflake, and the investigation of fast ion interaction with turbulence in configurations with a poloidal magnetic field.



# Appendix A

## Neutral pressure measurements

### A.1 TORPEX gauge calibration curves

Two of the gauges used on TORPEX for the neutral pressure measurements provide gas-type dependent values. These are the Compact Cold Cathode Gauge IKR 251, indicated in Fig. A.1 (a), and the Compact Full Range Gauge PKR 251, shown in Fig. A.1 (b)<sup>1</sup>. In Fig. A.2-A.3 we show the calibration curves available on the corresponding operating instructions. In the range below  $10^{-5}$  mbar, the pressure indication is linear. For gases other than air, the pressure can be determined by means of the following conversion expression:

$$p_{\text{eff}} = K p_{\text{meas}}, \tag{A.1}$$

with the  $K$  for the different gases indicated in Tab. A.1.

Gas type	Xe	Kr	Ar	H <sub>2</sub>	Ne	He
$K$	0.4	0.5	0.8	2.4	4.1	5.9

**Table A.1** | Plasma parameters referring to the examples in Fig. 1.4.

We note that the pressure measured with the gauge IKR 251 corresponds to that upstream the turbo pump, as can be observed in Fig. A.1 (a). This is generally lower than that inside the vacuum vessel. Therefore, the gauge PKR 251 is typically used as reference.

<sup>1</sup>These corresponds to the *pressure 2* and *pressure 4* indicators on the TORPEX control panel, respectively.

## Appendix A. Neutral pressure measurements

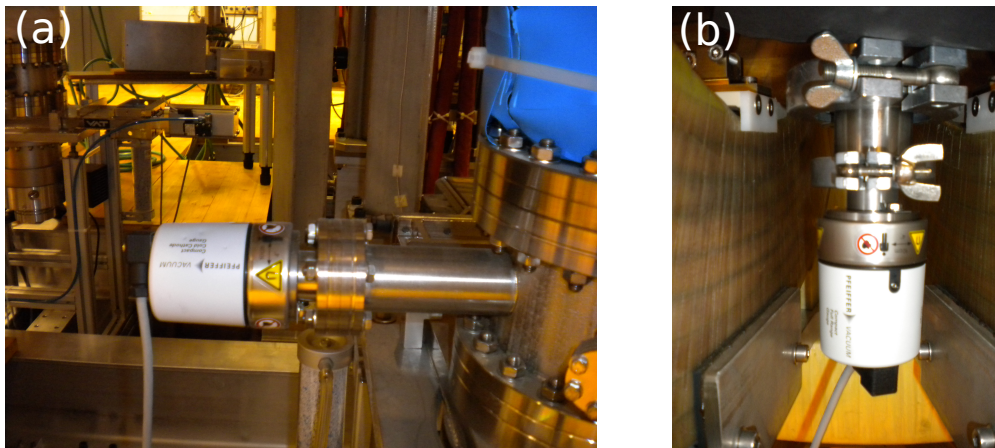


**Figure A.1** | (a) Photograph of the Compact Cold Cathode Gauge IKR 251. (b) Photograph of the Compact Full Range Gauge PKR 251.

Indicated pressure (gauge calibrated for air)

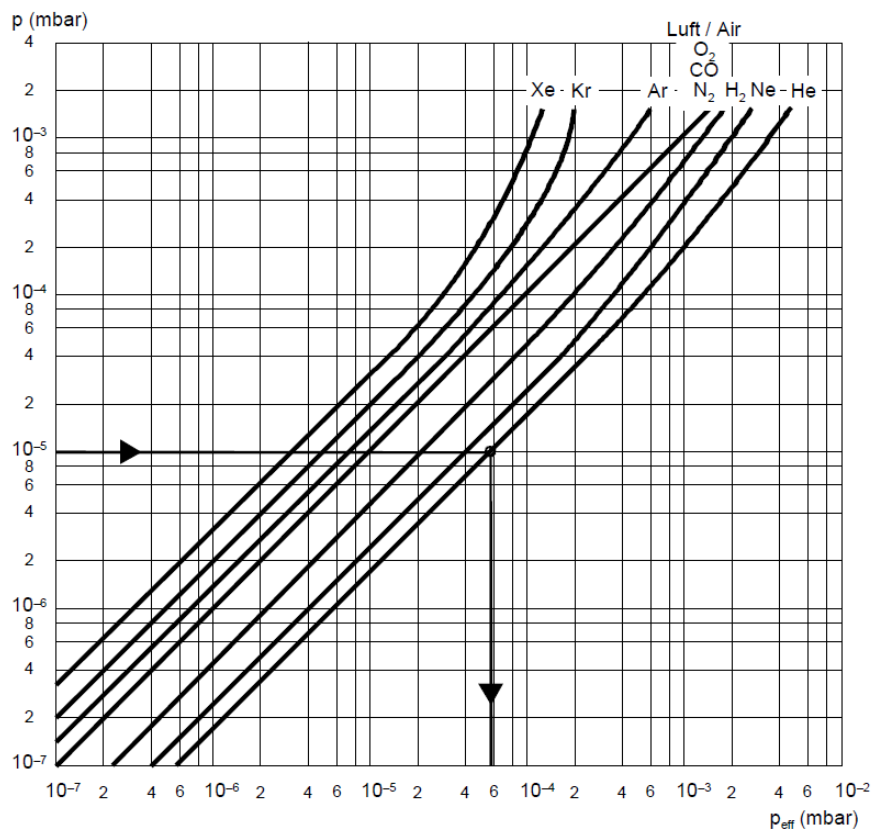


**Figure A.2** | Calibration curves for the Compact Cold Cathode Gauge IKR 251.

Indicated pressure (gauge calibrated for air)

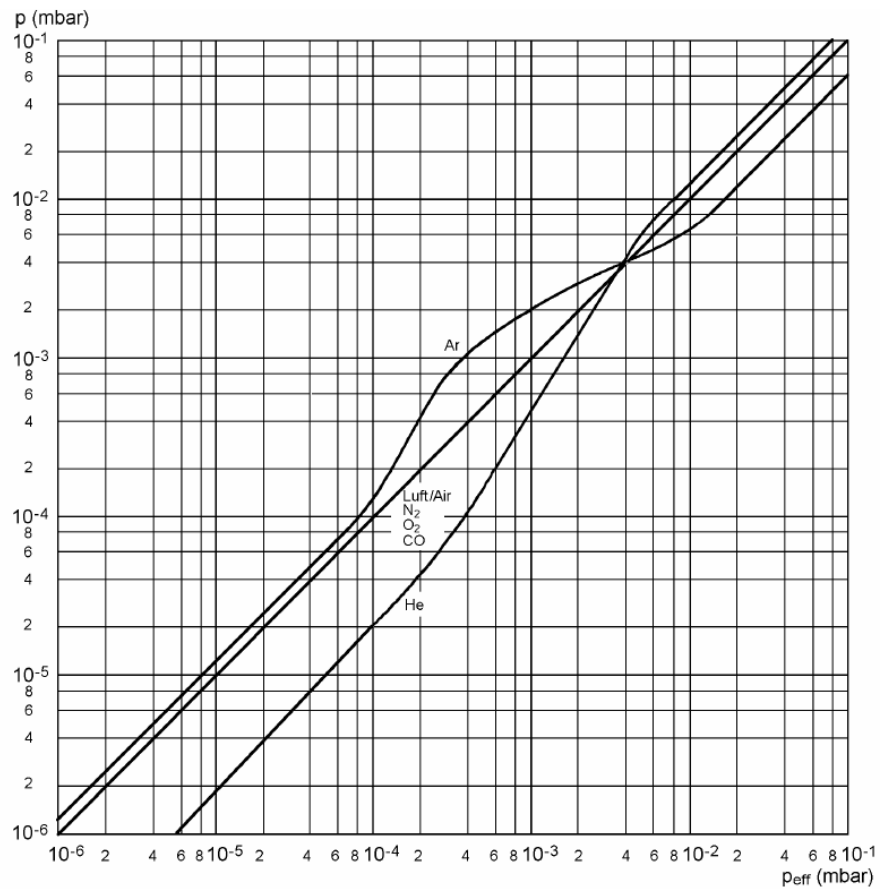


**Figure A.3** | Calibration curves for the Compact Full Range Gauge PKR 251.



# Appendix B

## Toroidal conductor technical notes

### B.1 Procedure for the TC vertical displacement or disassembling

In this section, we summarize the procedure to change the vertical position of the TC and to disassemble it.

1. Increase the pressure inside TORPEX up to the atmospheric value. At this point, the vacuum safe covers of the horizontal and vertical supports can be removed.
2. Disconnect the cables of the power supply from the top of the feed-through, as indicated in Fig. B.1 (a).

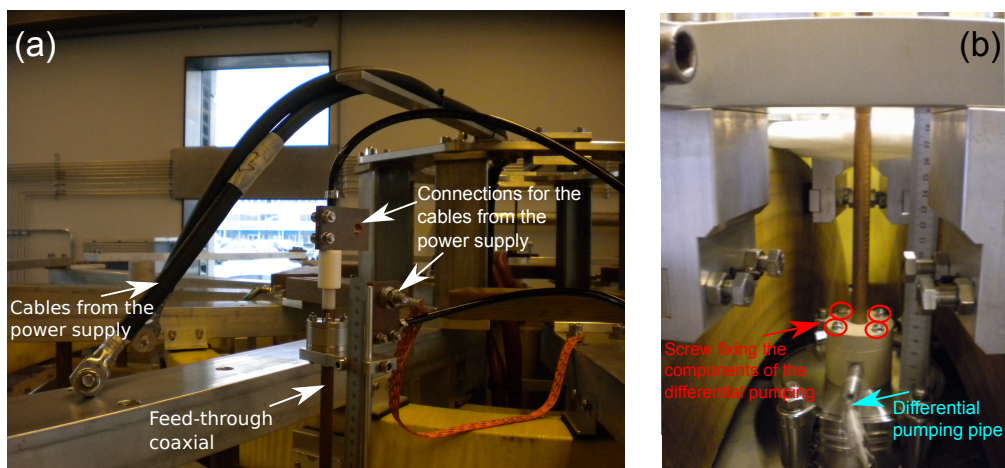


**Figure B.1** | (a) Top view of TORPEX, with the cables of the power supply disconnected from feed-through. (b) Photograph of the vacuum differential pumping of the feed-through, indicated with the cyan arrow. The screws fixing it are indicated with the red arrows.

## Appendix B. Toroidal conductor technical notes

3. Remove the screws fixing the feed-through components with the vacuum differential pumping and disconnect the differential pumping pipe, as indicated in Fig. B.1 (b) with the red and cyan arrows, respectively.
4. Remove the lateral supports. First, move the screw fixing the lateral position as close to the flange as possible, at the position indicated in Fig. B.2 (a) with the red arrow. At this point, the clamps of the flange can be removed while the support is sustained. Then, the support can be pulled outward as far as possible, so that there is enough space between the support and the vacuum vessel to remove the two screws fixing the stainless steel wire to the support, shown in Fig. B.2 (a). Once the lateral supports are removed, the four lateral wires can pass through the small aperture on the junction, as indicated in Fig. B.2 (b) for the vertical support.

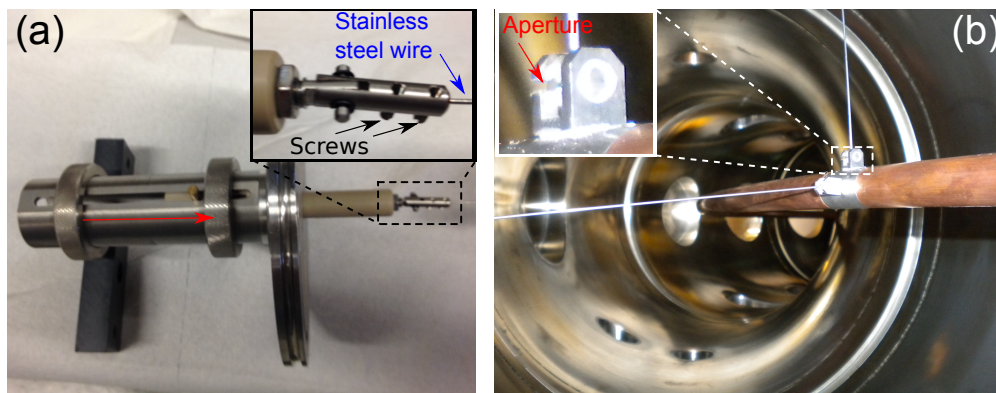


**Figure B.2** | (a) Picture of one lateral support with the red arrow indicating the position where the supporting screw has to be set. Zoomed view of the two screws fixing the stainless steel wire. (b) Photograph of the TC inside TORPEX, with a detail of the part of the junction supporting the stainless steel wire. The latter can be removed through the aperture indicated in the inset.

5. As the absence of any diagnostic along the vertical path of the TC is verified (in particular HEXTIP), it is possible to start to pull the system up. The easiest procedure consists in doing steps of a few vertical centimeters, with one person pushing the TC up at the locations of the vertical supports, and a second person on the top of TORPEX to progressively adjust the vertical position of the sustaining screws. In Fig. B.3 (a) we show a photograph of the TC on the top of vacuum vessel, with an image in Fig. B.3 (b) of how the feed-through would look like once the system is pulled up is shown.

At this point the vacuum vessel can be sealed, fixing the covers of the vertical supports, and putting back in place the differential pumping of the TC feed-through.

It can occur that at least one of the four arcs constituting the TC must be removed to completely open one of the mobile sectors of TORPEX. Before proceeding, all the openings of the turbo pumps on the bottom of the vacuum vessel must be covered to avoid that anything could fall inside. Then, the pins indicated in Fig. B.3 (a) that fix the copper arc on the junction must be removed using the tool shown in Fig. B.4 (a). Consequently, the tool indicated in Fig. B.4 (b) is

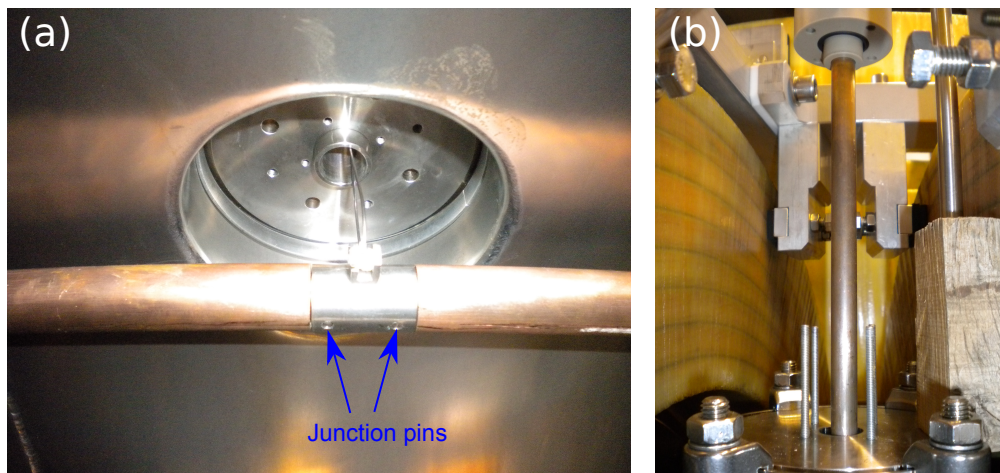


**Figure B.3** | (a) Photograph of the TC on the top of the vacuum vessel. (b) Photograph of the feed-through once the system is pulled up.

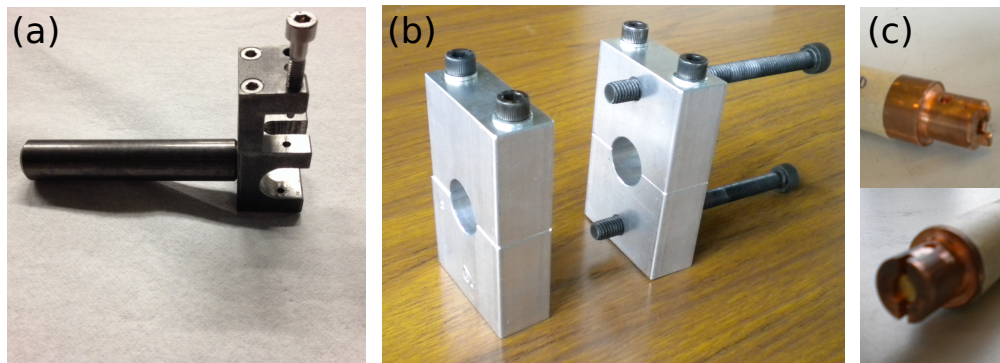


**Figure B.4** | (a) Tool to insert or remove the pins to fix the arc extremities on the junctions, indicated in Fig. B.3 (c). (b) Photograph of the tool used to remove the extremity of the arcs constituting the TC from their junctions. (c) Photographs of the two extremities of an arc.

used to push the arc out of the junction. We note that each arc is not symmetric, namely the two extremities are different, as shown in Fig. B.4 (c)<sup>1</sup>.

## B.2 Remote control system

As the PS is manually switched on, it can be remotely controlled with the TORPEX Control Graphical User Interface (GUI) through the electronic module showed in Fig. B.5 (a). The switch between *Consigne* and *Consigne Gated* indicated on the top in Fig. B.5 (b) allows to choose between a voltage signal following a wave form provided in input<sup>2</sup>, or a gated signal *On-Off*. The buttons shown in Fig. B.6 (a) are used to remotely operate the electronic unit, according to the logical diagram of the commands illustrated in Fig. B.6 (b). In Fig. B.6 (c) we

<sup>1</sup>Once the arc is removed, note the junction corresponding to each extremity.

<sup>2</sup>This has to be implemented at the software level on the TORPEX Control.

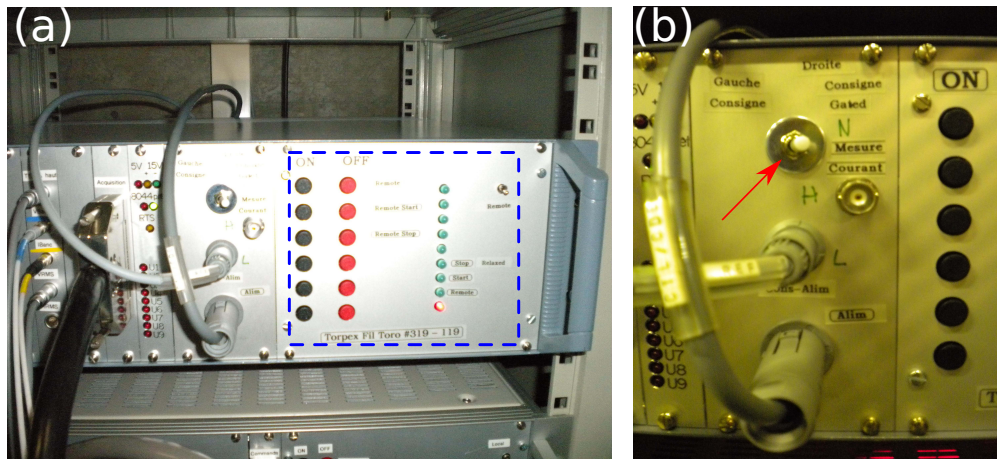


**Figure B.5** | (a) Electronic module for the remote control of the TC power supply. (b) Detail of the switch to set a gated voltage signal or following a specific wave form provided in input.

indicate the corresponding operations on the TORPEX GUI. The sequence of the commands to operate the system is indicated in the following.

### B.2.1 Activate

1. Switching on the remote control: both the lights of the *Remote* LED and the *Stop relaxed* LED switch on, meaning that now the *STOP* function is not activated.
2. Activating the power supply to be able to receive the trigger (charging some capacitors): the *Start* LED is switched on.

### B.2.2 Deactivate

3. Setting the state of the system back to the *REMOTE* state of the logical diagram shown in Fig. B.6 (b), corresponding to the *Enable other actions* of the GUI in Fig. B.6 (c), which means that the *STOP* function can be activated now to dis-activate the power supply (step number 4.).
4. Dis-activating the power supply, so that the *stop-relaxed* LED is switched off.
5. Setting the state of the system back to the *REMOTE* state of the logical diagram, corresponding to the *Enable other actions* of the GUI. The *stop-relaxed* LED is back switched on.
6. As both the *START* and *STOP* of the GUI are in the *Enable other actions* state, corresponding to the *REMOTE* state of the logical diagram, the remote control can be switched off.



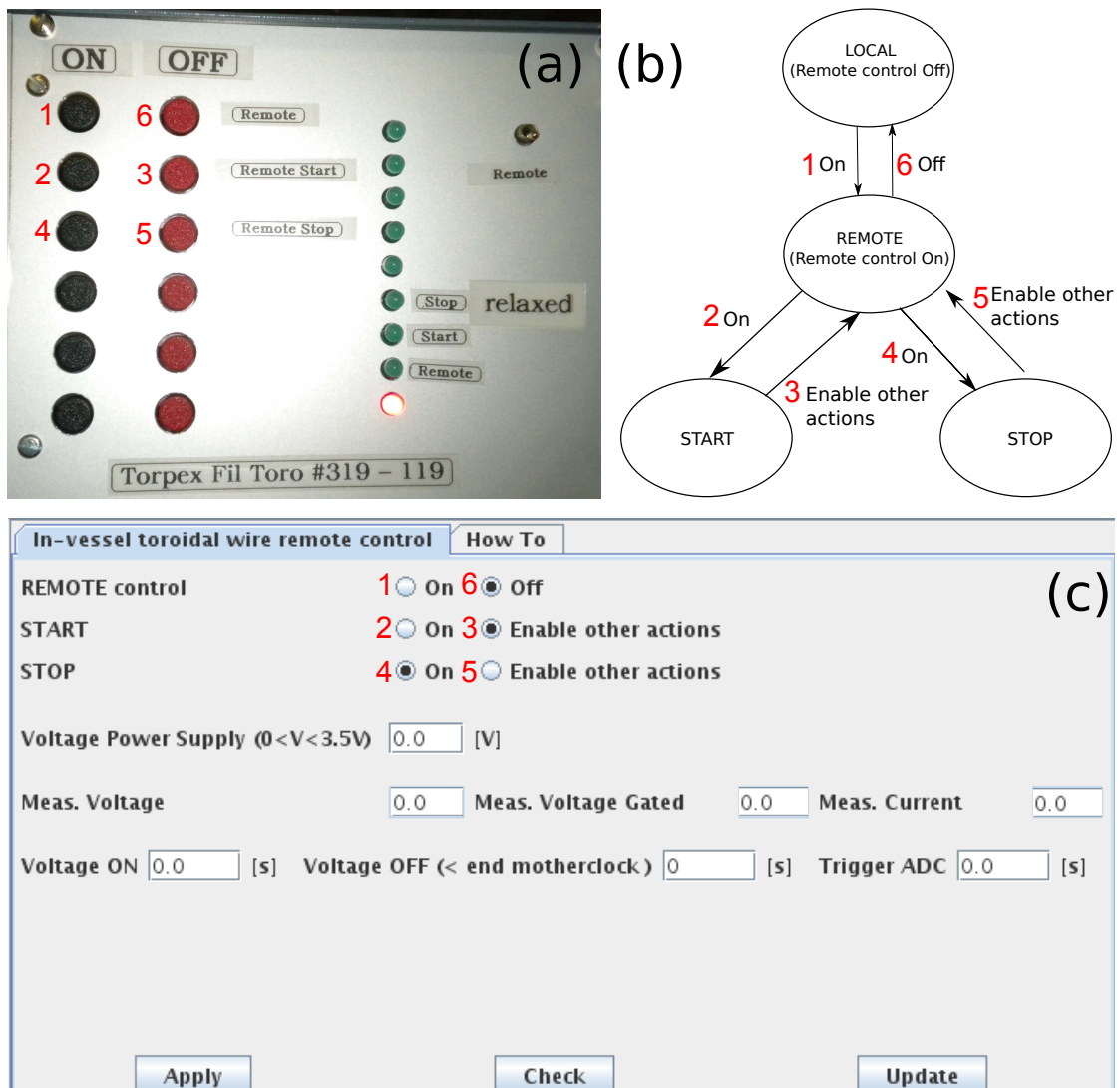


**Figure B.6** | (a) Detail of the electronic unit for the remote control of the power supply. (b) Logical diagram of the commands. (c) GUI for the power supply remote control.

### B.2.3 Operation

The voltage of the PS corresponds to 8 times the value set on the *Voltage Power Supply* field. With the current total resistance of the circuit, a current of approximately 630 A is obtained with an input value of  $V=2.4$  V on the GUI. Then the *Apply-Check-Update* buttons have to be selected to apply the value on the DAQ of the remote control, to check if the value is properly set and update the actual value on the GUI panel (*Meas. Voltage*)<sup>3</sup>, respectively. Then the start and the end of the current profile has to be set on *Voltage ON [s]* and *Voltage OFF [s]*, considering  $t = 0$ s that of the mother-clock. Note that the *Voltage OFF [s]* value has to be within the end of the mother-clock. As the discharge is executed, this value is read by the slave.

<sup>3</sup>The *Meas. Voltage Gated* and *Meas. Current* are meaningless up to now.

### B.2.4 Control word programming

The programmable timer of the electronic module consists of three independent *Counters*, indicated in Fig B.7 (a) with *Counter#0*, *Counter#1* and *Counter#2*. The communication with the timer is performed by control word programming, providing a number for each counter to define its operation mode<sup>4</sup>. Our command is [48, 112, 184], which corresponds to [00110000, 01110000, 10111000] in binary. This can be decoded using the scheme of the control word programming shown in Fig B.7 (b|c). The resulting commands are:

- 00110000 : *Counter#0*: Reading/Loading of LSB Followed by MSB, Mode 0, Binary Count
- 01110000 : *Counter#1*: Reading/Loading of LSB Followed by MSB, Mode 0, Binary Count (B.1)
- 10111000 : *Counter#2*: Reading/Loading of LSB Followed by MSB, Mode 4, Binary Count

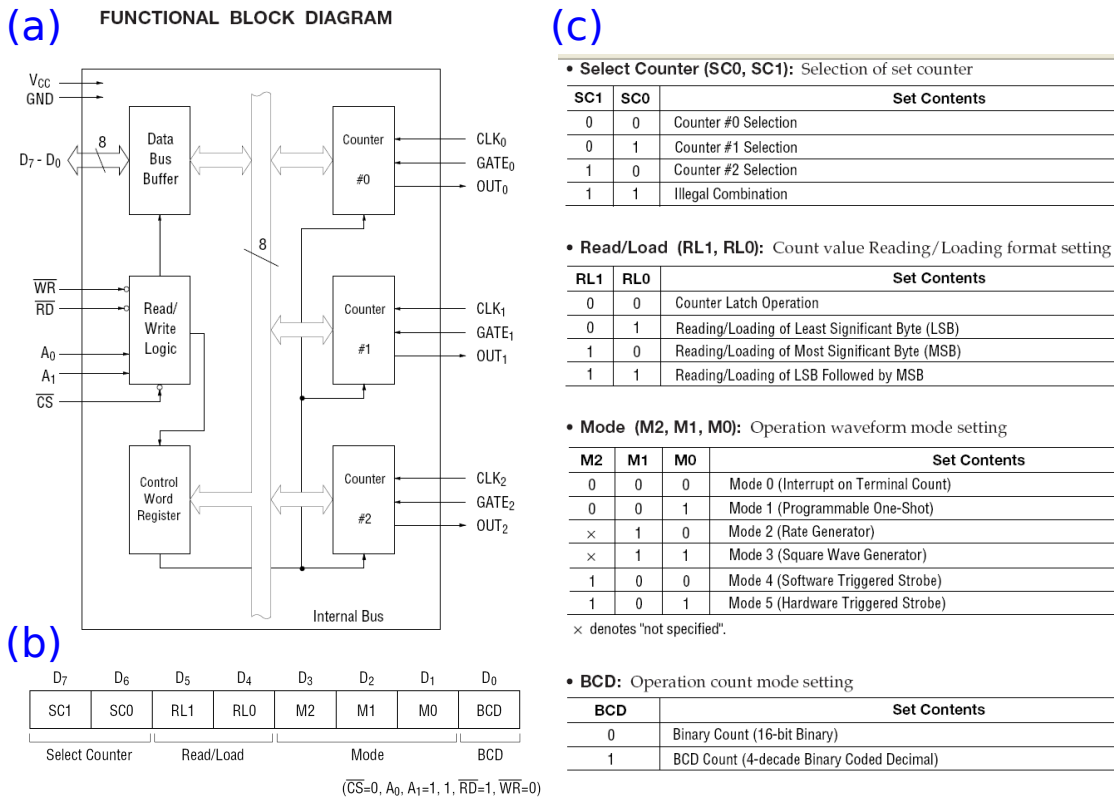


**Figure B.7** | (a) Functional block diagram of the timer. (b) Scheme of the control word programming. (c) Legend of the information provided with by the control word programming.

We set *Counter#0* and *Counter#1* on Mode 0, so that they provide together the *ON-OFF gated* mode of current profile, as shown in the simplified schematic of Fig. B.8. The *Counter#2* is on Mode 4, corresponding to the *trigger*.

<sup>4</sup>This can be found in the file named *PIO\_ITWIRE\_template.xml*.

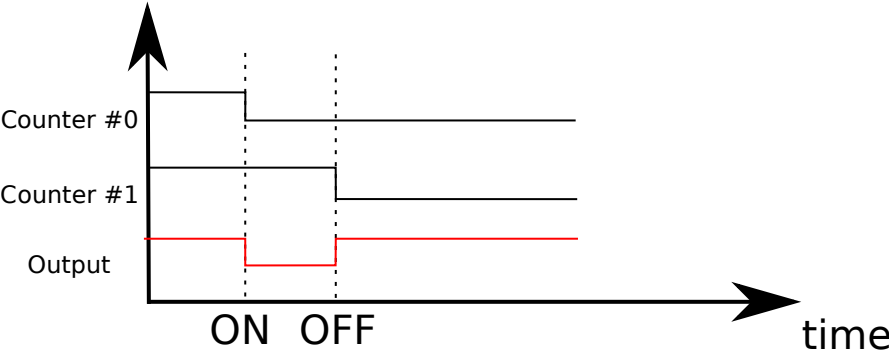
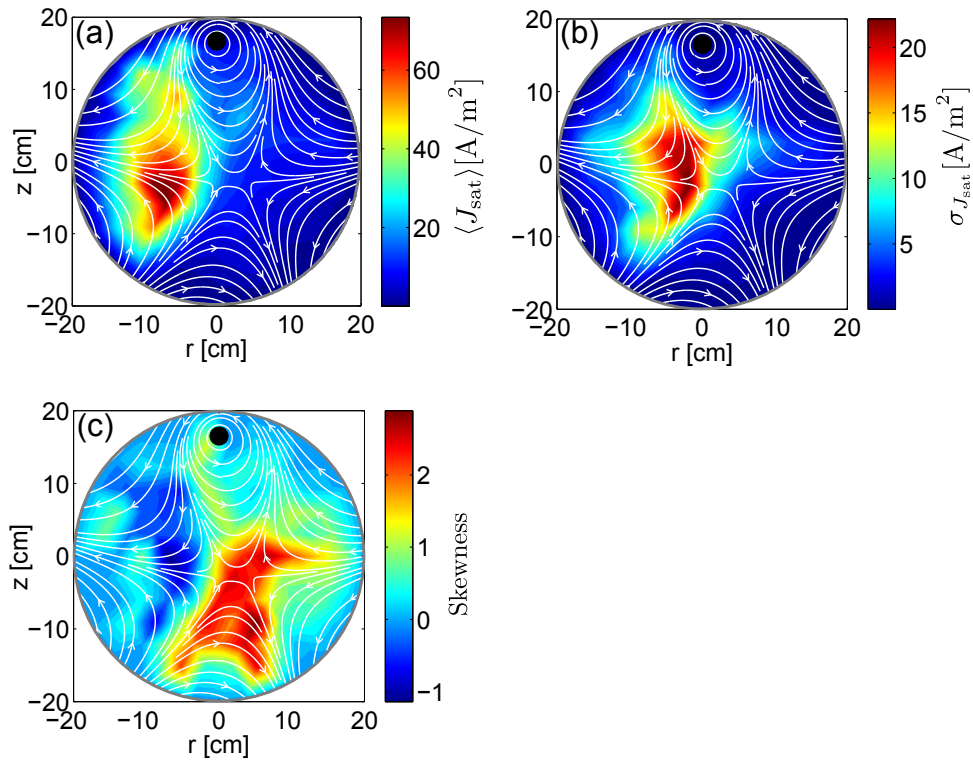


Figure B.8 | Simplified schematic of the ON-OFF mode provided by the first two counters.



## Magnetic snowflake

The experimental feasibility of a second order null point (snowflake) is verified on TORPEX. The plasma  $J_{\text{sat}}$  profiles are shown in Fig. C.1, driving a toroidal conductor current of  $\approx 900$  A. The implemented toroidal field of  $\approx 750$  Gauss corresponds to an electron cyclotron resonance layer at  $r_{\text{EC}} \approx -14$  cm. The produced plasma is mostly localized on the HFS region of open flux surfaces. We can observe a high value of skewness on the snowflake legs on the LFS. Further investigations are foreseen in this configuration.



**Figure C.1** | (a) Time averaged  $J_{\text{sat}}$  measurements. (b)  $J_{\text{sat}}$  standard deviation. (c)  $J_{\text{sat}}$  skewness. Discharge #66282.



# Acronyms

**1D** one-dimensional.

**2D** two-dimensional.

**3D** three-dimensional.

**AC** alternating current.

**AIA** Atmospheric Imaging Assembly.

**Ar** argon.

**CAS** conditional average sampling.

**Cu** copper.

**D** deuterium.

**DC** direct current.

**DTFT** discrete-time Fourier transform.

**DW** drift wave.

**EC** electron cyclotron.

**ELM** edge-localized modes.

**EM** electromagnetic.

**ERCH** electron cyclotron resonance heating.

**FAPA** field-aligned probe array.

## Acronyms

---

**FMLP** flash-mounted Langmuir probe.

**FRIPLE** five-tip triple probe.

**FWHM** full width at half maximum.

**GEA** gridded energy analyzer.

**GPI** gas puff imaging.

**GUI** Graphical User Interface.

**H<sub>2</sub>** hydrogen.

**He** helium.

**HEX-MT** HEXTIP movable twins.

**HEXTIP** hexagonal turbulence imaging probe.

**HFS** high field side.

**ICF** Inertial Confinement Fusion.

**ICRH** ion cyclotron resonance heating.

**JET** Joint European Torus.

**LFS** low field side.

**LP** Langmuir probe.

**MCF** Magnetic Confinement Fusion.

**NBI** neutral beam injection.

**Ne** neon.

**NIF** National Ignition Facility.

**OFE** oblique field electrode.

**O-mode** ordinary-mode.

**PDF** probability distribution function.

**PR** poloidal row.

**PS** power supply.



- PSD** power spectral density.
- RF** radio-frequency.
- RFX** Reverse-Field eXperiment.
- SDO** Solar Dynamics Observatory.
- SDR** statistical dispersion relation.
- SMT** simple magnetized torus.
- SOL** scrape-off layer.
- TC** toroidal copper conductor.
- TFC** toroidal field coils.
- TORPEX** TORoidal Plasma EXperiment.
- UH** upper hybrid.
- VFC** vertical field coils.
- X-mode** extraordinary-mode.



# Repeatedly used symbols

$a_{ec}^{eff}$  Effective diameter of the feed-through external conductor.

$a_{ec}^i$  Inner diameter of the feed-through external conductor.

$a_{ec}^o$  Outer diameter of the feed-through external conductor.

$a_{ic}^{eff}$  Effective diameter of the feed-through internal conductor.

$a_{ic}^i$  Inner diameter of the feed-through internal conductor.

$a_{ic}^o$  Outer diameter of the feed-through internal conductor.

$\alpha_{Cu}$  Copper linear thermal expansion.

$a$  Toroidal conductor section radius.

$A$  Toroidal conductor surface.

$\beta$  Thermal over magnetic pressure ratio.

$R_0$  TORPEX major radius.

$a_0$  TORPEX minor radius.

$R$  Radial distance from the center of the torus.

$c_s$  Ion sound speed.

$c_{s,Cu}$  Copper specific heat.

$d_{Cu}$  Copper density.

$f_{CE}$  Electron cyclotron frequency.

$f_{CI}$  Ion cyclotron frequency.

## Repeatedly used symbols

---

$F_h$  Hoop force.

$f_{pe}$  Electron plasma frequency.

$I_{ft}$  Toroidal conductor flat-top current.

$L$  Toroidal conductor inductance.

$x$  Plasma ionization degree.

$I_{pr}$  LP measured current.

$I_{sat}^e$  Electron saturation current.

$I_{sat}^i$  Ion saturation current.

$I_{TC}$  In-vessel toroidal conductor.

$J_{sat}$  Ion saturation current density.

$\tilde{J}_{sat}$  Ion saturation current density fluctuations.

$k_{Cu}$  Copper resistivity thermal coefficient.

$\lambda_D$  Debye length.

$L_n$  Density gradient scale length.

$\ell$  Toroidal conductor length.

$M$  Toroidal conductor mass.

$n_e$  Electron density.

$P_{rf}^{HP}$  TORPEX pulsed high power radio-frequency.

$P_{rf}^{LP}$  TORPEX continuous low power radio-frequency.

$n_n$  TORPEX neutral gas density.

$\nu_{ee}$  Electron-electron frequency collision.

$\nu_{eH}$  Electron-neutral collision frequency.

$\nu_{iH}$  Ion-neutral collision frequency.

$p_n$  TORPEX neutral gas pressure.

$B_\theta$  TORPEX poloidal field.

$\rho_{\text{Cu}}^*$  Copper resistivity at 273 K.

$\rho_e$  Electron Larmor radius.

$\rho_i$  Ion Larmor radius.

$\rho_s$  Ion sound radius.

$R$  Toroidal conductor resistance.

$q$  Safety factor.

$S$  Toroidal conductor section.

$T_e$  Electron temperature.

$T_i$  Ion temperature.

$B_\phi$  TORPEX toroidal field.

$B_{\phi,0}$  TORPEX toroidal field at  $r=0$  cm.

$B_\phi^{\text{inv}}$  TORPEX toroidal in the clock-wise direction from the top.

$B_\phi^{\text{nor}}$  TORPEX toroidal in the counter clock-wise direction from the top.

$B_z$  TORPEX magnetic field generated by the vertical field coils.

$V_{\text{fl}}$  Plasma floating potential.

$V_{\text{pl}}$  Plasma electrostatic potential.

$V_{\text{pr}}$  Probe electrostatic potential.

$v_{\text{th,e}}$  Electron thermal velocity.

$v_{\text{th,i}}$  Ion thermal velocity.



# Bibliography

- [1] <http://sdo.gsfc.nasa.gov/data/>.
- [2] <http://www.helioviewer.org/>.
- [3] P. Foukal. *Solar Astrophysics*. John Wiley & Sons, 1990.
- [4] A. Eddington. The internal constitution of stars. *The Observatory*, XLIII:341–358, 1920.
- [5] S. Atzeni and J. Meyer-Ter-Vehn. *The Physics of Inertial Fusion*. Oxford Science Publications, 2009.
- [6] F.F. Chen. *Introduction to Plasma Physics and Controlled Fusion*. Springer, 2006.
- [7] W. Baumjohann and R.A. Treumann. *Basic Space Plasma Physics*. Imperial College Press, 1996.
- [8] T.J. Boyd and J.J. Sanderson. *The Physics of Plasmas*. Cambridge University Press, 2003.
- [9] M.A. Lieberman and A.J. Lichtenberg. *Principles of Plasma Discharges and Material Processing*. John Wiley & Sons, 2005.
- [10] R.F. Post. Controlled fusion research — an application of the physics of high temperature plasmas. *Review of Modern Physics*, 28:338, 1956.
- [11] G.H. Miller et al. The National Ignition Facility: enabling fusion ignition for the 21st century. *Nuclear Fusion*, 44:S228, 2004.
- [12] O.A. Hurricane et al. Fuel gain exceeding unity in an inertially confined fusion implosion. *Nature*, 506:343–348, 2014.
- [13] <https://lasers.llnl.gov/>.
- [14] <http://www.ccfе.ac.uk/>.

## Bibliography

---

- [15] H.-S. Bosch et al. Technical challenges in the construction of the steady-state stellarator Wendelstein 7-X. *Nuclear Fusion*, 53:126001, 2013.
- [16] Max-Planck Institut für Plasmaphysik Matthias W Hirsch.
- [17] J. Wesson. *Tokamaks*. Oxford University Press, Cambridge, 2004.
- [18] L.E. Zakharov et al. Understanding disruptions in tokamaks. *Physics of Plasmas*, 19:055703, 2012.
- [19] V.S. Strelkov. History of the T-10 tokamak: Creation and development. *Plasma Physics Reports*, 27:819–824, 2001.
- [20] M. Keilhacker et al. High fusion performance from deuterium-tritium plasmas in JET. *Nuclear Fusion*, 39:209, 1999.
- [21] K. Ikeda et al. Progress in the ITER physics basis. *Nuclear Fusion*, 47(6):S1–S413, 2007.
- [22] A. Loarte et al. Progress in the ITER physics basis; Chapter 4: Power and particle control. *Nuclear Fusion*, 47:203, 2007.
- [23] B. Lipschultz et al. Plasma surface interaction, scrape-off layer and divertor physics: implications for ITER. *Nuclear Fusion*, 47:1189–1205, 2007.
- [24] V.A. Soukhanovskii et al. Divertor heat flux mitigation in high-performance H-mode discharges in the national spherical torus experiment. *Nuclear Fusion*, 49:095025, 2009.
- [25] M.S. Tillack et al. Summary of the ARIES town meeting: 'Edge plasma physics and plasma material interactions in the fusion power plant regime'. *Nuclear Fusion*, 53:027003, 2013.
- [26] [www.eurofusion.org](http://www.eurofusion.org).
- [27] A.J. Wootton et al. Fluctuations and anomalous transport in tokamaks. *Physics of Fluids B*, 2:2879, 1990.
- [28] S.J. Zweben et al. Edge turbulence measurements in toroidal fusion devices. *Plasma Physics Controlled Fusion*, 49:S1–S23, 2007.
- [29] J.A. Boedo. Edge turbulence and SOL transport in tokamaks. *Journal of Nuclear Materials*, 390:29–37, 2009.
- [30] S. Krasheninnikov. Multifaceted physics of edge plasma in magnetic fusion devices. *Plasma Physics Controlled Fusion*, 53:074017, 2011.
- [31] N.J. Lopes Cardozo. Perturbative transport studies in fusion plasmas. *Plasma Physics Controlled Fusion*, 37:799–852, 1995.
- [32] W. Horton. Drift waves and transport. *Review of Modern Physics*, 71:735–778, 1999.



- 
- [33] D.A. D'Ippolito et al. Convective transport by intermittent blob-filaments: Comparison of theory and experiment. *Physics of Plasmas*, 18:060501, 2011.
- [34] N. Vianello et al. Direct observation of current in type-i edge-localized-mode filaments on the ASDEX upgrade tokamak. *Physical Review Letters*, 106:125002, 2011.
- [35] C. Silva et al. Reciprocating probe measurements of ELM filaments on JET. *Plasma Physics Controlled Fusion*, 51:105001, 2009.
- [36] A. Kirk et al. Evolution of filament structures during Edge-Localized Modes in the MAST tokamak. *Physical Review Letters*, 96:185001, 2006.
- [37] R.J. Maqueda et al. Primary edge localized mode filament structure in the National Spherical Torus Experiment. *Physics of Plasmas*, 16:056117, 2009.
- [38] W. Fundamenski et al. A model of ELM filament energy evolution due to parallel losses. *Plasma Physics Controlled Fusion*, 48:109, 2006.
- [39] P.B. Snyder et al. Progress in the peeling-ballooning model of the edge localized modes: Numerical studies of nonlinear dynamics. *Physics of Plasmas*, 12:056115, 2005.
- [40] A. Fasoli et al. Electrostatic ion cyclotron waves in a steady-state toroidal plasma. *Plasma Physics Controlled Fusion*, 31:313, 1989.
- [41] C. Riccardi et al. Experimental analysis of drift waves destabilization in a toroidal plasma. *Physics of Plasmas*, 4:3749, 1997.
- [42] C. Riccardi and Å. Fredriksen. Waves and coherent structures in the turbulent plasma of a simple magnetized torus. *Physics of Plasmas*, 8:199, 2001.
- [43] A. Fasoli et al. Electrostatic turbulence and transport in a simple magnetized plasma. *Physics of Plasmas*, 13:055902, 2006.
- [44] K.W. Gentle and H. He. Texas Helimak. *Plasma Science and Technology*, 10:284–289, 2008.
- [45] T. Pierre. Toroidal magnetized plasma device with sheared magnetic field lines using an internal ring conductor. *Review of Scientific Instruments*, 84:013504, 2013.
- [46] A. Fasoli et al. Electrostatic instabilities, turbulence and fast ion interactions in the TORPEX device. *Plasma Physics Controlled Fusion*, 52:124020, 2010.
- [47] S.T. Bramwell et al. Universality of rare fluctuations in turbulence and critical phenomena. *Nature*, 396:552–554, 1998.
- [48] G. Falkovich et al. Particles and fields in fluid turbulence. *Review of Modern Physics*, 73:913–975, 2001.

## Bibliography

---

- [49] G.L. Eyink and K.R. Sreenivasan. Onsager and the theory of hydrodynamic turbulence. *Review of Modern Physics*, 78:87–135, 2006.
- [50] H. Faist and B. Eckhardt. Traveling waves in pipe flow. *Physical Review Letters*, 91:224502–1, 2003.
- [51] D.C. Alix et al. Acoustic characterization of wake vortices in ground effect. *43rd AIAA Aerospace Sciences Meeting and Exhibit*, 2005.
- [52] M. Trevethan et al. Turbulence and turbulent flux events in a small estuary. *Environmental Fluid Mechanics*, 10:345–368, 2010.
- [53] R. Narasimha et al. Turbulent flux events in a nearly neutral atmospheric boundary layer. *Philosophical Transactions of the Royal Society A: Mathematical, Physical and Engineering Sciences*, 365:841–858, 2007.
- [54] R.Z. Sagdeev. The 1976 oppenheimer lectures: Critical problems in plasma astrophysics. i. turbulence and nonlinear waves. *Review of Modern Physics*, 51:1–9, 1979.
- [55] S.A. Balbus et al. Instability, turbulence, and enhanced transport in accretion disks. *Review of Modern Physics*, 70:1–53, 1998.
- [56] W.H. Matthaeus et al. Coronal heating by magnetohydrodynamic turbulence driven by reflected low-frequency waves. *The Astrophysical Journal*, 523:L93–L96, 1999.
- [57] I. Furno et al. Plasma turbulence, suprathreshold ion dynamics and code validation on the basic plasma physics device TORPEX. *Journal of Plasma Physics*, 2015.
- [58] S.H. Muller et al. Effects of a vertical magnetic field on particle confinement in a magnetized plasma torus. *Physical Review Letters*, 93:165003, 2004.
- [59] S.H. Muller et al. Basic turbulence studies on TORPEX and challenges in the theory-experiment comparison. *Physics of Plasmas*, 12:090906, 2005.
- [60] G. Plyushchev. *Interaction of Supra-Thermal Ions with Turbulence in a Magnetized Toroidal Plasma*. PhD thesis, EPFL, CRPP, 2009. [infoscience.epfl.ch/record/141951/files/EPFL\\_TH4543.pdf](http://infoscience.epfl.ch/record/141951/files/EPFL_TH4543.pdf).
- [61] F. Avino et al. The new TORPEX in-vessel toroidal conductor for the generation of a poloidal magnetic field. *Review of Scientific Instruments*, 85:033506, 2014.
- [62] M. Podesta et al. Plasma production by low-field side injection of electron cyclotron waves in a simple magnetized torus. *Plasma Physics Controlled Fusion*, 47:1989–2002, 2005.
- [63] K. Rypdal et al. Microwave-plasma in a simple magnetized torus. *Physics of Plasmas*, 4:1468, 1997.
- [64] I.H. Hutchinson. *Principles of Plasma Diagnostics*. Cambridge University Press, 2002.

- [65] P.C. Stangeby. *The Plasma Boundary of Magnetic Fusion Devices*. Institute of Physics Publishing Bristol and Philadelphia, 2000.
- [66] K-U. Riemann. The Bohm criterion and sheath formation. *Journal of Applied Physics*, 24:493–518, 1991.
- [67] F.M. Poli et al. Transition from drift to interchange instabilities in an open magnetic field line configuration. *Physics of Plasmas*, 15:032104, 2008.
- [68] C. Theiler. *Basic Investigation of Turbulent Structures and Blobs of Relevance for Magnetic Fusion Plasmas*. PhD thesis, EPFL, CRPP, 2011. [infoscience.epfl.ch/record/169605/files/EPFL\\_TH5228.pdf](http://infoscience.epfl.ch/record/169605/files/EPFL_TH5228.pdf).
- [69] I. Furno et al. Mechanism for blob generation in the TORPEX toroidal plasma. *Physics of Plasmas*, 15:055903, 2008.
- [70] C. Theiler et al. Practical solutions for reliable triple probe measurements in magnetized plasmas. *Review of Scientific Instruments*, 82:013504, 2011.
- [71] B. Labit et al. Two-dimensional time resolved measurements of toroidal velocity correlated with density blobs in magnetized plasmas. *Review of Scientific Instruments*, 79:086104, 2008.
- [72] I. Furno et al. Pre-sheath density drop induced by ion-neutral friction along plasma blobs and implications for blob velocities. *Physics of Plasmas*, 21:012305, 2014.
- [73] S. Chen et al. Instantaneous direct display system of plasma parameters by means of triple probe. *Journal of Applied Physics*, 36:2363, 1965.
- [74] S.H. Muller. *Turbulence in Basic Toroidal Plasmas*. PhD thesis, EPFL, CRPP, 2006. [infoscience.epfl.ch/record/89659/files/EPFL\\_TH3672.pdf](http://infoscience.epfl.ch/record/89659/files/EPFL_TH3672.pdf).
- [75] [http://www.vacom-shop.de/epages/VacomShop.sf/en\\_GB/?ViewObjectID=32405&Currency=EUR](http://www.vacom-shop.de/epages/VacomShop.sf/en_GB/?ViewObjectID=32405&Currency=EUR).
- [76] <http://www.d-tacq.com/acq196cpci.shtml>.
- [77] P.C. Stangeby et al. The nature of plasma fluxes to surfaces nearly tangential to the magnetic field. *Nuclear Fusion*, 32:2079–2089, 1992.
- [78] I.H. Hutchinson. Flowing plasmas and absorbing objects: analytic and numerical solutions culminating 80 years of ion-collection theory. *Plasma Physics and Controlled Fusion*, 52:124005, 2010.
- [79] M. Weinlich et al. Flush mounted langmuir probes in an oblique magnetic field. *Physics of Plasmas*, 4:2151, 1997.
- [80] M. Cacace et al. Langmuir probes design for the actively cooled divertor baffle in WEST. *Fusion Engineering and Design*, 93:15–18, 2015.

## Bibliography

---

- [81] G.F. Matthews et al. Investigation of the fluxes to a surface at grazing angles of incidence in the tokamak boundary. *Plasma Physics and Controlled Fusion*, 32:1301, 1990.
- [82] C. Theiler et al. Properties of convective cells generated in magnetized toroidal plasmas. *Physics of Plasmas*, 19:082304, 2012.
- [83] I. Furno et al. Direct two-dimensional measurements of the field-aligned current associated with plasma blobs. *Physical Review Letters*, 106:245001, 2011.
- [84] A. Fasoli et al. Basic investigations of electrostatic turbulence and its interaction with plasma and suprathermal ions in a simple magnetized toroidal plasma. *Nuclear Fusion*, 53:063013, 2013.
- [85] D. Iraji et al. Imaging of turbulent structures and tomographic reconstruction of TORPEX plasma emissivity. *Physics of Plasmas*, 17:122304, 2010.
- [86] D. Iraji. *Fast imaging of turbulent plasmas in the TORPEX device*. PhD thesis, EPFL, CRPP, 2011. [infoscience.epfl.ch/record/165761/files/EPFL\\_TH5073.pdf](http://infoscience.epfl.ch/record/165761/files/EPFL_TH5073.pdf).
- [87] A. Bovet et al. Three-dimensional measurements of non-diffusive fast ion transport in TORPEX. *Plasma Physics Controlled Fusion*, 55:124021, 2013.
- [88] A. Bovet. *Suprathermal ion transport in turbulent magnetized plasmas*. PhD thesis, EPFL, CRPP, 2015. [infoscience.epfl.ch/record/205009/files/EPFL\\_TH6527.pdf](http://infoscience.epfl.ch/record/205009/files/EPFL_TH6527.pdf).
- [89] P. Ricci et al. Turbulence phase space in simple magnetized toroidal plasmas. *Phys. Rev. Lett.*, 104:145001, 2010.
- [90] C. Theiler et al. Cross-field motion of plasma blobs in an open magnetic field line configuration. *Physical Review Letters*, 103:065001, 2009.
- [91] F.M. Poli et al. Development of electrostatic turbulence from drift-interchange instabilities in a toroidal plasma. *Physics of Plasmas*, 14:052311, 2007.
- [92] P. Ricci et al. Simulation of plasma turbulence in scrape-off layer conditions: the GBS code, simulation results and code validation. *Plasma Physics and Controlled Fusion*, 54:124047, 2012.
- [93] S.I. Krasheninnikov et al. Recent theoretical progress in understanding coherent structures in edge and SOL turbulence. *Journal of Plasma Physics*, 74:679–717, 2008.
- [94] J.R. Myra et al. Blob birth and transport in the tokamak edge plasma: Analysis of imaging data. *Physics of Plasmas*, 13:092509, 2006.
- [95] I. Furno et al. Experimental observation of the blob-generation mechanism from interchange waves in a plasma. *Phys. Rev. Lett.*, 100:055004, 2008.
- [96] M. Podesta et al. Cross-field transport by instabilities and blobs in a magnetized toroidal plasma. *Physical Review Letters*, 101:16–19, 2008.

- 
- [97] C. Theiler et al. Convective cells and blob control in a simple magnetized plasma. *Physical Review Letters*, 108:1–5, 2012.
- [98] B. Labit et al. Universal statistical properties of drift-interchange turbulence in TORPEX plasmas. *Physical Review Letters*, 98:255002, 2007.
- [99] F. Sattin et al. On the statistics of edge fluctuations: comparative study between various fusion devices. *Plasma Phys. Controlled Fusion*, 51:055013, 2009.
- [100] P. Ricci et al. Langmuir probe-based observables for plasma-turbulence code validation and application to the TORPEX basic plasma physics experiment. *Physics of Plasmas*, 16:055703, 2009.
- [101] P. Ricci et al. Methodology for turbulence code validation: Quantification of simulation-experiment agreement and application to the TORPEX experiment. *Physics of Plasmas*, 18:032109, 2011.
- [102] B. Lehnert. On the possibilities of ring-current configurations as a fusion device. *Plasma Physics*, 10:281, 1968.
- [103] S. Skellet. The Culham superconducting levitron. *Cryogenics*, October:563–568, 1975.
- [104] W.M. Haynes. *Handbook of Chemistry and Physics*. CRC Press, 2014.
- [105] E.B. Rosa et al. Formulas and tables for the calculation of mutual and self-inductance. *Scientific Papers of the Bureau of Standards*, 169, 1916.
- [106] Smythe. *Static and Dynamic Electricity*. International Series in Pure and Applied Physics, 1950.
- [107] N.W. Ashcroft and N.D. Mermin. *Solid State Physics*. Brooks/Cole, 1976.
- [108] R.A. Matula. Electrical resistivity of Copper, Gold, Palladium and Silver. *Journal of Physical and Chemical Reference Data*, 8:1147, 1979.
- [109] H.B. Dwight. Two cases of calculation of mechanical forces in electric circuits. *Electric Circuits*, page 570, 1927.
- [110] C. Schott et al. High accuracy magnetic field measurements with a hall probe. *Review of Scientific Instruments*, 70:2703, 1999.
- [111] M. Podesta. *Plasma Production and Transport in a Simple Magnetized Toroidal Plasma*. PhD thesis, EPFL, CRPP, 2007. <http://infoscience.epfl.ch/record/100034>.
- [112] M. Podesta et al. Experimental characterization and modelling of the particle source in an Electron-Cyclotron wave driven toroidal plasma. *Plasma Phys. Controlled Fusion*, 48:1053–1062, 2006.

## Bibliography

---

- [113] O.E. Garcia et al. Interchange turbulence in the TCV scrape-off layer. *Plasma Physics Controlled Fusion*, 48:109, 2006.
- [114] P. Stoica and R. Moses. *Introduction to Spectral Analysis*. Prentice Hall, 1997.
- [115] J.M. Beall et al. Estimation of wavenumber and frequency spectra using fixed probe pairs. *Journal of Applied Physics*, 53:3933, 1982.
- [116] F.M. Poli et al. Experimental characterization of drift-interchange instabilities in a simple toroidal plasma. *Physics of Plasmas*, 13:102104, 2006.
- [117] N. Iwama et al. A correlation method for estimating wave-number spectrum moments of fluctuations. *Applied Physics Letters*, 31:783, 1977.
- [118] S.H. Muller et al. Probabilistic analysis of turbulent structures from two-dimensional plasma imaging. *Physics of Plasmas*, 13:100701, 2006.
- [119] R.J. Adrian. Conditional eddies in isotropic turbulence. *Physics of Fluids*, 22:2065, 1979.
- [120] H. Johnsen et al. Conditional eddies in plasma turbulence. *Physics of Fluids*, 30:2239, 1987.
- [121] O. Kluber et al. MHD mode structure and propagation in the ASDEX tokamak. *Nuclear Fusion*, 31:907, 1991.
- [122] S.I. Braginskii. Transport processes in a plasma. *Rev. Plasma Phys.*, 1:205, 1965.
- [123] C. Wersal et al. A first-principle self-consistent model of plasma turbulence and kinetic neutral dynamics in the tokamak scrape-off layer. *Nuclear Fusion*, submitted.
- [124] S. Jolliet et al. Aspect ratio effects on limited scrape-off layer plasma turbulence. *Physics of Plasmas*, 21:022303, 2014.
- [125] A. Masetto et al. Low-frequency linear-mode regimes in the tokamak scrape-off layer. *Physics of Plasmas*, 19:112103, 2012.
- [126] A. Masetto. *Turbulent regimes in the tokamak scrape-off layer*. PhD thesis, EPFL, CRPP, 2014. [infoscience.epfl.ch/record/200160/files/EPFL\\_TH6197.pdf](http://infoscience.epfl.ch/record/200160/files/EPFL_TH6197.pdf).
- [127] C.S. Pitcher et al. Experimental divertor physics. *Plasma Phys. Control. Fusion*, 39:779–930, 1997.
- [128] J.A. Boedo et al. Electric field-induced plasma convection in tokamak divertors. *Physics of Plasmas*, 7:1075, 2000.
- [129] D. D’Ippolito et al. Convective transport by intermittent blob-filaments: Comparison of theory and experiment. *Physics of Plasmas*, 18:060501, 2011.
- [130] T.D. Rognlien et al. Two-dimensional electric fields and drifts near the magnetic separatrix in divertor tokamaks. *Physics of Plasmas*, 6:1851, 1999.

- [131] M.J. Schaffer et al. Large ExB convection near the divertor X-point. *Journal of Nuclear Materials*, 290-293:530–536, 2001.
- [132] S.H. Muller et al. Studies of blob formation, propagation and transport mechanisms in basic experimental plasmas (TORPEX and CSDX). *Plasma Phys. Control. Fusion*, 51:055020, 2009.
- [133] B. Shanahan et al. Modelling of magnetic nulls using non-aligned coordinate systems in BOUT++. In *42nd European Physical Society Conference on Plasma Physics*, 2015.





# Acknowledgements

During my academic journey in the field of plasma physics, I had the luck from the very beginning to be surrounded by people with outstanding scientific competences, but most of all with remarkable human qualities. I feel I first own an acknowledgment to Dr Gianluca Pucella and in particular to Dr Onofrio Tudisco, who guided me in my Master studies and contributed to set the path that drove me to the CRPP. Without him, I strongly doubt I would have even started such a unique experience in Lausanne. Before beginning my Ph.D, I honestly thought I would have hardly met supervisors of comparable willingness, but I was wrong. I want to deeply thank my supervisors Prof. Ambrogio Fasoli and Dr Ivo Furno for the role they had during the last four years. I think they were perfectly complementary. I thank Ambrogio for his constant guide and the useful discussions. I really appreciated his support and his ability to always underline the positive aspects in every situation. Being assistant of some of his teaching courses was a great experience, in particular that of Plasma Physics III. I am grateful to Ivo for his ability to provide supervision with the right frequency, putting the right pressure to achieve the goals we set. I think he possesses the teaching skills and passion that every supervisor should have, with the ability to convey to his students curiosity and enthusiasm. He is the clear example that a good supervisor has to be more than merely an high-level scientist. I want to remark the pleasure of sharing with both Ivo and Ambrogio activities outside the scientific framework.

Être un expérimentateur m'a donné le plaisir de travailler avec la plupart du personnel du CRPP, qui constitue une équipe exceptionnelle. J'aimerais bien remercier tous les scientifiques, en particulier le Prof. Paolo Ricci, qui à été toujours très disponible pour répondre à mes questions.

Merci beaucoup à l'atelier et bureau de construction. René, Jürgen et Patrice, pour avoir suivi surtout la première et la plus délicate phase technique de mon projet de thèse. Merci Roger pour nous avoir aidés pendant l'installation du fil toroidal. William, Régis, Nelson, André et Christian M., qui ont été toujours sympathiques et disponibles pour résoudre mes problèmes techniques, de quoi que ce soit. Merci aussi à Robert, qui pendant ces années avait la porte de son bureau toujours ouverte pour m'aider à avancer avec différents projets. Je veux remercier le service électrique, en particulier Damien, Steve et Ugo. Merci aussi à Blaise et Philippe, qui ont suivi la partie électronique de mes expériences. Merci au service informatique, avec Pierre et Xavier qui étaient constamment disponibles. Merci au service du vide, Frédéric et en particulier à Omar, pour m'avoir aidé aussi avec des soucis pas liés directement au vide

## Acknowledgements

---

de TORPEX. Il a vraiment été une personne sur laquelle compter. Je dois aussi mentionner et remercier la compétence et la rigueur des secrétaires, en particulier Edith, pour être toujours prête à résoudre les problèmes logistiques avec le sourire.

A special role during a Ph.D is played by the Ph.D colleagues, in particular at the CRPP, where they constitute an international group of extremely clever students. This gave me the possibility to constantly exchange ideas and points of view with people having different backgrounds, which is a unique experience. Not to mention the moments we shared outside the lab. I want to thank them all.

I must thank Silvano, Daniele and Federico N., sharing with them a lot of laughs. You constantly reminded me that a simple joke could be enough to shed some light on a bad day. A special thanks goes to Karim, Jonathan E, Kyle, Joaquim and Christian. I think it's not easy to find people as intelligent as friendly. I am grateful for the great moments we spent together, including the discussions and experiences we performed in the lab. It really meant a lot to me. Giant Josef, during the the last four years you are probably the person I have spent the most time with, sharing with you our flat. You first saved me from the nightmare of finding an apartment in Lausanne, and then turned out to be the perfect housemate. You are a great guy and I am sure our friendship will continue after our experience at the CRPP. Thank you for everything.

Mon cher Alexandre Dominique Bovet, tu as été un excellent collègue, compagnon de bureau, ami et aussi enseignant de français. Si j'arrive presque à parler une troisième langue c'est en grande partie en raison de ta patience à corriger mes fautes de langue, encore, et encore. Je suis honoré de t'avoir rencontré.

La parte forse più difficile dell'allontanarsi dal proprio paese d'origine è data dalla distanza, non solo territoriale, che si potrebbe venire a creare con le persone più care. Giammarco, Lorenzo, Niccolo e Davide, vi ringrazio di cuore per essere sempre stati pronti a rivederci durante quei pochi giorni di rientro a casa. Ciò ha significato davvero molto e ha dimostrato che per alcune amicizie, le distanze territoriali non sono in fin dei conti determinanti. Grazie al mio amico e collega Matteo Mitrano, con cui ho avuto il piacere di mantenere i contatti e le piacevoli discussioni mi hanno permesso di distrarmi dalla routine quotidiana. Un grazie speciale alla mia famiglia biologica, Giannina, Mauro e Marco, per la totale disponibilità ed il supporto che mi avete dato in questi anni, ed anche alla famiglia acquisita, Caterina, che hai sempre segnato i miei rientri a Roma con la tua accoglienza e le tue doti culinarie.

Ci tengo a chiudere i ringraziamenti rivolgendomi ad una persona speciale, che come poche altre avrebbero fatto, ha sopportato questi quattro anni di distanza con uno sforzo che poche persone possono capire fino in fondo. Rosa, grazie per la pazienza e la forza che hai avuto. Te ne sono profondamente grato e lo terro sempre presente nell'avvenire che ci apprestiamo ad affrontare insieme. Grazie davvero.

*Lausanne, 20 July 2015*

Fabio Avino

# Fabio Avino

Nationality: Italian

Date of Birth: 21.06.1986



## Contact

E-mail: fabioavino1986@gmail.com

Cell: (+39) 3286924236 / (+41) 216936588

## Education

### Ph.D in Physics

Centre de Recherches en Physique des Plasmas (CRPP), EPFL

Lausanne (Switzerland)  
**June 2011 – July 2015**

### Master Degree in Physics

University of Roma "La Sapienza" - Frascati ENEA centre

Graduated with 110 cum laude/110.

Roma (Italy)  
**Sep. 2008 – Oct. 2010**

### Bachelor's Degree in Physics

University of Roma "La Sapienza"

Graduated with 110 cum laude/110.

Roma (Italy)  
**Sep. 2005 – Oct. 2008**

## Fellowships

### Internship at the Joint European Torus

EFDA JET, Culham Science Centre

Abingdon (United Kingdom)  
**Nov. 2010 – Feb. 2011**

## Teaching experiences

### Teaching assistant:

General Physics I  
General Physics II  
General Physics III  
Plasma Physics III

Autumn 2011, Autumn 2012  
Spring 2012, Spring 2013  
Autumn 2013, Autumn 2014  
Spring 2014

### Student supervision:

G. Wuilloud - TPIV project  
G. Wuilloud - Minor project  
S. Patrick - Erasmus project

Spring 2014  
Autumn 2014  
Autumn 2014 - Spring 2015

## Awards

**Recognition for exceptional assistantship work at EPFL**

2014

## Conference contributions (as first author)

1. **F. Avino**, A. Bovet, A. Fasoli, I. Furno, J. Loizu, A. Masetto, and P. Ricci. *"First fluctuation measurements in the new confined plasma configuration of the TORPEX device"*. 17<sup>th</sup> **Joint EU-US Transport Taskforce Meeting in combination with the 4<sup>th</sup> EFDA Transport Topical Group Meeting**, Padova, Italy, 3-6 September 2012, (poster).

2. **F. Avino**, A. Bovet, A. Fasoli, I. Furno, J. Loizu, A. Masetto, P. Ricci. "*First results on the plasma fluctuations of the TORPEX device in the new magnetic field configurations*". **2<sup>nd</sup> PhD Event in Fusion Science and Engineering**, Abbaye des Prémontrés, Pont-à-Mousson, France, 22-25 October 2012, (poster + talk).
3. **F. Avino**, A. Bovet, A. Fasoli, I. Furno, S. Jolliet, J. Loizu, A. Masetto, and P. Ricci. "*Study of plasma fluctuations in new closed flux-surface configurations of the TORPEX experiment*". **Joint Annual Meeting of the Austrian Physical Society and Swiss Physical Society**, JKU Linz, Austria, 3-6 September 2013, (talk).
4. **F. Avino**, A. Bovet, A. Fasoli, I. Furno, and P. Ricci. "*Plasma turbulence studies in the TORPEX basic plasma physics device: from concentric flux surfaces to single-null X-points*". **41st European Physical Society Conference on Plasma Physics**, Berlin, Germany, 23-27 June 2014, (poster).

### Peer-reviewed publications

1. **F. Avino**, A. Fasoli, I. Furno, P. Ricci, and C. Theiler. "*X-point effect on plasma blob dynamics*", submitted to **Physical Review Letters**.
2. I. Furno, **F. Avino**, A. Bovet, A. Diallo, A. Fasoli, K. Gustafson, D. Iraj, B. Labit, J. Loizu, S.H. Muller, G. Plyushchev, M. Podestà, F.M. Poli, P. Ricci, and C. Theiler. "*Plasma turbulence, suprathermal ion dynamics and code validation on the basic plasma physics device TORPEX*", **Journal of Plasma Physics** 2015.
3. M. Spolaore, N. Vianello, I. Furno, D. Carralero, M. Agostini, J. A. Alonso, **F. Avino**, R. Cavazzana, G. De Masi, A. Fasoli, C. Hidalgo, E. Martines, B. Momo, A. Scaggion, P. Scarin, S. Spagnolo, G. Spizzo, C. Theiler, and M. Zuin. "*Electromagnetic turbulent structures: A ubiquitous feature of the edge region of toroidal plasma configurations*", **Physics of Plasmas** 22, 012310 (2015).
4. **F. Avino**, A. Fasoli, I. Furno, S. Jolliet, and P. Ricci. "*Basic characterization of TORPEX electrostatic modes in closed field line configurations*", **Physics of Plasmas** 21, 122115 (2014).
5. **F. Avino**, A. Fasoli, and I. Furno. "*The new TORPEX in-vessel toroidal conductor for the generation of a poloidal magnetic field*", **Rev. Sci. Instrum.** 85, 033506 (2014).
6. P. Martin, M.E. Puiatti, P. Agostinetti, M. Agostini, J.A. Alonso, V. Antoni, L. Apolloni, F. Auriemma, **F. Avino**, A. Barbalace, M. Barbisan, T. Barbui, S. Barison, M. Barp, M. Baruzzo, P. Bettini, M. Bigi, R. Bilel, M. Boldrin, T. Bolzonella, D. Bonfiglio, F. Bonomo, M. Brombin, A. Buffa, C. Bustreo, A. Canton, S. Cappello, D. Carralero, L. Carraro, R. Cavazzana, L. Chacon, B. Chapman, G. Chitarin, G. Ciaccio, W.A. Cooper, S. Dal Bello, M. Dalla Palma, R. Delogu, A. De Lorenzi, G.L. Delzanno, G. De Masi, M. De Muri, J.Q. Dong, D.F. Escande, F. Fantini, A. Fasoli, A. Fassina, F. Fellin, A. Ferro, S. Fiameni, J.M. Finn, C. Finotti, A. Fiorentin, N. Fonnesu, J. Framarin, P. Franz, L. Frassinetti, I. Furno, M. Furno Palumbo, E. Gaio, E. Gazza, F. Ghezzi, L. Giudicotti, F. Gnesotto, M. Gobbin, W.A. Gonzales, L. Grando, S.C. Guo, J.D. Hanson, C. Hidalgo, Y. Hirano, S.P. Hirshman, S. Ide, Y. In, P. Innocente, G.L. Jackson, S. Kiyama, S.F. Liu, Y.Q. Liu, D. López Bruna, R. Lorenzini, T.C. Luce, A. Luchetta, A. Maistrello, G. Manduchi, D.K. Mansfield, G. Marchiori, N. Marconato, D. Marcuzzi, L. Marrelli, S. Martini, G. Matsunaga, E. Martines, G. Mazzitelli, K. McCollam, B. Momo, M. Moresco, S. Munaretto, L. Novello, M. Okabayashi, E. Olofsson, R. Paccagnella, R. Pasqualotto, M. Pavei, S. Peruzzo, A. Pesce, N. Pilan, R. Piovan, P. Piovesan, C. Piron, L. Piron, N. Pomaro, I. Predebon, M. Recchia, V. Rigato, A. Rizzolo, A.L. Roquemore, G. Rostagni, A. Ruzzon, H. Sakakita, R. Sanchez, J.S. Sarff, E. Sartori, F. Sattin, A. Scaggion, P. Scarin, W. Schneider, G. Serianni, P. Sonato, E. Spada, A. Soppelsa, S. Spagnolo, M. Spolaore, D.A. Spong, G. Spizzo, M. Takechi, C. Taliercio, D. Terranova, C. Theiler, V. Toigo, G.L. Trevisan, M. Valente, M. Valisa, P. Veltri, M. Veranda, N. Vianello, F. Villone, Z.R. Wang, R.B. White, X.Y. Xu, P. Zaccaria, A. Zamengo, P. Zanca, B. Zaniol, L. Zanotto, E. Zilli, G. Zollino and M. Zuin. "*Overview of the RFX-mod fusion science programme*", **Nucl. Fusion** 53, 104018 (2013).

7. A. Fasoli, **F. Avino**, A. Bovet, I. Furno, K. Gustafson, S. Jolliet, J. Loizu, D. Malinverni, P. Ricci, F. Riva, C. Theiler, M. Spolaore, and N. Vianello. "*Basic investigations of electrostatic turbulence and its interaction with plasma and suprathermal ions in a simple magnetized toroidal plasma*", **Nucl. Fusion** 53, 063013 (2013).
8. O. Tudisco, A. Canton, P. Innocente, C. Mazzotta, V.G. Petrov, A.A. Petrov, **F. Avino**, G. Rocchi. "*New diagnostics for density measurement on Frascati Tokamak upgrade*", **Nuclear Instruments and Methods in Physics Research A** 270, 20 (2013).
9. V.G. Petrov, A.Yu. Malysheva, V.K. Markova, A.A. Petrova, **F. Avino**, R. de Angelis, and O. Tudisco. "*First Results from Plasma Density Measurements in the FTU Tokamak by Means of a Two-Frequency Pulsed Time-of-Flight Refractometer*", **Plasma Physics Reports** 38, 343 (2013).
10. M. Gelfusa, A. Murari, P. Gaudio, A. Boboc, D. Mazon, **F. Avino**, I. Lupelli, F.P. Orsitto, O. Tudisco, and JET-EFDA Contributors. "*New Approximations and Calibration Methods to Provide Routine Real-Time Polarimetry on JET*", **IEEE Transactions on Plasma Science** 40, 1149 (2012).

## Employment

June 2011 - July 2015 : Research assistant at EPFL, Lausanne, Switzerland.

2008 - 2010 : Assistant at Laboratori didattici Pontecorvo, University of Roma "La Sapienza", Italy.

Last updated: July 20, 2015